Advances in laser spectroscopy of superheavy elements: Resonance ionization spectroscopy on ^{253,254,255}Es and a new gas-jet based high-resolution spectroscopy setup

Dissertation

zur Erlangung des Grades
"Doktor der Naturwissenschaften"
im Promotionsfach Chemie

am Fachbereich Chemie, Pharmazie, Geographie und Geowissenschaften
der Johannes Gutenberg-Universität Mainz

Steven Nothhelfer

geb. in Nastätten

Mainz, März 2022

1. Berichterstatter:	Personenbezogene Daten
2. Berichterstatter:	Personenbezogene Daten
Tag der mündlichen Prüfung:	Personenbezogene Daten

Die vorliegende Arbeit wurde in der Zeit vom April 2019 bis März 2022 im Helmholtz-Institut Mainz unter der Anleitung von [redacted] angefertigt.

Ich versichere, dass ich diese Arbeit eigenständig verfasst und keine anderen als die angegebenen Hilfsmittel (Literatur, Apparaturen, Materialien) verwendet sowie Zitate kenntlich gemacht habe.

Ort, Datum	Steven Nothhelfer

"I do not know what I may appear to the world;
but to myself I seem to have been only like a boy
playing on the seashore, and diverting myself in
now and then finding a smoother pebble or a prettier
shell than ordinary, whilst the great ocean of
truth lay all undiscovered before me"
Sir Isaac Newton

Abstract

Laser resonance ionization spectroscopy (RIS) is a versatile and sensitive technique to unveil fundamental properties of both the atomic structure and the nuclear structure of the atomic nucleus. With regard to these investigations, the region of heavy and superheavy elements is of particular interest as the valence shell electrons are strongly influenced by relativistic effects, electron-electron correlations, and quantum electrodynamic effects leading to distinct atomic properties and chemical behavior in comparison to their lighter chemical homologues. Einsteinium (Es, $Z = 99$) and fermium (Fm, $Z = 100$) are the heaviest elements which can be produced in weighable quantities in high-flux research reactors. The elements beyond fermium ($Z > 100$), e.g. nobelium (No, $Z = 102$), are only produced through fusion-evaporation or multinucleon transfer (MNT) reactions. Low production rates of at most a few particles per second pose an experimental challenge. Furthermore, the radionuclides must also be decelerated from a few tens of MeV to rest and neutralized to perform RIS.
The first part of this thesis describes the construction, development, characterization, and optimization of a new gas-jet apparatus for high-resolution laser spectroscopy of heavy and superheavy elements. This new setup combines the high-resolution gas-jet laser ionization developed at KU Leuven and known techniques from the RAdiation Detection Resonance Ionization Spectroscopy (RADRIS) method. In the latter the stopping of highly charged recoil ions from fusion-evaporation in a gas-filled cell as well as ion collection, neutralization, and desorption from a heated filament has proven to be overall highly efficient and is therefore used in the new gas-jet setup. Based on simulations a first layout was derived and assembled. Measurements were performed on $^{\text{nat}}$Yb and $^{154\text{-}156}$Yb leading to major design changes of the flow channel, the de Laval nozzle, the radiofrequency quardrupole (RFQ), as well as the conception of two new transport electrodes. After the implementation of these changes further measurements on $^{\text{nat}}$Yb and ^{174}Yb were performed. A spectral resolution of $\leq 400\,\text{MHz}$ was obtained being sufficient for the anticipated on-line studies of nobelium.
The second part is dedicated to RIS performed on the rare isotopes ^{253,254,255}Es. With sample sizes ranging down to femtograms ($\approx 2\,\text{pg}$ ^{253}Es, $\approx 4\,\text{pg}$ ^{254}Es, $\approx 4\,\text{fg}$ ^{255}Es), the measurements were performed at the Resonance Ionization Spectroscopy in Collinear geometry (RISIKO) mass separator in Mainz. Ten ground-state transitions were investigated in ^{254}Es with the hyperfine structure being resolved in five transitions. The ground-state transition at 351.5 nm was measured additionally in the isotopes ^{253,255}Es, giving access to the isotope shifts for $^{253\text{-}255}$Es. Analysing the spectra yielded hyperfine structure constants A and B for all three isotopes. The nuclear spins of $I(^{254}\text{Es}) = 7$ and $I(^{255}\text{Es}) = 7/2$ were deduced, in agreement with the so far only tentatively assigned literature values. Additionally, the magnetic-dipole moments of $\mu_I(^{254}\text{Es}) = 3.42(7)\mu_\text{N}$ and $\mu_I(^{255}\text{Es}) = 4.14(10)\mu_\text{N}$ and the spectroscopic electric quadrupole moments of $Q_s(^{254}\text{Es}) = 9.6(1.2)\,e\text{b}$ and $Q_s(^{255}\text{Es}) = 5.1(1.7)\,e\text{b}$ were derived experimentally. The extracted magnetic-dipole moment of ^{254}Es corrects the less precise literature value of $\mu_I(^{254}\text{Es}) = 4.35(41)\mu_\text{N}$.

Zusammenfassung

Die Resonanz-Ionisations-Spektroskopie (RIS) ist eine vielseitige und sensitive laserspektroskopische Methode, um fundamentale Eigenschaften der Atomstruktur sowie auch der Kernstruktur der Atomkerne zu enthüllen. Im Hinblick auf diese Untersuchungen sind die schweren und superschweren Elemente von besonderem Interesse, da die Elektronenhülle stark von relativistischen Effekten, Elektron-Elektron Korrelationen und quantenelektrodynamischen Effekten beeinflusst wird und zu abweichenden atomaren Eigenschaften sowie chemischem Verhalten im Vergleich zu ihren leichteren chemischen Homologen führen kann. Einsteinium (Es, $Z = 99$) und Fermium (Fm, $Z = 100$) sind die schwersten Elemente, welche in wägbaren Mengen in einem Hochfluss-Reaktor erbrütet werden können. Alle schwereren Elemente ($Z > 100$) wie z.B. Nobelium (No, $Z = 102$) können nur in Fusions-Verdampfungs-Reaktionen oder in Multinukleonen-Transfer-Reaktionen erzeugt werden. Geringe Produktionsraten von maximal ein paar Teilchen pro Sekunde, das Abbremsen der Radionuklide von einigen Dutzend MeV in den Ruhezustand und deren Neutralisation als Voraussetzung für RIS stellen eine experimentelle Herausforderung dar.
Der erste Teil dieser Arbeit behandelt den Aufbau, die Entwicklung, die Charakterisierung und die Optimierung eines neues Gas-jet Aufbaus für hochauflösende Laserspektroskopie an schweren und superschweren Elementen. Der Aufbau kombiniert die an der KU Leuven entwickelte hochauflösende Gas-Jet Laserionisation mit Techniken von der RADRIS (von engl. *RAdiation Detection Resonance Ionization Spectroscopy*) Methode. In Letzterer hat das Stoppen von hochgeladenen Rückstoßkernen aus der Fusions-Verdampfungs-Reaktion in einer Gas-gefüllten Zelle in Kombination mit Ionensammlung, Neutralisation und Desorption von einem heißen Filament eine hohe Gesamteffizienz bewiesen und wird daher in der neuen Apparatur verwendet. Auf Basis von Simulationen wurde ein erster Entwurf der Apparatur entwickelt und aufgebaut. Messungen an $^{\text{nat}}$Yb und $^{154\text{-}156}$Yb zeigten, dass Design-Änderungen des Strömungskanals, der de Laval Düse, des Radio-Frequenz-Quadrupol (RFQ), sowie zwei neue Transportelektroden benötigt wurden. Nach deren Einbau wurden weitere Messungen an $^{\text{nat}}$Yb und ^{174}Yb durchgeführt, wobei eine spektrale Auflösung $\leq 400\,\text{MHz}$ erzielt werden konnte. Dies ist ausreichend für die geplanten Online-Messungen an Nobelium.
Der zweite Teil behandelt die RIS an ^{253,254,255}Es. Diese Messungen wurden an geringen Probenmengen bis hinunter in den Femtogramm-Bereich ($\approx 2\,\text{pg}$ ^{253}Es, $\approx 4\,\text{pg}$ ^{254}Es, $\approx 4\,\text{fg}$ ^{255}Es) an dem *Resonanzionisations-Spektroskopie in kollinearer Geometrie* (RISIKO) Massenseparator in Mainz durchgeführt. Hierbei wurden zehn Grundzustandsübergänge in ^{254}Es untersucht, wobei die Hyperfeinstruktur in fünf dieser Übergänge aufgelöst werden konnte. Der Grundzustandsübergang bei 351.5 nm wurde zudem für die Isotope ^{253,255}Es gemessen. Neben der Isotopieverschiebung konnten aus den gemessenen Hyperfeinstrukturen die Konstanten A und B extrahiert werden, sowie die bisher vorläufig zugeordneten Kernspins $I(^{254}\text{Es}) = 7$ und $I(^{255}\text{Es}) = 7/2$ bestätigt werden. Weiterhin konnten die magnetischen Dipolmomente $\mu_I(^{254}\text{Es}) = 3.42(7)\mu_\text{N}$ und $\mu_I(^{255}\text{Es}) = 4.14(10)\mu_\text{N}$ sowie die spektroskopischen elektrischen Quadrupolmomente $Q_s(^{254}\text{Es}) = 9.6(1.2)\,e\text{b}$ und $Q_s(^{255}\text{Es}) =$

5.1(1.7) eb experimentell bestimmt werden. Das hier bestimmte magnetische Dipolmoment von ^{254}Es korrigiert den bisher deutlich ungenauer bestimmten Literaturwert von $\mu_I(^{254}\mathrm{Es}) = 4.35(41)\mu_\mathrm{N}$.

Contents

IV. Appendix

1. Introduction

In this work the focus is on the actinides, which span the region from actinium (Ac, $Z = 89$) to lawrencium (Lr, $Z = 103$). Their atomic structure is strongly influenced by relativistic effects, electron-electron correlations, and quantum electrodynamic (QED) effects, which often lead to several close-lying atomic levels and possible changes in the ground-state configuration (see Fig. 2.3) compared to non-relativistic models [1, 2]. The impact of these effects on the atomic structure gain in importance when going to heavier elements, even influencing binding energies of the valence electrons and as a result chemical properties [3]. Due to the lack of abundant isotopes with suitable half-lives and the scarcity of available material from breeding processes (see section 5.2) [4, 5], fusion-evaporation reactions (see section 3.1) [6, 7], and multinucleon transfer (MNT) reactions [6] the atomic structure of most actinides is only partially known, with information quickly diminishing from einsteinium (Es, $Z = 99$) onwards [1].
The nuclear structure of the actinides is also of interest, as the stabilization by nuclear shell effects competes with the Coulomb repulsion between the protons in the nucleus [1, 8]. Most actinide nuclei are well deformed and exhibit interesting traits, including, e.g., the octupole deformation and the appearance of K-isomers [1]. Going to the nuclei of superheavy elements (SHE, $Z \geq 104$ [9]), a central depression in the proton distribution is predicted, originating from the strong Coulomb repulsion within the nucleus, which may result in so-called bubble nuclei [1, 10].
The nuclear liquid-drop model (LDM) predicts instant spontaneous fission for all elements with $Z \geq 104$ as the repulsive force between the protons in the nucleus is sufficient to overcome the attractive nuclear strong force [9, 11, 12]. As isotopes of elements up to oganesson (Og, $Z = 118$) were successfully produced and detected by their α-decay [1, 13, 14], a more sophisticated model was required. In the nuclear shell model (SM) protons and neutrons occupy shells in the nucleus in analogy to electrons in the atomic shell [15, 16]. The nucleons have an intrinsic spin of 1/2 (fermions) and thus obey the Pauli principle, but in contrast to electrons minimize their total spin. Instead of the long range Coulomb force acting on the electrons, the nuclear strong force acting on the nucleons only has a short range. Consequently, the nuclear and atomic shells are entirely different [17]. Spin-orbit coupling in the nucleus results in splitting of the nuclear shells, whereas large energy gaps between these nuclear shells result in an increased nuclear stability. The number of nucleons needed to reach this increased stability are called magic numbers (2, 8, 20, 28, ...) and are generally applicable to isotopes close to stability [15, 18]. The introduction of nuclear shells stabilizes the nucleus and prevents spontaneous fission as shown in Fig. 1.1. An isomeric state is observed in the case of a second energy minimum at a higher nuclear deformation, which can decay either by internal transitions into the ground state or by spontaneous fission. In comparison to the lighter spherical magical nuclei, spherical heavy nuclei are no longer stable. Thus, new shells form in deformed heavy nuclei, e.g., at neutron numbers $N = 152$ and $N = 162$ [19, 20, 21], with their strength being sensitive to changes in the nuclear shape [20, 22, 23]. The size of the gap at $N = 152$ depends on the atomic number Z, being most

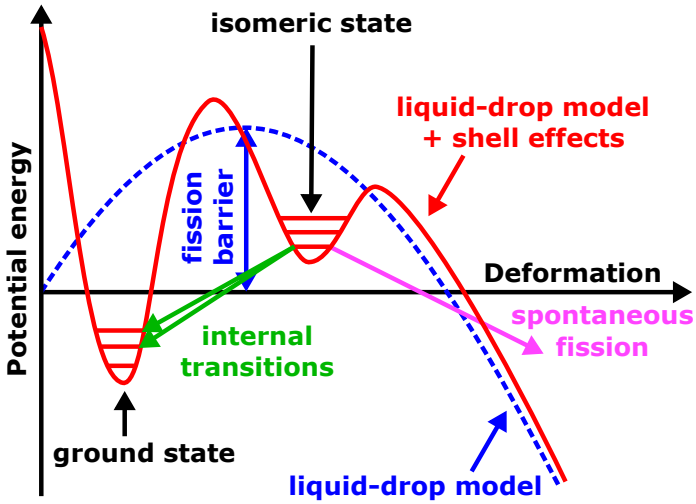

Figure 1.1.: Schematic comparison of the potential energy as a function of the nuclear deformation for the nuclear LDM (blue) and the nuclear SM (red). The fission barrier in the nuclear LDM vanishes for $Z \approx 104$. Nuclear shell effects stabilize the nucleus against spontaneous fission. Both the ground state and the isomeric state are populated in nuclear reactions. The figure is adapted from [24].

pronounced in fermium (Fm, $Z = 100$) and smaller for lighter and heavier elements [23]. This observation can be explained by a weak proton shell appearing at $Z = 100$ [20]. As the $N = 152$ shell closure is accessible in the heaviest actinides (see Fig. 5.2), a detailed study of their nuclear structure evolution is thus important.

An indirect way to study (the strength of) these shell effects is by probing the atomic shell. This offers indirect access to the nuclear structure, as the interplay between the nucleus and the surrounding electrons results in small perturbations in the atomic level structure known as hyperfine structure (HFS) [25, 26]. High-precision methods and instruments are required to resolve this HFS splitting. One such method is laser resonance ionization spectroscopy (RIS) [27, 28], which step-wise excites and ionizes electrons in an atomic shell and can be highly efficient if a sufficient photon flux is provided. Due to the unique, fingerprint-like structure of each element's atomic structure this technique is also highly element selective. From the obtained laser spectroscopic data one can determine atomic level energies, transition strengths, lifetimes, and the first ionization potential (IP), which is closely linked to the chemical behavior of each element [1, 29]. From the HFS one can extract the nuclear spin I, the spectroscopic electric quadrupole moment Q_s and the magnetic-dipole moment μ_I, with the latter being sensitive to the single-particle nature of the valence nucleon. The intrinsic quadrupole moment Q_0 can be related to Q_s and reflects the nuclear deformation [3]. Rich information on the underlying nuclear structure can be gained by comparing measured electromagnetic moments to theoretical predictions from, e.g., the nuclear shell-model [1, 3, 30]. From isotope shift (IS) measurements one can obtain changes in nuclear mean-square charge radii $\delta \langle r^2 \rangle$ with nuclear radii being sensitive to the nuclear structure such as deformation and shell effects. The nuclear mean-square charge radii often exhibit kinks around shell

closures. Thus, laser spectroscopy can be used to explore the behavior of nuclear systems [1, 25].

Precise atomic structure measurements have been performed for most elements up to the actinide region, but is sparse for the heaviest elements as suitable atomic transitions are scarcely known experimentally due to the low production quantities [1, 31]. Thus, information on the isotopes of einsteinium are scarce in literature with only 45 atomic levels reported for neutral einsteinium [31, 32, 33, 34, 35, 36] (see section 5.1). ^{253}Es ($T_{1/2} = 20.47\,\mathrm{d}$) was investigated with optical spectroscopy using µg-scale samples, yielding atomic transitions, hyperfine structure (HFS) splittings, and an assignment of the nuclear spin to $I = 7/2$ [32, 33]. A more accurate measurement of the ground-state HFS via atomic-beam magnetic-resonance (ABMR) enabled the determination of the nuclear dipole moment to $\mu_I = 4.10(7)\mu_\mathrm{N}$ and the spectroscopic electric quadrupole moment to $Q_s = 6.7(8)\,e\mathrm{b}$ for ^{253}Es [34]. The isotope ^{254}Es ($T_{1/2} = 275.7\,\mathrm{d}$) was studied by embedding in an iron crystal lattice and measuring the angular anisotropy of its α-particle emission. Assuming a nuclear spin of $I = 7$, taken from a tentative assignment from decay spectroscopy, a nuclear magnetic moment of $|\mu_I(^{254}\mathrm{Es})| = 4.35(41)\mu_\mathrm{N}$ was derived [37, 38, 39]. Furthermore, the first ionization potential (IP) was determined to $51\,358(2)\,\mathrm{cm}^{-1}$ by RIS [35]. The isomer $^{254\mathrm{m}}$Es ($T_{1/2} = 39\,\mathrm{h}$) was investigated additionally and a spin of $I = 2$ assigned [34]. In this work, more modern laser spectroscopy techniques allowed to reveal new insights on the atomic and nuclear structure of the isotopes ^{253,254,255}Es located above the $N = 152$ deformed shell closure. The prominent 351.5 nm ground-state transition was measured in all three isotopes, and four additional ground-state transitions were measured only in ^{254}Es. The very high efficiency of RIS inside a hot cavity allowed to work on pg and even fg sized samples [1, 40, 41].

For elements beyond fermium, where only accelerator based production paths are available, the RAdiation Detection Resonance Ionization Spectroscopy (RADRIS) technique [42, 43] at the velocity filter Separator for Heavy Ion reaction Products (SHIP) at GSI was successfully applied. For nobelium (No, $Z = 102$) several atomic levels and the first IP were measured for the first time [44, 45]. Furthermore, the isotope shifts of the $5f^{14}7s^2\ {}^1S_0 \rightarrow 5f^{14}7s7p\ {}^1P_1$ transition were measured for $^{252\text{-}254}$No and the hyperfine splitting in ^{253}No was partly resolved, leading to the extraction of nuclear ground-state properties [44, 46]. The precision was limited by the achieved spectral line width of about 3 - 5 GHz, resulting from the laser bandwidth (typically 1 - 6 GHz) and essentially by the collisional broadening induced by the buffer gas at 100 mbar (typically 3 - 4 GHz) [46]. By performing laser spectroscopy in a hypersonic gas-jet a narrow spectral profile can be combined with a high total efficiency [47, 48, 49]. A full width at half maximum (FWHM) of < 400 MHz was obtained for several lighter actinium isotopes [49], an improvement of about one order of magnitude compared to the RADRIS results [44, 46]. This improvement is achieved by the homogeneous low-pressure and low-temperature environment in the gas-jet effusing from a buffer-gas cell through a de Laval nozzle. This enables high-resolution spectroscopy while the use of a high-power and high-repetition rate laser system (10 kHz) ensures a high ionization efficiency of up to 10% [47, 50]. Additionally, the continuous operation of the gas-jet enables the study of shorter-lived isotopes compared to the RADRIS technique, which relies on separated cycles of sample collection and laser spectroscopy.

The scope of this thesis covers advances in laser spectroscopy in the region of the heaviest actinides and superheavy elements. Part I presents a new experimental setup dedicated to high-resolution laser spectroscopy of the heaviest elements, aiming at high overall efficiency, low extraction times, and high neutralization efficiency of the recoil ions from SHIP. Thus, the new setup merges the high neutralization efficiency of the RADRIS method with the high resolution of the in-gas-jet technique in a compact design in order to overcome the limitations of these state-of-the-art techniques. Part II covers new insights on the atomic and nuclear structure of the einsteinium isotopes $^{253\text{-}255}$Es using RIS in a hot cavity, forming a more complete picture of the atomic and nuclear properties of the heavy actinide einsteinium.

2. Theoretical background

This chapter gives an overview of the underlying theories needed to understand this work providing the mathematical background and notations used. As this chapter will only be a brief summary, profound and more detailed descriptions can be found in various textbooks as [36, 51, 52, 53, 54, 55, 56, 57, 58] or in reviews as [1, 3, 30].

2.1. Atomic structure

Information on atomic energy levels and their interaction with electromagnetic radiation and nuclear structure is the basis for experimental and evaluation methods in this thesis. The following sections will give a brief introduction into the atomic structure starting with the Schrödinger equation for the hydrogen atom. Deviations between the measured hydrogen spectrum and the solutions of the Schrödinger equation will be explained, giving rise to the fine structure, the hyperfine structure, and the Lamb shift. Afterwards, the isotope shift between two isotopes is discussed, before going to more complex many-electron systems. Here, atomic calculation methods to calculate atomic properties of many-electron systems will be shortly introduced. At the end, a brief explanation of electronic transitions between atomic levels and the resulting spectral lineshape will be presented.

2.1.1. One-electron system - hydrogen atom

This section will cover the hydrogen atom as it serves as the most simple atomic system. Besides other one-electron systems like, e.g. He^+ and Li^{++}, hydrogen is the only neutral atom for which the Schrödinger equation can be analytically solved assuming a point-like nucleus [53]. In spherical coordinates (r, ϑ, φ) and using only the relative coordinate r in respect to the system's center of mass, the Schrödinger equation can be expressed as

$$-\frac{\hbar^2}{2\mu}\Delta\Psi(r,\vartheta,\varphi) - \frac{Ze^2}{4\pi\epsilon_0 r}\Psi(r,\vartheta,\varphi) = E\Psi(r,\vartheta,\varphi). \tag{2.1}$$

Here, the reduced mass μ is calculated from the mass of the electron m_1 and the nucleus m_2, respectively, and is defined as $\mu = (m_1 \cdot m_2)/(m_1 + m_2)$. The Laplace operator is given by Δ. $V_C(r) = -\frac{Ze^2}{4\pi\epsilon_0 r}$ describes the Coulomb interaction between the electron and the nucleus with the vacuum permittivity ϵ_0, the electron charge $-e$, and the charge $+Z \cdot e$ of the nucleus. This equation can be solved using the separation ansatz

$$\Psi(r,\vartheta,\varphi) = R_{n,l}(r) \cdot Y_l^m(\vartheta,\varphi) \tag{2.2}$$

with the radial function $R_{n,l}(r)$ and the angular spherical harmonics $Y_l^m(\vartheta,\varphi)$ [53]. These normalized wavefunctions, so called orbitals, are explicitly described by their quantum numbers consisting of the principal quantum number n ($n = 1, 2, 3, ...$), the angular momentum quantum number l ($l = 0, 1, 2, ..., n-1$), and the magnetic quantum number m

$(m = -l, -l+1, ..., l-1, l)$. Here, n defines the size (K-, L-, M-,... shell), l the shape (s, p, d, f,...), and m the orientation of the orbital in space. The energy eigenvalue E_n associated with a state with principal quantum number n of the hydrogen atom described by the Schrödinger eqn. 2.1 with a proton number of $Z = 1$ can be calculated to

$$E_n = -\frac{\mu \cdot Z^2 \cdot e^4}{8\epsilon_0^2 \cdot h^2 \cdot n^2} = -\frac{\mu \cdot e^4}{8\epsilon_0^2 \cdot h^2 \cdot n^2} = -R_y \cdot \frac{1}{n^2} \tag{2.3}$$

with the Rydberg constant $R_y = 13.605\,693\,122\,994(26)\,\text{eV}$ [53, 59]. Since this is a bound system, the energy is given as a negative value. For $n \to \infty$ the energy E_∞ converges to 0 eV, which corresponds to an unbound system. The energy difference between the atomic ground state and the zero-point energy (E_∞) is defined as the ionization potential (IP), which is required to lift the electron from its atomic ground state to the ionization continuum. In the case of the hydrogen atom the IP corresponds to $\approx 13.6\,\text{eV}$ [53].
Deviations are observed when comparing the results from the Schrödinger equation with the experimental results of the hydrogen atom. To explain these experimental results, the quantum mechanical model needs to be extended, which will be covered in the next sections [53].

2.1.2. Fine structure

Deviations between the measured energy eigenvalues and the energy eigenvalues derived from the Schrödinger eqn. 2.1 can be explained by taking the spin-orbit coupling and the relativistic mass increase of the electron during its motion around the nucleus into account. Including the fine structure corrections, the total energy of a state (n, l, j) can be calculated from the Dirac equation [53, 57] to

$$E_{n,j} = E_n \left[1 - \frac{Z^2\alpha^2}{n}\left(\frac{1}{j+1/2} - \frac{3}{4n}\right)\right] \tag{2.4}$$

with the total angular momentum j and the fine-structure constant $\alpha = e^2/(4\pi\epsilon_0\hbar c)$, which is also known as Sommerfeld's constant [53]. Here, $\hbar$ is defined as $\hbar = h/(2\pi)$ with the Planck constant h. In the Coulomb field the energy of an electronic state (n, l, j) is independent from the angular momentum quantum number l, resulting in the same energy for levels with same n and j (degenerate) [53, 57].
Comparing the exact relativistic solution of the Dirac eqn. 2.4 and the non-relativistic energy levels of eqn. 2.3, three relativistic effects can be distinguished [53, 57]:

- Spin-orbit coupling: Magnetic interaction between the magnetic spin moment of the electron with the magnetic field created by its orbital motion. A splitting of energy levels into doublets ($l \geq 1$) is a consequence of the possible parallel or anti-parallel spin s orientations in regard to the orbital angular momentum l. Here, the total angular momentum j is defined as $j = l + s = l \pm 1/2$ [53].

- Darwin term: Non-localization effects due to the interaction of the electron with the electric field of the nucleus, leading to a shift in s-orbital energies. The Darwin term

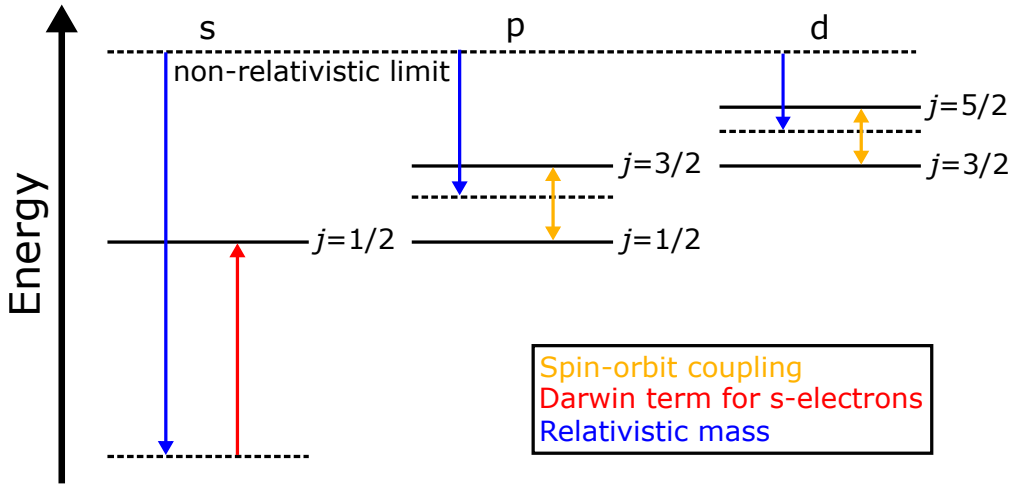

Figure 2.1.: The theoretical positions of the hydrogen energy levels for the $n = 3$ shell by calculating the fully relativistic Dirac equation. The influence of the spin-orbit interaction, the relativistic mass correction, and the Darwin term for s-electrons are shown. The figure is adapted from [57].

can be calculated to $\Delta E_\mathrm{r} = \frac{E_\mathrm{nr} Z^2 \alpha^2}{n} \left(\frac{3}{4n} - \frac{1}{l+1/2} \right)$ with the non-relativistic energy E_nr [53].

- The relativistic mass increase of the electron moving around the nucleus taking the relativistic energy $E = c \cdot \sqrt{m_0^2 c^2 + p^2} - m_0 c^2 + E_\mathrm{pot}$ into account. Here, the momentum is described by p, the speed of light by c, the "rest mass" of the photon by m_0, and the potential energy by E_pot [53].

A schematic illustration of the influence of the three effects on the energy levels of hydrogen is shown in Fig. 2.1. The fine structure splitting typically affects the levels by an order of magnitude of 10^{-3} eV [60] and decreases with increasing quantum numbers n and l, but increases proportional to $E_n \cdot Z^2$ [53]. Therefore, the fine structure is relatively large in heavy atoms.

2.1.3. Lamb shift

For the simple case of the one-electron atom hydrogen the predictions of the Dirac eqn. 2.4 are very precise. It was stated in the last section, that the energy levels with same quantum numbers n and j should be observed at the same energy. In reality, a small energy discrepancy between for example the $2\,\mathrm{S}_{1/2}$ level and the $2\,\mathrm{P}_{1/2}$ level was measured, with a shift of the $2\,\mathrm{S}_{1/2}$ level to a higher energy (lower binding energy) [57]. The explanation of this effect [61] requires quantum electrodynamics (QED) describing electromagnetic interactions. It originates from the interaction of the electron with virtual photons generated from vacuum fluctuations resulting in a jitter of the electron in the Coulomb field of the nucleus due to the photon recoil. Here, the law of conservation of energy is not violated but a correction

of the potential energy experienced by the electron is a result. This interaction removes the degeneracy of atomic levels and causes a small shift of the energy terms, which depends on the spatial probability of presence of the electron in the Coulomb field of the nucleus and therefore on the quantum numbers n and l. The Lamb shift is largest for s-state electrons, because the effect is most pronounced for electrons close to the nucleus [53, 57].

2.1.4. Hyperfine structure

Hyperfine structure (HFS) splitting arises from the coupling of the total angular momentum J of the atomic shell with the nuclear spin I. The nuclear spin I is a characteristic property of a nucleus and has either an integer or an half-integer value depending on the nuclide. Due to the strong pairing effects in the nuclear interaction leading to the fact that always two neutrons and two protons fill the same orbital, the nuclear spin is determined by the last unpaired nucleons. Therefore, four different nuclear constitutions for the neutrons and protons are possible as shown in Table 2.1, whereas even-even nuclides necessarily have a spin of 0 due to the nucleon pairing. The following properties are observed in a nucleus with spin quantum number I [56]:

- An angular momentum of magnitude $[I(I+1)]^{1/2}\hbar$.
- An angular momentum component $m_I\hbar$ on a specified quantization axis (z-axis) with $m_I = I, I-1, ..., -I$.
- In the case of $I > 0$ the nucleus has a magnetic moment μ_I with a constant magnitude and an orientation, which is determined by the value of m_I.

According to these properties the spin and the magnetic moment of the nucleus may lie in $2I+1$ different orientations relative to a specified axis [56].

Magnetic hyperfine structure

The magnetic interaction of an atomic nucleus ($I \neq 0$) with the electron shell leads to a coupling of the nuclear spin I and the total angular momentum J of the electron shell to

Table 2.1.: Overview over the nuclear spin quantum number I for different nuclear constitutions. Adapted from [56].

Proton number	Neutron number	I
even	even	0
even	odd	half-integer (1/2, 3/2,...)
odd	even	half-integer (1/2, 3/2,...)
odd	odd	integer (1,2,...)

the atomic total angular momentum $F = J + I$ with $|I - J| \leq F \leq I + J$, resulting in an hyperfine splitting energy [30] of

$$\Delta E_{\text{HFS,magn.}} = \frac{A}{2}C \text{ with } C = F(F+1) - J(J+1) - I(I+1). \tag{2.5}$$

Here, the magnetic hyperfine coupling constant A is characteristic of an atomic level and defined by

$$A = \frac{\mu_I \cdot B_J}{I \cdot J}\,, \tag{2.6}$$

with the magnetic field B_J of the electronic shell at the nucleus [30]. This dependence contains spectroscopically accessible information about the magnetic moment μ_I of a nucleus. The magnetic interaction is dominated by the interaction of the magnetic moment of the nucleus with the magnetic field B_J generated by the electrons [30].
An unknown nuclear moment of one isotope can be calculated from the known moment of a reference isotope ("ref") of the same element using

$$\mu = \frac{A \cdot I}{A_{\text{ref}} \cdot I_{\text{ref}}}\,\mu_{\text{ref}}\,. \tag{2.7}$$

This relationship is only accurate for a point-like nucleus [3]. Two additional finite-size effects arise especially for heavier nuclei [30, 62]:

- Bohr-Weisskopf effect ϵ_{BW}: The finite distribution of the magnetic currents inside the nucleus of a finite size. This effect is the main reason of the magnetic anomaly of the observed HFS within isotopic chains. The study of magnetic anomalies offers a way to investigate the change of the effective nuclear radii within isotopic chains when adding neutrons to the nucleus [62, 63].
- Breit-Crawford-Rosenthal-Schawlow correction ϵ_{BR}: The finite distribution of the electric charge inside the nucleus. It is usually several times smaller compared to the Bohr-Weisskopf effect [62, 64].

These effects are usually accounted for by the two factors

$$A = A_{\text{point}}(1 + \epsilon_{\text{BR}})(1 + \epsilon_{\text{BW}}) \tag{2.8}$$

giving rise to the so-called hyperfine anomaly [30] in the ratio of the A factors between two isotopes A_1 and A_2, which is defined as

$$\frac{A_1}{A_2} \approx \frac{g_I(1)}{g_I(2)}(1 +^1 \Delta^2). \tag{2.9}$$

Here, g_I is the Landé g-factor and ${}^1\Delta^2$ the differential hyperfine anomaly [30]. The Landé g-factor can be used to calculate the magnetic dipole moment to $\mu_I = g_I \mu_{\text{N}} I$. Here, the nuclear magneton is defined as $\mu_{\text{N}} = e\hbar/2m_p$ with the proton mass m_p [30, 65].
The hyperfine anomaly is on the order of $< 1\%$ and is often negligible [66]. As a consequence,

the hyperfine anomaly often lies within the experimental uncertainties, as reported later in this work. Microwave spectroscopy is a useful tool to determine the hyperfine anomaly if the effect is too small to be measured with laser spectroscopy [30, 67].

Electric hyperfine structure

The next possible higher order of an electric moment after the monopole term (Coulomb attaction of the central nucleus) is the quadrupole term, which arises from the energy of the orientation of the charge distribution in the nucleus in the inhomogeneous electric field of the electron shell and can only be spectroscopically probed in nuclei with a nuclear spin of $I > 1/2$ [30]. The corresponding energy shift is given by

$$\Delta E_{\mathrm{HFS,electr.}} = B \, \frac{\frac{3}{4}C(C+1) - I(I+1)J(J+1)}{2I(2I-1)J(2J-1)} \tag{2.10}$$

with C as defined in the last section and the electric hyperfine coupling constant B defined by

$$B = \frac{eQ_s}{h} \left\langle \frac{\delta^2 V}{\delta z^2} \right\rangle_{r=0} . \tag{2.11}$$

Therefore, B is linked to the nuclear spectroscopic electric quadrupole moment Q_s with $V_{zz}(0)$ being the electric field gradient at the nucleus [30].
An unknown nuclear moment of one isotope can be calculated from the known moment of a reference isotope ("ref") of the same element [3] using

$$Q_s = \frac{B}{B_{\mathrm{ref}}} \, Q_{s,\mathrm{ref}} \, . \tag{2.12}$$

The electric hyperfine structure only appears for nuclei with $I > 1/2$ and electronic states with $J > 1/2$, shifting the magnetic hyperfine levels in a characteristic way depending on the oblate ($Q < 0$) or prolate ($Q > 0$) shape of the nucleus [30]. For well deformed nuclei, the spectroscopic electric quadrupole moment Q_s can be linked to the intrinsic quadrupole moment Q [68], which is a parameter for the deformation of a nucleus, using

$$Q \; = \; \frac{(I+1)(2I+3)}{3K^2 - I(I+1)} \cdot Q_s \tag{2.13}$$

with K being the projection of the nuclear spin I upon the symmetry axis of the nucleus.

Total hyperfine structure

The combined magnetic and electric hyperfine structure leads to energy shifts and splittings due to the interaction of the nucleus with the electronic shell [3] and can be calculated by

$$\Delta E_{\mathrm{HFS}} = \Delta E_{\mathrm{HFS,magn.}} + \Delta E_{\mathrm{HFS,electr.}} = \frac{A}{2}C + B \, \frac{\frac{3}{4}C(C+1) - I(I+1)J(J+1)}{2I(2I-1)J(2J-1)} \tag{2.14}$$

The hyperfine structure typically affects the level energies by an order of magnitude of 10^{-4} eV [60].
Hyperfine transitions are allowed for $\Delta F = 0, \pm 1$ with $F = 0 \leftrightarrow F' = 0$ being forbidden between two hyperfine levels F and F' [69].
The nuclear spin can be determined from the atomic hyperfine structure. If $I < J$, the spin can be extracted from the number of observed hyperfine components. If $I > J$, the relative intensities as well as the distances between the hyperfine components are signatures of the spin. The theoretical line intensities $I_{F \to F'}$, the so-called Racah intensities, arising from the fine structure levels with total angular momentum J and J' [30] can be expressed as

$$I_{F \to F'} \propto (2F+1)(2F'+1) \underbrace{\begin{Bmatrix} F & F' & 1 \\ J' & J & I \end{Bmatrix}^2}_{\text{Wigner } 6j\text{-symbol}} . \tag{2.15}$$

As a rule of thumb, components with $\Delta F = \Delta J$ have the highest intensity for transitions between high-J states [69]. In principle these intensities aid in the assignment of individual components and an unknown nuclear spin, but due to various experimental effects the measured ratios can be altered, e.g. by saturation effects or sample depletion.
Looking at eqn. 2.5, eqn. 2.10, and eqn. 2.14 one can see, that the splitting of a transition due to hyperfine interaction contains information on the atomic nucleus like the nuclear spin I, magnetic dipole moments μ_I, and spectroscopic electric quadrupole moments Q_s in a nuclear model-independent way. If the hyperfine structure splitting can be fully resolved, the splitting pattern and the individual Racah intensities of the hyperfine peaks derived from eqn. 2.15 allow to determine the nuclear spin I. The size of the splitting is determined by the hyperfine structure parameters A and B, which are linked to the nuclear magnetic dipole moment μ_I and the spectroscopic electric quadrupole moment Q_s of the nucleus, respectively. To extract the nuclear moments, the electronic parts of these interactions, namely the magnetic field B_J of the electronic shell at the nucleus and the electric-field gradient $V_{zz}(0)$, have to be known. Both can be either deduced from HFS measurements on reference isotopes with known nuclear moments or otherwise from atomic calculations, with the latter being typically needed for the heavy actinides and the transactinides [1].

2.1.5. Isotope shift

Isotopes are nuclides of the same element (same proton number Z) with a different number of neutrons N leading to volume and nuclear mass changes. The strength of the interaction between the nucleus and the electrons changes as the nuclear volume changes, leading to different electron binding energies and therefore slightly differing atomic level energies.
The isotope shift (IS) $\delta\nu^{A_0,A_1}$ of an electronic transition is linked to the interaction of the atomic orbitals with the effective nuclear volume. By measuring such isotope shifts across an isotopic chain one can probe changes in the nuclear size and shape, which are reflected in the nuclear charge distribution. The isotope shift $\delta\nu^{A_0,A_1}$ of an atomic transition in two

different isotopes A_0 and A_1 with mass numbers m_{A_0} and m_{A_1} is defined as

$$\delta\nu^{A_0,A_1} = \nu^{A_1} - \nu^{A_0} = \underbrace{K_{\mathrm{MS}} \cdot \frac{m_{A_1} - m_{A_0}}{m_{A_0} \cdot m_{A_1}}}_{\text{Mass shift}} + \underbrace{F_{\mathrm{FS}} \cdot \left(\delta\langle r^2 \rangle^{A_0,A_1} + \frac{C_2}{C_1} \delta\langle r^4 \rangle^{A_0,A_1} + ... \right)}_{\text{Field shift}}, \quad (2.16)$$

providing a measure of the change in the mean-square charge radius $\delta\langle r^2 \rangle^{A_0,A_1}$ [1, 30]. Here, K_{MS} and F_{FS} are the mass-shift (MS) and field-shift (FS) constants, respectively. The expansion parameters C_i (C_1, C_2,...) represent the higher order terms of the charge radii changes, which have to be taken into account for the heaviest elements [1]. Here, the assumption of the electronic wave function to be constant over the nuclear volume is no longer valid, thus requiring the expansion terms [70], which have to be determined by theory [1, 71].
The mass shift can be further separated into the normal mass shift (NMS) and the specific mass shift (SMS), respectively [30]. It can be written as

$$K_{\mathrm{MS}} = \underbrace{K_{\mathrm{NMS}}}_{\text{Normal mass shift}} + \underbrace{K_{\mathrm{SMS}}}_{\text{Specific mass shift}} \quad \text{with } K_{\mathrm{NMS}} = m_e \cdot \nu^{A_0}. \quad (2.17)$$

The NMS accounts for the change in the center-of-mass motion of the nucleus, which changes with the mass of the nucleus and is therefore dependent on the neutron number. This effect leads to a positive shift for the heavier isotope, which can be exactly calculated. The SMS on the other hand accounts for electron-electron correlations and can have a positive or negative sign. The SMS cannot be exactly calculated and requires theory input [30, 70].
The mass shift is more pronounced for lighter nuclei as a large relative change is caused by adding a single neutron compared to heavy nuclei, which is reflected in the $1/(m_{A_0} \cdot m_{A_1})$ dependence in eqn. 2.16.
The field shift accounts for the change in the electron energy in consequence of the finite size of the nucleus, which shifts the energy levels of electrons which have a finite probability inside the nucleus. The shift is proportional to $Z^2/\sqrt[3]{A'}$ [30, 70] with the atomic mass number A', therefore being more pronounced in heavier nuclei. This energy shift is proportional to the mean-square charge radius of the nucleus $\langle r^2 \rangle$ and the probability density of the electron inside of the finite size of the nucleus $|\Psi_e(0)|^2$ [30]. The mean-square charge radius is dependent on the charge density function $\rho(\vec{r})$ [3] and can be written as

$$\langle r^2 \rangle = \frac{\int_0^\infty \rho(\vec{r}) r^2 d^3r}{\int_0^\infty \rho(\vec{r}) d^3r}. \quad (2.18)$$

The change in the mean-square charge radius $\delta\langle r^2 \rangle^{A_0,A_1}$ can be determined from the isotope shift, which can be measured, e.g., by laser spectroscopy. In order to extract the change in the mean-square charge radius $\delta\langle r^2 \rangle^{A_0,A_1}$ the field shift constant F_{FS} needs to be calculated or calibrated [30], e.g., by electron-scattering experiments [73] or a King-plot analysis [72]. In the case of a King-plot analysis the isotope shifts are measured between various isotopes (mass numbers $A', A'', A''', ...$) and a reference isotope (mass number A) in two spectral lines ("a" and "b"). The measured isotope shifts are then multiplied by a modifying factor "μ" so that the modified mass shifts will be independent on the nuclear masses. A plot of the

modified shifts in one spectral line against the modified shifts in another spectral line should then result in a straight line [72, 74], which is defined by

$$\underbrace{\mu^{A,A'} \cdot \delta\nu_b^{A,A'}}_{y} = \underbrace{\frac{F_{\mathrm{FS}}^b}{F_{\mathrm{FS}}^a} \cdot \mu^{A,A'} \cdot \delta\nu_a^{A,A'}}_{m \cdot x} + \underbrace{\left(K_{\mathrm{MS}}^b - \frac{F_{\mathrm{FS}}^b}{F_{\mathrm{FS}}^a} K_{\mathrm{MS}}^a \right)}_{b}. \tag{2.19}$$

Here, the ratio of the field shifts $F_{\mathrm{FS}}^b/F_{\mathrm{FS}}^a$ is given by the slope m of the line, whereas the intercept b with the y-axis is defined by $(K_{\mathrm{MS}}^b - (F_{\mathrm{FS}}^b/F_{\mathrm{FS}}^a) \cdot K_{\mathrm{MS}}^a)$. A schematic King-plot is shown in Fig. 2.2 [72]. If no experimental data exist the field shift constant can only be semi-empirically estimated or calculated theoretically [75].
In order to extract absolute radii, the knowledge of at least one reference value for a specific isotope is mandatory, e.g. obtained from electron-scattering experiments. In general, reference data are rather rare for elements above plutonium (Pu, $Z = 94$), as the experimental

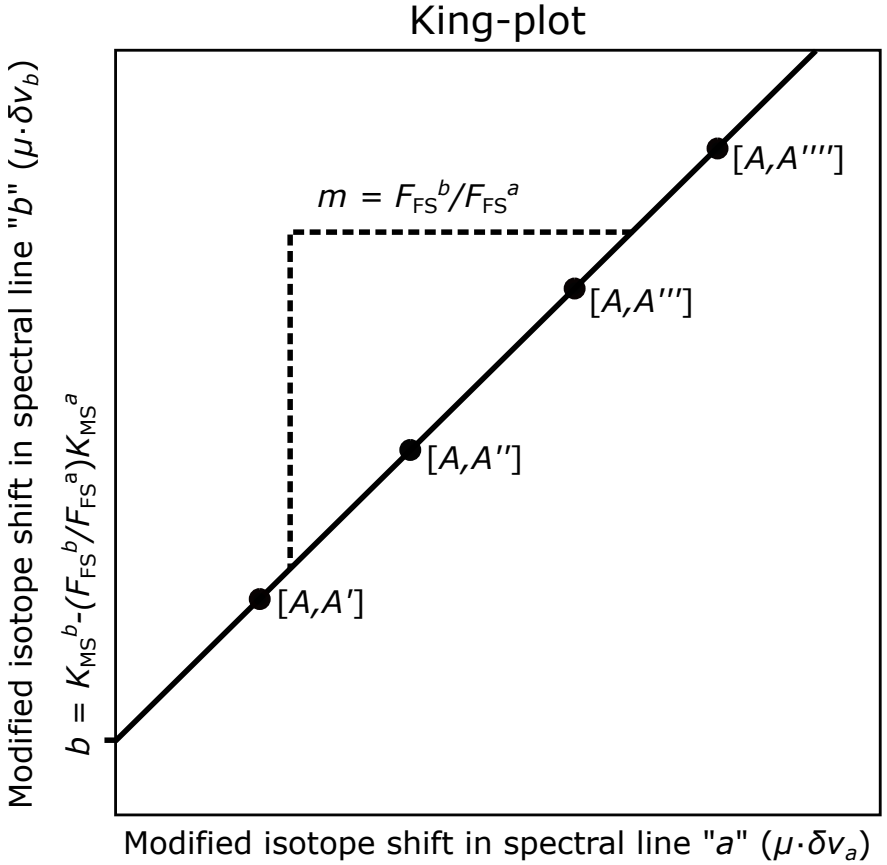

Figure 2.2.: Schematic King-plot adapted from [72]. The modified shifts in spectral line "b" are plotted against the modified shifts in spectral line "a", whereas the results for four pairs of isotopes are displayed (black circles). The ratio of the field shifts $F_{\mathrm{FS}}^b/F_{\mathrm{FS}}^a$ is defined by the slope m of the line, whereas the intercept b with the y-axis is given by $(K_{\mathrm{MS}}^b - (F_{\mathrm{FS}}^b/F_{\mathrm{FS}}^a) \cdot K_{\mathrm{MS}}^a)$.

methods to extract these reference data are usually only applicable to stable or extremely long-lived nuclides [1]. As a result, atomic theory becomes essential in order to extract nuclear properties for heavy and superheavy elements, whereas atomic calculations of the nuclear properties reach an accuracy of a few percent at best [1].

2.1.6. Many-electron systems

The Schrödinger equation for a many-electron atom is highly complicated due to electron electron interactions. An important consequence of these interactions is that orbitals of the same principal quantum number n but different values of l are no longer degenerate. Furthermore, a numerical treatment and approximation methods are needed as no analytical expression can be given for the orbitals and energies. One such approximation is the so-called orbital approximation [56], where each electron is occupying its own orbital, described by

$$\Psi(r_1, r_2, ...) = \Psi(r_1)\Psi(r_2)... \,. \tag{2.20}$$

This approximation is a useful starting point for describing chemical properties and atomic structures. For many-electron systems multiple rules are applied in order to express the electronic configuration [56].
The Pauli exclusion principle applies to fermions (half-integer spin particles) and is therefore applicable to electrons ($m_s = \pm 1/2$). It states that in the case of electrons only two electrons may occupy any given orbital. If two electrons occupy the same orbital the electron spins must be paired, resulting in a zero net spin angular momentum. Here, one electron has a magnetic spin quantum number of $m_s = +\frac{1}{2}$ and the other electron of $m_s = -\frac{1}{2}$ [56].
According to the fine structure splitting the energies of subshells (different l) of the same main quantum number n follow the energy ordering s < p < d < f. Extending this trend to different shells n is called the building-up principle or Aufbau principle. The occupation order of the shells and subshells [56] is given by

$$1s \quad 2s \quad 2p \quad 3s \quad 3p \quad 4s \quad 3d \quad 4p \quad 5s \quad 4d \quad 5p \quad 6s \quad 4f \,... \,. \tag{2.21}$$

For multi-electron atoms the electrons are distributed into the different energy levels (n, l, m_l, m_s) so that the total energy for the ground state of each atom is minimal (energy minimization). Every electron shell can be occupied by a maximum of $2n^2$ electrons, each conclusively described by n, l, m_l, and m_s. Here, each subshell can be occupied by a maximum of $2(2l + 1)$ electrons [53]. When degenerate orbitals of a subshell are available, which is the case for all $2l + 1$ different m_l states without an external magnetic field, electrons occupy different orbitals of a given subshell with a single electron before doubly occupying any of these orbitals. When this case happens, Hund's maximum multiplicity rule also applies, saying that an atom in its ground-state adopts an electronic configuration with the greatest number of unpaired electrons. The reason for that is that electrons in the same orbital experience more repulsion due to the Coulomb interaction in comparison to electrons in different orbitals. Consequently, in order to place two electrons in the same orbital the spin pairing energy must be expended, which is avoided in the case of degenerated orbitals [56].

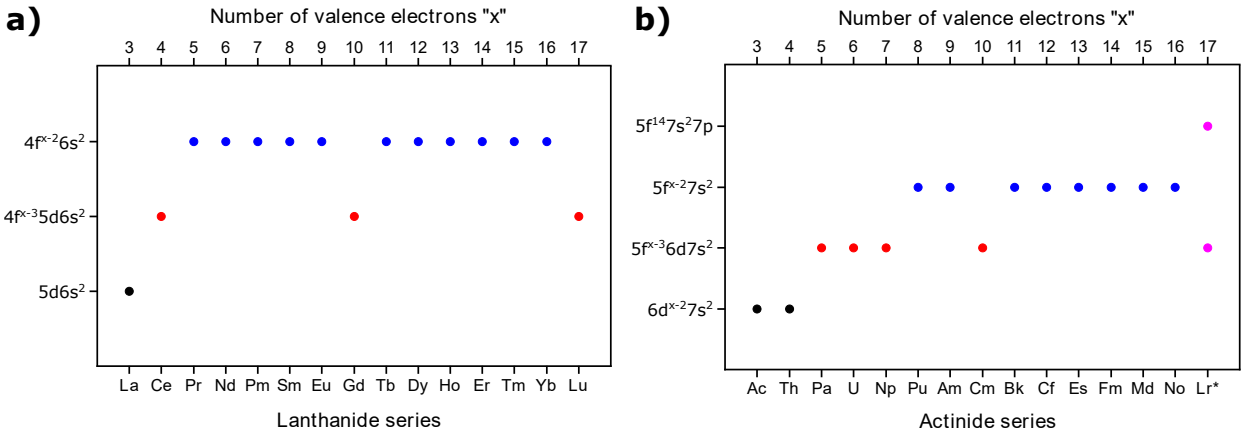

Figure 2.3.: Electronic ground-state configurations of f-block atoms, namely the Lanthanide series (a) and Actinide series (b). For Lr only the predicted configurations are given. The "x" denotes the valence electron number for the respective element. Adapted from [36].

As this work is focussed on heavy and superheavy element research the electronic configurations for the atoms in the lanthanide series, spanning the region from lanthanum (La, $Z = 57$) to lutetium (Lu, $Z = 71$), and actinide series, spanning the region from actinium (Ac, $Z = 89$) to lawrencium (Lr, $Z = 103$), are given in Fig. 2.3. It can be seen that adding successive electrons lowers the relative energy levels of the electron shell being filled, resulting in different ground-state configurations. In the case of the actinides the 5f, 6d, 7s, and 7p orbitals are relevant for the ground-state configurations, giving access to a variety of electron configurations and therefore to a large number of atomic levels. The atomic structure of most actinides is only partially known due to the lack of abundant isotopes with suitable half-lives and the scarcity of available material, with information quickly diminishing from einsteinium onwards due to the reduced availability [1].
The magnetic interactions due to the magnetic moments of electrons and atomic nucleus (HFS, see section 2.1.4) need to be considered on top of the Coulomb force between each electron and the atomic nucleus as well as the electrostatic interactions between the electrons. These interactions result, in analogy to one-electron atoms, in a splitting of the energy terms in different hyperfine structure components [53].
In multi-electron systems the individual angular momentum quantum numbers may couple in different ways to the total angular momentum J. Two limiting cases, namely the L-S-coupling in light atoms and the j-j-coupling in heavy atoms, will be discussed in the following [53].

L-*S*-coupling

If the coupling energies between the individual electron's spin and angular momentum are large compared to the individual coupling energy of single electron's spin and angular momentum, the individual orbital angular momentum l_i and spins s_i couple to a total orbital

angular momentum L and total spin S

$$L = \sum_i l_i \text{ and } S = \sum_i s_i \,. \tag{2.22}$$

The total angular momentum J of the electron shell [53] is then defined by

$$J = L + S. \tag{2.23}$$

The state is described with a term symbol [53] defined by

$$n^{2S+1}L_J \,. \tag{2.24}$$

Here, $L = 0, 1, 2, ...$ is written as S, P, D,... terms and the term $2S + 1$ denotes the spin multiplicity. The L-S-coupling applies especially to light atoms with small atomic number Z [53].

j-j-coupling

If the individual coupling energy of single electron's spin s and orbital angular momentum l is large compared to the coupling energies between the individual electron's spin and orbital angular momentum, l_i and s_i couple to an individual angular momentum for each electron

$$j_i = l_i + s_i \,. \tag{2.25}$$

The angular momenta j_i of the individual electrons [53] then couple to the total angular momentum J

$$J = \sum_i j_i \,. \tag{2.26}$$

The j-j-coupling [53] applies especially to heavy atoms with high atomic number $Z > 60$ and for higher excited atomic levels. As in this work einsteinium isotopes with $Z = 99$ are investigated this coupling mechanism is predominant. In the limiting case of the j-j-coupling the total orbital angular momentum L and total spin S are not defined anymore, therefore no differentiation of the atomic terms in S, P, D,... terms and well defined multiplets is given. This results in more complex spectra [53].

2.1.7. Atomic calculations

As already stated in the isotope shift section 2.1.5 no stable or long-lived reference isotopes are available in the heavy and superheavy elements. Thus, atomic theory becomes essential in order to extract nuclear properties from the experimentally measured observable. Atomic calculations of the electronic structure of the heaviest elements are especially challenging due to increasing relativistic effects ($\approx 10\,\text{eV}$ in oganesson ($Z = 118$) [76]), electron-electron correlations, and QED effects ($\approx 10 - 350\,\text{cm}^{-1}$ in nobelium ($Z = 102$) and lawrencium ($Z = 103$) [77, 78]). Several state-of-the art many-body methods such as the multi-configuration

Dirac-Hartree-Fock (MCDHF) method, the relativistic coupled cluster (RCC) approach, and the configuration interaction (CI) approach can be used to study the atomic properties, although with a limited accuracy on the order of a few hundredths of an eV [1, 2, 79, 80]. These atomic properties include the energy of atomic states with the corresponding configuration, the lifetime of states, the Einstein-coefficients A_{ki}, and the element-specific ionization potential. The following sections will give a short introduction into the atomic calculations in multi-electron systems using different approximation methods.

2.1.7.1. Hartree-Fock (HF) method

The Hartree-Fock (HF) [55, 81, 82, 83, 84] approximation is based on the central field approximation and allows to approximately calculate the wave functions and orbital energies of multi-electron systems. The wave function for a system with N-electrons is, in agreement with the Pauli exclusion principle, given by a Slater determinant [81, 82] expressed as

$$\Psi(1,2,3,...,N) = \frac{1}{\sqrt{N!}} \begin{bmatrix} \Psi_1(1) & \Psi_1(2) & \Psi_1(3) & \cdots & \Psi_1(N) \\ \Psi_2(1) & \Psi_2(2) & \Psi_2(3) & \cdots & \Psi_2(N) \\ \Psi_3(1) & \Psi_3(2) & \Psi_3(3) & \cdots & \Psi_3(N) \\ \vdots & \vdots & \vdots & & \vdots \\ \Psi_N(1) & \Psi_N(2) & \Psi_N(3) & \cdots & \Psi_N(N) \end{bmatrix} \tag{2.27}$$

with the one-particle states $\Psi_1, ..., \Psi_N$. The total wavefunction $\Psi_i(r) = \phi_i(r) \cdot \zeta_i(\eta)$ can be separated into a radial part $\phi_i(r)$ and a spin dependent part $\zeta_i(\eta)$. The Hartree-Fock equation for a N-electron system in the central potential is defined as

$$-\frac{1}{2}\nabla^2\phi_i(r)+V_{\text{ext}}\phi_i(r)+\left(\sum_{j\neq i}^{N}\int\frac{\phi_j^*(r')\phi_j(r')}{|r-r'|}dr'\right)\phi_i(r)-\sum_{j\neq i}^{N}\left(\int\frac{\phi_j^*(r')\phi_i(r')}{|r-r'|}dr'\right)\phi_j(r)=\epsilon_i\phi_i(r). \tag{2.28}$$

Here, the kinetic energy of the $i-$th electron is described by the first term and the Coulomb potential of the nucleus by V_{ext}. The correction to the Coulomb potential due to the centrally-symmetric average of the electrostatic repulsion between the electrons is covered in the third term. The last term accounts for the effective exchange potential due to the Pauli principle, which only has an influence on electrons with parallel spins. In order to solve the Hartree-Fock equation 2.28 it is converted [83] to

$$-\frac{\hbar^2}{2m}\frac{d^2u_{nl}}{dr^2}+\left(\frac{l(l+1)\hbar^2}{2mr}-\frac{e^2}{4\pi\epsilon_0 r}[Z-Y_{nl}(r)]+\epsilon_{nl,nl}\right)u_{nl}=\frac{e^2}{4\pi\epsilon_0 r}X_{nl}(r)+\sum_{n'}\epsilon_{n'l,nl}u_{nl} \tag{2.29}$$

with the atomic number Z, the angular momentum quantum number l and the mass m. The functions $Y_{nl}(r)$ and $X_{nl}(r)$ depend on the radial eigenfunction u_{nl} and represent corrections to the Coulomb potential and the exchange function, respectively [83]. In order so solve eqn. 2.29 an iterative approach is used. Suitable eigenfunctions $u_{n'l'}$ are chosen to calculate the

Coulomb potential $Y_{nl}(r)$ and the exchange function $X_{nl}(r)$. Thus, eqn. 2.29 is determined for the orbital $u_{n,l}$ and can be integrated in the next step, resulting in a new set of improved functions. These improved functions can be used to repeat this iterative process, which is done until reaching self-consistency [83].
The biggest disadvantage of the Hartree-Fock approximation is the neglection of so-called correlations, e.g. the Coulomb-correlation due to the use of an averaged central potential. Thus, the calculated energies are only a rough approximation [83].

2.1.7.2. Multiconfiguration Dirac-Hartree-Fock (MCDHF) method

The multiconfiguration Dirac-Hartree-Fock (MCDHF) method is a relativistic and quantum electrodynamic (QED) extension of the Hartree-Fock approximation and describes open-shell atoms [83, 85]. This method is also an *ab-initio* procedure, which does not rely on experimental parameters.
Starting point is the one-particle Dirac equation with the Dirac-Coulomb-Breit-Hamiltonian H_{DCB} [85] defined as

$$H_{DCB} = H_{DC} + \sum_{i>j}^{N} B_{ij}. \tag{2.30}$$

Here, the Dirac-Coulomb-Hamiltonian is defined as $H_{DC} = \sum_i h_D(r_i) + \sum_{i>j} \frac{1}{r_{ij}}$, the one-electron Dirac operator as h_D, and the Breit correction term as B_{ij} [83, 85]. The latter stands for the relativistic corrections to the electron-electron interaction and, in the case of frequency independence, can be written as

$$B_{ij} = -1/2 r_{ij} \cdot [(\alpha_i \cdot \alpha_j + (\alpha_j \cdot r_{ij}) \cdot (\alpha_i \cdot r_{ij})/r_{ij}^2)] \tag{2.31}$$

with the Dirac-matrices α_i. It is important to note that all contributions $\alpha^4 Z^3$ are neglected [85].
The MCDHF method describes a bound atomic wavefunction $\Psi(PJM)$ as a linear combination of so-called configuration state functions (CSF) [85] and can be written as

$$\Psi(PJM) = \sum_{v}^{A} c_v |\gamma_v PJM\rangle. \tag{2.32}$$

Here, A accounts for the number of configuration functions, whereas the mixing coefficient of the respective base is described by c_v [85].
As a starting point an initial wave-function is chosen in the MCDHF approach. Afterwards the mixing coefficients c_v are determined by diagonalization of the Hamiltonian matrix. The optimization of the solution is done by calculating the influence of the atomic nucleus and its $N-1$ electrons on each individual electron. The wavefunctions gained by this approach are optimized until self-consistency is reached [86, 87].

2.1.7.3. Relativistic Coupled Cluster (RCC) method

The consideration of the interaction between the electrons, the so-called electron-correlations, is important to accurately describe heavy many-electron systems. The coupled-cluster (CC) method [77, 88, 89], which is also known as exponential formalism e^S, takes these electron-correlations into account. The wavefunction Ψ_{CC} is connected to the solutions of the Hartree-Fock equation Ψ_0 [88, 89] via the excitation operator S

$$\Psi_{CC} = e^S \cdot \Psi_0. \tag{2.33}$$

Starting point is the Dirac-Coulomb-Breit-Hamiltonian H_{DCB} from eqn. 2.30 analogously to the MCDHF-calculations.
In the so-called Fock space coupled-cluster (FSCC) approach [88, 90] the space associated with the Hamiltonian operator H_{RCC} is transformed into a K-dimensional subspace P and a subspace Q with $Q = 1 - P$ orthogonal to the former subspace. The energy eigenvalues of the system are obtained by diagonalizing of the corresponding effective Hamiltonian H^{eff} accosicated with the subspace P. FSCC is a very powerful tool for atomic calculations, but the convergence and accuracy depend on the partitioning of the function space P and Q. This problem can be solved by the Intermediate Hamiltonian Fock-space coupled cluster (IHFSCC) approch [91].

2.1.7.4. Configuration interaction (CI) method

Another method is the configuration interaction linearised single-double coupled cluster (CI + all orders) approximation [92, 93, 94, 95]. Here, the starting point is the frozen core Dirac-Fock (DF) potential V^{N-M} [92] with N being the total number of electrons in the neutral atom and M being the number of valence electrons. For the valence electrons the effective Hamiltonian $\hat{H}^{eff}$ is the sum of the individual single-electron Hamiltonian $\hat{h}_1(r_i)$ and an operator $\hat{h}_2(r_i, r_j)$, which represents the interaction between the valence electrons [94]. The effective Hamiltonian can be expressed as

$$\hat{H}^{eff} = \sum_{i=1}^{M} \hat{h}_1(r_i) + \sum_{i<j} \hat{h}_2(r_i, r_j). \tag{2.34}$$

Here, the single-electron Hamiltonian $\hat{h}_1$ for a valence electron is defined as

$$\hat{h}_1 = c\alpha \mathrm{p} + (\beta - 1)mc^2 - \frac{Ze^2}{r} + V^{N-M} + \hat{\Sigma}_1. \tag{2.35}$$

$\hat{\Sigma}_1$ is the correlation potential operator representing the correlation interaction of a valence electron with the core, with its matrix element [94] given by

$$\Sigma_{mv} = \rho_{mv}(\tilde{\epsilon}_v - \epsilon_m). \tag{2.36}$$

ρ_{mv} is an excitation coefficient of the atomic wave function from the valence state v to another excited state m. The Dirac-Fock energy of the lowest orbital for the particular partial wave

is expressed by $\tilde{\epsilon}_v$ and the Dirac-Fock energies of corresponding single-electron basis states are expressed by ϵ_m. The valence electrons interactions $\hat{h}_2(r_i, r_j)$ are defined by the sum of the Coulomb interaction and the correlation correction operator $\hat{\Sigma}_2$ [94], representing the screening of the Coulomb interaction between valence electrons by core electrons, and can be written as

$$\hat{h}_2(r_i, r_j) = \frac{e^2}{|r_i - r_j|} + \hat{\Sigma}_2(r_i, r_j). \tag{2.37}$$

The many-electron wave function Ψ for the valence electrons [94] can be expressed as

$$\Psi = \sum_i c_i \Phi_i(r_1, ...r_M) \tag{2.38}$$

with the functions Φ_i being constructed from the single-electron valence basis states retrieved from the potential V^{N-M}. The c_i coefficients and many-electron energies are extracted by solving the matrix eigenvalue problem [94] as

$$(H^{eff} - E)X = 0 \quad \text{with} \quad H_{ij}^{eff} = \langle \Phi_i | \hat{H}^{eff} | \Phi_j \rangle \ ; \ X = \{c_1, c_2, ..., c_n\}. \tag{2.39}$$

The linearized coupled-cluster method is used to calculate the correlation correction operators. The B-spline method [96] is used to construct a single-electron basis for $\hat{\Sigma}_{1,2}$ calculations and for building many-electron basis states Φ_i for the CI calculations [94].

2.1.7.5. Method comparison

The best computational results for atoms with one valence electron above a closed-shell core is achieved with all-order techniques based on different versions of the coupled-cluster (CC) method [95]. Some relativistic CC (RCC) calculations were additionally performed for many-electron atoms with more complicated electron structures with an accuracy of about 1%, providing accurate results for superheavy elements. Most RCC calculations are restricted to rather simple shell structures with at most two electrons or holes outside of closed shells [97]. Here, neglecting the three-particle correlations is the most obvious shortcoming of the method. Moreover, the CC method treats valence-valence and core-valence correlations at the same level of approximation, whereas the former correlations are much stronger than the latter [97]. Other methods than the CC approach are necessary to treat many-electron atoms accurately. Such calculations can be performed using the multiconfiguration Dirac-Hartree-Fock (MCHDF) method and the configuration interaction (CI) approach, because these multiconfiguration expansions are conceptional much simpler if electrons occur in one or several open shells [97, 98]. The MCDHF method is flexible with regards to the shell structure and the computations of excitation and decay rates. Nevertheless, the MCDHF method often suffers on the size of the wave function expansions, which need an explicit treatment [99]. In the CI method, very accurate results for superheavy elements can be achieved, whereas the accuracy is limited only by the incompleteness of the set of configurations used to perform the calculation. One has to select only a small fraction of a large number of possible configurations for a many-electron atom, thus usually partially or fully neglecting

core excitations, which significantly limits the accuracy of the method. As CI fails to fully account for the core-valence and core-core correlations, it is natural to combine it with other methods, e.g. giving rise to the configuration interaction many-body perturbation theory (CI + MBPT) method, to reach a high accuracy for atoms with more than one valence electron [97]. As a result, the computational method is selected depending on the system under consideration.
In recent years, atomic calculations have been performed using the above methods for various elements up to the SHE region [98, 100]. For example, *ab initio* calculations in lawrencium (Lr, $Z = 103$) were performed using the RCC approach, the MCDHF method and the CI approach [78]. Despite the progress in atomic calculations, einsteinium (Es, $Z = 99$) still remains inaccessible for such calculations due to large electron correlations in open f-shell systems. Nevertheless, progress in calculating open f-shell systems [98] was achieved in the past years as observed in the fermium calculations [101], indicating that further progression can be expected in the future.

2.1.8. Electronic transitions

The investigation of resonant transitions between two different atomic levels with the energies E_1 and E_2 allows us to probe the properties of distinct atomic levels [53]. Here, an photon with energy

$$\Delta E = E_2 - E_1 = h \cdot \nu = h \cdot \frac{c}{\lambda} \tag{2.40}$$

is absorbed or emitted, where ν is the frequency and λ the wavelength of the photon. The Planck constant is described by h.
One distinguishes between three atomic transition mechanisms [53]:

- (Stimulated) Absorption: Absorption of a photon $h \cdot \nu$ from an external radiation field, leading to excitation of an electron from E_1 to E_2. The transition probability is proportional to the spectral energy density, which is dependent on the frequency, the number of photons, and the Einstein coefficient of the (stimulated) absorption B_{12} [53].

- Stimulated emission: Electronic transition from an excited state E_2 to a energetically lower-lying state E_1 through the interaction of the atom with an external radiation field, leading to the emission of a photon $h \cdot \nu$ with the same properties as the initial photon (energy, direction of propagation, polarization, phase). The transition probability is proportional to the spectral energy density and the Einstein coefficient of the stimulated emission B_{21} [53].

- Spontaneous emission: An excited atom can also emit a photon $h \cdot \nu$ spontaneously, whereby the photon is emitted in a random direction and the electron decays to a lower energy level. The transition probability is independent from an external radiation field and is only dependent on the Einstein coefficient of spontaneous emission A_{21}. The

lifetime τ_2 of an excited atomic state E_2 is connected to this Einstein coefficient A_{21} by $\tau_2 = 1/A_{21}$, if no other decay channels are present [53].

The Einstein coefficients describe the strength and therefore the intensity of an atomic transition [53].
Not every atomic transition according to equation 2.40 can be observed in a recorded spectrum. In addition to the conservation of energy the conservation of angular momentum and certain symmetries play a decisive role, leading to selection rules for optical transitions [53]. Electric dipole transitions are only "allowed" when the selection rules

$$\Delta L = \pm 1, \;\; \Delta M_L = 0, \pm 1, \;\; \Delta J = 0, \pm 1, \;\; J = 0 \nleftrightarrow J = 0 \tag{2.41}$$

are fulfilled. Besides electric dipole transitions there are electric quadrupole transitions, magnetic-dipole transitions, and multi-photon transitions with transition probabilities which are multiple orders of magnitude smaller and therefore called "forbidden" transitions [53].

2.1.9. Spectral lineshapes

The frequency of a transition between two atomic levels is not strictly monochromatic. Independent from the spectral resolution of the measurement method a frequency distribution $I(\nu)$ of the emitted or absorbed intensity around a center frequency ν_0 is observed, which is denoted as natural linewidth and a consequence of Heisenberg's uncertainty principle. The frequency interval $\delta\nu = |\nu_2 - \nu_1|$ between the frequencies ν_1 and ν_2 for which the intensity $I(\nu)$ is sagged to $I(\nu_0)/2$ is called full width at half maximum (FWHM). An understanding of the transition line shapes and the involved shape distortion and broadening effects is essential to distinguish closely adjacent peaks and to precisely determine the energetic positions of resonances. An overview will be presented, whereby more information can be found in various textbooks, e.g. [51, 53, 54, 102].

Natural linewidth

An excited atomic state has a finite lifetime $\tau_2 = 1/A_{21}$. According to Heisenberg's uncertainty principle this finite lifetime is connected to an intrinsic energy uncertainty. The measured resonance can be described by a Lorentzian line profile $I(\omega)$ as

$$I(\omega) = I_0 \cdot \frac{\gamma/2\pi}{(\omega - \omega_0)^2 + (\gamma/2)^2} \quad \text{with} \quad \omega = 2\pi\nu \,. \tag{2.42}$$

Here, the FWHM is described by γ, the angular frequency by ω, and the resonance intensity by I_0 [53]. The natural linewidth of the resonance is defined by the FWHM of this Lorentzian profile and can be calculated as

$$\delta\omega_{\text{nat}} = \gamma = A_{21} = \frac{1}{\tau_2} \quad \text{or} \quad \delta\nu_{\text{nat}} = \frac{\gamma}{2\pi} = \frac{A_{21}}{2\pi} = \frac{1}{2\pi\tau_2} \tag{2.43}$$

with the Einstein coefficient A_{21}. It can be seen that the natural linewidth is directly related to the lifetime τ_2 of the excited state [52, 53].

For a transition between two atomic states with respective lifetimes τ_1 and τ_2 the resulting linewidth [53] can be calculated by

$$\delta\nu_{\text{nat,trans}} = \frac{1}{2\pi}\left(\frac{1}{\tau_1} + \frac{1}{\tau_2}\right) = \delta\nu_{\text{nat},1} + \delta\nu_{\text{nat},2}\,. \tag{2.44}$$

Doppler broadening

If an atom moves with a velocity v with respect to the source of light, the resonance frequency ν_0 is shifted to a frequency ν according to the Doppler effect [53] by

$$\nu = \nu_0 \cdot \left(1 + \frac{v}{c}\right) \tag{2.45}$$

with the speed of light c.
In thermal equilibrium the atoms of a gas have a Maxwell-Boltzmann velocity distribution. The spectral line broadening originates from different velocities being in resonance with the incident radiation at different Doppler shifts. The profile of the Doppler-broadened spectral line [51] can be described by

$$I(\nu) = I(\nu_0) \cdot \exp\left[-\left(\frac{\nu - \nu_0}{\nu_0 \cdot v_w/c}\right)^2\right] \quad \text{with} \quad v_w = \sqrt{\frac{2k_\text{B}T}{m}}\,. \tag{2.46}$$

This is a Gaussian profile with the most likely speed v_w, maximum intensity $I(\nu_0)$, temperature T, mass m, Boltzmann constant k_B, and center frequency ν_0. The FWHM of this Gaussian profile can be calculated as

$$\delta\nu_{\text{Doppler}} = \frac{\nu_0}{c} \cdot \sqrt{\frac{8k_\text{B}T \cdot \ln(2)}{m}}\,. \tag{2.47}$$

The Doppler width increases linearly with the frequency ν_0 and is proportional to $\sqrt{T}$ and $1/\sqrt{m}$ for increasing temperature T and mass m [51, 53].
In the case of hot cavity environments as present in the einsteinium measurements discussed later in this work the Doppler broadening is the limiting factor of the spectral resolution being in the GHz regime. For the einsteinium measurements a Doppler broadening of $\approx 1 - 3\,\text{GHz}$ was observed depending on the temperature in the hot cavity.

Pressure broadening

The pressure broadening or collision broadening is caused by elastic and inelastic collisions between two atoms A and B, shifting the energy of the atomic levels E_1 and E_2. The shift depends on the structure of the electronic shells of both atoms and on the distance between those. The energy shift is different for each atomic level and can be positive for repulsive interactions or negative for attractive interactions [53].
The total transition probability A_eff for the transition between two states E_2 and E_1 is now

dependent on the spontaneous emission coefficient A_{21} and the collision-induced relaxation probability R_{21} [53], resulting in

$$A_{\text{eff}} = A_{21}(\text{spontaneous}) + R_{21} \quad \text{with} \quad R_{21} = N_{\text{B}} \cdot \sigma_{21} \sqrt{\frac{8k_{\text{B}}T}{\pi\mu}}. \tag{2.48}$$

Here, the reduced mass of both collision partner A and B is described by μ and the collision cross-section by σ_{21}. An increased linewidth is observed, which can be attributed either to elastic collisions or to a collision-induced shortening of the effective lifetime $\tau_{\text{eff}} = 1/A_{\text{eff}}$ of the excited state. In the latter, the increased linewidth can be calculated as $\delta\nu_{21} = A_{\text{eff}}/2\pi = 1/(2\pi\tau_{\text{eff}})$. According to eqn. 2.48 the linewidth is increasing linearly with the density N_{B} of atom B or in other words with increasing pressure of this component [53].

Power broadening

In order to explain this additional line broadening, a two-level system will be shortly discussed. In this system, only stimulated absorption, stimulated and spontaneous emission are considered. Furthermore, the intensity of the field $I(\nu)$ is considered to be constant in time. The steady-state solutions $\bar{N_1}$ (state 1) and $\bar{N_2}$ (state 2) [102] can be derived to

$$\bar{N_1} = \frac{1 + 1/2 \cdot I(\nu)/I^{\text{sat}}(\nu)}{1 + I(\nu)/I^{\text{sat}}(\nu)} N \tag{2.49}$$

and

$$\bar{N_2} = \frac{1/2 \cdot I(\nu)/I^{\text{sat}}(\nu)}{1 + I(\nu)/I^{\text{sat}}(\nu)} N \tag{2.50}$$

with $N = N_1 + N_2 = \bar{N_1} + \bar{N_2}$. N_1 and N_2 are the populations of the ground state and excited state, respectively. Here, the saturation intensity $I^{\text{sat}}(\nu)$ [102] is defined as

$$I^{\text{sat}}(\nu) = \frac{h\nu A_{21}}{2\sigma(\nu)} \tag{2.51}$$

with the frequency dependent cross-section $\sigma(\nu)$. The absorption coefficient $a(\nu)$ [102] is then

$$a(\nu) = \sigma(\nu)(\bar{N_1} - \bar{N_2}) = \frac{a_0(\nu)}{1 + I(\nu)/I^{\text{sat}}(\nu)} \quad \text{with} \quad a_0(\nu) = \sigma(\nu)N. \tag{2.52}$$

As the ratio $I(\nu)/I^{\text{sat}}(\nu)$ increases, the absorption coefficient $a(\nu)$ "saturates" and becomes smaller and smaller as $I(\nu)$ increases. In the case of $I(\nu) >> I^{\text{sat}}(\nu)$ the ground state and excited state are equally ($\bar{N_1} \approx \bar{N_2} \approx N/2$) populated. Saturation of an absorbing transition arises from the excitation of the excited level, which increases stimulated emission and reduces the stimulated absorption [102].

Another interpretation of saturation is possible considering a homogeneously broadened transition having a Lorentzian lineshape of width $\delta\nu_0$. The absorption coefficient $a(\nu)$ [102] can be defined as

$$a(\nu) = a_0(\nu_0)\frac{\delta\nu_0^2}{(\nu-\nu_0)^2+\delta\nu_0'^2} \quad \text{with} \quad \delta\nu_0' = \delta\nu_0\sqrt{1+I(\nu)/I^{\text{sat}}(\nu)}. \tag{2.53}$$

The width $\delta\nu_0$ of the transition increases by the factor $\sqrt{1+I(\nu)/I^{\text{sat}}(\nu)}$. The saturation of the transition with increasing intensity can be interpreted as an effective power broadening of the linewidth [102].
The saturation intensity $I^{\text{sat}}(\nu)$ [57] of a transition can be estimated using

$$I^{\text{sat}}(\nu) = \frac{\pi}{3}\cdot\frac{hc}{\lambda^3\tau}. \tag{2.54}$$

Here, the wavelength of the excitation step is represented by λ, the lifetime of the upper level by τ, the speed of light by c, and the Planck constant by h. Equation 2.54 was derived in the steady state of a two-level system using a continuous wave (cw) laser for excitation and therefore only serves as an estimate of the saturation intensity for the pulsed lasers used in this work.
An additional effect has to be considered for high-resolution applications using pulsed laser systems originating from the synchronization of the laser pulses. Delaying the ionization laser to a time when the excitation laser pulse is already over can suppress the effect of power broadening [103], because the population at the outer wings of the spectral line shows a very ephemeral character, which is only pronounced during the excitation laser pulse [104]. The efficiency can be almost maintained if the lifetime of the excited state is sufficiently long.

2.2. Nuclear models

The nuclear strong force is not precisely known, which is why a number of nuclear models have been developed in order to predict *a priori* the nuclear properties and behavior. Here, each nuclear model is able to explain only a part of the experimental knowledge about nuclei due to their complexity [7, 54, 105].
An early theoretical model is the nuclear liquid-drop model (LDM) [106, 107], where the nucleus is described as a liquid droplet. The nuclear LDM correlates very well with the overall behavior of binding energies and masses but cannot explain the existence of magic numbers [7]. Magic numbers stand for certain nucleon (proton and neutron) numbers at which an increased stability compared to other nuclei is observed, concluding the observation of a shell closure in the atomic nucleus. These experimental findings motivated the development of a new theoretical model, the nuclear shell model [17, 108], capable of explaining this observation. As the understanding of nucleon shells is important for this work, a brief introduction will be given.

2.2.1. Nuclear shell model

The nuclear shell model (SM) is a quantum mechanical treatment of the atomic nucleus and able to describe the observed magic numbers. These magic numbers correspond to closed nucleon shells in analogy to a noble gas configuration of the electronic shell in an atom [17, 108]. The corresponding Schrödinger equation can be solved for a Woods-Saxon potential, which is a widely accepted analytical form used to describe the potential well. It is obtained by folding a square-well potential with an harmonic oscillator potential [7] and can be written as

$$V = \frac{V_0}{1 + \exp[(r - R)/a]}. \tag{2.55}$$

Here, V_0 describes the depth of the potential ($\approx -50\,\mathrm{MeV}$), a is a constant measuring the surface diffuseness of nuclei ($\approx 0.5\,\mathrm{fm}$), R is defined as the distance from the center at which $V = V_0/2$, and r describes the distance of the nucleons to the center of the nucleus [7].

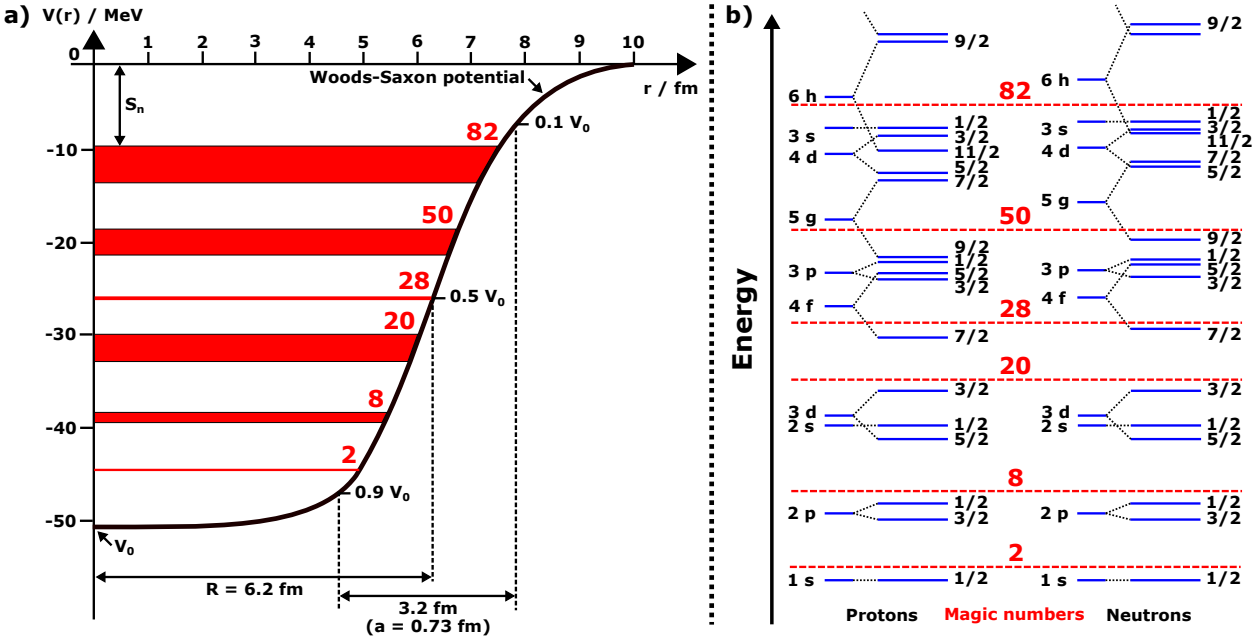

Figure 2.4.: a) Realistic representation of the conditions of the nuclear SM. The neutron states of a nucleus with $N = 82$ in the Woods-Saxon potential with its parameters R and a considering spin-orbit coupling are shown. S_n describes the separation energy of the last neutron. Figure adapted from [54, 109]. b) Nuclear level energies according to the nuclear shell model for protons (left) and neutrons (right). For protons and neutrons the level structure with (right, j quantum numbers) and without consideration of spin-orbit coupling (left, quantum numbers nl) is shown. The magic numbers, which corresponds to the total number of levels up to this energy, are indicated in red. Figure adapted from [110].

The Woods-Saxon potential is shown in Fig. 2.4 a. Only the consideration of the spin-orbit coupling results in the correct energetic order of the closed shells and explains the observed magic numbers. More information can be found in various textbooks, e.g. [7, 54, 109].
The single-particle energy level structures for the nucleons are shown in Fig. 2.4 b. As a result of the nucleon spin-orbit coupling ($j = l + s$) the l-degeneracy of the energy levels is lifted, whereas each level can be filled with $2j + 1$ nucleons. In the case of large energy gaps between different energy levels one speaks of so-called magic numbers. The level sequence resulting after the introduction of spin-orbit splitting is given separately for protons and neutrons, since the additional Coulomb potential present for the protons causes somewhat different level sequences for the two types of nucleons [109]. The nuclear SM postulates that the properties of a nucleus are only determined by a single, unpaired valence neutron n and / or proton p, resulting in a total angular momentum J and parity π defined as

$$J = |j_p - j_n|, |j_p - j_n| + 1, ..., j_p + j_n \quad \text{and} \quad \pi = (-1)^{l_p + l_n} . \tag{2.56}$$

For even-even nuclei the nuclear spin is always zero.
The nuclear shell model accurately predicts certain properties of the nuclei as, e.g., the total angular momentum J, the nuclear spin I, and the parity π. The model is no longer adequate to describe strongly deformed nuclei and nuclear properties such as nuclear moments [17].

2.2.2. Nilsson model

The nuclear SM treats the atomic nucleus as a spherical shape, which is only true for undeformed nuclei and therefore only succeeds to describe nuclei near the magic numbers with closed or nearly closed shells, but fails to adequately describe nuclei outside the closed shells. In the nuclear SM the nucleus is considered approximately as a system of independent, i.e. not directly interacting nucleons in the potential well. This is, of course, an approximation

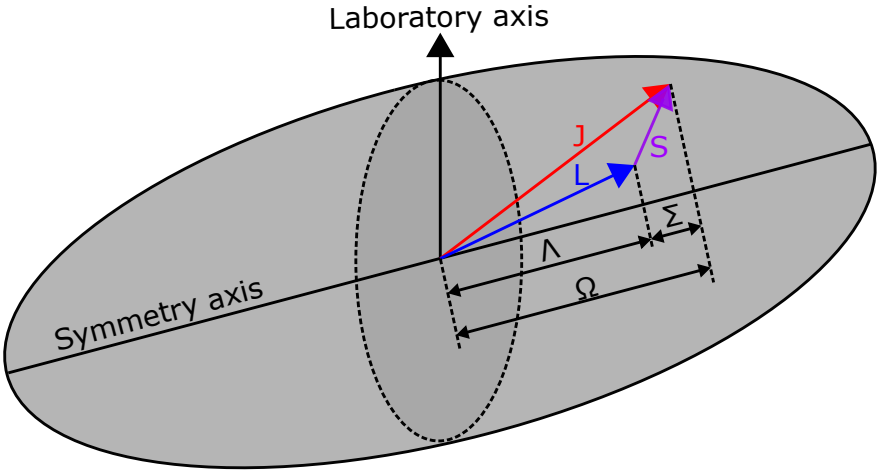

Figure 2.5.: Schematic overview over the asymptotic quantum numbers for the Nilsson model. The figure is adapted from [24] and [111].

neglecting the residual interactions between the nucleons. These residual interactions between the nucleons lead to the deformation of the nucleus [109], which can for example be observed around atomic masses $A \approx 25$ (Mg, Al), $150 < A < 190$ (nucei of the rare earth elements), and $A > 220$ (actinides and superheavy elements) [112, 113]. Therefore a new model is needed taking the deformation of an atomic nucleus into account. A model capable of explaining nuclear deformations with axial symmetry is the Nilsson model [111, 113] using a deformed (elliptic) harmonic oscillator potential. In the Nilsson model, any deformation results in a energy shift for the associated energy levels, giving rise to two consequences. First, shell gaps can change with respect to the deformation due to the different responses of the energy levels, which can result in vanishing existing shell gaps and the occurence of new gaps. Second, ground-state orbitals of heavier spherical isotopes can be occupied in lighter nuclei by means of single-particle excitations at a given deformation as a result of the energy difference between energy levels, which vary dependent on the deformation.
For large deformations the J, L, and S quantum numbers are no longer sufficient to fully describe the configurations of the nucleons. A new set of numbers Ω, Λ, and Σ is introduced with $\Omega = \Lambda + \Sigma$. Ω, Λ, and Σ describe the projections of J, L, and S on the symmetry axis [115], which is shown in Fig. 2.5. In addition, the principal quantum number is defined as $N = n_z + n_\perp$, with the oscillator quantum numbers parallel (n_z) and perpendicular ($n_\perp$) to the symmetry axis originating from the axially symmetric harmonic oscillator approach for describing the nuclear potential. A nuclear orbital can be desribed by the Nilsson quantum numbers $\Omega[Nn_z\Sigma]$.
The energy levels and shell gaps of nuclear oribtals are predicted from the Nilsson model as a function of the deformation, which is shown in a so-called Nilsson diagram Fig. 2.6 and Fig. 2.7. In these diagrams the single-particle energy levels for the proton (Fig. 2.6) and neutron (Fig. 2.7) as a function of the deformation parameter ϵ_2 are shown. In the case of einsteinium isotopes Nilsson quadrupole deformation parameter ϵ_2 of $\epsilon_2 = 0.217$ (^{253}Es), $\epsilon_2 = 0.208$ (^{254}Es), and $\epsilon_2 = 0.208$ (^{255}Es) are expected [114]. For ^{255}Fm a quadrupole deformation parameter of $\epsilon_2 = 0.217$ [114] is predicted. Looking at Fig. 2.6 one can see that the proton configurations $\pi_{3/2}[521]$ and $\pi_{7/2}[633]$ are the predicted orbitals in this deformation region, originating from the spherical orbitals $2\,\mathrm{f}_{7/2}$ and $1\,\mathrm{i}_{13/2}$, respectively. These $2\,\mathrm{f}_{7/2}$ and $1\,\mathrm{i}_{13/2}$ orbitals are relevant for the shell gap of spherical superheavy nuclei at $Z = 114$. Considering increasing deformation, the deformed proton orbitals $\pi_{3/2}[521]$ and $\pi_{7/2}[633]$ originating from the spherical orbitals are dropping strongly in energy. Thus, these orbitals can be investigated in deformed nuclei such as einsteinum and fermium isotopes. The proton configuration $\pi_{3/2}[521]$, which is the assigned ground-state configuration in the isotope ^{251}Es, and $\pi_{7/2}[633]$, which is the assigned ground-state configuration in the isotopes ^{249,253}Es, are energetically close-lying, making a change in the proton orbital along the einsteinium isotope chain possible [116]. Ground-state assignments of light einsteinium isotopes with $A < 249$ are still uncertain, whereas the two low-lying Nilsson levels $\pi_{7/2^+}[633]$ and $\pi_{3/2^-}[521]$ may alternate as ground states [117, 118, 119]. The predicted neutron configurations in the mentioned deformation region are the $\nu_{7/2^+}[613]$ and $\nu_{9/2^-}[734]$ orbitals, which are relevant for the $N = 152$ deformed shell closure and shown in Fig. 2.7. The $\nu_{7/2}[613]$ and $\nu_{9/2}[734]$ orbitals originate from the spherical orbitals $1\,\mathrm{i}_{11/2}$ and $1\,\mathrm{j}_{15/2}$, respectively, and are there-

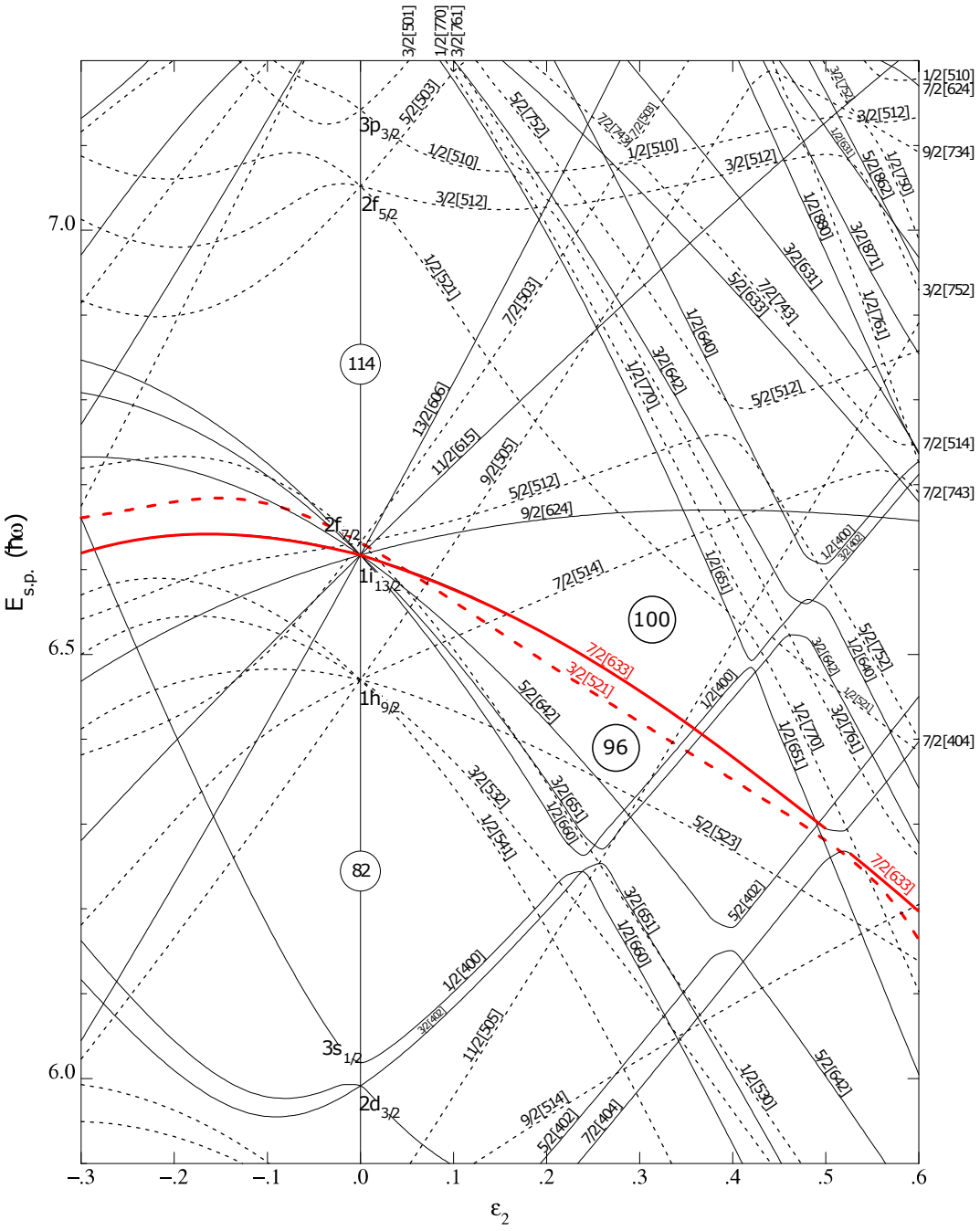

Figure 2.6.: Nilsson diagram for protons with $Z \geq 82$. The single-particle energy $E_{\text{s.p.}}$ is plotted as a function of the quadrupole deformation parameter ϵ_2. The $\pi_{3/2}[521]$ and $\pi_{7/2}[633]$ proton configurations are energetically close-lying (marked red), making a change in the proton orbital along the einsteinium isotope chain possible. Here, deformation parameters of $\epsilon_2 = 0.217$ (^{253}Es), $\epsilon_2 = 0.208$ (^{254}Es), and $\epsilon_2 = 0.208$ (^{255}Es) are predicted [114]. The figure is adapted from [24].

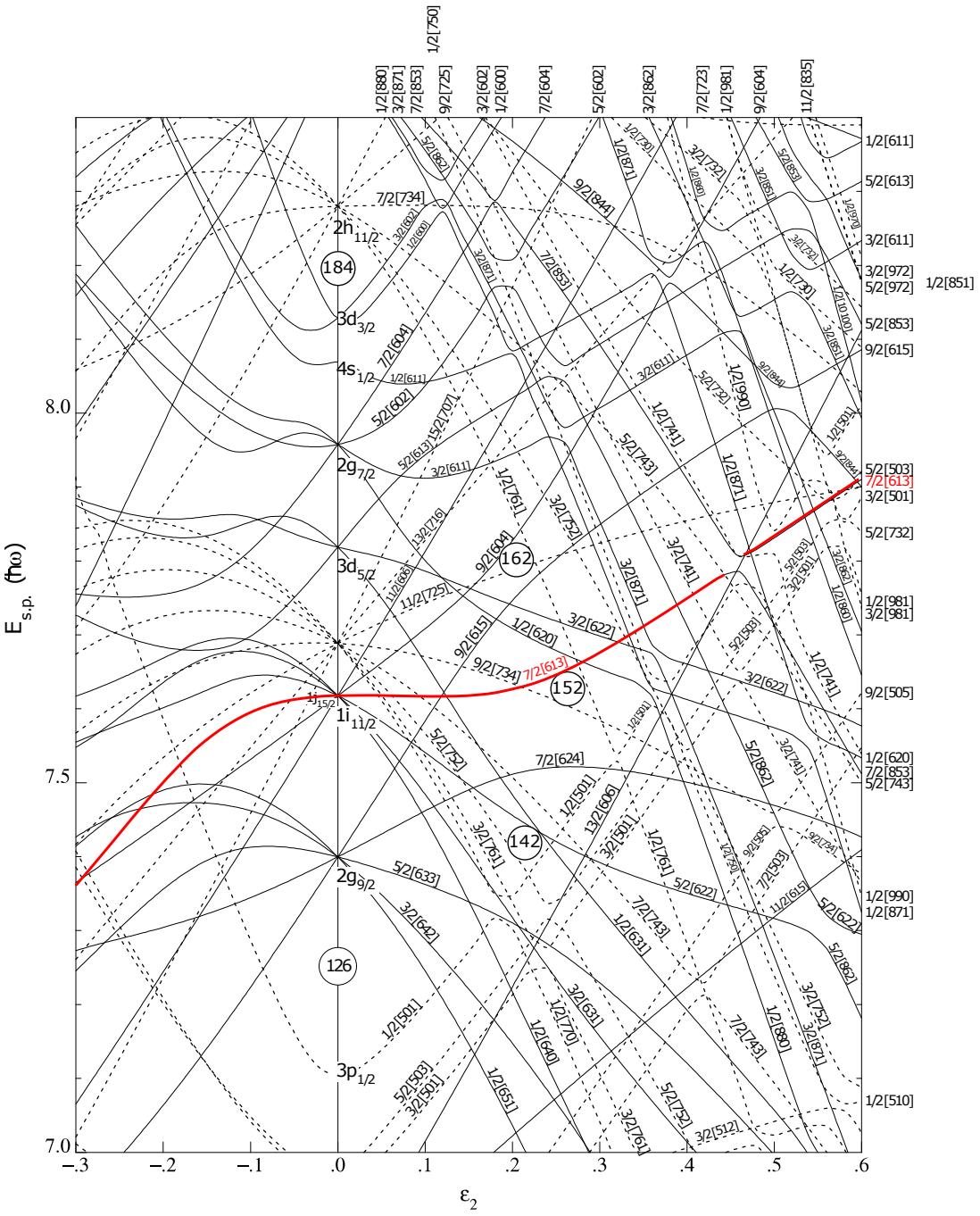

Figure 2.7.: Nilsson diagram for neutrons with $N \geq 126$. The single-particle energy $E_{\text{s.p.}}$ is plotted as a function of the quadrupole deformation parameter ϵ_2. The $\nu_{7/2}[613]$ neutron configuration is the ground-state configuration of the isotone ^{255}Fm ($\epsilon_2 = 0.217$ [114]) and therefore proposed for ^{254}Es ($\epsilon_2 = 0.208$ [114]) (marked red). The figure is adapted from [24].

fore relevant for the shell gap of spherical superheavy nuclei. For slightly more deformed nuclei with $\epsilon_2 = 0.3$ the neutron configurations $\nu_{1/2^+}[620]$ and $\nu_{1/2^-}[761]$ are energetically close-lying to the $\nu_{7/2}[613]$ and $\nu_{9/2}[734]$ orbitals. Thus, these orbitals could also be relevant for the ground-state configuration at slightly larger deformation.
Comparing measured electromagnetic moments (μ_I, Q_s) to the theoretical predictions from the nuclear SM provides rich information on the underlying nuclear structure [1]. For example the intrinsic quadrupole moment Q, which can be calculated from the spectroscopic electric quadrupole moment Q_s according to eqn. 2.13, is related to the deformation parameter ϵ_2 [68] by

$$Q = \frac{4}{5}\epsilon_2 Z R^2 (1 + \frac{\epsilon_2}{2} + \frac{4}{9}\epsilon_2^2 - \frac{49}{162}\epsilon_2^3 + ...) \tag{2.57}$$

with the nuclear radius $R = 1.2A^{1/3}\,\mathrm{fm}$, the mass number A, and the nuclear charge Z [34]. The deformation parameter β_2 is related to the Nilsson quadrupole deformation parameter ϵ_2 [24] by

$$\beta_2 = \sqrt{\pi/5}\left(\frac{4}{3}\epsilon_2 + \frac{4}{9}\epsilon_2^2 + \frac{4}{27}\epsilon_2^3 + \frac{4}{81}\epsilon_2^4 + ...\right). \tag{2.58}$$

More information about the Nilsson model including mathematical descriptions can be found in e.g. [24, 111, 113, 120]. For more realistic descriptions of the single-particle configurations a finite depth potential, e.g. the Woods-Saxon potential, can be used instead of the deformed harmonic oscillator potential.

3. Experimental techniques

3.1. Production of the heaviest elements

The heaviest elements with $Z > 100$ can be produced in fusion-evaporation reactions at accelerator facilities (on-line) like GSI in Darmstadt, where elements available in sufficient amounts are irradiated with heavy ions (e.g. $^{48}Ca^{10+}$). The low cross-sections of these type of reactions result in rates of at most a few particles per second [1, 7]. In addition, the high kinetic energies of the radionuclides of a few tens of MeV as well as the short half-lives of a few minutes at most for many of the heaviest elements provide additional challenges when designing experiments [7, 121].
In fusion-evaporation reactions, a projectile nucleus (p, atomic number Z') is accelerated to a characteristic kinetic energy and bombarded onto a nucleus of a typically stable atom (target T, atomic number Z) at rest. If the projectile enters the target nucleus despite the large Coulomb repulsion, a so-called compound nucleus (CN) can form, which then is in a highly excited state. In most cases, the CN immediately fissions, but through the evaporation of one or more particles (ejectiles) it can stabilize to a lowly excited evaporation residue nucleus (EVR, atomic number $Z + Z'$). Typically, neutrons, protons or α-particles are evaporated as ejectiles in the production of the heaviest elements [6, 7].
A possible reaction with x neutrons as ejectiles can be expressed as

$$ {}^{A}Z({}^{A'}Z', x\mathrm{n})^{A+A'-x}(Z + Z') \tag{3.1} $$

with the mass numbers of projectile and target indicated by A and A', respectively.
This fusion-evaporation process can only initiate when the nucleons of the projectile get close enough to the central attractive well of the target nucleus and experience the attractive nuclear force. However, a charged projectile also experiences the long range repulsive Coulomb force of the positively-charged nuclei of the target. The energy conditions when a charged projectile reacts with a target nucleus are shown schematically in Fig. 3.1, whereas the necessary energy to surmount the Coulomb barrier E_{CB} [6, 122] can be expressed as

$$ E_{\mathrm{CB}} = \frac{Z \cdot Z' \cdot e^2}{r_{\mathrm{C}}} \tag{3.2} $$

with r_{C} being the distance of closest approach (Coulomb radius) between the nuclei. Considering also a finite probability for barrier penetration, a minimum kinetic energy (threshold energy E_{thr}) is required for charged particles to initiate a fusion reaction [6, 7], which can be expressed as

$$ E_{\mathrm{thr}} = -Q\left(1 + \frac{m_{\mathrm{p}}}{m_{\mathrm{T}}}\right). \tag{3.3} $$

Here, the Q-value is the energy of the reaction and can be written as

$$ Q = -\Delta m c^2 = (m_{\mathrm{p}} + m_{\mathrm{T}} - m_{\mathrm{CN}}) \cdot c^2, \tag{3.4} $$

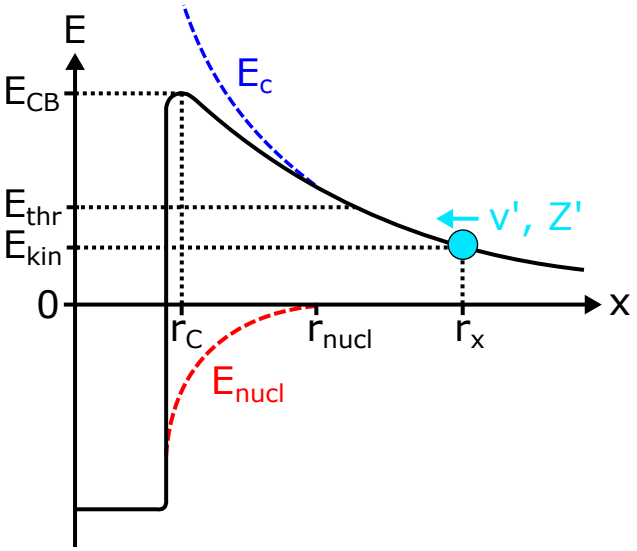

Figure 3.1.: A charged projectile (v', Z') experiences a Coulomb repulsion E_C when approaching a target nucleus in a distance x, decreasing the projectile's kinetic energy $E_{kin,p}$. If the kinetic energy reaches a value of zero before overcoming the Coulomb barrier E_{CB}, the projectile is reflected from the target nucleus before it can experience the attractive nuclear potential E_{nucl}. Nevertheless, a nuclear reaction can already occur at a minimum projectile energy E_{thr} due to a finite probability for barrier penetration. Figure adapted from [122].

whereas energy-releasing reactions are represented by positive Q-values and energy-absorbing reactions by negative Q-values. For projectiles with a kinetic energy $E_{kin,p}$ and a kinetic recoil energy $E_{kin,CN}$ of the CN according to the conservation of momentum ($m_p \cdot v_p = m_{CN} \cdot v_{CN}$), the inner excitation energy E^* [6] of the CN can be calculated out of the energy balance (target at rest) of the fusion reaction as

$$E^* = Q + E_{kin,p} - E_{kin,CN}. \tag{3.5}$$

Thus, the inner excitation energy depends on the Q-value of the reaction and the kinetic energy of the projectile. Fusion reactions are classified according to the excitation energy of the CN. Fusion reactions of light projectiles (e.g. $Z = 5 - 22$ [7]) with heavy target nuclei (e.g. actinides) are called "hot" fusion reactions. In these reactions, a CN with an excitation energy of about 30 - 40 MeV is formed due to a small Q-value and the conservation of momentum resulting in a small kinetic energy of the CN. Here, the de-excitation of the CN into an EVR implies the emission of three or four neutrons, each reducing the excitation energy of the CN by about 9 MeV according to the binding energy of one neutron, and several γ-rays. Fusion reactions of heavy projectiles (e.g. $Z = 18 - 30$ [7]) with heavy target nuclei (e.g. lead) are called "cold" fusion reactions. Here, a CN with an excitation energy of about 10 - 20 MeV is formed due to the larger Q-value and the higher excitation energy of the CN. Thus, one to two neutrons are evaporated in the de-excitation of the CN [123, 124]. The stabilization of the CN can result in different combinations of radionuclide and ejectile

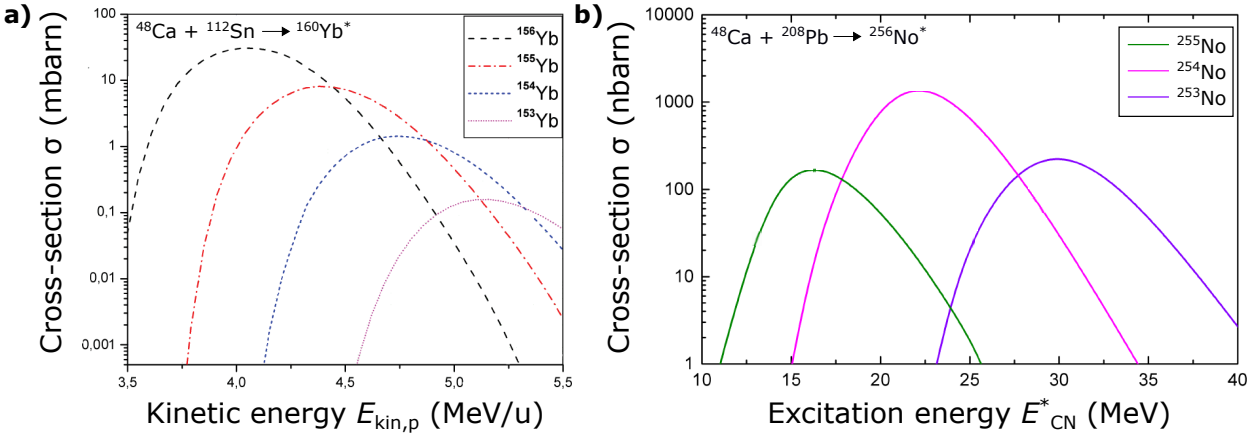

Figure 3.2.: Excitation functions for the evaporation residues (EVR) in the fusion-evaporation reactions ^{112}Sn(^{48}Ca, xn) (a) and ^{208}Pb(^{48}Ca, xn) (b). The figures are adapted from [125, 126]. There, the excitation functions were calculated using the HIVAP code [36, 127, 128].

("exit-channel") depending on the kinetic energy of the projectile. Each exit-channel is individually populated depending on the kinetic energy of the projectile, which corresponds to a certain excitation energy of the CN. The correlation function $\sigma = f(E_{\mathrm{kin,p}})$ is called the excitation function and describes the dependence of the reaction cross-section σ on the kinetic energy of the projectile. Fig. 3.2 shows the excitation functions for the evaporation residues (EVR) in the fusion-evaporation reactions ^{112}Sn(^{48}Ca, xn) (a) and ^{208}Pb(^{48}Ca, xn) (b).

The production of ^{154}Yb ($T_{1/2} = 0.409\,\mathrm{s}$), ^{155}Yb ($T_{1/2} = 1.793\,\mathrm{s}$), and ^{156}Yb ($T_{1/2} = 26.1\,\mathrm{s}$), used in the on-line commissioning of the gas-jet setup in this work, was carried out using the fusion reactions ^{112}Sn(^{48}Ca, 6n)^{154}Yb, ^{112}Sn(^{48}Ca, 5n)^{155}Yb, and ^{112}Sn(^{48}Ca, 4n)^{156}Yb. At a calcium projectile energy of 4.55 MeV/u, which was used in the reactions performed throughout this work, ^{154}Yb, ^{155}Yb, and ^{156}Yb are formed with cross-sections of $\sigma_{^{154}\mathrm{Yb}} \approx 0.8\,\mathrm{mbarn}$, $\sigma_{^{155}\mathrm{Yb}} \approx 7\,\mathrm{mbarn}$, and $\sigma_{^{156}\mathrm{Yb}} \approx 4\,\mathrm{mbarn}$, respectively [125].

For the planned on-line production of the nobelium isotopes ^{253}No ($T_{1/2} = 1.62\,\mathrm{min}$) and ^{254}No ($T_{1/2} = 51\,\mathrm{s}$), the reactions with the highest cross-sections and most accessible target materials are ^{207}Pb(^{48}Ca, 2n)^{253}No and ^{208}Pb(^{48}Ca, 2n)^{254}No [46]. At a calcium projectile energy of 4.55 MeV/u ($E^*_{\mathrm{CN}} = 23.35\,\mathrm{MeV}$), which results in the highest production rate for ^{254}No, the isotopes ^{253}No and ^{254}No are formed with cross-sections of $\sigma_{^{253}\mathrm{No}} \approx 0.5\,\mathrm{nbarn}$ and $\sigma_{^{254}\mathrm{No}} \approx 2\,\mu\mathrm{barn}$ [129], respectively. Furthermore, the isotope ^{255}No ($T_{1/2} = 3.52\,\mathrm{min}$) is produced in the reaction ^{208}Pb(^{48}Ca, 1n)^{255}No with a cross-section of $\sigma_{^{255}\mathrm{No}} = 7\,\mathrm{nbarn}$ [125]. Besides the production of ^{254}No in its ground state, a $K = 8^-$ isomeric state ($T_{1/2} = 266\,\mathrm{ms}$) is populated with an isomeric ratio of $\approx 30\%$ [18, 130]. It is planned to study this isomer in future beam times with the new gas-jet based setup (see part I).

3.2. SHIP

The velocity filter Separator for Heavy Ion reaction Products (SHIP) at GSI in Darmstadt was developed for the efficient separation of the fusion products from the primary beam [131, 132]. A schematic illustration of SHIP is shown in Fig. 3.3.
A rotating target wheel consisting of 8 separately inserted target foils with a typical thickness of 0.5 mg/cm^2 can be found at the beginning of the velocity filter SHIP. The wheel is rotating to enlarge the beam-on-target surface and to allow for a cooling of the target foils. These foils consist of isotopically pure tin or lead for the production of ytterbium or nobelium isotopes, respectively. The foils are irradiated with an $^{48}Ca^{10+}$ beam from the UNIversal Linear ACcelerator (UNILAC) with a kinetic energy of a few MeV/u (see section 3.1) and average beam intensities of $\approx 6.24 \cdot 10^{12}$ particles/s to produce the desired fusion product [133]. A quadrupole triplet is used to focus the divergent ion beam consisting of the remaining primary beam and the recoiling fusion products. To separate the fusion products from the primary beam, a charge and mass independent velocity separation with static fields is used

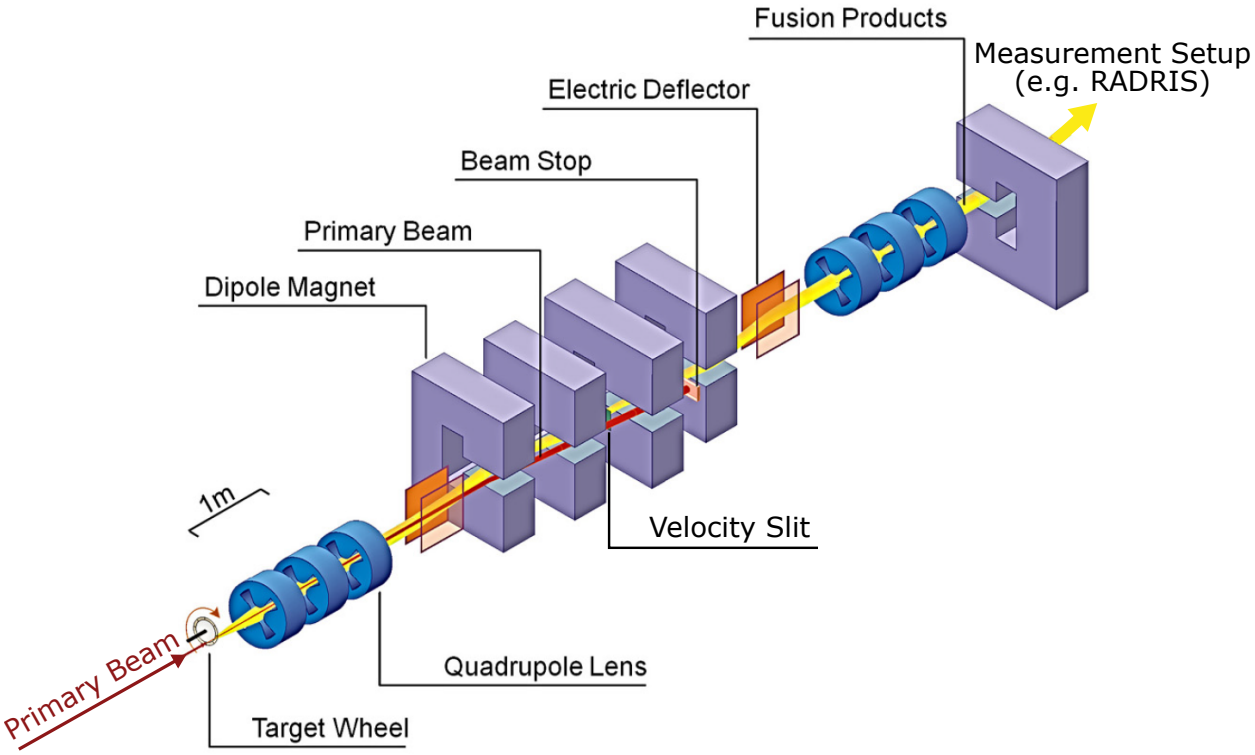

Figure 3.3.: Schematic illustration of the velocity filter SHIP. The primary beam from the UNILAC hits a rotating target wheel. The recoiling fusion products (yellow) are separated in flight from the remaining primary beam and other unwanted species (red) by means of magnetic and electrostatic fields. Quadrupole lenses properly focus the beam consisting of the fusion products before entering the experiment. Figure adapted from [43].

[132]. Here, magnetic and electric fields are mostly superimposed and operated in a cross-geometry. The velocity filter can only be passed by ions with appropriate velocity without being deflected. Here, the electrostatic force and the Lorentz force affect the particles, thus resulting in the force

$$\vec{F} = q\vec{E} + q(\vec{v}\mathrm{x}\vec{B}). \tag{3.6}$$

For particles with a velocity

$$|\vec{v}| = \frac{|\vec{E}|}{|\vec{B}|} \tag{3.7}$$

the forces cancel each other and thus the particles can pass through the filter. The velocity can be chosen through the appropriate choice of electric and magnetic fields. After the separation another quadrupole triplet is used to focus the beam consisting of the fusion products. At the end of SHIP a dipole magnet serves for the further separation of scattered high-energy primary particles, before the fusion product beam is delivered to the measurement setup. The background rate due to transfer products passing through SHIP at a primary beam current of $\approx 6.24 \cdot 10^{12}$ particles/s is ≈ 1 ion/min [131]. A time-of-flight (TOF) and a 16-strip silicon-detector are used to identify the fusion products [131, 132].

3.3. Thermalization of fusion products in buffer-gas cells

The radionuclides recoiling out from the target have kinetic energies of up to tens of MeV. Thus, in any planned spectroscopy experiment the first step must be to slow down the radionuclides of interest to thermal energies. This can be achieved preferably in a so-called buffer-gas stopping cell [1, 43], where the nuclides dissipate kinetic energy through scattering with gas molecules. This is in most cases combined with the use of an additional solid degrader that the particles have to pass before entering the gas volume. Without such a degrader, fully stopping the ions in a buffer gas would require very long paths, thus leading to the construction of undesirably large buffer-gas stopping cells. In some cases it is enough to use the thin entrance window foil separating the vacuum section of the preceding transport beamline from the buffer-gas environment as the only solid degrader. In the buffer-gas cell an inert gas like helium or argon is used to avoid the formation of ion-chemical compounds. Such chemical compounds would render any atomic spectroscopy experiment impossible. Depending on the kinetic energies of the incoming ions and the thickness of the solid degrader, gas pressures of $\approx 30 - 500$ mbar are used. Lower gas pressures could also be used, but the argument with the undesirable large design of the buffer-gas cell applies again. A significant fraction of the slowed down radionuclides remain charged in the buffer-gas environment. The charge state distribution depends on the ionization potential of the ion of interest compared to the ionization potential of the buffer-gas atoms. In the case of nobelium and ytterbium the ions remain singly-charged if stopped in an argon buffer-gas. In order to avoid charge exchange with impurities, a crucial prerequisite is the usage of high-purity buffer gas with impurities on a ppb level. In order to achieve this, purification

methods should be employed to assure highest cleanliness. Additionally, the gas-cell should fulfill ultrahigh vacuum requirements.
The first buffer-gas stopping cell was applied in 1985 on fusion-evaporation reaction products at the Ion-Guide Isotope-Separator On-Line (IGISOL) facility [134]. Meanwhile, this technique was implemented in numerous experiments all over the world [1, 43, 126] as, e.g., the RADRIS [42, 135] and SHIPTRAP [136, 137] experiments at GSI, the new gas-jet based high-resolution spectroscopy setup (see part I) at Helmholtz Institute Mainz (HIM), and the RIKEN Projectile fragment Separator (RIPS) experiment [138]. The RADRIS method and the new gas-jet based setup make use of the resonance ionization spectroscopy (RIS) technique after the thermalization of the radionuclides in the buffer gas, which will be discussed in the next section.

3.4. Resonance ionization spectroscopy

The laser spectroscopy technique used in this work is known as resonance ionization spectroscopy (RIS). More information about this technique, which was first demonstrated in 1972 [27], can be found in various articles as [28, 139, 140] and textbooks as [141], which were used as the foundation for this chapter.
The atoms are step-wise resonantly excited until the ionization process occurs, producing a free electron and an ion of the element of interest. Due to the unique, fingerprint-like structure of each element's atomic structure this technique is highly element-selective by using well tuned laser wavelengths with suitable spectral widths. Additionally, high isotopic selectivity can be achieved by using high-resolution techniques.
Fig. 3.4 shows an schematic overview over a two-step excitation and ionization process. The

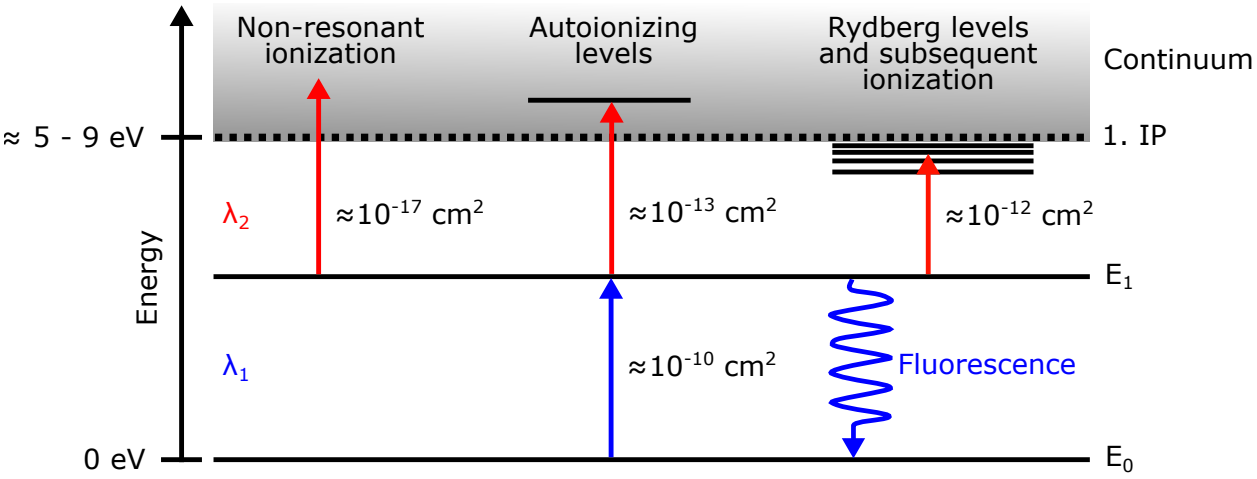

Figure 3.4.: Schematic overview over the different excitation and ionization schemes for resonance ionization with typical cross-sections. The ionization step can be performed non-resonantly or by using autoionizing or Rydberg states. For more details see text. Figure adapted from [139].

multitude of levels in an atomic system allows for various possible excitation schemes. The most common way is to use two or three excitation steps to overcome the ionization potential of about 5 - 9 eV, which is the energy range for $>80\%$ of the elements [139]. Increasing the number of resonant transitions in an excitation scheme increases the selectivity of the process. At the same time, however, all resonant transitions must be saturated in order to maintain the high efficiency, which is not always achievable. Therefore, the choice of the excitation scheme is often a trade-off between selectivity and efficiency [142].
The resonant excitation process is an efficient process with absorption cross-section for photons in the order of $\sigma = \lambda^2/2\pi \approx 10^{-10}\,\mathrm{cm}^2$ for atoms at rest. The excitation probability $dW(t)$ is defined by

$$dW(t) = \sigma \cdot J(t) \cdot dt \tag{3.8}$$

with the photon flux $J(t)$. In order to saturate the resonant excitation transition under the assumption of an excitation probability of 100 % ($dW(t) = 1$), a typical atomic lifetime of $dt = 10\,\mathrm{ns}$ for the excited state, and a cross-section of $\sigma \approx 10^{-10}\,\mathrm{cm}^2$, a photon flux of about

$$J(t) \approx \frac{1\,\mathrm{photon}}{10^{-10}\,\mathrm{cm}^2 \cdot 10 \cdot 10^{-9}\,\mathrm{s}} = 10^{18}\,\frac{\mathrm{photons}}{\mathrm{cm}^2 \cdot \mathrm{s}} \tag{3.9}$$

is needed. Typically pulsed laser systems are used in order to saturate these transitions. The low duty cycle of pulsed lasers means at the same time that the peak photon flux during a pulse is several orders of magnitude higher compared to the flux of a cw laser with similar average power. Therefore, the use of a cw laser makes it harder to saturate transitions, especially the ionizing transition with smaller cross-sections of $10^{-17} - 10^{-12}\,\mathrm{cm}^2$. Thus, a lower ionization efficiency is reached with a cw laser compared to a pulsed laser with the same average power. Nevertheless, the use of narrowband continuous wave laser systems may be favorable in some cases as the narrow bandwidth (often $< 1\,\mathrm{MHz}$) allows for accurate measurements of the hyperfine splittings and isotope shifts, where high resolution and high isotopic selectivity is required [139, 142].
For the ionization step three different ionization techniques can be used. The non-resonant excitation of an electron into the continuum above the IP has very low cross-sections in the order of $10^{-17}\,\mathrm{cm}^2$, corresponding to an average power of a few watts for a pulsed laser with a temporal pulse width of 8 ns, a beam diameter of 1 mm, and a repetition rate of 10 kHz. To avoid this drawback, elements with a rich atomic spectrum, e.g. lanthanides and actinides, can use autoionizing and Rydberg states as the ionizing steps. In the case of autoionization two electrons are simultaneously excited in high-lying states with the total energy of the doubly-excited atom located above the first ionization potential. After a short time (typically $\ll 1\,\mathrm{ns}$ [139]) the correlation between the electrons leads to the transfer of the excitation energy from one electron to the other, creating a free electron and a positively charged ion. Here, cross-sections of typically $10^{-13}\,\mathrm{cm}^2$ are observed, hence reducing the power requirements on the laser systems. Alternatively, the electron can be excited into a high-lying Rydberg level close to the IP. A Rydberg level describes a state in which one valence electron is located in an orbital with a high principal quantum number n far away from the other shell electrons. The binding energy of an electron in a Rydberg level close to

the IP is very small as shown in eqn. 2.3, whereby the valence electron can be separated from the atom through small perturbations as collisions, electric fields, far-infrared photons, or from black body radiation. This process has a cross-section of $10^{-12}\,\mathrm{cm}^2$. Both autoionizing and Rydberg states require resonant excitation using a tunable laser.
Three measurement methods, which make use of the RIS technique, were important for this work and will therefore be covered in the following.
One measurement method is the laser ionization in a hot cavity. By applying resonant laser radiation inside a hot cavity, one can excite and ionize the element of interest. An increased ionization efficiency is gained due to the confinement of the evaporated neutrals inside of the hot cavity, resulting in a prolonged interaction time with the laser radiation. The achievable spectral resolution is limited by the Doppler broadening originating from the thermal velocities of the atoms in the cavity, being typically in the range of a few GHz. Compared to, e.g., the RADRIS technique, this method can be realized in off-line and on-line facilities, but has restrictions with respect to the half life of nuclides that can be studied as the involved effusion process is rather slow. Additionally, it prevents experiments on refractory elements as it relies on the radionuclides interacting with the cavity walls for atomization and neutralization, where the high melting point of these elements would cause them to adsorb on the walls [1]. The in-source laser spectroscopy technique is used in various Isotope Separator On-Line (ISOL) facilities such as Isotope Separation On-Line DEvice (ISOLDE) at CERN [143, 144, 145] and Isotope Separator and ACcelerator (ISAC) at TRIUMF [146, 147]. Furthermore, the technique was used in this work at the Resonance Ionization Spectroscopy in Collinear geometry (RISIKO) mass separator [148] of the Laser Resonance Ionization Spectroscopy for Selective Applications (LARISSA) group at Johannes Gutenberg-University Mainz in the measurements of the einsteinium isotopes ^{253,254,255}Es. Thus, a detailed description of the RISIKO setup can be found in chapter 5.3.
Another technique to be introduced is the RAdiation Detected Resonance Ionization Spectroscopy (RADRIS) method [42, 135], which is schematically shown in Fig. 3.5. Heavy and superheavy elements are produced in fusion-evaporation reactions at GSI, Darmstadt. The velocity filter SHIP separates the fusion products from the primary beam before entering the buffer gas cell at $\approx 90\,\mathrm{mbar}$ argon pressure, stopping and thermalizing the recoils of interest as singly-charged ions (Fig 3.5 a). The ions are guided via electrostatic fields onto the tip of a filament made from tantalum (Ta) wire, where the ions are accumulated (Fig 3.5 b) before being neutralized and desorbed by pulse heating the filament (Fig 3.5 c). A neutral atom cloud from the filament expands in the gas and is two-step photoionized (Fig 3.5 d). The photoions are guided via electrodes towards a silicon detector (Fig 3.5 e), which detects the radioactive decay (Fig 3.5 f). The RADRIS method is highly sensitive and efficient for radionuclides featuring an alpha- or fission-decay branch. The stopping in a buffer-gas cell for thermalization of highly charged recoil ions, ion-guiding via electric fields, and the high neutralization efficiency based upon neutral desorption from a heated tantalum filament are implemented in a new, compact setup, which will be covered in part I of this thesis.
One last technique developed for heavy elements is the laser spectroscopy in a well-collimated, supersonic or hypersonic gas-jet created by a nozzle emerging from a high-pressure buffer-gas-stopping cell [47, 149]. Combined with a high-repetition rate laser system a high spectral

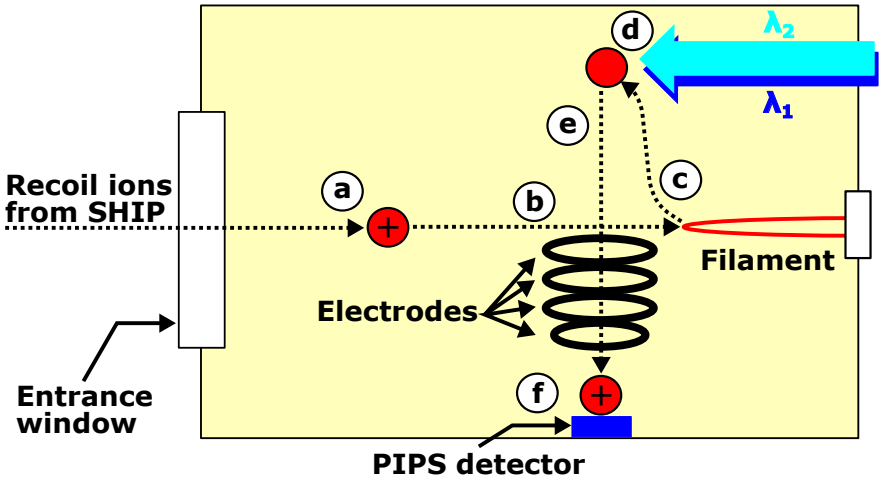

Figure 3.5.: Schematic overview of the RADRIS method. The recoil ions from SHIP enter the buffer gas cell, where they are thermalized (a). The ions are guided towards a wired filament, where the recoil ions are accumulated (b) before they are re-evaporated from the filament by pulse heating (c). An atom could is created, in which the neutral atoms are two-step photoionized using two laser beams of wavelengths λ_1 and λ_2 (d). The re-ionized fusion products are guided to and accumulated on the passivated implanted planar silicon (PIPS) detector (e), where the radioactive-decay is detected (f).

resolution can be achieved while maintaining a high efficiency. The spectral resolution for laser spectroscopy improves considerably compared to spectroscopy inside of a buffer-gas due to the low temperature and density as well as the very low lateral velocities in the gas-jet. Here, the atom longitudinal velocity is about 550 m/s, which is mainly determined by the extraction velocity of the argon buffer gas. Therefore, an interaction region of ≈ 55 mm of the gas-jet with a 10 kHz-repetition-rate laser system is needed to address all atoms in the gas-jet by at least one laser pulse. The two-step or three-step-laser ionized ions are then guided towards the detection region using a radiofrequency ion guide. This technique was successfully implemented at KU Leuven, Belgium, demonstrating high efficiency combined with high-resolution laser spectroscopy on actinium isotopes [49]. To improve the technique a new laboratory was established, enabling detailed characterization of supersonic and hypersonic gas-jets created by different de Laval nozzles [50, 150]. The in-gas-jet technique is implemented in a new, compact setup, which will be covered in part I of this thesis.

3.5. Radiofrequency quadrupole ion guides

In 1953 the quadrupole mass spectrometer (QMS) was developed by W. Paul [151], which uses the focusing and defocusing forces of a high-frequency electric quadrupole field and the stability properties of the ion motion for mass separation [151, 152, 153]. Ion traps as, e.g., the Paul trap, which serve to store ions in a spatially limited area, were developed by

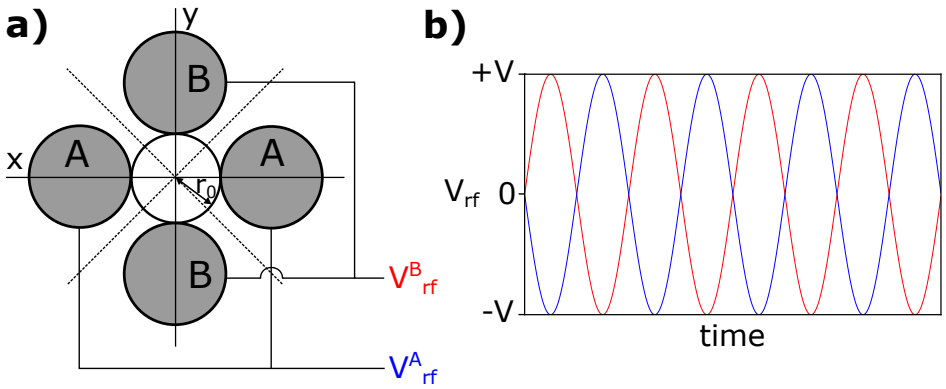

Figure 3.6.: a) Profile of a quadrupole consisting of cylindrically shaped rod electrodes. The electric field is zero along the dashed lines. b) Time dependence and relative phase of the applied RF-field. Figure adapted from [156].

extending the methods of two-dimensional focusing as observed, e.g., in a radiofrequency quadrupole (RFQ) to three dimensions [154, 155].
A RFQ consists of four hyperbolically or cylindrically shaped rod electrodes, which extend in the z-direction and are arranged in a square in the xy-plane as shown in Fig. 3.6. The pairs of electrodes facing each other are kept at the same potential composed of a direct current (DC) and an alternating current (AC) component, whereas the two pairs are supplied by the AC component at opposing phase [156].
Ions can be stabilized in the xy-plane if the applied voltage consists of a DC voltage U and a radiofrequency (RF) voltage V with frequency ω, resulting in the total potential Φ_0 given by

$$\Phi_0 = U + V\cos(\omega t). \tag{3.10}$$

The polarity of the voltage between the electrodes then changes periodically, so that the ions are stabilized and destabilized alternating in the x- and y-direction. This leads on time average to a stabilization in both directions x and y for certain ion masses and to destabilization for other masses, whereby the mass selection is determined by the frequency ω and the ratio of U/V of direct and radiofrequency voltage amplitude [53]. In the case of a linear quadrupole geometry the total potential Φ_0 applied to the electrodes gives rise to a pseudopotential V_{pseudo}. This pseudopotential has the form of a parabolic well [157] and can be described by

$$V_{\text{pseudo}}(r) = \frac{e}{m}\left(\frac{V}{r_0^2\omega}\right)^2 r^2. \tag{3.11}$$

Here, r_0 is the distance from the central axis to the RFQ electrodes, e is the ion charge, and m is the ion mass. Thus, an harmonic oscillator potential is seen by an ion when transmitted through the RFQ [157].
The equation of motions dictate which parameter sets result in a stable ion motion and are

defined as

$$\frac{d^2x}{dt^2} + \frac{e}{m_i r_0^2}(U + V\cos(\omega t))x = 0 \tag{3.12}$$

and

$$\frac{d^2y}{dt^2} - \frac{e}{m_i r_0^2}(U + V\cos(\omega t))y = 0. \tag{3.13}$$

Defining the dimensionless parameters a, b, and τ as

$$a = \frac{4qU}{mr_0^2\omega^2}, \tag{3.14}$$

$$b = \frac{2qV}{mr_0^2\omega^2} \tag{3.15}$$

and

$$\tau = \frac{1}{2}\omega t, \tag{3.16}$$

eqn. 3.17 and 3.18 can be rewritten as the so-called Mathieu equations

$$\frac{d^2x}{d\tau^2} + (a + 2b\cos(2\tau))x = 0 \tag{3.17}$$

and

$$\frac{d^2y}{d\tau^2} - (a + 2b\cos(2\tau))y = 0. \tag{3.18}$$

Depending on the size of the a and b parameters the Mathieu equations will result in stable or unstable solutions. In the case of stable solutions the ions will oscillate with a confined amplitude in the x- and y-direction, so that the ions can traverse the quadrupole field in z-direction without hitting the electrodes. In the case of unstable solutions the oscillation amplitude is exponentially increasing in x- or y-direction, so that the ions cannot traverse the quadrupole field in z-direction without hitting the electrodes after a short distance. The stable areas can be visualized in an a-b-diagram as shown in Fig. 3.7. It is important to note that these stability areas only depend on a and b and not on the initial conditions of the injected particles. As both parameters a and b are dependent on the mass m of the particle, it is possible to choose these parameters so that only particles of the desired mass m can travel through the RFQ [53].
For a given choice of the voltages U and V all masses m lie on a straight line $a/b = 2U/V =$ constant, whereas only the masses inside of the stability area are transported. The position of a certain mass $m = 4qU/(a \cdot r_0^2\omega^2)$ is only dependent on the a-parameter for predefined parameters r_0 and ω. The closer the working line comes to the tip of the stability area, the narrower becomes the transmitted mass range Δm. Thus, by choosing the ratio a/b one can freely choose the mass resolving power within certain limits simply by changing the voltage

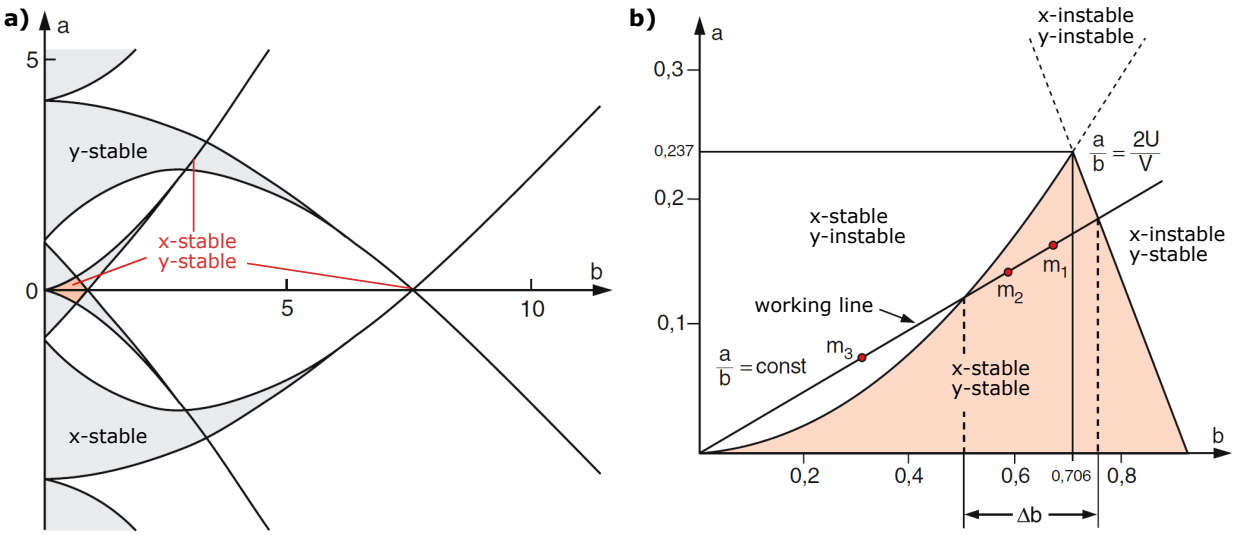

Figure 3.7.: a) Stability diagram for stable solutions for the x- and y-movement. The overlapping areas of stable solutions in both directions are indicated. b) Detail of the upper half of the first stability area. The working line (solid black line) is determined by the ratio $a/b = 2U/V =$ constant. Figure adapted from [53].

ratio U/V [53].
The RF-fields only radially confines the charged particles in an ion guide. Additional fields are needed in the RFQ to confine or dictate the motion of the charged particles along the axis (z-direction). This can be achieved by using DC potentials, which can be realized by electrode segmentation, causing an axial field gradient that can be used for dragging the ions through the RFQ and speeding up the transit of the ion beam through the RFQ structure [158]. It is even possible to temporarily collect and store ions as it is done for instance in ion bunchers, where a buffer gas is used to cool an ion beam. This cooling greatly improves the ion beam emittance and energy spread [159, 160].

Part I.

A new gas-jet based high-resolution spectroscopy setup

4. Gas-jet setup

The aim of this work was to perform high-resolution laser spectroscopy on actinides as already stated in the introduction chapter. A prerequisite for such investigations is the use of capable measurement methods. One such method is the RADRIS technique [42, 135], which was introduced in the last chapter. Here, RIS is performed inside of the buffer-gas, before guiding the ions towards a silicon detector where the radioactive decay is measured. The technique is limited in its achievable spectral resolution by Doppler broadening and especially by the pressure broadening in the regime of a few GHz. Additionally, half-live dependent decay losses due to the cycle operation are observed, limiting the access to radionuclides with half-lives $> 1\,\mathrm{s}$.
Thus, a new apparatus is developed for operation behind the SHIP velocity filter at GSI to overcome these limitations observed with the RADRIS technique. The new setup combines a buffer-gas-stopping cell for thermalization of highly charged recoil ions [161], electric fields for ion-guiding, and a wired filament for efficient ion collection and neutralization [135] from the RADRIS method with the high-resolution gas-jet laser ionization technique developed at KU Leuven [150]. This new gas-jet apparatus was introduced in references [162, 163] and will be explained in more detail in this work.

4.1. A new gas-jet apparatus @ HIM

This chapter will be a description of the newly developed gas-jet apparatus, which was introduced and explained in detail in [162]. Starting first with a conceptual design, the underlying concepts and the supporting simulations will be discussed. Following the first on-line measurement campaign at the velocity filter SHIP [132], the design was adapted with new features.

4.1.1. Conceptual design

The new gas-jet setup combines the RADRIS concept of stopping highly charged recoil ions in a gas-filled cell [161] and ion collection and neutral desorption from a heated filament [135] with the high-resolution gas-jet laser ionization developed at KU Leuven [150]. A schematic overview is shown in Fig. 4.1 and will be shortly explained. In order to be used at the velocity filter SHIP [132] at GSI, Darmstadt, a compact and transportable setup was designed and built. The gas-jet apparatus consists of three main sections: a high-pressure (30-100 mbar, depending on nozzle throat and pumping system) gas cell for stopping, transporting and neutralizing recoil ions, a jet chamber for performing high-resolution laser spectroscopy, and a detector chamber for ion or radioactive decay detection.
Highly energetic and highly charged fusion-evaporation residues (recoil ions) are separated from the primary beam by the velocity filter SHIP and enter the gas cell (length: 30 cm, diameter: 25 cm) filled with 30 - 100 mbar argon buffer gas through a thin window foil (titanium foil of thickness 3.5 µm). The window foil separates the gas-filled volume from the

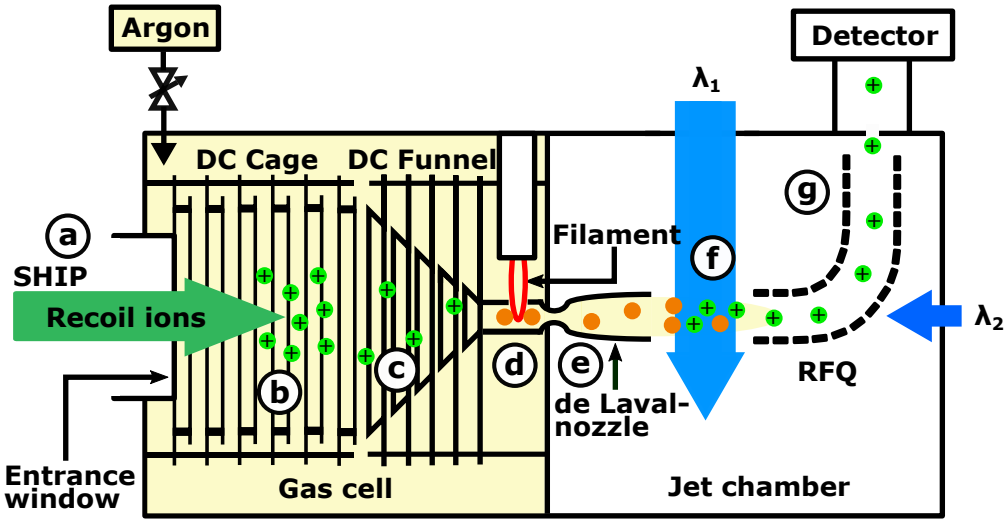

Figure 4.1.: Conceptual design of the gas-jet setup. Recoil ions, entering the gas cell through the entrance foil (a), are stopped and thermalized in 30 - 100 mbar argon buffer gas (b). The singly charged ions are extracted (c) onto the filament by applying DC gradients on the cage (≈ 1.34 V/cm) and funnel (≈ 76.5 V/cm) structures, where adsorption, neutralization, and desorption occurs (d). The atoms are transported to the de Laval nozzle via gas flow, where a gas-jet is formed (e). Resonance ionization spectroscopy is performed on the atoms seeded in the jet (f), ionizing the species of interest. The ions are guided using a 90°-bent RFQ towards the detector, where the ions are detected (g). For more information and operation parameters see text and [48].

vacuum of SHIP and reduces the energy of the incoming recoil ions. The recoil ions are then thermalized in the argon gas and converted to a singly-charged state (Fig. 4.1 b). The choice of the gas is important, as it affects the stopping power, the charge state of the recoil ions, as well as the gas-jet formation. Due to these reasons argon was chosen as buffer gas, as it provides a larger stopping power and recombination coefficient compared to helium [47, 164, 165]. Applying electrostatic voltages at a set of cylindrical electrodes (cage, simulations: 230 V - 210 V), a set of electrodes with decreasing diameter (funnel, simulations: 210 V - 180 V), and at the resistively heated tantalum filament (simulations: -150 V) guides and focus the singly-charged recoil ions towards the filament in a mean transport time of 95 ms. The voltage gradient is required due to the large gas volume needed to efficiently stop the recoil ions (see section 4.1.2). The gas flow is too slow to transport short-lived ions without considerable losses due to radioactive decay. The voltage gradient enables a fast transport (estimated 95 ms but strongly dependent on the applied voltage gradient) of the recoil ions (Fig. 4.1 c), allowing access to short-lived species (e.g. nobelium) with this setup. Further insight into the expected transport time will be given in chapter 4.1.2. The filament is placed inside of a flow channel in the proximity of the extraction nozzle and is permanently heated. The recoil ions are adsorbed at the filament, neutralized, and then desorbed as neutral atoms. This process is only efficient when the filament temperature is

high enough to release the neutral atoms, e.g., about 1050 °C for nobelium from tantalum (Fig. 4.1 d). The neutral desorption of nobelium from a tantalum wire was studied in detail for the RADRIS technique [42, 133]. Drawbacks of this filament technique are the possible background count rate due to surface ionization as well as the formation of oxides due to impurities in the gas or at the surface of the filament. Therefore, the choice of the filament material is crucial for successful experiments [125].
The desorbed neutral atoms are transported by the argon gas flow towards a de Laval nozzle, where a low-density and low-temperature gas-jet seeded with the recoil ions will be formed from the effusing gas. The density of the jet is determined by the background pressure in the jet chamber (length: 31 cm, diameter: 25 cm) of $\approx 7 \cdot 10^{-3} - 1 \cdot 10^{-1}$ mbar and the temperature by the jet speed. For a Mach 5 gas-jet this temperature is about 50 K, where the Mach number M is defined as the ratio of the stream velocity v to the local speed of sound c, i.e. $M = v/c$. In order to form a long collimated gas-jet suitable for high-resolution laser spectroscopy, the pressures of the gas cell (stagnation pressure, p_0) and the jet chamber (background pressure, p_{bg}) have to be matched to a nozzle-specific ratio (Fig. 4.1 e) [50]. The final achievable mass flow in the apparatus is limited by the pumping capacity of about 1300 L/s of the turbomolecular pump in use for the jet chamber. At room temperature a Mach number of ≈ 8 results in an argon stream velocity of about 550 m/s, which determines the length of the ionization zone for performing laser spectroscopy in the jet. For a 10 kHz-repetition-rate laser system one pulse is generated each 100 µs resulting in a length of the ionization zone of 5.5 cm [47]. The laser beams (λ_1 and λ_2 in Fig. 4.1) are arranged, so that the laser beams propagate anticollinear or perpendicular to the gas-jet. The atoms in the supersonic or hypersonic gas-jet are re-ionized through two-step resonant laser ionization spectroscopy (Fig. 4.1 f). The photo-ions are guided to a detector using a 90°-bent radio frequency quadrupole (RFQ), where the ions are detected (Fig. 4.1 g). A 90°-bent RFQ is used to separate neutral particles from the laser-ionized ions, as only the ions are affected by the RFQ voltages. The RFQ (new design, see section 4.7.3) is typically operated with a field gradient of -0.9 V/cm and a RF amplitude of 400 V_{PP} at a resonance frequency of ≈ 1 MHz. In order to achieve a high vacuum condition inside of the detector cell of $\approx 10^{-5} - 10^{-4}$ mbar, a prerequisite for the use of a channel electron multiplier (CEM, Dr. Sjuts KBL 25RS) detector, the detector cell is separated from the jet chamber by a differential pumping stage. For off-line studies on long-lived or stable isotopes a CEM can be used, while a silicon detector is anticipated for on-line measurements of short-lived α-decaying nuclides for decay detection.

4.1.2. Simulation studies

After explaining the concepts underlying the new gas-jet setup the following chapters will summarize the results of simulation studies on ion trajectories, gas flow dynamics, and heat transfer inside of the gas cell. These simulations combined with the conceptual design explained in the previous section were mandatory to conceptualize a detailed layout of the setup. These simulations were performed prior to this work, are summarized in [162] and will be discussed in the following subsections for completeness.

4.1.2.1. Gas cell stopping distribution

As already mentioned in section 4.1.1, the choice of the gas is important for the stopping power, the charge transfer, and the formation of the gas-jet. This section will cover the simulations performed on the stopping power using a 30 mbar-argon-filled gas cell. The stopping range of uranium-ions with kinetic energies of around 36 MeV were simulated after penetrating a titanium foil of thickness 3.5 µm using SRIM (Stopping and Range of Ions in Matter) [166, 167]. The stopping distributions in longitudinal and transversal range are shown in Fig. 4.2. Uranium is used for this simulation because it is the heaviest ion for which a detailed stopping power is known. The energy of 36 MeV corresponds to the recoil energy of nobelium produced in the fusion-evaporation reaction ^{208}Pb(^{48}Ca, 2n)^{254}No resulting from the primary ^{48}Ca beam with a kinetic energy of 200 MeV. Looking at Fig. 4.2 one can see that the point-like entrance beam after penetrating the foil (zero point on the longitudinal range) is scattered along the transversal range due to collisions with argon atoms. A point-like entrance beam was simulated as SRIM does not allow for a realistic spatial distribution of the incoming particle as, e.g., a beam size of about 50 x 22 mm^2 for ^{155}Yb [42]. The longitudinal and transversal distances traveled by the uranium ions with the corresponding probabilities indicated as histograms can be seen, whereas the most probable distance can be found around 50 mm after the entrance window on the beam axis. This

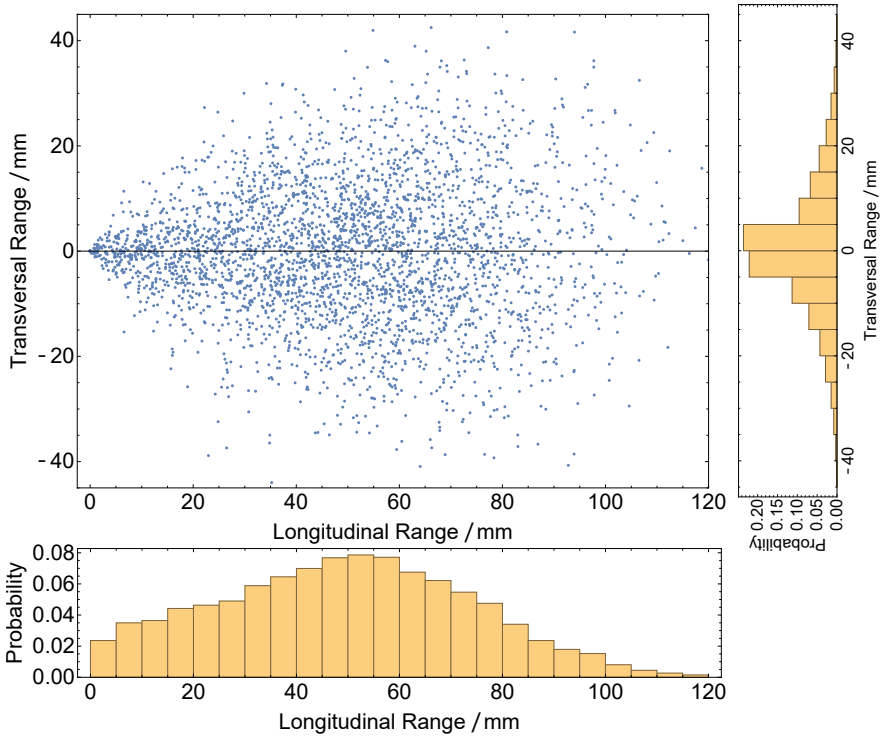

Figure 4.2.: Simulated stopping distribution using uranium ions (blue dots) in 30 mbar argon. The histograms are showing the probabilities for the distance travelled in longitudinal and transversal range. The simulations were performed by [redacted]. Figure taken from [163].

simulation was mandatory in order to estimate the necessary dimensions of the gas cell for efficient stopping of recoil ions in on-line measurement campaigns. Based on the simulations and the beam size of the incoming particles a length of $\approx 10\,\text{cm}$ and a diameter of $\approx 13\,\text{cm}$ of the stopping volume is needed to efficiently stop the uranium-ions. As SRIM simulations overestimate stopping powers in gaseous materials, the active gas-stopping volume of the gas-stopping cell is increased by a factor of $\approx 50\,\%$ with respect to the simulation estimates. This observation is congruent with practical experience when designing gas-stopping cells for heavy and superheavy ions in an energy range in the order of 30 MeV to 50 MeV [126, 168]. The stopping volume in the transversal range was increased to $\approx 16\,\text{cm}$ (diameter cage electrodes) and in the longitudinal range to $\approx 15\,\text{cm}$ (distance between the entrance window foil and the first funnel electrode). This adjustment compensates for the overestimation of the stopping distribution from SRIM, the deviating stopping powers of uranium and nobelium [126], and the deviation of the point-like entrance beam from a realistic beam expansion.

4.1.2.2. Ion trajectories in the gas cell

After stopping and thermalizing the reaction products in the argon buffer gas, the next step is to look into the ion trajectories inside of the gas cell. Short transport times are necessary to avoid decay losses, and a high accumulation efficiency on the filament is desired. Typically,

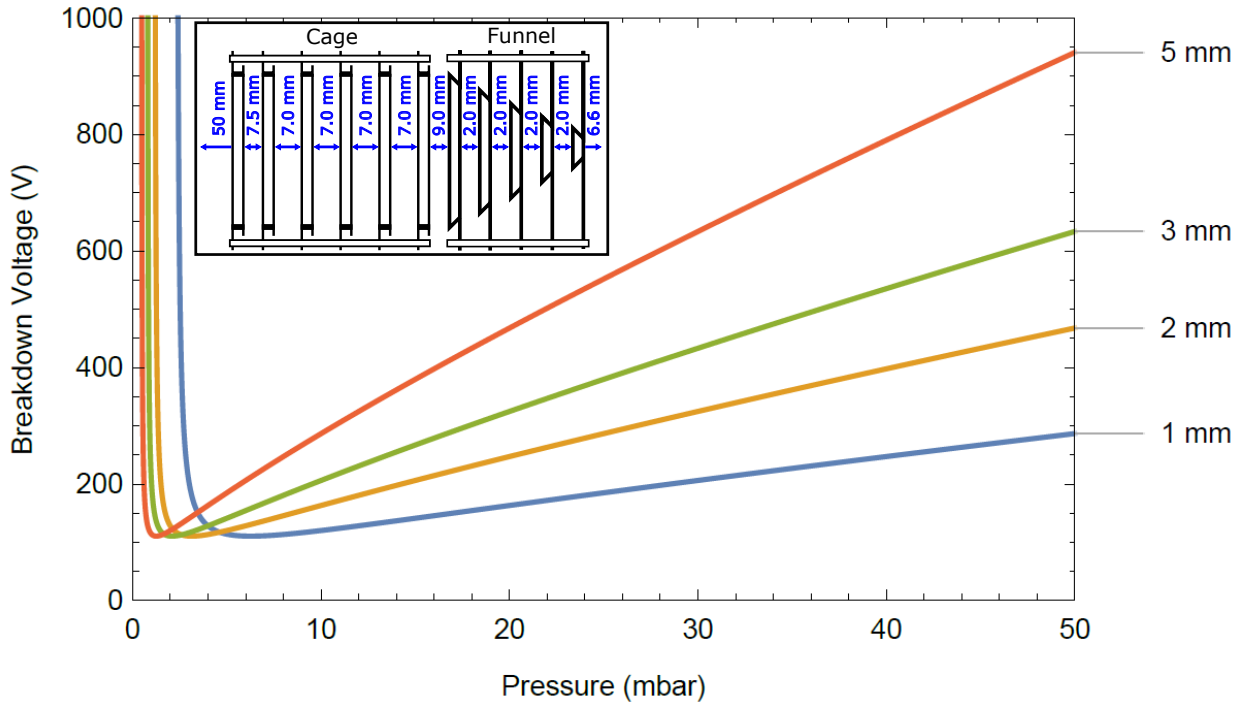

Figure 4.3.: Simulated Paschen curves for argon: Breakdown voltage in dependence of the distances between the electrodes and the cell wall. The inset image shows the distances between the individual electrodes. Adjusted from [163].

modern gas-stopping cells use a combination of a DC gradient together with a so-called RF funnel. An RF funnel is a set of closely packed electrodes, where an RF voltage is applied in order to guide the ions to the filament or the extraction nozzle throat [169]. Due to our limitations in the pumping system and the usage of a de Laval nozzle with a 1 mm throat, the use of argon buffer gas at a pressure of ≥ 30 mbar forbids the application of an RF funnel. The reason for that is the need of RF amplitudes of about 500 V to prevent the reaction products from hitting the electrodes. The funnel electrodes are closely spaced together with a minimum distance between each electrode of 2 mm and as described by Paschen's law (see appendix eqn. A.1), sparking would occur around ≈ 330 V (at 30 mbar) as shown in Fig. 4.3. Therefore, only the use of DC gradients are applicable inside of the gas cell. Considering the minimum spacings between the entrance window, the cage electrodes, and the funnel electrodes at 30 mbar argon pressure, a maximum DC gradient from ≈ 590 V (first cage electrode) to ≈ -200 V (filament) should be achievable, limiting the transport time to approx. ≥ 33 ms. In reality, the effective distances between the electrodes are smaller [163], resulting in smaller applicable DC gradients (see Fig. 4.4) and therefore longer transport times. The motion of the ions is damped inside of the argon buffer gas, whereby their trajectories closely follow the electric field lines. Consequently, inside of the stopping cell a combination of a large diameter drift region (cage), in which the ions are fully thermalized and stopped, and a converging region (funnel), providing a focusing field towards the filament as well as a collimation of the gas flow is used.
Using the SIMION software [170] the trajectories of the ions inside of the gas cell were calculated, using a set of six cage and five funnel electrodes. In addition, a voltage was applied to the flow channel around the filament and to the filament itself. In the simulations, functions adding viscous damping based on ion mobilities in argon were included. The initial start positions of the ions were obtained from the SRIM simulations discussed in chapter 4.1.2.1. Further constraints were given by the maximum voltages applicable to each electrode before discharges may occur, approximated for a argon pressure of 30 mbar using the Paschen law and minimum distances between electrodes and the cell wall. The breakdown voltages are shown in Fig. 4.3 and were investigated in [163]. The inset image in Fig. 4.3 shows the distances between the individual electrodes and towards the mounting walls.
The trajectories were simulated for 50 ions projected on the symmetry plane, which is shown in Fig. 4.4. In order to maximize the ion number entering the flow channel surrounding the filament, the voltages were refined during the simulations. Using the shown voltage set, 76% of the ions with a mean transport time of 95 ms were successfully extracted to the filament. Higher extraction efficiencies could not be reached due to the large field gradient required close to the filament in order to keep up a point-charge like geometry. In a next step, the simulation code was extended to include hard-sphere collisions and diffusion models, so that diffusion-induced transport losses could be estimated. By doing that, the extraction efficiency dropped to about 70%.

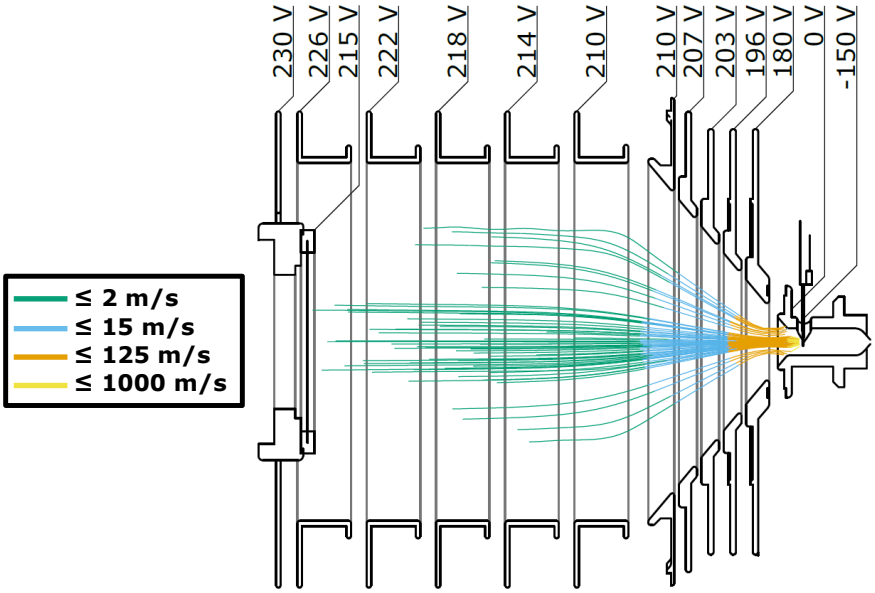

Figure 4.4.: Simulated trajectories of 50 ions for a certain set of voltages after thermalization in the argon buffer gas. The voltage of each electrode is given on the top, while the color code represents the velocity of the ion as indicated in the legend. Over 70% of the stopped ions were extracted to the filament, for more details see text. The simulation was performed by [redacted] [162].

4.1.2.3. Ion trajectories in the jet and detector cell

Since the last section 4.1.2.2 was about the ion trajectories in the gas cell, this chapter will discuss the ion trajectories in the jet and detector cell after laser ionization in the gas-jet. The ions will be first transported by a 90°-bent RFQ (rod radius = 6 mm, free radius = 12 mm), followed by a so-called mini-RFQ (rod radius = 2 mm, free radius = 4 mm) [158]. This mini-RFQ collimates the ion beam and guides it through a differential pumping stage with a hole diameter of 2.6 mm. Afterwards the ions are attracted by the voltage applied to the detector. For the simulations, the jet was approximated as a cone of 5 mm diameter and 60 mm length. Afterwards, the jet widens at a 10° angle for 400 mm. At the start of the jet the ions have a velocity of 550 m/s, which is reduced by collisions with the gas atoms inside or outside of the jet. At 460 mm distance from the nozzle, the ions are fully slowed down to 0 m/s. The simulations were performed using 10 ions, which were randomly distributed inside of the gas-jet volume. There are multiple reasons why the simulated ion number was limited to only 10 ions. Due to the simulation of gas pressure (gas-jet, background pressure p_{bg}) after the nozzle, time steps of 10 µs were used between each ion position. These small time steps resulted in a total simulation time of approx. 13 s for one set of voltage. In order to extract the best transport settings, many simulations were performed with different voltages applied to the RFQ, the mini-RFQ, and the extraction plate. In some of these simulations the voltages of two electrodes were ramped against each other, increasing the number of simulations significantly. Lastly, the ion trajectories in the simulated area were dense as

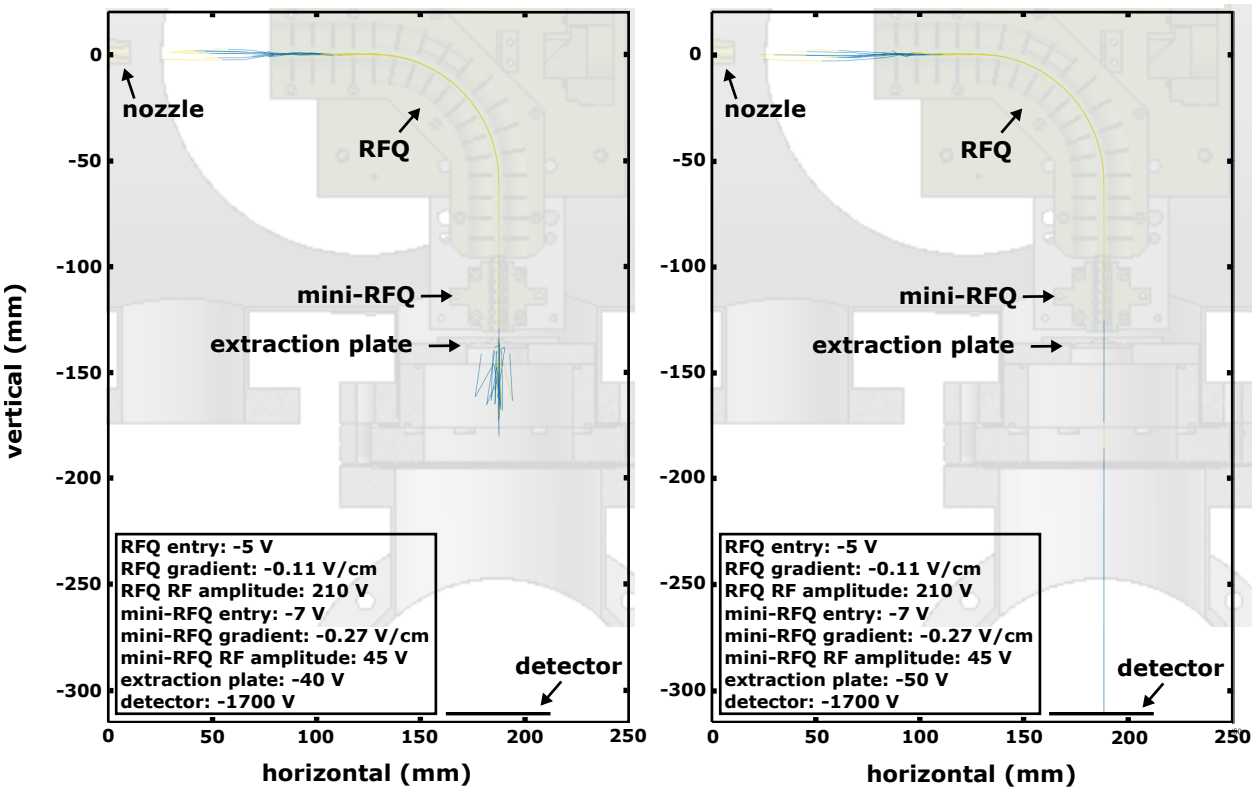

Figure 4.5.: Simulation of the ion trajectories through the RFQ and mini-RFQ towards the detector using 10 ions with randomly distributed start positions. The difference between the left and the right simulation is the voltage applied on the extraction plate. At -40 V (left side) the ions are re-attracted towards the extraction plate and not transported towards the detector. At -50 V (right side) the ions are transported towards the detector with a mean extraction time of around 550 - 600 µs, depending on the starting position. The simulations were performed by [redacted].

the trajectories approach each other in the RFQ due to cooling, which usually resulted in either all or none of the ions reaching the detector. The voltages and RF amplitudes were optimized, so that all ions were extracted with a mean time of around 550 - 600 µs. The detector was modeled as a plate for the simulations. The performed simulations for two different voltage sets (denoted in the box in each simulation) are shown in Fig. 4.5. It is important to note that a minimum voltage of -50 V at the extraction plate is needed in order to transport the ions to the detector. If the voltage is too small, the ions are re-attracted towards the plate as shown in Fig. 4.5 a.

4.1.2.4. Gas flow and heat transfer

Using the COMSOL Multiphysics® software [172] numerous simulations of the argon gas flow inside of the gas cell have been executed. The goal was to optimize the gas cell geometry

for high-resolution in-gas-jet laser spectroscopy experiments on nobelium isotopes. The gas cell geometry was chosen in a way that a laminar gas flow through the small flow channel surrounding the filament until reaching the nozzle throat is ensured. This goes hand in hand with a fast extraction from the filament towards the nozzle throat, therefore minimizing diffusion and decay losses and suppressing the influence of filament heating on the gas-jet temperature. This is crucial, since the gas-jet temperature impacts the spectral resolution achievable via laser spectroscopy.
The gas cell design is shown in Fig. 4.6. The simulations were performed for a gas cell made of stainless-steel (AISI 4340) at a 30 mbar argon stagnation pressure and a temperature of 300 K. A nozzle throat diameter of 0.6 mm was used, because it was planned to install such a nozzle in the future. The simulations used the compressible-flow physical model, which is valid for Mach numbers $M < 0.3$. Because of that, the simulation could only include the region with subsonic flow, e.g., until the converging part of the de Laval nozzle reaches an inner diameter of 1.2 mm [47]. Ref. [47] was used to determine the inflow velocity, determined by volume flow rate conservation. A free tetrahedral mesh was implemented with a normal and an extremely fine element dimensions for the body and exit region of the gas cell in the simulations.

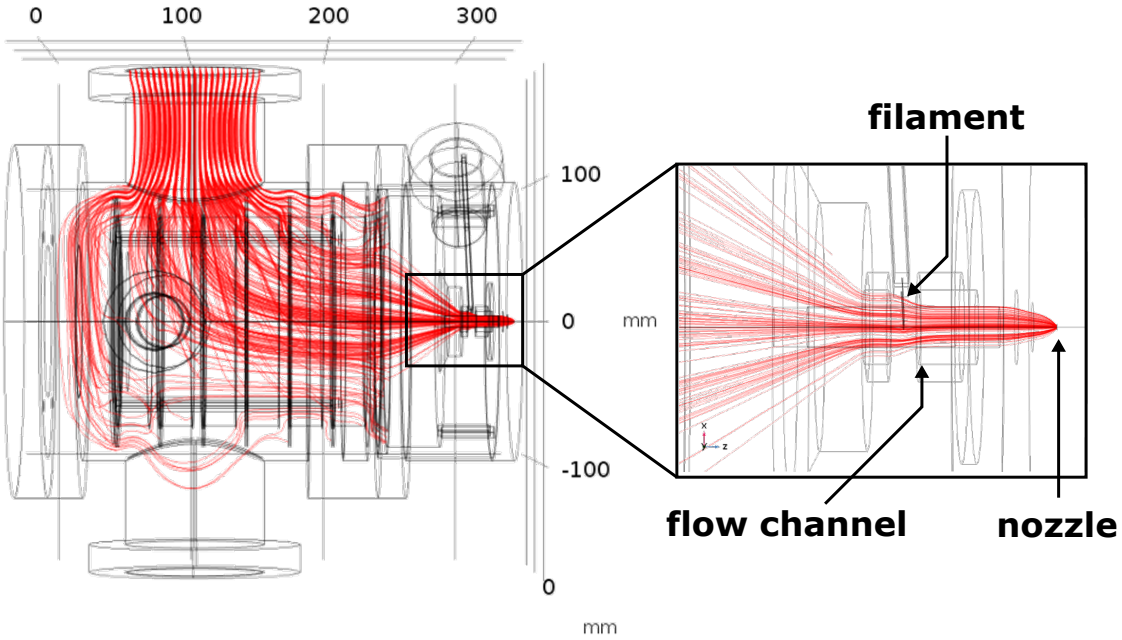

Figure 4.6.: Streamlines of the argon flow in the gas cell, assuming a homogeneous inflow from the top part. The gas flow is disturbed at the cage structure, in the region, where the ions are extracted via electric field gradients. The flow channel features a cut-out in order to enable the filament placement. The inset shows the homogeneous gas flow in the flow channel towards the nozzle, where due to the neutralization step the atoms are transported only by the gas flow. The simulation was performed by [redacted] [162, 171].

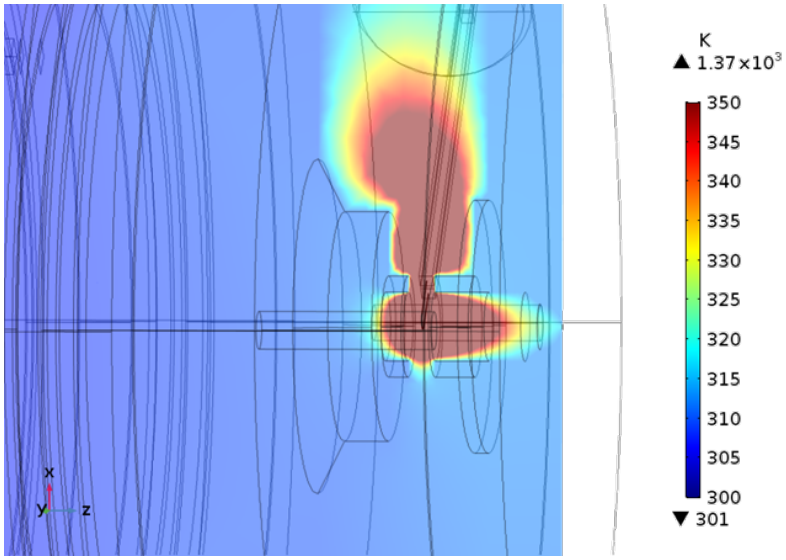

Figure 4.7.: Temperature equilibrium profile around the filament. The argon gas is heated by the filament temperature, reaching around 320 K at the nozzle exit. This increased temperature leads to a broadening of the spectral resolution from 138 MHz to 144 MHz. The simulation was performed by [redacted] [162, 171].

In order to study the influence of the gap for the filament holder and the large central-body volume on the flow behavior in the flow channel of the gas cell, the laminar flow package was used. The simulated streamlines are displayed in Fig. 4.6 and show a homogeneous laminar flow in the extraction region of the gas cell. Using the Particle Tracing for Fluid Flow package, the extraction time of the sample atoms from the filament to the nozzle throat was determined. One thousand nobelium atoms were simulated as spheres with an atomic radius of 200 pm and randomly distributed over the central part of the filament. For a flow channel diameter of 15 mm and using the gas-velocity field as the initial velocity condition, the atoms reach the nozzle throat in 56 - 57 ms undergoing Brownian motion in time steps of 10^{-10} and 10^{-7} s.
Heat-transfer simulations were performed next to simulate the influence of the hot filament on the gas temperature, which would influence the jet temperature and therefore the spectral resolution. For the simulations the chamber walls were surrounded by air at atmospheric pressure except for the wall containing the nozzle exit hole, which was set to 0.3 Torr. The simulations also took the heat transfer to the surroundings into account. The 0.125 mm thick tantalum filament was fixed to a temperature of 1373 K and the walls were initially set to 300 K. The influence of the permanently heated filament on the stagnation temperature and consequently on the gas-jet temperature was studied using the COMSOL Multiphyiscs Nonisothermal Flow package. In this package, the Laminar Flow and the Heat Transfer in Fluids are coupled to simulate the heat transfer by the argon buffer gas. Fig. 4.7 shows the obtained temperature equilibrium in the gas cell. As indicated by the color scheme for the different temperatures, the argon gas reaches around 320 K at the nozzle exit. Assuming

a Mach-8.5-nozzle, this temperature increase corresponds to a temperature increase in the gas-jet of about 0.8 K. Adding that to 12 K, reached without heating the filament [47], the jet temperature increases to 12.8 K, corresponding to an expected broadening of the spectral resolution from 138 Mhz to 144 MHz [47]. This indicates, that the heating effect of a filament of this size is negligible on the spectral resolution. In order to reduce the extraction time of the neutral atoms via gas flow, it was decided to shorten the extraction region of the gas cell by 5 mm and to increase the gas velocity by reducing the flow channel diameter to 12 mm. These changes resulted in an increase of the temperature at the nozzle exit to 325 K, resulting in an expected spectral resolution of 145 MHz, and a reduced extraction time of 28 - 32 ms.

4.2. Layout and construction

An iterative process of simulations and redesigns led to a final design of the setup, which is shown in Fig. 4.8. The gas cell dimensions were derived from the stopping volume simulated by SRIM, assuming a minimum stagnation pressure of 30 mbar in the gas cell. Here, uranium-ions with kinetic energies of around 36 MeV, which corresponds to the recoil energy of ^{254}No in the fusion reaction ^{208}Pb(^{48}Ca, 2n)^{254}No, were stopped in an average distance of ≈ 5 cm. 30 mbar is the lower limit for operation for a nozzle throat diameter of 1 mm. Increasing the stagnation pressure p_0, e.g., by minimizing the nozzle throat diameter, would reduce the required stopping volume to < 5 cm due to an increase of collisions between the ions and the argon gas atoms. The nozzle throat diameter is an important parameter as the nozzle-dependent ratio between the stagnation pressure p_0 in the gas-cell and the background pressure p_{bg} in the jet-cell decides the quality of the formed jet. The current pumping system cannot achieve the optimal ratio at high pressures of approximately > 100 mbar as the background pressure is too high in this case. Thus, a decrease of the nozzle throat would result in a smaller gas flow and therefore in a lower background pressure.
After the entrance window, the six cage electrodes are placed. This cage structure has a length of 164.5 mm and an inner diameter of 160 mm, placed inside of a CF250 vacuum chamber. An electrostatic potential gradient is applied along the cage. The ions are then guided towards the flow channel and filament by a funnel structure of total length 63.2 mm, consisting of five electrodes with gradually decreasing diameters. The flow channel has an inner diameter of 12 mm and a total length of 34.6 mm. The filament holder was designed so that the filament tip reaches inside of the flow channel and ends on the central axis. The following nozzle was designed in collaboration with KU Leuven. Here, detailed studies on the nozzle shape, length and the characterization of the resulting gas-jets were performed [50, 150]. The created gas-jet is seeded by the atoms of interest, which are excited and ionized by laser radiation. The ions are transported towards the detector by a 90°-bent RFQ structure in order to separate atoms and ions, and in addition enabling laser radiation access anticollinear to the gas-jet. The RFQ is followed by a mini-RFQ structure to simplify the transition to the jet chamber through the differential pumping stage. The RFQ is placed ≈ 80 mm behind the nozzle throat.
In order to study rare isotopes with low production rates, the chamber parts must fulfill a

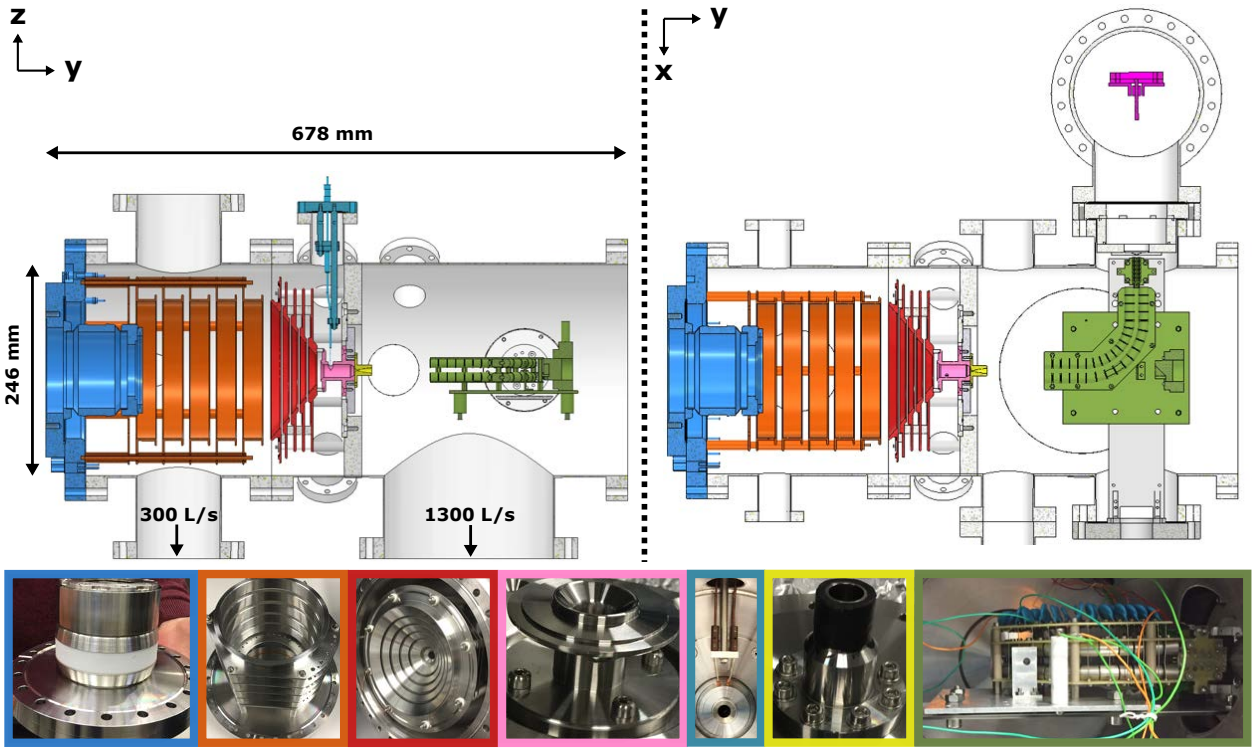

Figure 4.8.: Technical drawings of the new gas-jet setup. Left: Cut view in the $y-z$ plane. The left volume, representing the gas cell, contains from left to right the entrance window (blue), the cage (orange), the funnel (red), the flow channel (pink) and the filament (cyan). The right volume, representing the jet cell, contains the nozzle (yellow), view ports for the lasers and a 90°-bent RFQ in combination with a mini-RFQ (green) for ion extraction. Right: Cut view in the $x-y$ plane. Here, the mini-RFQ as well as the channel electron multiplier (magenta) are visible. For details see text. The bottom shows photographs of the most crucial chamber parts, linked to the cut views through colored frames. See ref. [162].

few conditions. One of these is the use of 316L stainless steel for the chamber as well as the electrodes to ensure low outgassing, necessary to reach ultra-high vacuum conditions. Different CF100, CF63, and CF40 flanges are integrated into the gas cell and jet cell in order to enable the mounting of, e.g., the filament, laser entrance windows, electric connection feedthroughs, and vacuum diagnostics. A circuit diagram for the pumping system, the vacuum diagnostics, as well as the mandatory valves is shown in Fig. 4.9. The gas cell volume was evacuated by a 300 L/s (for N_2) turbo molecular pump Leybold MAG W300 P (backing pump: Edwards nXDS10i, shared with detector cell), the jet-cell using a 1300 L/s (for N_2) turbo molecular pump Edwards STP-H1303CV3 (backing pump: Edwards XDS35i), which is built for high gas throughput, and the detector cell using a Pfeiffer Vacuum TMU 1600M. A butterfly valve was placed in front of the jet cell turbopump, allowing the regulation of the background pressure in the jet cell p_{bg} and used to match the ratio between p_0 and p_{bg} for ideal jet formation [50]. Without baking the system pressures of $3 \cdot 10^{-8}$ mbar (gas

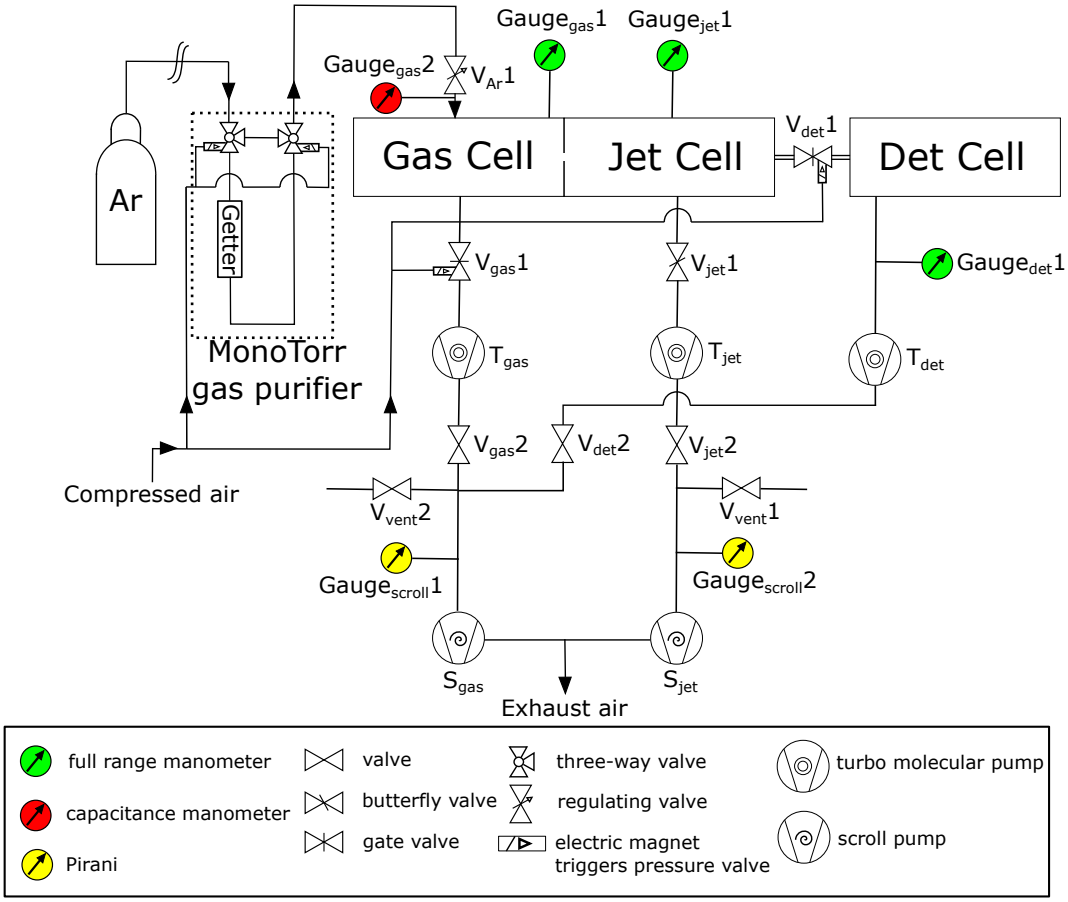

Figure 4.9.: The circuit diagram shows the pumping system, the vacuum diagnostics, the purification of the argon as well as valves in use for the new gas-jet setup.

cell), $2 \cdot 10^{-7}$ mbar (jet cell) and $5 \cdot 10^{-8}$ mbar (detector cell) were reached. In order to avoid impurities in the gas cell, hampering the efficiency of the setup due to unwanted neutralization and molecule formation from collisions, high purity argon buffer gas (99.9999% purity) is additionally purified by a heated Getter (SAES Pure Gases, MonoTorr PS4-MT3) to the ppb level before gas cell injection. It was possible to permanently operate the system at 30 mbar.

4.3. Model system - Ytterbium

The previous section was focused on the technical point of view of the gas-jet apparatus. Starting from a conceptual idea, simulations were performed to design a first version of the setup. The following sections will now focus on the measurements performed during this work. The goal was to characterize and optimize the setup, so that future on-line measurement campaigns are not limited through, e.g., efficiency, extraction and transport times, and spectral resolution. Therefore, multiple tests and measurements were performed in order to

obtain these properties.
The measurements were performed using ytterbium (Yb, $Z = 70$) as a model system. Ytterbium is the lighter chemical homolog of nobelium (No, $Z = 102$), which is one of the major elements to be investigated with the new gas-jet setup (see Fig. 4.10). Therefore similar chemical and physical behavior is expected. In addition, both elements have accessible ground-state transitions exciting the $^1S_0$ level to the $^1P_1$ level (Yb: 398.9 nm, No: 333.76 nm), sharing a similar lifetime of the excited state (Yb: ≈ 5 ns, No: ≈ 2 ns) as well as a similar transition strength (Yb: $A_{ki} = 1.9 \cdot 10^8\,\mathrm{s}^{-1}$, No: $A_{ki} \geq 6.3 \cdot 10^7\,\mathrm{s}^{-1}$) [77, 173, 174]. This enables to investigate efficiency losses as well as saturation of the transition due to the achievable laser powers. With this information, the laser power needed to saturate the transition in nobelium can be estimated.
If not stated differently in the respective section, the measurements were performed using a continuously heated ^{nat}Yb filament instead of the wired filament inside of the flow channel. This ^{nat}Yb filament consisted of a tantalum strip of a width of around 3-4 mm, a length of 15-30 mm and a thickness of less than 100 µm. This tantalum strip was folded in order to form a small pocket, in which a metallic ytterbium foil of natural abundances, with a thickness of 25 µm and dimensions of around 3 mm x 3 mm was inserted. By resistively heating this ^{nat}Yb filament, neutral ytterbium was evaporated inside of the flow channel and transported towards the de Laval nozzle via gas flow, enabling the possibility to perform RIS inside of the gas-jet.

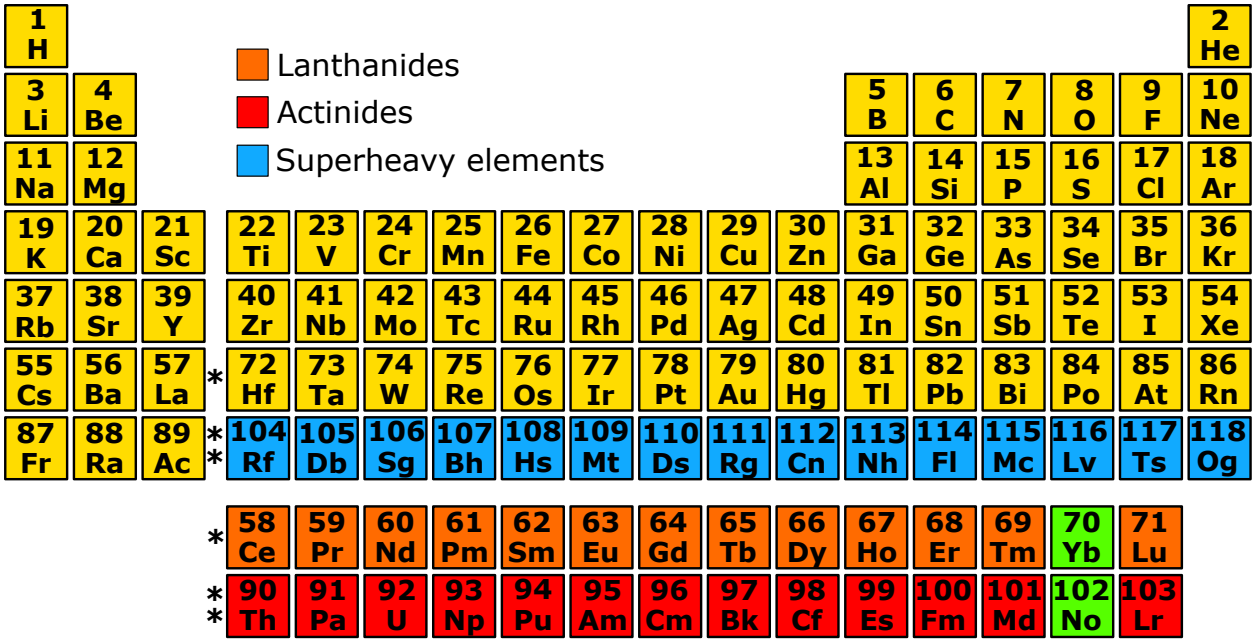

Figure 4.10.: Overview over the periodic table, highlighting ytterbium and nobelium (green).

4.4. 100 Hz Laser system @ HIM

This chapter will cover the 100 Hz laser system which was used to perform laser resonance ionization spectroscopy before and during the beam time campaign. Pulsed, tunable, and narrowband laser systems are essential in order to improve the achievable spectral resolution and saturate the transitions of interest. After the beam time campaign a 10 kHz repetition rate laser system was installed, which will be covered in chapter 4.8. Both laser systems share the use of continuous wave (cw) seed lasers. Here, either a diode laser (Toptica DL Pro) with a wavelength range of 770 - 810 nm and a maximum output power of 100 mW or a dye laser (Sirah Matisse 2 DR) pumped by a frequency doubled 532 nm Nd:YAG (Spectra Physics Millenia Pro) with a wavelength range of 550 - 760 nm and a maximum output power of 3 W are used. The wavelength is monitored by using a wavelength meter (High Finesse WS7-30) with an absolute accuracy of 30 MHz (3 σ). For its calibration, a frequency stabilized He:Ne laser (SIOS SL03, 632.9909968 nm) is used.
For the 100 Hz repetition rate laser system, the seed laser is coupled into a 4-stage dye amplifier (Sirah PulsAmp4x). This dye amplifier is pumped by a 100 Hz Nd:YAG pulse laser (Edgewave Innolas Spitlight DPSS) using the second harmonic generation (SHG) with pulse energies of 50 - 120 mJ. The incoming seed light is amplified to single pulses with energies in the energy range of mJ and afterwards frequency doubled using a frequency conversion stage (Sirah SFM-1064). The crucial advantage of this laser system is the linewidth of the generated pulses. The 50 kHz narrow linewidth of the cw seed laser is maintained in the amplification process and the final linewidth, in the range of 100 MHz, is determined through the Fourier limitation due to the short pulse length of 8 ns.
Depending on the wavelength of interest, different combinations of dyes and solvents have to be used for the 4-stage dye amplifier, e.g., Styryl 11 in ethanol for the first excitation step in ytterbium of 398.9 nm. The frequency tripling (third harmonic generation (THG), 355 nm) of the 100 Hz Nd:YAG pulse laser can be used simultaneously to excite a dye laser (Lambda Physik FL2000) with Exalite 389 dye solved in p-dioxane, in order to produce laser light with the wavelength of 385.7 nm, used for excitation to an autoionizing step in ytterbium. Alternatively, the THG of the pulse laser can be directly used for non-resonant ionization. A schematic overview over the laser system is shown in Fig. 4.11.

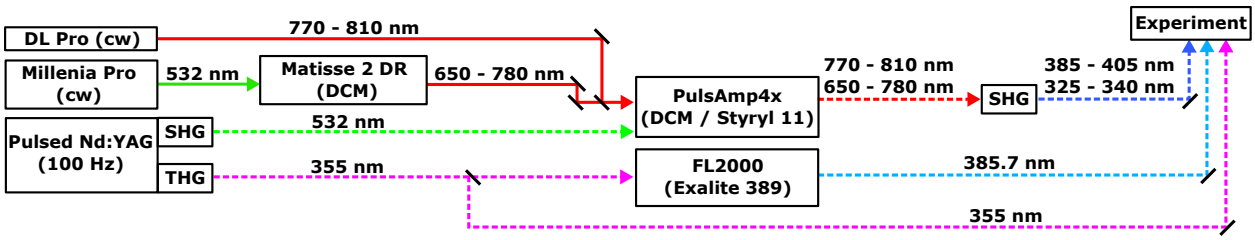

Figure 4.11.: Schematic overview over the 100 Hz repetition rate laser system. Solid lines indicate cw light and dashed lines pulsed light. For more details see text.

4.5. Pre-beam time measurements 2019

Before moving the gas-jet setup for the on-line measurement campaign to GSI, Darmstadt, the setup was assembled and tested at the laser laboratory at the Helmholtz Institute Mainz (HIM). At that time, only a laser system with a repetition rate of 100 Hz, which was introduced in the last section, was available. The setup which was investigated is shown in Fig. 4.8 together with pictures of the parts. There, a RFQ in combination with a mini-RFQ, as well as the Mach-5-nozzle from KU Leuven were installed. The excitation scheme applied to ytterbium is shown in Fig. 4.12. For excitation, the $4f^{14}6s^2\ {}^1S_0 \rightarrow 4f^{14}6s6p\ {}^1P_1$ transition at 25 068.22 cm^{-1} and for the ionization process, an autoionizing level at 50 991.8 cm^{-1} (FWHM 1.23 cm^{-1}, see appendix Fig. A.2) was chosen. ^{Nat}Yb consists of seven different isotopes ^{168,170,171,172,173,174,176}Yb. Due to the isotope shifts in addition with the hyperfine structures for some of these isotopes, a superposition of the individual transitions is expected [176, 177, 178].
In order to characterize the achievable spectral resolution with this setup, the excitation laser was applied anticollinear and the ionizing laser perpendicular (cross-geometry) to the gas-jet. Pulse energies of 75 - 85 nJ/pulse and 285 µJ/pulse were used for the excitation step and the ionization step, respectively. The linewidth of the excitation step was ≈ 100 MHz, limited through the short pulse length of 8 ns. Using the voltage set shown in Table 4.1, the count rate in dependence of the wavelength of the first excitation step was recorded. The measurement was performed at a stagnation pressure of 38.5 mbar and a background pressure of around $1{\cdot}10^{-2}$ mbar. Comparing the timing between laser pulses and detection, a mean flight time of 1.5 - 3.0 ms from ionization in the jet until reaching the detector was extracted.
Fig. 4.13 shows the recorded, background-corrected spectrum of ^{nat}Yb. The uncorrected

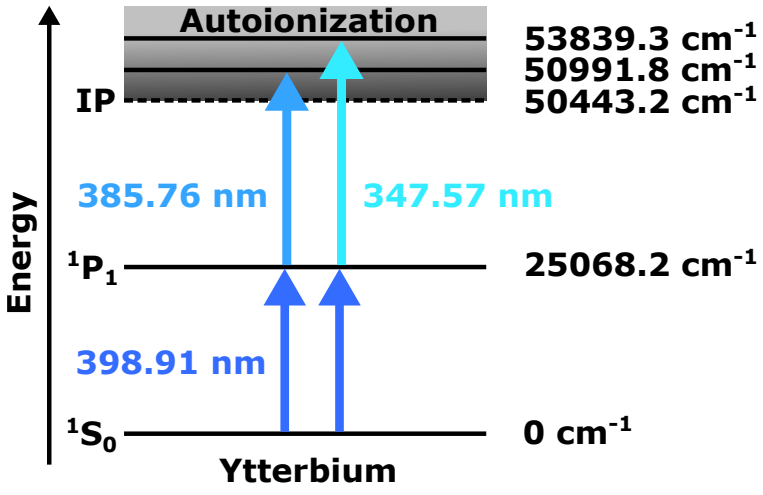

Figure 4.12.: Overview over the used laser ionization schemes with experimental level energies. The value for the IP is taken from [175]. The autoionizing step at 53 839.3 cm^{-1} was only used in section 4.10. All other measurements were performed using the autoionizing step at 50 991.8 cm^{-1}.

Table 4.1.: Optimized transport parameters for the detection of the first ytterbium signal.

Electrode	Setting
^{nat}Yb filament	-2 V
RFQ entry	-9 V
RFQ gradient	-0.027 $\frac{V}{cm}$
RFQ RF amplitude	500 V
RFQ RF	1.04 MHz
mini-RFQ entry	-9.5 V
mini-RFQ gradient	-0.137 $\frac{V}{cm}$
mini-RFQ RF amplitude	100 V
mini-RFQ RF	1.04 MHz
extraction plate	-38 V
detector	-1600 V

spectrum can be found in the appendix (Fig. A.1). In order to estimate the spectral resolution of the recorded spectrum, the most abundant isotopes ^{171,172,173,174,176}Yb were plotted underneath the measured signal (orange solid lines), taking isotope shifts as well as hyperfine structures into account [176, 177, 178]. Each of these isotopes were individually fit using a Gaussian lineshape with constant FWHM (dashed blue lines), and afterwards summed

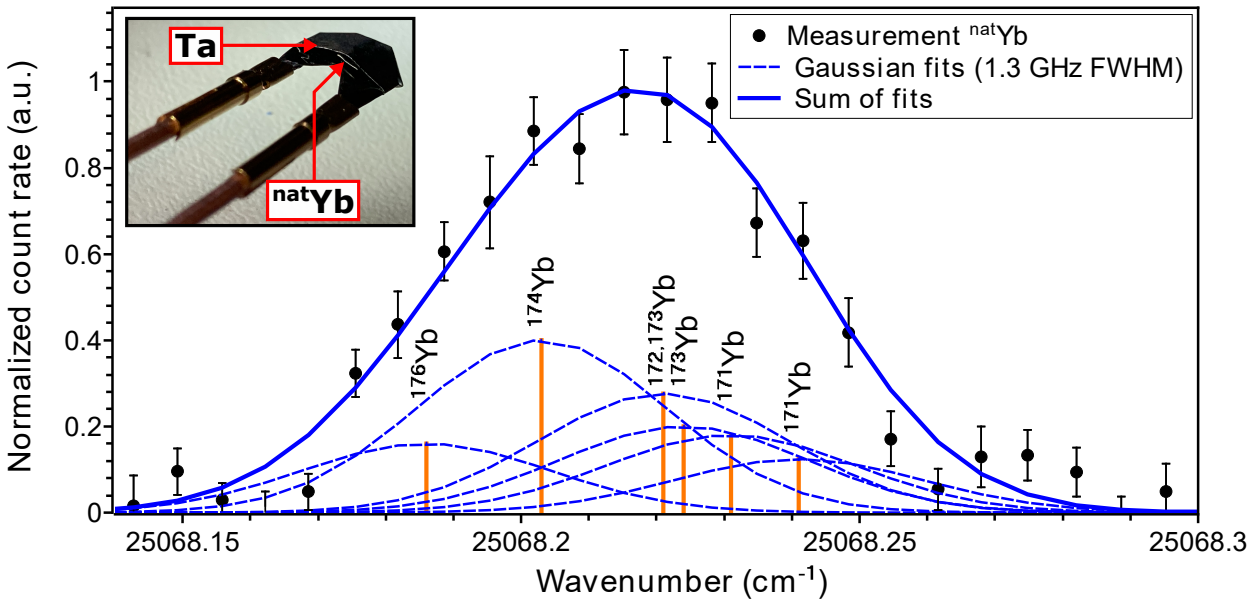

Figure 4.13.: Background-corrected ^{nat}Yb spectrum recorded with the high-stagnation-pressure nozzle (Mach-5-nozzle). For further details see text and appendix. The inset shows the ^{nat}Yb filament installed in front of the nozzle.

up proportionately to their relative strength, which is indicated by the different heights of the isotopes deduced from the natural abundances in addition to the intensities reported from fluorescence measurements [176]. The position and relative strength of each isotope (orange solid lines) and the FWHM for all individually fitted isotopes were fixed for each fit, whereas the FWHM was changed after each fit until it matched the measurement results. A FWHM = 1.3(0.3) GHz for each isotope (dashed blue line) was necessary to describe the experimental data with the sum of the individual fits (solid blue line). RIS measurements of atoms in a gas-jet should reach spectral resolutions of a few hundred MHz, indicating issues with the creation of a gas-jet. After the on-line campaign, tests at KU Leuven as well as new simulation studies indicated that no gas-jet was formed under the experimental pressure conditions. The Mach-5-nozzle, which was used to measure this spectrum, was designed to operate at around 350 mbar stagnation pressure. It was thought that scaling down the stagnation and background pressure would be enough to operate the system at 30 mbar. During the new tests it was determined that the gas-jet does not form below a stagnation pressure of approximately 100 mbar for the high-stagnation-pressure nozzles due to the absence of a boundary layer [171, 179], which explains the observed FWHM = 1.3(0.3) GHz.

4.6. Beam time 2019

For the on-line experiments a $^{48}Ca^{10+}$ ion beam from the UNILAC [131] was accelerated to beam energies of about 218.4 MeV (4.55 MeV/u). The ion source of the UNILAC can be operated in a pulse-to-pulse switching mode at 50 Hz with a pulse-length of 5 ms [186]. Out of these 50 pulses per second, 5 pulses were delivered to our experiment. An ion beam current of $\approx 1.25 \cdot 10^{13}$ particles/s was measured at a beam stop placed inside of SHIP (see Fig. 3.3). The $^{48}Ca^{10+}$ ion beam was guided onto the rotating target wheel with 8 target segments. Each segment consisted of a thin carbon foil (48 µg/cm^2) sputtered with ^{112}SnS (40 µg/cm^2) and ^{208}PbS (455 µg/cm^2). Thus, each foil contained about 31 µg/cm^2 of ^{112}Sn and 395 µg/cm^2 of ^{208}Pb. The reason for using a target consisting of these two isotopes is the possibility to switch on-the-fly between the production of ytterbium and nobelium isotopes (see section 3.1) by changing the transmission settings of SHIP.

Table 4.2.: Decay properties of the ytterbium isotopes and the α-decaying daughter-nuclei.

Isotope	$T_{1/2}$	α-decay probability (%)	Q_α (keV)	Daughter-nuclei	Ref.
^{150}Dy	7.17 min	36.0	4351.3	α: ^{146}Gd / EC: ^{150}Tb	[180]
^{151}Ho	35.2 s	22.0	4695.0	α: ^{147}Tb / EC: ^{151}Dy	[181]
^{152}Er	10.3 s	90.0	4934.4	α: ^{148}Dy / EC: ^{152}Ho	[182]
^{154}Tm	8.1 s	54.0	5094	α: ^{150}Ho / EC: ^{154}Er	[183]
^{154}Yb	0.409 s	92.6	5474.2	α: ^{150}Er / EC: ^{154}Tm	[183]
^{155}Yb	1.793 s	89.0	5337.6	α: ^{151}Er / EC: ^{155}Tm	[184]
^{156}Yb	26.1 s	10.0	4811	α: ^{152}Er / EC: ^{156}Tm	[185]

^{155}Yb was produced with a production rate of ≈ 26 ions/s in the fusion-evaporation reaction ^{112}Sn(^{48}Ca, 5n)^{155}Yb with a cross-section of ≈ 7 mb (see Fig. 3.2). Furthermore, the isotope ^{154}Yb was produced in the ^{112}Sn(^{48}Ca, 6n)^{154}Yb reaction with a rate of ≈ 7 % of the ^{155}Yb production rate [187]. ^{156}Yb was produced with an even lower rate than ^{154}Yb although no specific production yields were studied. The decay properties of the ytterbium isotopes and the α-decaying daughter-nuclei [188] are summarized in Table 4.2. The fusion-evaporation

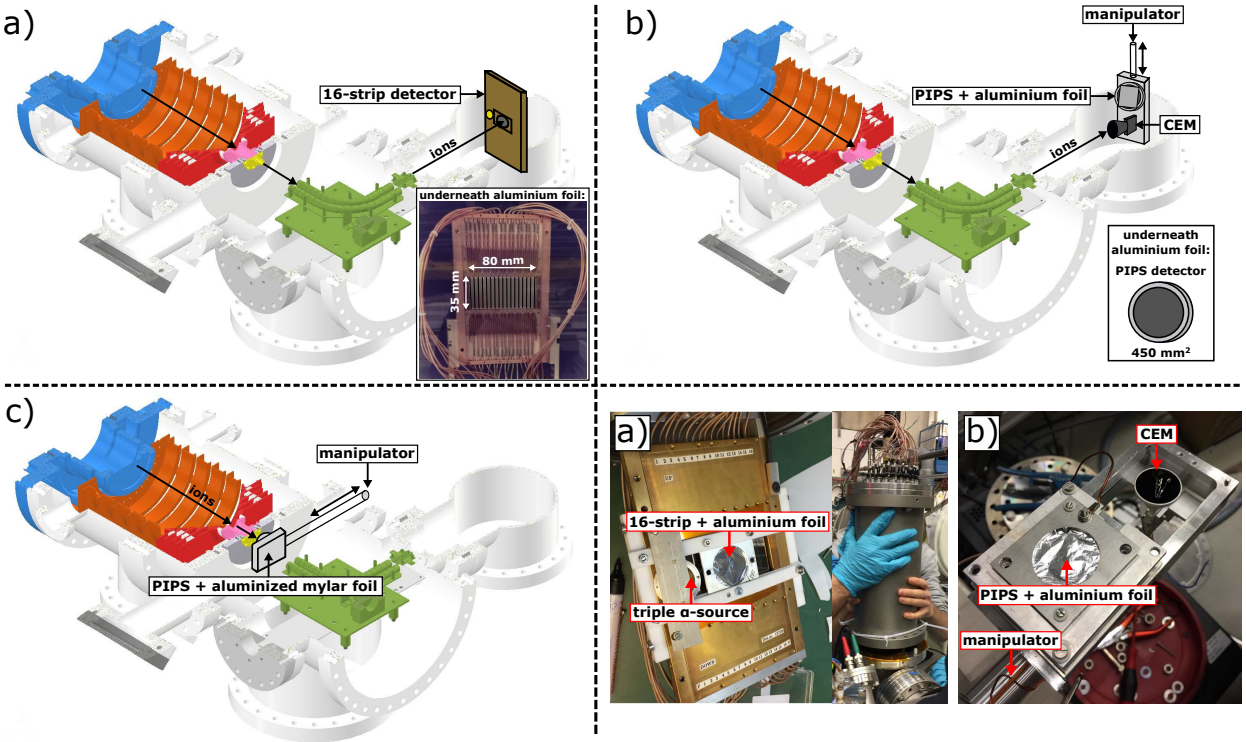

Figure 4.14.: Overview over the different detector setups used during beam time. a) Position-sensitive 16-strip silicon detector with an active area of 80 x 35 mm^2, which was covered by an aluminium foil (200 µg/cm^2) to apply a voltage of -1700 V and guide the reaction products onto the foil. A triple-α source was installed next to the 16-strip area for the possibility of an internal calibration. Pictures of the 16-strip detector are shown in the bottom right box. b) Possibility to choose between a channel electron multiplier (CEM) and a passivated implanted planar silicon (PIPS, active area: 450 mm^2) detector by changing the detector position using a manipulator. An aluminium foil (200 µg/cm^2) was placed in front of the PIPS detector to apply a voltage of -1700 V and guide the reaction products onto the foil. Pictures of the CEM and PIPS detector are shown in the bottom right box. c) PIPS detector mounted between the nozzle and the RFQ structure on a manipulator. A voltage of -300 V was applied to the aluminized mylar foil (3.5 µm thickness). This detector setup was used to measure the α-spectrum in Fig. 4.20.

residues were separated from the $^{48}Ca^{10+}$ primary beam by SHIP (see section 3.2), implanted into the argon-filled stopping cell ($p_0 \approx 30\,\text{mbar}$, $p_{bg} \approx 1 \cdot 10^{-2}\,\text{mbar}$), and then guided towards a 125 µm-thick tantalum wired filament as explained in chapter 4.1.1.
Different detector setups were used to detect the reaction products after ionization using the RIS technique as shown in Fig. 4.14. A position-sensitive 16-strip silicon detector with an active area of $80\,\text{x}\,35\,\text{mm}^2$ was used (see Fig. 4.14 a) to detect the α-particles from the reaction products guided onto an aluminium foil ($200\,\mu\text{g/cm}^2$) biased at -1700 V. Later, the 16-strip silicon detector was replaced by a PIPS (radioactive decay detection, aluminium foil ($200\,\mu\text{g/cm}^2$) biased at -1700 V) and CEM (ion detection) detector, both mounted onto a manipulator structure (see Fig. 4.14 b) enabling to switch between these two detectors without venting the setup. No beam-related signal was observed using the 16-strip silicon detector or the PIPS detector even after attempting the following approaches:

- The voltages of the funnel and cage electrodes were checked to be in accordance with the simulated potentials for ion extraction from the gas cell.
- Various thickness of the aluminium-coated mylar degrader foil of 1.0 µm, 1.5 µm, 2.5 µm, 4.0 µm, 5.0 µm, and 6.5 µm at the crossover between SHIP and gas-jet setup were tested to vary the stopping range of the reaction products in the gas cell volume.
- Due to problems with contamination as shown in Fig. 4.15, e.g. ^{nat}Yb, the filament ($\gg 1350\,°\text{C}$) and the setup ($\approx 125\,°\text{C}$) were heated for multiple hours while pumping to reduce the amount of contaminants in the flow channel and the chamber.
- Pulse heating of the tantalum filament using a 1 s cycle consisting of 500 ms ion collection, 300 ms filament on ground, and 200 ms pulse heating.

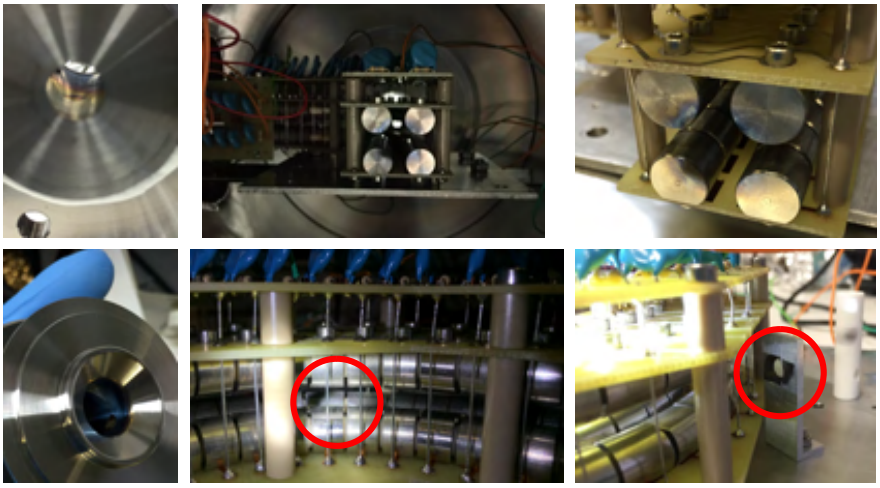

Figure 4.15.: Visible contaminations of the flow channel (left) and the RFQ rods (middle and right) after the beam time campaign. The jet cell CF40 window for the anticollinear laser beams was coated as well, but no picture taken.

The CEM detector was used to characterize the transport behavior and time through the setup. Fig. 4.16 shows the extraction time of gas cell-related ions relative to the UNILAC beam (operated at 1 Hz) entering the gas cell at $t = 0$ s. Here, the transported ions were either beam-related ytterbium ions (^{154,155,156}Yb) or originated from the ytterbium and lutetium contamination from off-line measurements. The transport time was measured in dependence of the potentials applied on the cage and funnel structure. For this measurement, the filament was on ground potential and not heated. The RFQ gradient was set to -0.065 V/cm and the mini-RFQ gradient to -0.137 V/cm. Comparing the different potential settings, it is visible that in all three cases a first, narrow peak in count rate was observed at $\approx$ 15 ms, whereas a higher electric field gradient across the cage led to losses in count rate of about a factor of 3 (blue triangle). A second, broad peak in count rate with a longer extraction time was also observed, which seemed to have a shorter extraction time for the higher electric field gradient across the cage (blue triangle) compared to the other two potential settings (black circle and red square). The origin of the second peak is unknown, whereas a possible explanation could be an unknown molecular species. In the case of an unknown molecular

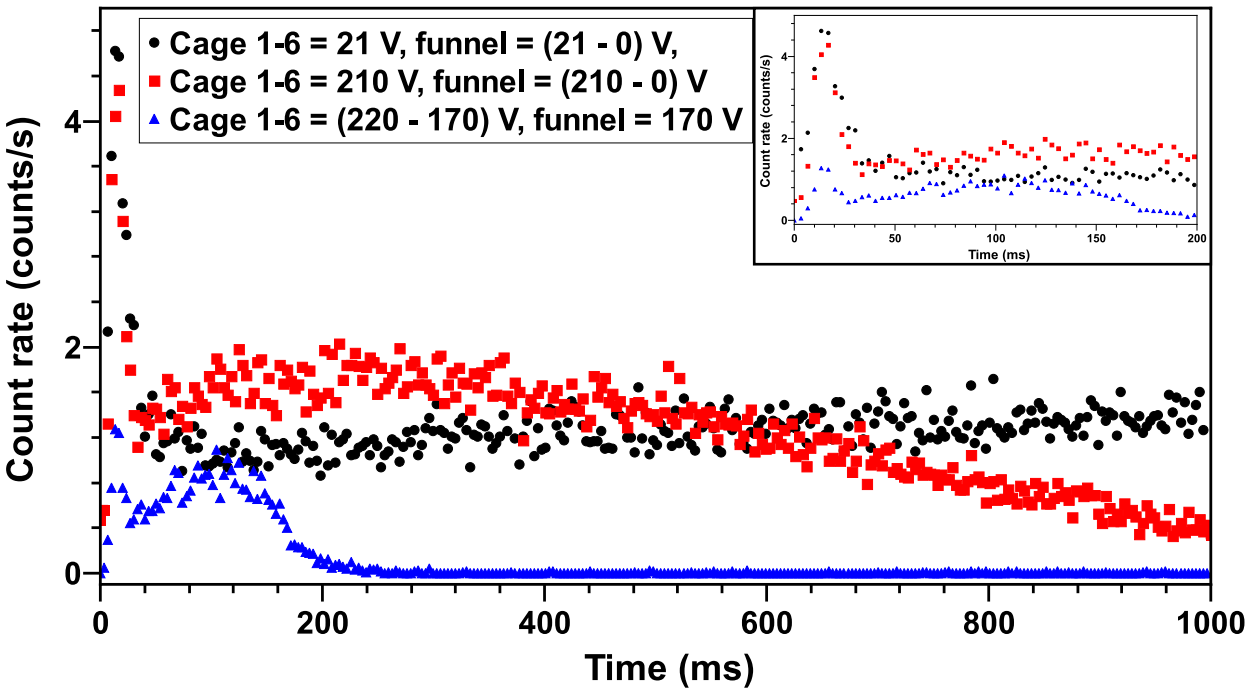

Figure 4.16.: Measured transport time of gas cell (30 mbar argon) related ions relative to the UNILAC beam (operated at 1 Hz) entering the gas cell at $t = 0$ s. Here, the ions were either beam-related ytterbium ions (^{154,155,156}Yb) or originated from the ytterbium and lutetium contamination from off-line measurements. The ions were transported towards the CEM detector using different DC cage and DC funnel voltages. No voltage or current was applied to the filament, thus the reaction products were not neutralized. The uncertainties of approximately $\pm(15 - 30)$ % are not shown for better visibility. The inset shows a zoom-in.

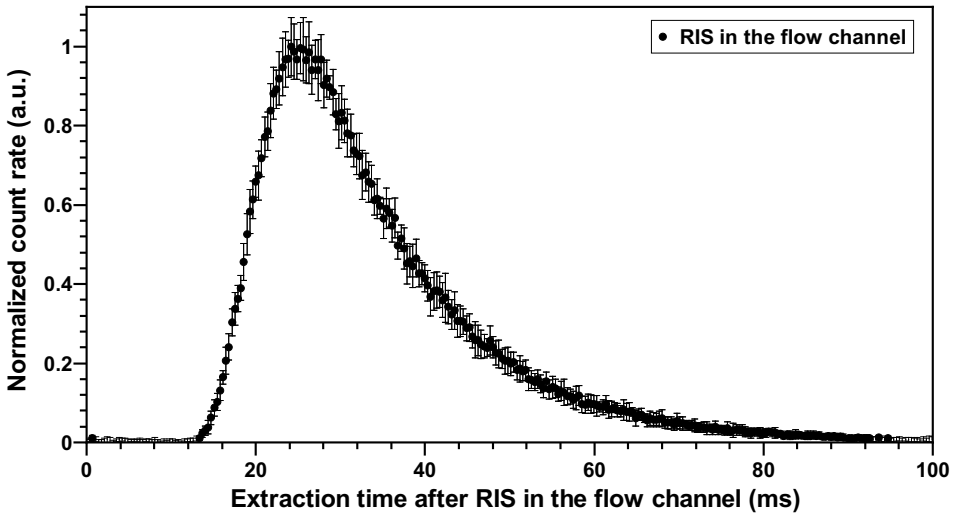

Figure 4.17.: The UNILAC-beam was blocked and thus did not enter the gas-cell, which was operated at 30 mbar. A ^{nat}Yb filament was installed in the flow channel and heated. The atoms were resonantly ionized inside the flow channel and the extraction time to the CEM measured. The time was measured relative to the laser pulses, with the laser system being operated at a 10 Hz repetition rate.

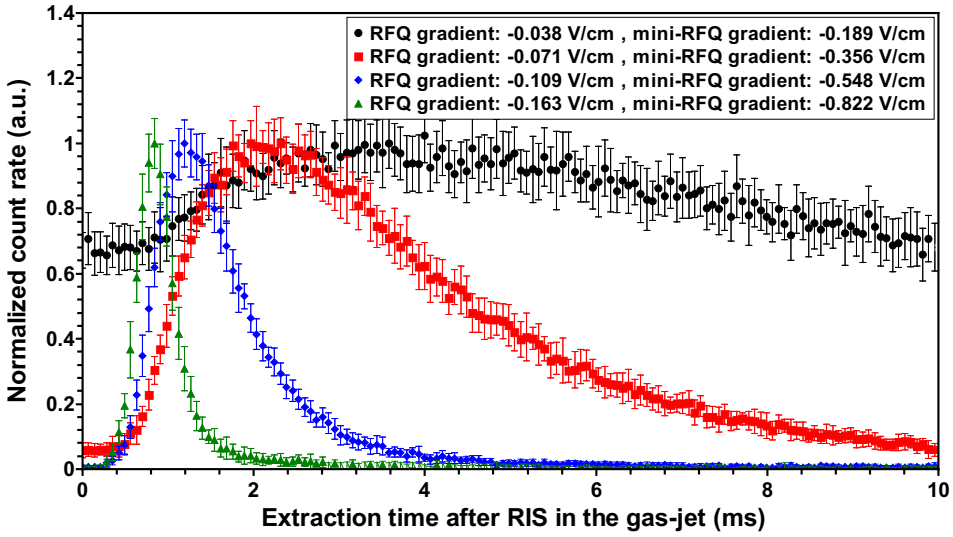

Figure 4.18.: The UNILAC-beam was blocked and thus did not enter the gas-cell, which was operated at 30 mbar. A ^{nat}Yb filament was installed in the flow channel and heated. The atoms were resonantly ionized in the gas-jet and the extraction time to the CEM measured for different RFQ and mini-RFQ gradients, as indicated by the different colors. The time was measured relative to the laser pulses (FES: 55 µJ/pulse, SES: 140 µJ/pulse), with the laser system being operated at a 100 Hz repetition rate.

species with a mean extraction time of ≈ 110 ms (blue triangle) the mass can be calculated as $m \approx 8300$ u under the assumption of the same kinetic energy for the molecular species and for the transported species (assuming ^{155}Yb) with a mean extraction time of ≈ 15 ms. As the calculated mass seems unrealistic, it is unclear what is the origin of the broad peak at longer extraction times.
The extraction time of laser ions from the flow channel was investigated using a ^{nat}Yb filament in the flow channel to confirm the simulation results. For this measurement the RFQ and the mini-RFQ gradient were set to -0.0375 V/cm and -0.189 V/cm, respectively, and the laser repetition rate was reduced to 10 Hz. RIS was performed inside of the flow channel behind the filament and in front of the nozzle. Fig. 4.17 shows the extracted time structure. It can be seen that the ions were detected between ≈ 15 ms and ≈ 80 ms, with an average extraction time of ≈ 25 ms. These extraction times are not fully in agreement with the simulated gas flow extraction time, where all ions were extracted in a time of 28 - 32 ms. Additionally, the extraction time in the RFQ and mini-RFQ for different voltage gradients was investigated using ^{nat}Yb and is shown in Fig. 4.18. Here, the atoms were resonantly ionized in the gas-jet with a laser repetition rate of 100 Hz. As expected, higher gradients led to a faster mean extraction time in addition to a more narrow time distribution around the mean time.
The ion yield in ^{nat}Yb was compared using an autoionizing state at 50 991.8 cm^{-1} and different Rydberg states as shown in Fig. 4.19, whereas in the latter the ion yield was a factor of ≥ 4 lower. No saturation of the laser intensity was observed for the autoionizing state up to

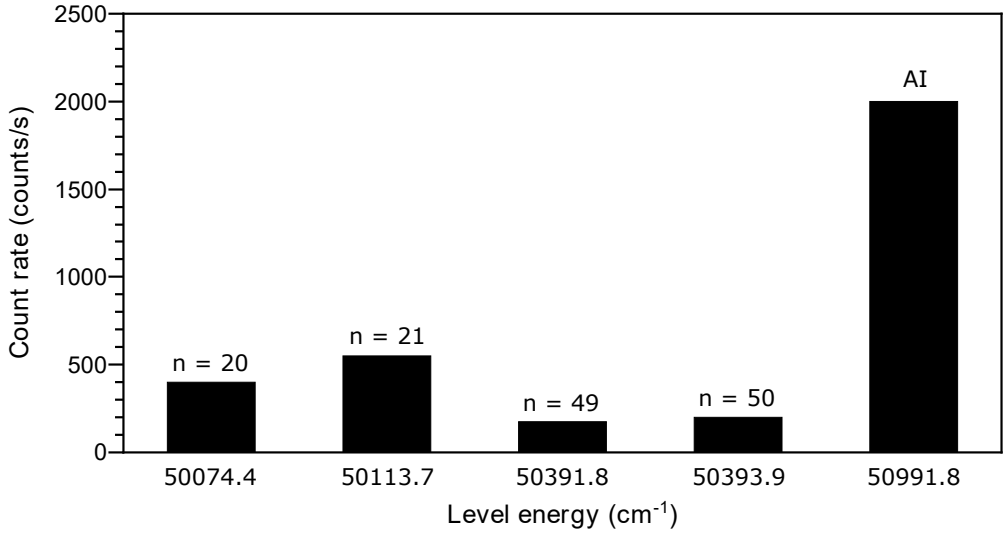

Figure 4.19.: Comparison of the ion yield for ^{nat}Yb when using an autoionizing level or different Rydberg states as the ionization step (SES). The laser system was operated at a 100 Hz repetition rate. The FES was operated at 25 068.2 cm^{-1} (90 µJ/pulse) and the SES was scanned around 25 923.4 cm^{-1} (150 µJ/pulse). The Rdyberg states are indicated by the respective principal quantum number n.

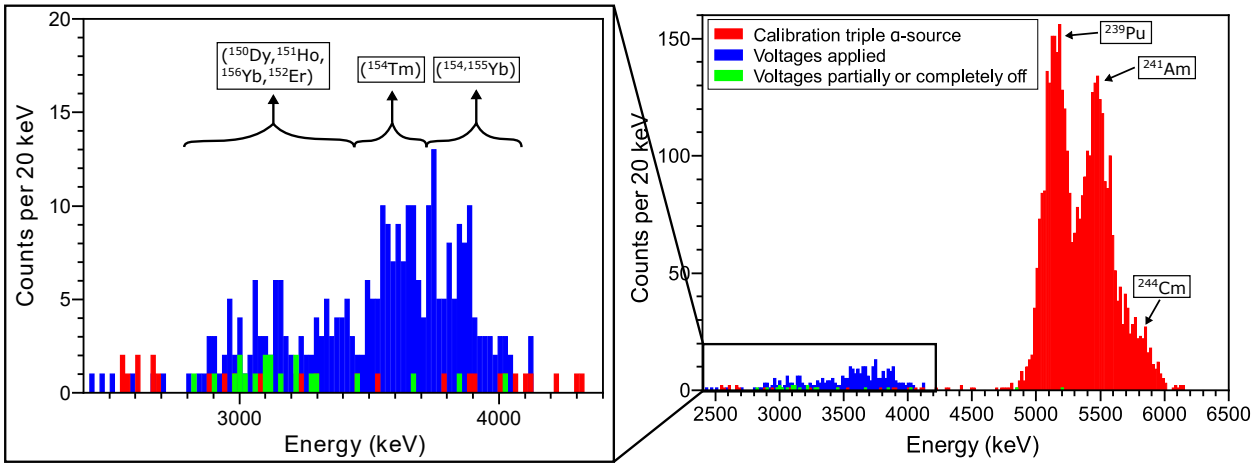

Figure 4.20.: Recorded α-spectrum behind the nozzle indicating beam-related signal from radioactive atoms (green histograms) and radioactive ions (blue histogram). The calibration signal (red histograms) was recorded in a separate vacuum chamber using a triple-α source, indicating a discrepancy to the measured α-energies inside the gas-jet apparatus (blue and green histograms). In the zoom-in (left) an uncertain assignment of the isotopes is indicated in brackets. The α-spectrum related to the UNILAC-beam was measured over a time span of 4 hours.

the maximum reachable laser energy of 600 µJ/pulse (see appendix Fig. A.2). The observed increase in count rate was linear, indicating that still more laser power was needed to saturate the AI step.

In the last detector setup (see Fig. 4.14 c) a PIPS detector was installed between the nozzle and the RFQ structure. An aluminized mylar foil (3.5 µm thickness) was placed in front of the detector and a voltage of -300 V applied in order to guide the beam-related $^{154\text{-}156}$Yb ions onto the aluminized mylar foil, where the ions stuck onto the foil surface due to the metallic character of ytterbium and aluminium. The ions were not implanted into the foil under these conditions. The reaction products were laser ionized inside of the flow channel behind the tantalum filament and the radioactive decay detected as shown in Fig. 4.20 (green and blue histograms). A calibration (red histograms) for the α-energies was performed in a separate vacuum chamber prior to the measurement using a triple-α source consisting of ^{239}Pu (5.157 MeV, 70.77 % intensity) [189], ^{241}Am (5.486 MeV, 84.8 % intensity) [190], and ^{244}Cm (5.805 MeV, 76.9 % intensity) [191]. In the recorded beam-related α-spectrum energies of 2.8 - 4.1 MeV were measured, which do not coincide with the α-energies of the possible reaction products $^{154\text{-}156}$Yb and the daughter-nuclei along the decay chains (see Table 4.2). Thus, the measured spectrum could originate from the isotopes ^{150}Dy, ^{151}Ho, ^{152}Er, ^{154}Tm, and ^{154,155,156}Yb assuming an energy shift by about 1.5 MeV to lower energies. This possibility is favored by comparing the recorded α-spectrum of Fig. 4.20 to the α-spectrum recorded in reference [188]. Without the energy shift, the measured low α-energies do not fit to the known lifetimes of some minutes and < 1 min (see Table 4.2) according to

the Geiger-Nuttall law [192, 193], respectively. It is unknown what could have caused such an energy shift. A tentative assignment assuming the energy shift of the measured signal was performed as indicated by the brackets on the left side of Fig. 4.20. Part of the signal originated from neutrals and was observed when no detector foil voltage and / or transport voltages were applied (green histograms). Mainly signal from ions with applied detector foil voltage and transport voltages were recorded (blue histograms).

4.7. Design changes after beam time campaign 2019

In the beam time campaign no laser-related signal of ^{155}Yb was obtained using radioactive decay and ion detection, and multiple limitations were identified. During the measurements, problems with the ion transport in the jet cell through the RFQ and mini-RFQ were observed. It was found, that the ideal transport settings for the RFQ and mini-RFQ changed over time. Additionally, a contamination of the flow channel and converging nozzle part with natural ytterbium and lutetium (Lu) was observed, which were used in off-line characterization measurements prior to the on-line measurements. A further origin of ion transport issues was found between the extraction plate and the detector. Due to the transport settings the ions were re-attracted towards the extraction plate instead of being transported towards the detector. Another limitation was given by the laser system in use. Instead of a 10 kHz-repetition-rate of the laser, a 100 Hz repetition rate laser was used, resulting in a loss in efficiency of 99%. Additionally, the autoionization (AI) step was not saturated during the measurements. The most crucial limitation was given by the nozzle. It was observed, that no gas-jet was created at a pressure of 30 mbar. The following sections will shortly explain the changes that were implemented after the 2019 beam time, as well as the newly installed 10 kHz repetition rate laser system.

4.7.1. New flow channel

A new flow channel was designed after the on-line measurement campaign to avoid a contamination by deposited atoms and to upgrade the functionality. Here, an insulator was added between the chamber and the channel, making it possible to apply a potential (see Fig. 4.21 a). In addition, two guiding pins were added to the flow channel holder, so that an easier and reproducable insertion of the filament was achieved.
Later, the flow channel was redesigned again. The reason for that was the observation of glow emission occuring between the hot filament and the channel. Glow emission is produced by the heated filament on a negative potential, in our case -120 V. After reaching a certain temperature, electrons are emitted from the hot filament and attracted to the nearest attractive potential, being the flow channel at ground potential. A passage of electric current through the argon gas forms a plasma, which ionizes the argon atoms and leads to the detection of a background signal. Higher temperatures as well as a higher voltage gradient favor the plasma creation, leading to an increased background rate. In order to reduce or avoid this phenomenon, the distance between the hot filament and the opening in the flow channel has to be increased. In addition, the potential difference between filament and flow channel

needs to be minimized to avoid plasma formation. For this reason the flow channel was cut in two parts, so that a potential on both parts can be applied, reducing the voltage gradient between the filament and the flow channel. Additionally, the opening for the filament was slightly increased (see Fig. 4.21 b). For both flow channels, the inner diameter of 12 mm was maintained, while the total length had to be shortened to a length of 26 mm due to the insulator and resulting gap between flow-channel and nozzle. The opening cone was shifted 1.8 mm closer to the filament, while maintaining the opening angle of the cone, in order to improve ion guiding onto the filament. The diverging part to match the nozzle transition of the former flow channel was implemented into the flow channel holder, as can be seen in Fig 4.21 a. The filament holder redesign moved the nozzle 1 cm closer to the gas cell, which also improved the overlap of the formed gas-jet with the perpendicular laser beams. As the laminar gas flow in the flow channel region is crucial for the transport of the atoms, COMSOL simulations were performed by [redacted] [171]. These simulations showed that this gap as well as a bigger hole for filament insertion has no negative influence on the

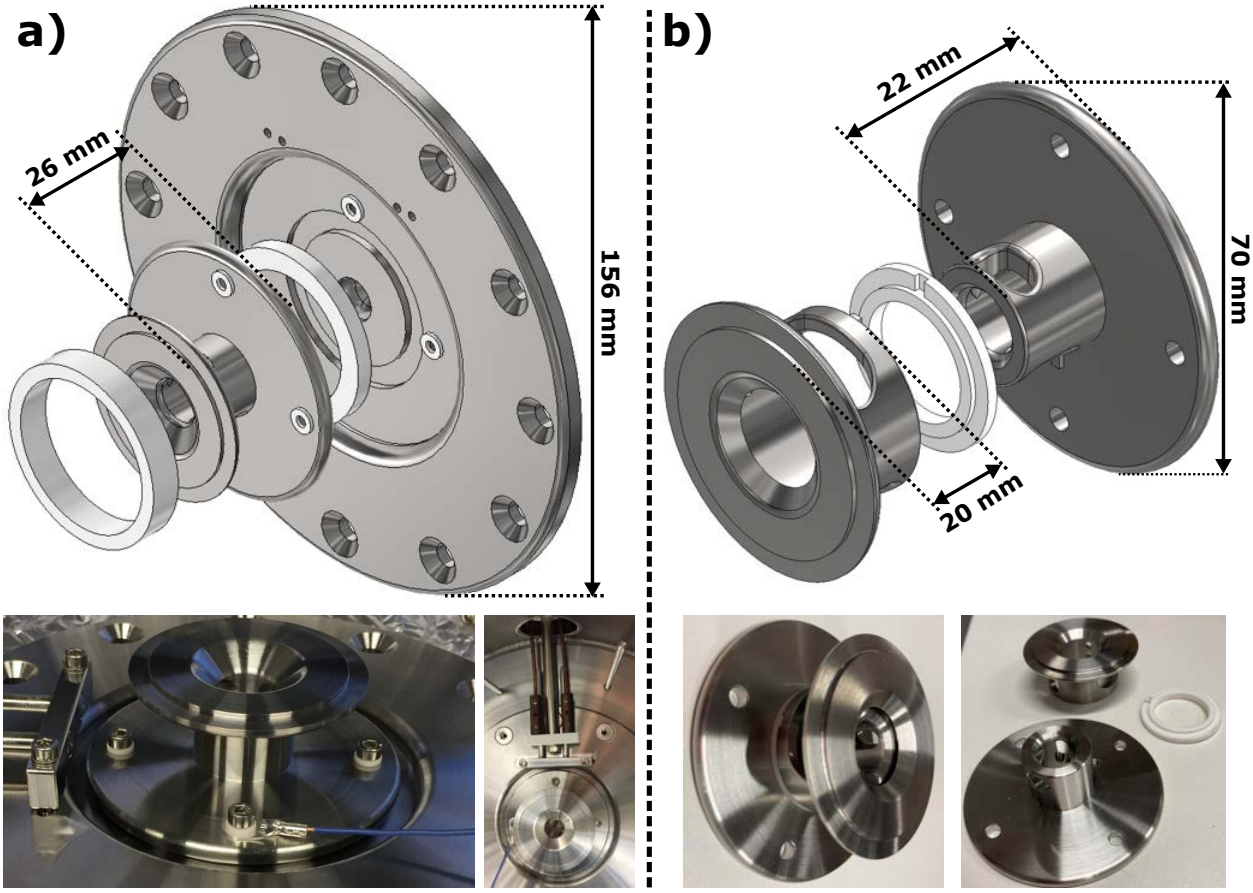

Figure 4.21.: a) Adding an insulator between the flow channel and its holder to be able to apply a potential. b) Redesign of the flow channel, in order to improve extraction of ions on the filament and getting rid of the observed glow emission of design a).

laminar gas flow or the extraction time.
First tests with the new flow channel (Fig. 4.21 b) were performed, indicating a reduction of the glow emission by applying a potential on both channel parts. As the glow emission did not completely vanish even with applied potentials, it has to be investigated in more detail in future experiments.

4.7.2. New de Laval nozzle

Two new nozzles (see Fig. 4.22 b and c) were simulated at the von Karman Institute for Fluid Dynamics (VKI), manufactured, and characterized at KU Leuven [171, 179, 195], before being installed in the gas-jet apparatus. These characterizations indicated that an upgrade of the pumping system is needed to reach better working conditions for both nozzles, namely higher stagnation pressures p_0 in the gas cell and lower background pressures p_{bg} in the jet cell. For further details on the new pumping system see section 4.7.5. Characterizations of both nozzles in the gas-jet apparatus were performed via laser induced fluorescence (LIF) measurements on dysprosium using the 404.6 nm ground-state transition ($A = 1.662 \cdot 10^8\,1/\mathrm{s}$ [196]) leading to the best working conditions reachable with the current pumping system. These fluorescence measurements will not be part of this work, but the optimal working conditions are summarized in Table 4.3. In the following sections more characterizations with these nozzles will be presented as well as the decision, which nozzle will be used in

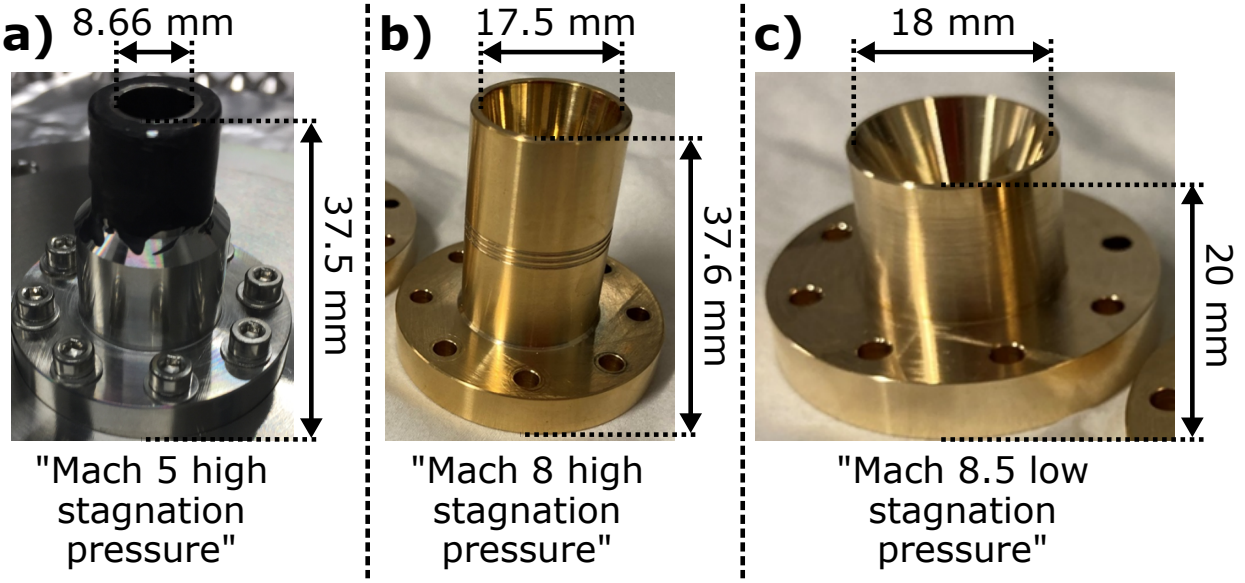

Figure 4.22.: Three different nozzles are shown of which two were simulated and designed for an operation at $p_0 = 350\,\mathrm{mbar}$ (high-stagnation-pressure) (a [49, 50, 194] and b [171, 179]). Another new nozzle was simulated and designed for an operation at $p_0 = 80\,\mathrm{mbar}$ (low-stagnation-pressure) (c [179, 195]). The dimensions for the nozzle length and nozzle exit diameter are indicated. All nozzles have a nozzle throat diameter of 1 mm.

Table 4.3.: Optimal working conditions at the gas-jet apparatus for the new nozzles extracted from fluorescence measurements conducted by [redacted] [197].

	Nozzle: "Mach 8"	Nozzle: "Mach 8.5"
p_0 (mbar)	125	80
p_{bg} (mbar)	$9 \cdot 10^{-3}$	$7 \cdot 10^{-3}$
Jet length (mm)	≈ 40	≈ 60
Jet diameter (mm)	≈ 2	≈ 6
FWHM (MHz)	$\approx 335(30)$	$\approx 215(35)$

future measurements.

4.7.3. New RFQ structure

The RFQ and mini-RFQ faced problems with charging up effects during the on-line campaign, changing the extraction voltages over time. Even without applying a DC gradient to the RFQ and mini-RFQ an ion transport was observed, which could be due to a transport solely by the RF field. Additionally, enabling and disabling the vacuum gauge in the jet chamber influenced the measured count rate. The charge-up effect could be either related to insulators being visible to the ion beam or due to the use of printed circuit boards (PCB) in combination with capacities and resistors inside of the jet cell. Therefore, it was decided to replace the old RFQ as well as the mini-RFQ. A new RFQ structure was designed, which is shown in Fig. 4.23. It consists of a 90°-bent RFQ with a radius of curvature of 80 mm. The length of each curved segment is ≈ 23 mm, the straight segments before and after the curved segments are 19 mm long and the last straight segment in front of the differential pumping stage is 24.5 mm long. In order to ensure the best approximation of the quadrupole field, the ratio (R_{rod}/r_0) of the rod radius R_{rod} to that of the free radius r_0 must be 1.148 [198]. Therefore, the rod radius in this design was chosen to be $R_{\text{rod}} = 6.87$ mm and the free radius to be $r_0 = 6$ mm, resulting in a ratio of 1.145 for this RFQ-structure. In order to avoid charge-up effects, the supporting structure boards were made of 316L stainless steel instead of printed circuit boards. The mixing of the DC voltages with the applied RF field was made on a printed circuit board outside of the jet chamber (see appendix Fig. A.4 a). Using a 40-pin feedthrough, the RFQ was connected with this mixing box (see appendix Fig. A.4 b). The resonance frequency of the RFQ was tuned to 1.080 MHz using transformer coils.
Another design change was to add a shielding plate in front of the first set of RFQ electrodes to avoid charge up effects, shielding visible insulators from the incoming gas-jet seeded with ions and radioactive species. A voltage can be applied to that shielding plate, attracting ions of the jet and improving the efficiency of the RFQ. In addition, another plate was installed, hindering ions going around the shielding plate to hit visible insulators. The dimensions of the RFQ are 123.9 mm in the direction of the jet and 135.5 mm in the direction to the detector chamber. Simulations of the ion extraction through the new RFQ design towards the detector were performed by [redacted] as explained in chapter 4.1.2.3 for a background

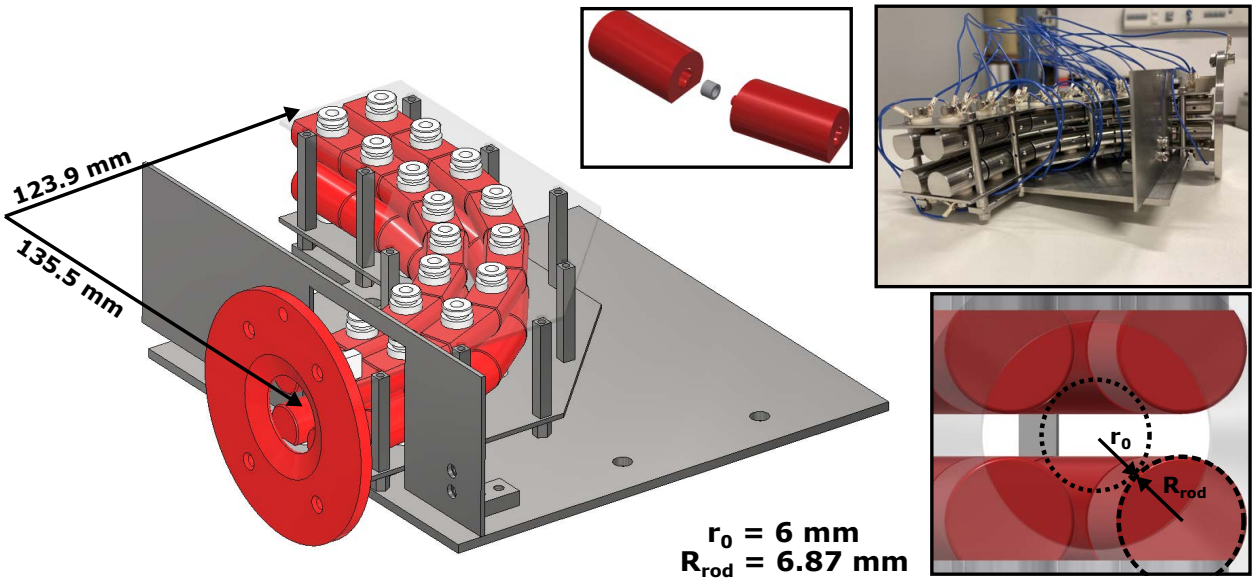

Figure 4.23.: A schematic RFQ design as well as the manufactured RFQ is shown. All parts besides the insulators (PEEK (Polyether ether ketone) and aluminium oxide) were made out of 316L stainless steel. The shielding plate and all electrodes are colored in red for improved visibility. The shielding plate at the entrance of the RFQ shields the insulators needed for mounting the electrodes. Additionally, a potential is applied to the shielding plate to attract ions that do not enter the RFQ. Another plate was installed to shield the remainder of the RFQ structure. The rods themselves were isolated from each other as shown in the inset on the top. The radius of the rods and the free radius were tuned in order to reach a ratio of 1.145.

pressure of $p_{\mathrm{bg}} = 1 \cdot 10^{-2}$ mbar. In these simulations the first set of electrodes was biased at -2 V and gradients of -0.75 V/cm, -1.51 V/cm, and -2.26 V/cm, respectively, applied between the first and last set of electrodes. Additionally, varying RF amplitudes from 50 - 600 V were investigated. The results indicated that a small gradient results in slower extraction times, while a high gradient leads to a broad ion beam due to reduced cooling time. As a consequence, the broad ion beam is deposited on the extraction plate. The simulations were used to deduce the optimal extraction settings, leading to a gradient between -0.75 V/cm and -1.51 V/cm and an RF amplitude of 350 - 600 V with a mean extraction time of around 150 µs.

4.7.4. New transport electrodes

Simulations indicated transport losses between the extraction plate and the detector as shown on the left side of Fig. 4.5. A negative potential was applied to the extraction plate and was therefore more attractive for the ions than the detector chamber, held at ground potential. Due to a distance of around 240 mm between the extraction plate and the detector, the high

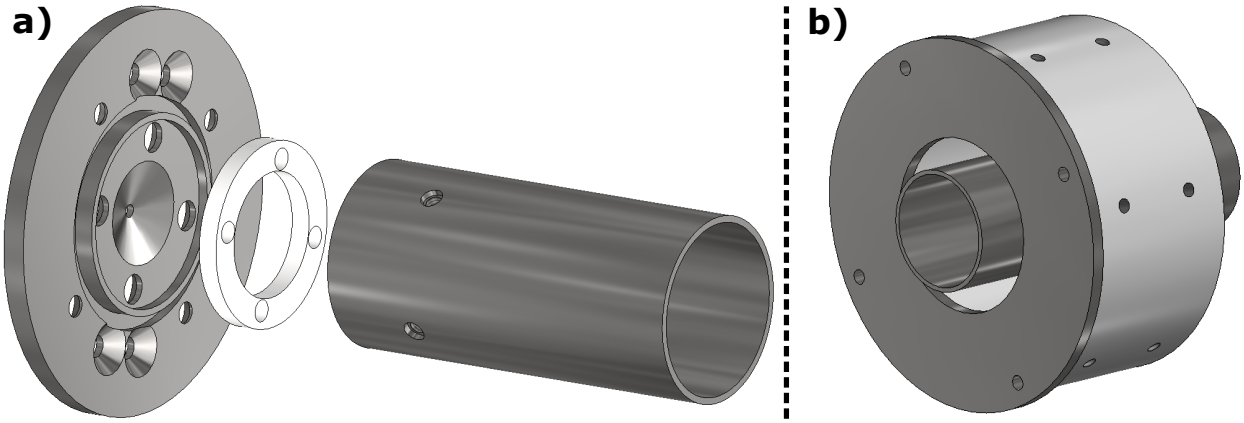

Figure 4.24.: a) Design of transport electrode 1 with an inner diameter of 25.8 mm, an outer diameter of 27.8 mm, and a length of 60 mm. An insulator was placed between the extraction plate and the transport electrode 1. b) Design of transport electrode 2 with an inner diameter of 25.8 mm, an outer diameter of 27.8 mm, and a length of 80 mm. The mounting insulator ring as well as the shielding plate are visible in addition to the electrode.

voltage of -1700 V applied on the detector was shielded by the chamber on ground potential. Thus, the ions were re-attracted to the extraction plate instead of being transported towards the detector.
Inserting two cylindrical electrodes (see Fig. 4.24), referred to as transport electrode 1 and 2, reduces the observed shielding effect and enables ion extraction towards the detector. Both electrodes have an inner diameter of 25.8 mm and an outer diameter of 27.8 mm. Transport electrode 1 has a length of 60 mm and is mounted to the extraction plate, whereas an insulation is achieved by a small insulator ring between the extraction plate and transport electrode 1. A gate valve separates the transport electrodes, leaving a gap of 65 mm. Transport electrode 2 has a length of 80 mm and is mounted to the chamber tube. An insulator ring is used to attach the electrode to the chamber. The mounting insulator ring is shielded by a stainless steel plate in order to avoid charging up effects of the insulator. Optimal voltage settings were extracted from simulations (see appendix Fig. A.5 a-c) and resulted in voltages of -40 V on transport electrode 1 (for the simulations connected to extraction plate) and of -300 V on transport electrode 2. These voltages result in ion trajectories reaching the detector in a mean flight time of around 150 µs.

4.7.5. Status quo setup

The previous sections summarized the limitations which were discovered during the 2019 on-line campaign. Therefore, a handful of new design changes as well as new chamber parts were realized and implemented into the existing setup. Fig. 4.25 shows the gas-jet system as of writing. The construction was extensively described in chapter 4.2. It is important to highlight the implemented changes, namely the new flow channel, the new nozzle, the new

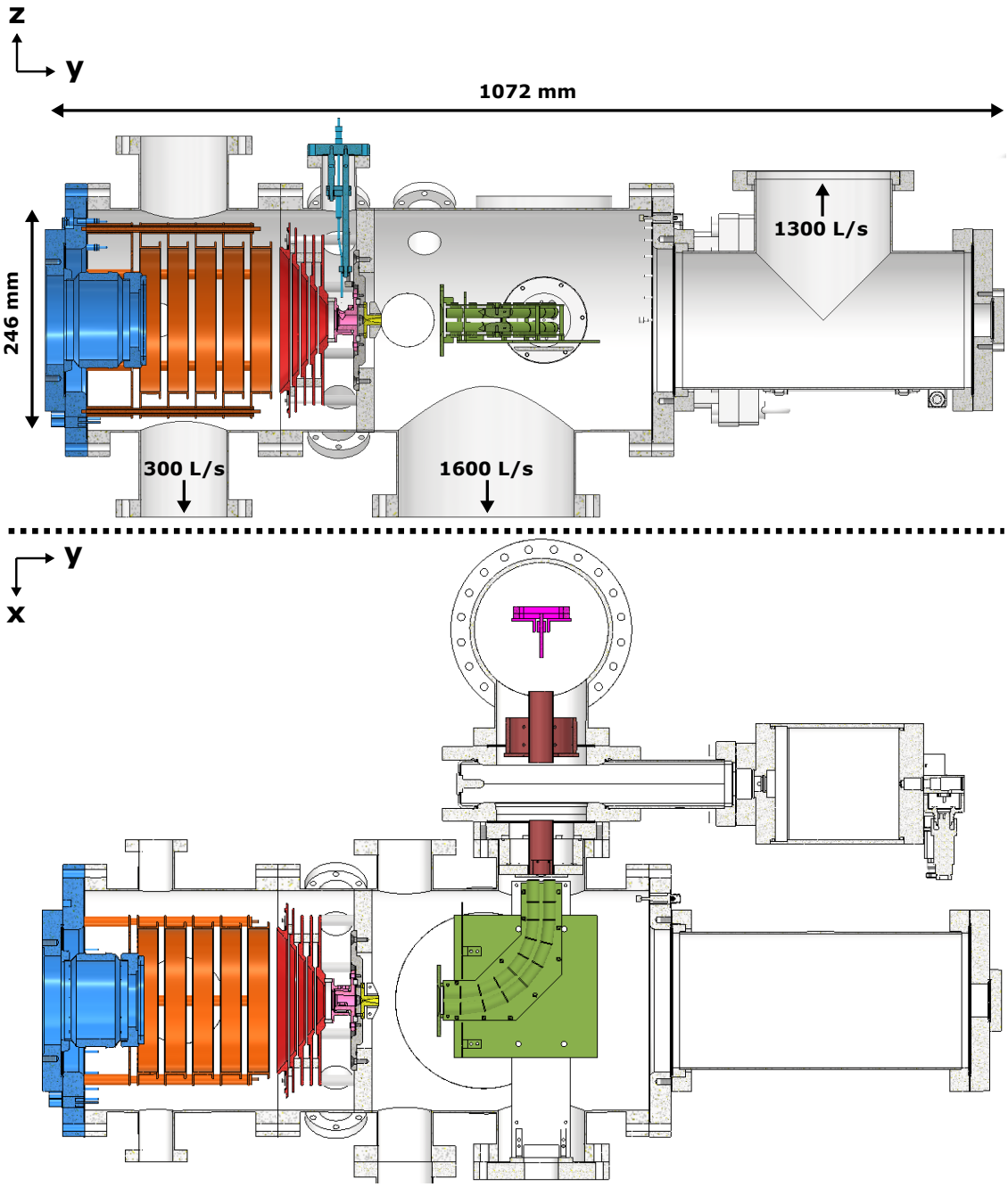

Figure 4.25.: Status quo of the gas-jet setup. The top shows a side-view and the bottom a top-view. Important changes compared to Fig. 4.8 are the new flow channel (pink), the new nozzle (yellow), the new RFQ (green) and two new transport electrodes (brown). In order to reach better vacuum conditions for the jet formation, a second turbo molecular pump was added to the detector chamber. For more details see text.

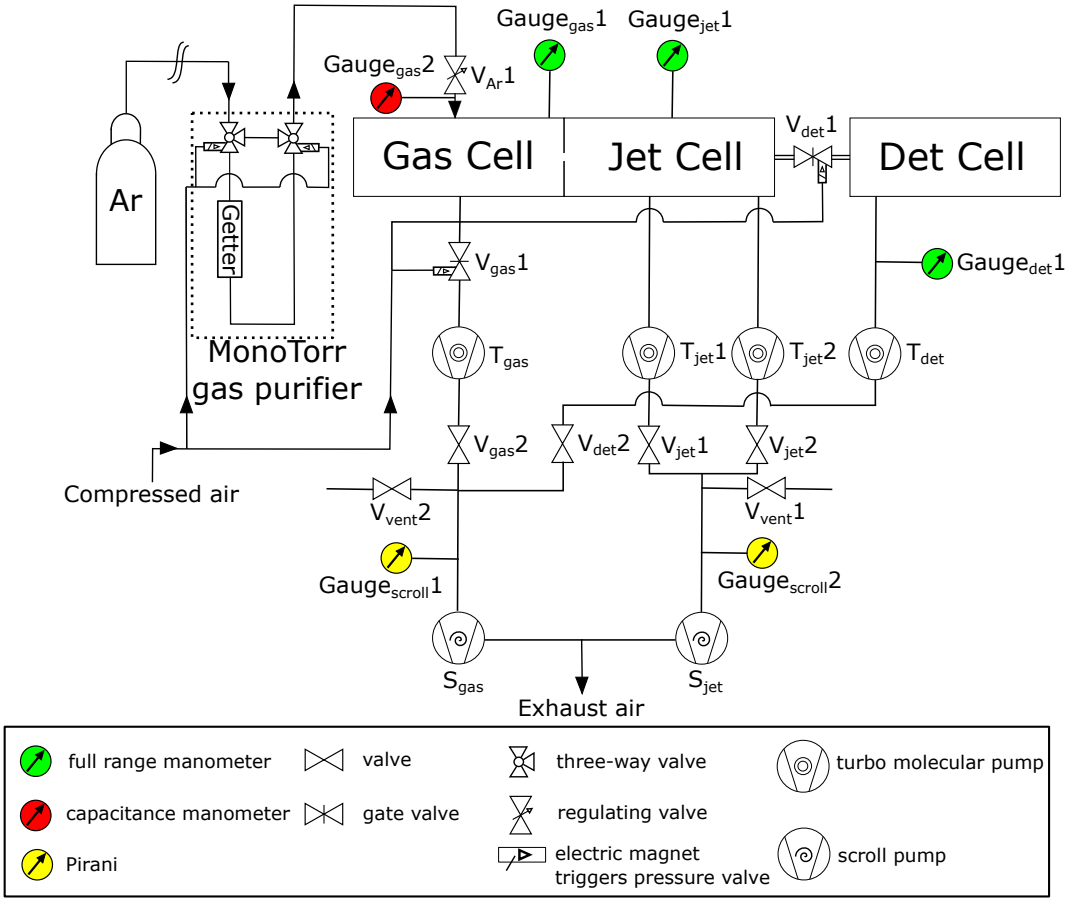

Figure 4.26.: Updated circuit diagram, which shows the pumping system, the vacuum diagnostics, the purification of the argon, as well as valves in use for the status quo of the setup.

RFQ, as well as two new transport electrodes. All these changes were necessary to improve or even enable the ion extraction from the gas cell towards the detector. In addition, the vacuum setup of the jet cell was improved so that optimal working conditions for the respective nozzle in use can be achieved, reaching the highest efficiency and spectral resolution. In addition to the 1300 L/s (for N_2) turbo molecular pump (Edwards STP-H1303CV3), a 1600 L/s (for N_2) high gas throughput turbo molecular pump (Edwards STPA1603C) was added. A CF160 t-piece had to be added to the jet cell to accommodate the pump as shown in Fig 4.25. The backing pump (Edwards XDS35i) was exchanged (Edwards iXL600) to reach better vacuum conditions for the turbo molecular pumps. The circuit diagram was updated for the current setup and is shown in Fig. 4.26. The butterfly valve, which was used in the first design stage to regulate the background pressure p_{bg} in the jet cell, was taken out in order to increase the tube diameter from 160 mm to 200 mm connecting the jet chamber with the turbopump (STPA1603C) achieving higher gas throughput. The background pressure is now regulated using the rotational speeds of both turbo molecular pumps, which can be regulated between 50 - 100% rotational speed. The limitation of the maximum achievable stagnation pressure

p_0 in the gas cell is the heat increase of both jet cell turbo molecular pumps, as they have a safety shut down when reaching temperatures slightly higher than 100°C. With this pumping setup, the highest achievable stagnation pressure is < 150 mbar.

4.8. 10 kHz laser system @ HIM

The flight time of the atoms in the gas-jet is 100 µs over 5.5 cm for a jet velocity of 550 m/s. As a result, each 100 µs a laser pulse is needed, so that each atom has the chance to see one laser pulse inside of the jet. This corresponds to a repetition rate of 10 kHz. Therefore, the laser system was upgraded to a repetition rate of 10 kHz. The dye circulators of the dye amplifier had to be exchanged for a bigger dye reservoir volume (4 L instead of 1 L), compensating the faster consumption of dye for higher repetition rate lasers. The 4-stage amplification was converted to a 2-stage amplification by the company. A multi longitudinal

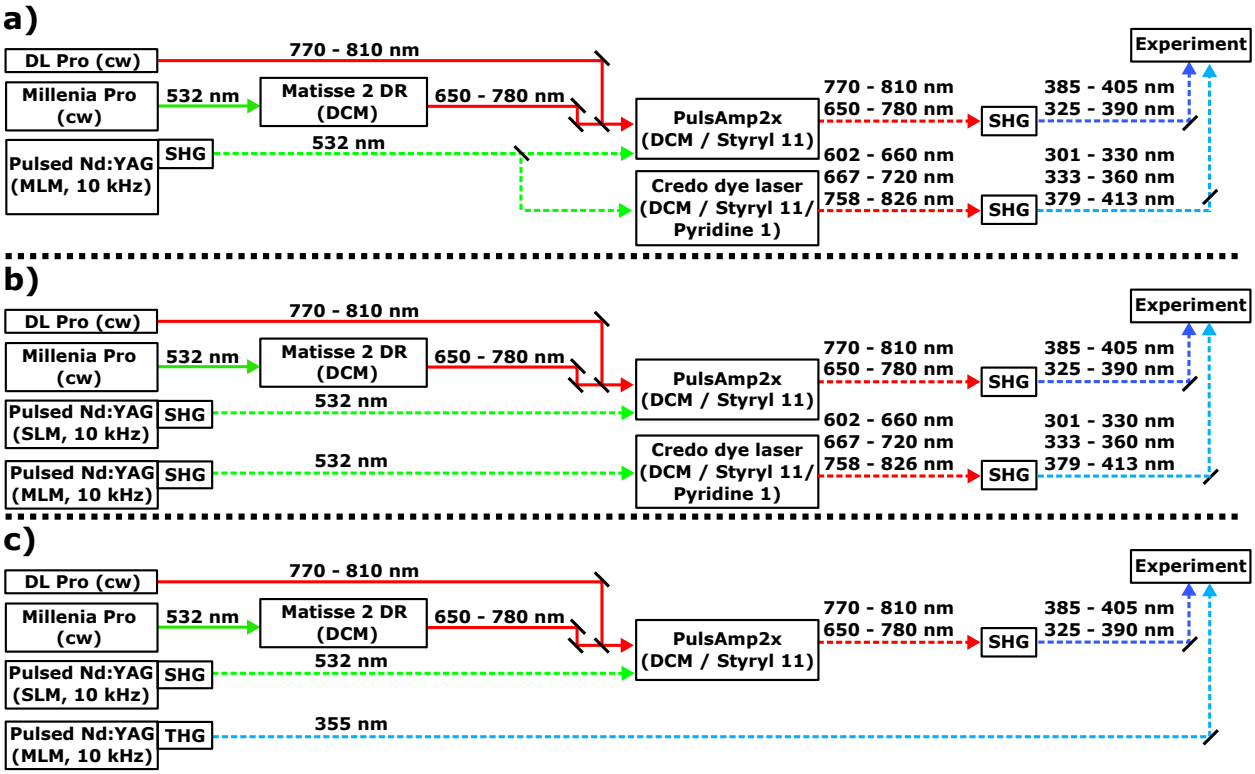

Figure 4.27.: Schematic overview over the 10 kHz-repetition-rate laser system. Solid lines indicate cw light and dashed lines pulsed light. a) Using the SHG module of the MLM laser for pumping the dye amplifier and the dye laser. b) Using the SLM laser to pump the PulsAmp2x and MLM laser (SHG) to pump the Credo dye laser. c) Using the THG module of the MLM laser for non-resonant ionization. Here, the SLM laser is pumping the dye amplifier. For more details see text.

Table 4.4.: Maximum energy output of the dye lasers for different dye and pump laser combinations.

Dye laser	Dye	Wavelength	Energy	Pump laser	Pump power
PulsAmp 2x	DCM	330 nm	7.0 µJ/pulse	SLM laser	40 W
PulsAmp 2x	Styryl 11	399 nm	20 nJ/pulse	SLM laser	40 W
PulsAmp 2x	Styryl 11	399 nm	300 nJ/pulse	MLM laser	45 W
Sirah Credo	DCM	315 nm	350 µJ/pulse	MLM laser	45 W
Sirah Credo	Pyridine 1	347.6 nm	5.8 µJ/pulse	MLM laser	45 W
Sirah Credo	Styryl 11	385.5 nm	3.5 µJ/pulse	MLM laser	45 W

mode (MLM) 10 kHz Nd:YAG pulse laser (Edgewave InnoSlab 2044) was installed, which features the possibility to choose and change between a SHG (90 W, 9 mJ/pulse) and a THG module (45 W, 4.5 mJ/pulse) with a pulse width of around 10 ns. The jitter, when externally triggering the pulse laser, was observed to be around 3 ns and is sufficient for measuring e.g. the $^1P_1$-state in ^{254}No with a lifetime of only about 2 ns [77].
Because no simultaneous operation of SHG and THG of the MLM pulse laser is possible, there are mutliple ways to operate the laser system. First, the SHG of the MLM pulse laser can be used as the pumping source for the 2-stage dye amplifier (PulsAmp 2x) and a second dye laser (Sirah Credo), both being pumped with 45 W (see Fig. 4.27 a). The maximum energy output of the dye lasers for different dyes is summarized in Table 4.4, whereas the wavelength is tunable within the range of the specific dye that is used, typically 60 nm. Additionally, a prototype single longitudinal mode (SLM) 10 kHz Nd:YAG pulse laser (Edgewave InnoSlab 1705), which was developed from Edgewave in cooperation with KU Leuven [199, 200], can be used to pump the 2-stage dye amplifier. SLM operation is achieved when the bandwidth of the net gain is smaller than the frequency spacing of the resonator modes. It has the downside that the achievable output power compared to the MLM pulse laser is lower (40 W, 4.0 mJ/pulse), but does not feature sidemodes, which are unfavorable for laser spectroscopy due to the possibility to overlap with hyperfine structure components. Using the SLM pulse laser to pump the 2-stage dye amplifier (see Table 4.4) gives the opportunity to use the full power output of 90 W of the MLM laser to pump the Sirah Credo dye laser (see Fig. 4.27 b). This laser setup was used to measure the RFQ efficiency using ^{169}Tm. Lastly, the THG module of the MLM pulse laser can be used for non-resonant ionization. If it is used for non-resonant ionization, the dye amplifier is pumped by the SHG of the SLM pulse laser (see Fig. 4.27 c).

4.9. Measurements after the major design changes

As explained in the last sections, multiple design changes were performed after the on-line campaign. The following sections will focus on the characterization of the newly designed features of the apparatus using the new 10 kHz laser system.

4.9.1. High-stagnation-pressure and low-stagnation-pressure nozzles

A new design of the high-pressure nozzle, denoted as the Mach-8-nozzle, was installed in the system [171, 179]. This nozzle design differs from the old high-pressure nozzle, denoted as the Mach-5-nozzle, in its dimensions (see Fig. 4.22), resulting in higher achievable Mach numbers and therefore a better spectral resolution. Together with the new 10 kHz-repetition-rate laser system the measurement shown in Fig. 4.13 was repeated in order to characterize the spectral resolution. In this measurement the excitation laser (398.91 nm) was applied perpendicular (elliptical shape, horizontal: $\approx 25 - 30$ mm, vertical : ≈ 5 mm) and the ionization laser (385.76 nm) anticollinear to the gas-jet. Pulse energies of 50 nJ/pulse and 1.6 µJ/pulse were used for the excitation step and the ionization step, respectively. Using the voltage set shown in Table 4.5, the count rate in dependence of the wavelength of the first excitation step was recorded at a stagnation pressure of around 76 mbar and a background pressure of around $3{\cdot}10^{-2}$ mbar.
Fig. 4.28 shows the measured, background-corrected spectrum of ^{nat}Yb. The background correction was carried out similar to Fig. 4.13. The evaluation of the spectral resolution was performed with the same procedure and will therefore not be covered here. A spectral resolution of $\approx 400(100)$ MHz was achieved, indicating that the design changes did improve the system. Sidemodes in the spectrum, caused by the multi-mode operation of the pump laser, are visible and indicated by pink arrows in Fig. 4.28. The sidemodes could explain the observed enhancement in count rate at 25 068.21 cm^{-1} compared to the fit. The inset at the upper right of Fig. 4.28 shows a fluorescence measurement performed under the named pressure conditions with ^{nat}Dy, which was measured in cooperation with [redacted] [197]. The red box roughly marks the interaction region with the laser beams during the measurement. The length of the formed gas-jet is around 2 - 3 cm. In order to produce a longer, more homogeneous jet with this nozzle, the stagnation pressure has to be increased to ≥ 125 mbar, which was achieved after improving the pumping system (see section 4.7.5).

Table 4.5.: Optimized transport parameters after new design changes.

Electrode	Setting
^{nat}Yb filament	-5 V
entrance plate	-1 V
RFQ entry	-8.8 V
RFQ exit	-25.8 V
RFQ RF amplitude	400 V
RFQ RF	1.080 MHz
extraction plate	-25.9 V
transport electrode 1	-300 V
transport electrode 2	-1000 V
detector	-2000 V

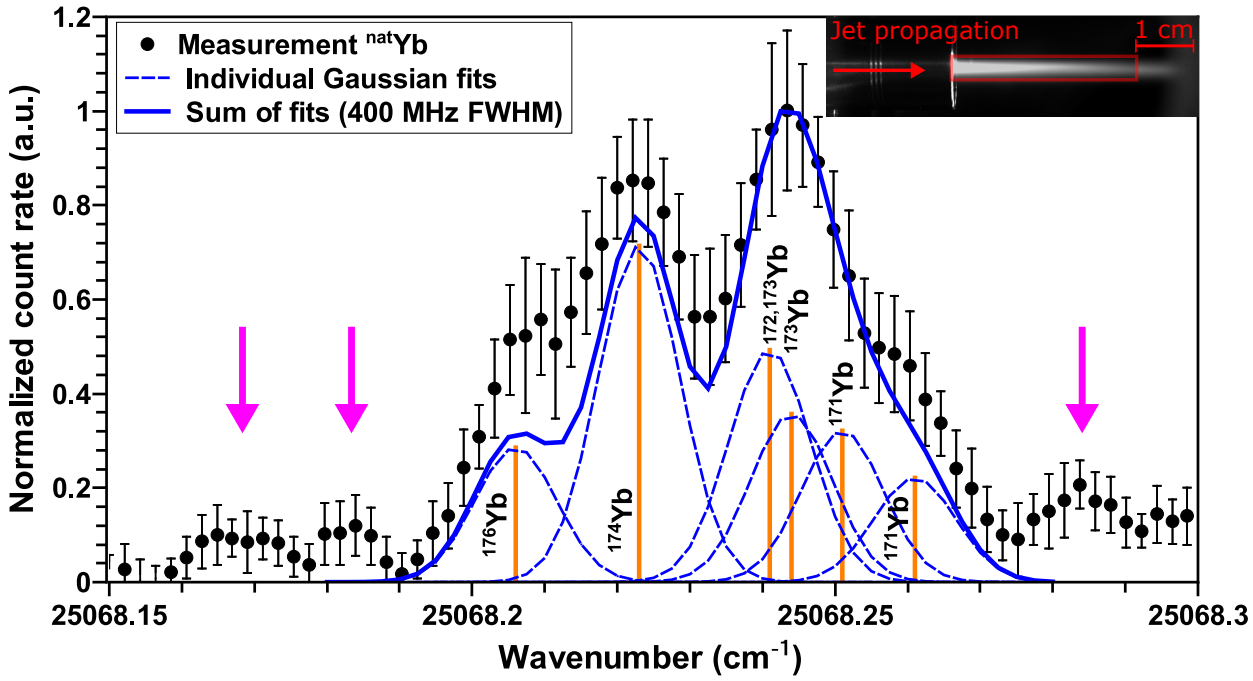

Figure 4.28.: Background-corrected ^{nat}Yb spectrum after new design changes and with the new laser system. The high-stagnation-pressure nozzle (Mach-8-nozzle) was installed. The inset on the upper right shows a fluorescence image from ^{nat}Dy, obtained in cooperation with [redacted]. A ^{nat}Yb filament as shown in the inset of Fig. 4.13 was used. Sidemodes in the spectrum, caused by the multi-mode operation of the pump laser, are indicated by pink arrows.

In addition to the new high-pressure nozzle, a new low-stagnation-pressure nozzle, denoted as Mach-8.5-nozzle, was simulated and designed in cooperation with KU Leuven [179, 195]. This nozzle was installed and the spectral resolution characterized. Instead of ^{nat}Yb a monoisotopic sample of ^{174}Yb was used in order to obtain a more precise evaluation of the spectral resolution due to the absence of a hyperfine splitting. A filament was prepared by dissolving monoisotopic $^{174}Yb_2O_3$ in 60 µL concentrated HNO_3 and 120 µL deionized H_2O. An aliquot of 20 µL ($\approx 10^{16}$ atoms) was deposited on a tantalum stripe (length ≈ 25 mm, width $\approx 2-3$ mm, thickness $= 0.025$ mm), dried, and coated with a layer of ≈ 880 nm titanium as a reduction agent to release neutral ytterbium. This ^{174}Yb filament was then installed in front of the nozzle and heated (see left inset Fig. 4.29).
The measurement was performed by applying the excitation laser (398.91 nm) perpendicular (elliptical shape, horizontal: $\approx 50-60$ mm, vertical: ≈ 5 mm) and the ionization laser (385.76 nm) anticollinear (beam size: $\approx 4\,\mathrm{x}\,4\,\mathrm{mm}^2$) to the gas-jet. Pulse energies of 40 nJ/pulse and 580 - 640 nJ/pulse were used for the excitation step and the ionization step, respectively. The count rate in dependence of the wavelength of the first excitation step was recorded at a stagnation pressure of 82.9 mbar and a background pressure of $2.58{\cdot}10^{-2}$ mbar as shown in Fig. 4.29. The pressure conditions were derived from the simulations performed

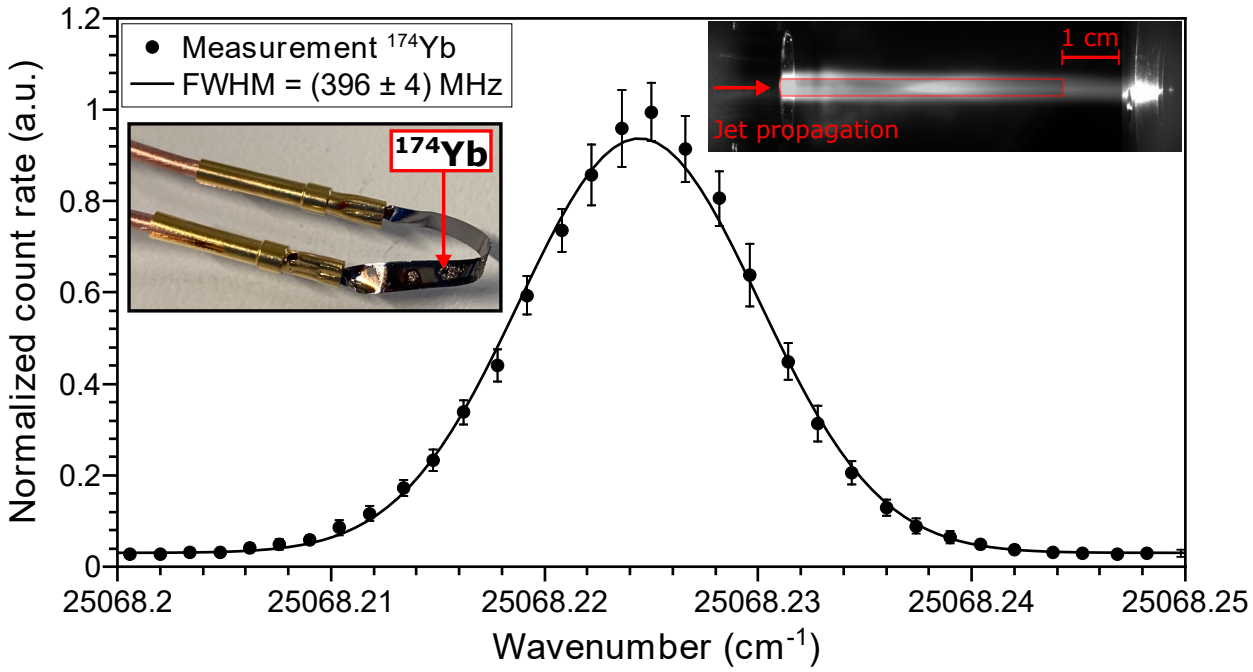

Figure 4.29.: ^{174}Yb spectrum after new design changes and with the new laser system. The low-stagnation-pressure (Mach-8.5-nozzle) nozzle was installed. The inset on the upper right shows a fluorescence image from ^{nat}Dy, obtained in cooperation with [redacted]. The left inset shows the ^{174}Yb filament installed in front of the nozzle.

at the von Karman Institute for Fluid Dynamics (VKI), in which these pressure conditions resulted in the best jet formation. A spectral resolution of (396 ± 4) MHz was obtained, whereas only a part of the jet was investigated in the measurement (see inset Fig. 4.29). The Mach-8.5-nozzle creates a jet with a bigger diameter of ≈ 6 mm compared to the Mach-8-nozzle investigated before with ≈ 2 mm. Instead of a homogeneous gas-jet over ≈ 6 cm, a shock disc at about 2 - 3 cm distance from the nozzle end is formed at these pressure conditions. The optimal experimental pressure conditions were extracted from fluorescence studies (similar to the inset images of Fig. 4.28 and 4.29) for different background pressures [197]. For the low-stagnation-pressure nozzle a stagnation pressure of 80 mbar combined with a background pressure of $7{\cdot}10^{-3}$ mbar resulted in the best jet formation. These fluorescence studies were performed by [redacted] and will not be part of this work, but it is important to note that the achievable spectral resolution and homogeneity can be further improved by operating at the optimal working conditions for both the high-stagnation-pressure nozzle (Mach-8-nozzle) and the low-stagnation-pressure nozzle (Mach-8.5-nozzle).
As indicated before, the length of the jet is important to efficiently excite and ionize the species of interest. Therefore, the jet length should be sufficiently long (≥ 55 mm) so that all ions in the jet have a chance to be excited by the pulse laser. Both high-stagnation-pressure nozzle (Mach-8-nozzle) and low-stagnation-pressure nozzles (Mach-8.5-nozzle) were investigated by RIS with the simulated pressure ratios, as the fluorescence measurements were not

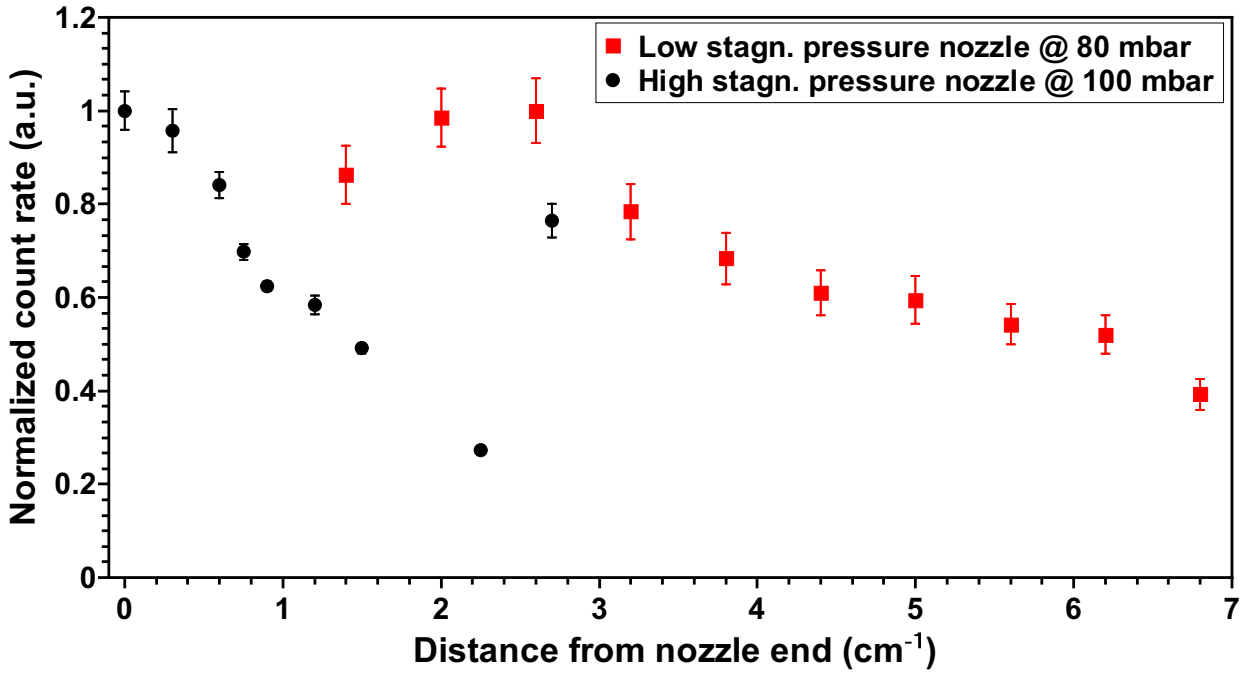

Figure 4.30.: Comparison of the gas-jet obtained from the high-stagnation-pressure nozzle (Mach-8-nozzle, black) at $p_0 = 100\,\text{mbar}$ and $p_{\text{bg}} = 2.7 \cdot 10^{-2}\,\text{mbar}$ and the low-stagnation-pressure nozzle (Mach-8.5-nozzle, red) at $p_0 = 80\,\text{mbar}$ and $p_{\text{bg}} = 2.5 \cdot 10^{-2}\,\text{mbar}$. Here, RIS was performed with the FES applied perpendicular to the gas-jet (beam size: 1 mm x 1 mm) and the SES applied anticollinear to the gas-jet (beam size: 4 mm x 4 mm). The count rate was measured for different distances between the nozzle end and the FES position along the middle axis of the jet.

yet performed at that time. Fig. 4.30 shows the normalized count rate in dependence on the distance of the nozzle end. For this measurement the excitation step (398.91 nm) was applied perpendicular to the jet with a beam size of 1 mm x 1 mm, and moved along the middle axis of the nozzle while the ionization step (385.76 nm) was applied anticollinear. By doing this the jet was probed step by step. It can be seen that the jet for the high-stagnation-pressure nozzle shows a fast signal drop of $\approx 75\%$ over a length of around 2.5 cm, which is in agreement with the extracted jet length of $\approx 40\,\text{mm}$ from the fluorescence measurements under optimized pressure conditions (see Table 4.3 and Fig. 4.28). On contrary, the low-stagnation-pressure nozzle has a longer jet length of around 6 - 7 cm, which was extracted from Fig. 4.30 and is in agreement with the fluorescence measurement results (see Table 4.3 and Fig. 4.29). Under these pressure conditions, the low-stagnation-pressure nozzle better matches the given requirements.
In order to investigate the spectral resolution of the jet, a similar measurement to that of the length characterization was performed for the low-stagnation-pressure nozzle. Here, the gas-jet was probed at different positions as can be seen in Fig. 4.31, and the spectral resolution at each point measured using a ^{174}Yb filament. The pressure conditions were

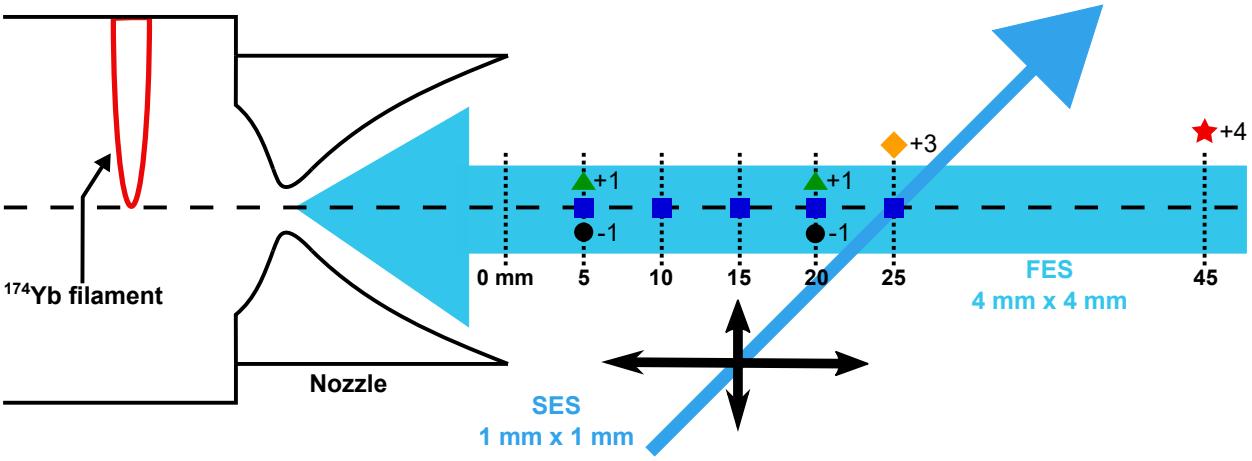

Figure 4.31.: Probing of the low-stagnation-pressure nozzle (Mach-8.5-nozzle) at different positions in the jet, as indicated by the different colored shapes. The first excitation step (FES) was applied anticollinear and the second excitation step (SES) perpendicular to the jet. The SES was moved horizontal and vertical in order to characterize different positions of the jet.

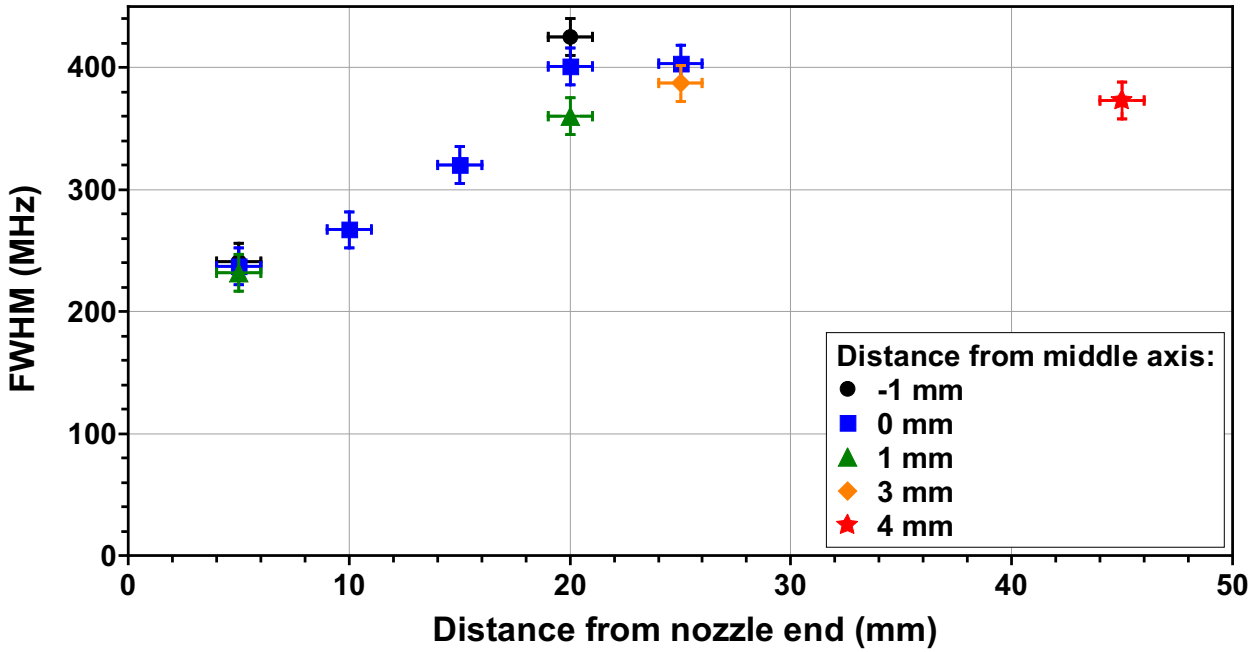

Figure 4.32.: Measured FWHM of the low-stagnation-pressure nozzle (Mach-8.5-nozzle) at different positions in the jet, as indicated by the different colored shapes. The measurement was performed with a ^{174}Yb filament at a stagnation pressure of $p_0 = 81\,\text{mbar}$ and a background pressure of $p_{\text{bg}} = 2.57 \cdot 10^{-2}\,\text{mbar}$.

a stagnation pressure of 81 mbar and a background pressure of $2.57{\cdot}10^{-2}$ mbar. Fig. 4.32 shows the extracted spectral resolution at different points in the jet. It is important to note that the FWHM is increasing with increasing distance from the nozzle. At a distance of 5 mm from the nozzle a spectral resolution of ≈ 240 MHz can be achieved, while at 45 mm the spectral resolution is ≈ 380 MHz. These results indicated that a uniform jet was not created. This hypothesis was proven with the fluorescence measurements and can be seen in the inset of Fig. 4.29.
One possible explanation for the deviation of the measured count rate from the dotted middle axis in Fig. 4.31 originates from the position of the filament. The ^{174}Yb filament in front of the nozzle determines the flowlines of ytterbium inside of the jet, which was investigated in detail in [179]. Therefore, a reproducible insertion of the filament is crucial for future measurements.
Looking at Fig. 4.31 and 4.32 one can see that under perfect measurement conditions no excitation and ionization should take place at a vertical distance of +3 mm and +4 mm from the dotted middle axis due to not being illuminated by the excitation laser light. However, measurements on these points were possible and spectral resolutions were determined. There are two possible explanations for this phenomenon. First, the second excitation step (SES) could be moved at an angle (downwards in Fig. 4.31) instead of perfectly horizontally. If this would be the case, the distance between the middle axis of the gas-jet and the SES beam spot would increase with increasing distance from the nozzle. This increased distance has then to be counteracted by increasing the step size, e.g. +3 mm and +4 mm, needed to overlap the SES with the middle axis again. Second, the nozzle could have been mounted slightly tilted, leading to a gas-jet which is expanding at an angle relative to the horizontal axis. Mounting the nozzle without a slight tilt would therefore be important and would need to be checked for future measurements.
In order to rule out that the linewidth of the laser $\delta\nu_{\text{laser}}$ is the limiting factor for the achievable spectral resolution (FWHM), the linewidth of a laser pulse with a Gaussian time profile and a width τ_{pulse} can be calculated using the equation [47]

$$\delta\nu_{\text{laser}} = 441/\tau_{\text{pulse}}. \tag{4.1}$$

The pulse width of the pump laser was investigated and was found to be $\tau_{\text{pulse}} \approx 9.6$ ns, corresponding to a limitation of the spectral resolution to $\delta\nu_{\text{laser}} = 46$ MHz. Using the relationship of a non-homogeneously broadened spectral line, whose broadening is caused by the Doppler broadening $\delta\nu_{\text{jet}}$ and the laser bandwidth $\delta\nu_{\text{laser}}$, the FWHM can be calculated by using the equation [47, 194]

$$\sqrt{(\delta\nu_{\text{laser}})^2 + (\delta\nu_{\text{jet}})^2} = \text{FWHM}. \tag{4.2}$$

Using a FWHM of 240 MHz results in a calculated Doppler broadening of 236 MHz, therefore being the limiting factor. Using the pulse width of the pump laser is only an estimation, as the pulse width of the dye amplifier (PulsAmp) should be used in the calculation. In a later experiment the pulse width of the SHG ($\lambda = 323.47$ nm) of the dye amplifier (PulsAmp) pumped by the single-longitudinal mode pump laser and seeded by the Sirah Matisse dye

laser ($\lambda = 646.94\,\text{nm}$) was investigated, resulting in $\tau_{\text{pulse}} = 4.6(3)\,\text{ns}$. This corresponds to a spectral resolution of $\delta\nu_{\text{laser}} = 96(6)\,\text{MHz}$. Using equation 4.2 a Doppler broadening of $\approx 220\,\text{MHz}$ can be calculated for a FWHM of 240 MHz. The achievable spectral resolution measured in the gas-jet is therefore not limited by the laser linewidth.
To summarize, two different nozzles were investigated and characterized in this chapter. Both of these nozzles have advantages and disadvantages regarding the use in the gas-jet setup. For instance, the high pressure nozzle has a smaller jet diameter compared to the low-stagnation-pressure nozzle, which is favorable due to the laser power needed to saturate the transition. An increase of the size of the laser beam reduces the power density and therefore requires a higher total power from the laser to saturate the transition. Assuming an interaction area (see Table 4.3) of $A_{\text{Mach-8}} = 40\,\text{mm} \cdot 2\,\text{mm} = 0.8\,\text{cm}^2$ for the high-stagnation-pressure nozzle (Mach-8-nozzle) and of $A_{\text{Mach-8.5}} = 50\,\text{mm} \cdot 6\,\text{mm} = 3.0\,\text{cm}^2$ for the low-stagnation-pressure nozzle (Mach-8.5-nozzle), pulse energies of $\approx 5.24\,\mu\text{J/pulse}$ ($\approx 52.4\,\text{mW}$, Mach-8-nozzle) and $\approx 20\,\mu\text{J/pulse}$ ($\approx 200\,\text{mW}$, Mach-8.5-nozzle) are required to saturate the transition at 398.91 nm ($I_{\text{sat}} = 655\,\text{W/m}^2$, see section 4.10). Since the equation for estimating the saturation intensity was derived under different conditions (see chapter 2.1.9), the calculated values should be treated with caution. Nevertheless, as neither the excitation nor the ionization step were saturated, a smaller beam diameter also helps to increase the signal. On the other hand, the low-stagnation-pressure nozzle has a longer jet of around 6 - 7 cm, which is needed to have an efficient interaction region of atoms in the jet with the laser pulses. The spectral resolution of both nozzles was found to be $\leq 400\,\text{MHz}$, sufficient for the planned on-line nobelium measurement (see part III). In order to decide on one of these nozzles, fluorescence measurements were performed to extract the optimal working conditions for both nozzles, specifying the diameter, jet length, and spectral resolution. These measurements were performed by [redacted] [197] and will not be part of this thesis. Nevertheless, the specifications under optimal working conditions are summarized in Table 4.3. Taking all important properties into account, the Mach-8.5 low-stagnation-pressure nozzle was chosen for future experiments.

4.9.2. Transport electrodes

A new set of two transport electrodes was installed between the extraction plate and the detector in order to shield the ground potential of the surrounding chamber. $^{\text{nat}}$Yb was produced in front of the nozzle and extracted towards the detector using the voltage set

Table 4.6.: Influence of transport electrode 1 and 2 voltages on the measured count rate with a maximum observed count rate of 1500 counts/s.

Transport electrode 1 (V)	Transport electrode 2 (V)	Signal (counts/s)
-350	0	0
0	-1000	0
-350	-1000	1500

shown in Table 4.5. Table 4.6 shows the influence of both transport electrodes on the measured count rate, clearly indicating that they are needed for an efficient extraction. No signal was observed, when one of the transport electrodes was set to ground.

4.9.3. RFQ efficieny

The transport efficiency of the new RFQ structure was investigated using the high-stagnation-pressure nozzle (Mach-8-nozzle) at a stagnation pressure of 121 mbar and a background pressure of $\approx 6 \cdot 10^{-2}$ mbar, which is assumed to be the approximate pressure in the RFQ. The measuring configuration is shown in Fig. 4.33 and the created gas-jet in the green inset box. A battery box with 45 V was built by connecting five 9 V block batteries. The positive terminal was used to bias a picoamperemeter (Keithley 6485). The ^{nat}Yb filament was resistively heated in front of the nozzle. Both the excitation (398.91 nm) and the ionizing (385.76 nm) laser beams propagated anticollinear to the gas-jet. In the first step the negative terminal was connected to the shielding plate and all RFQ electrodes (1). Ions impinging on the electrodes were detected by the picoamperemeter, leading to a measurable current of $\approx$ 20 pA. Afterwards the negative terminal was connected to both transport electrodes (2) and the voltage set from Table 4.5 applied on the shielding plate, the RFQ, and the extraction plate. In this configuration a current of $\approx$ 15 pA impinging on both transport

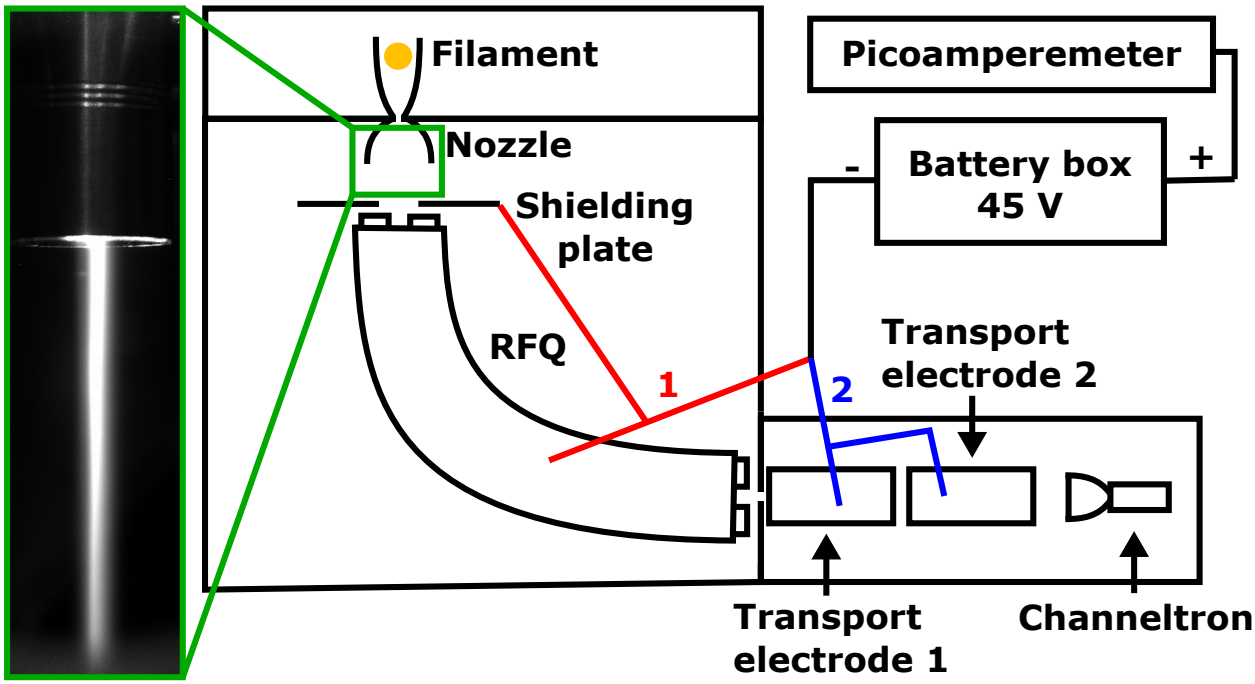

Figure 4.33.: Measuring configuration to measure the transport efficiency of the RFQ. A battery box (45 V) is connected to the shielding plate and RFQ (1), or to both transport electrodes (2) and the current of the impinging ions measured with a picoamperemeter. A fluorescence image of the $\approx$ 4 cm long jet, recorded by [redacted], is shown in the green inset.

Table 4.7.: Optimized transport parameters for measuring the RFQ efficiency using the low-stagnation-pressure nozzle.

Electrode	Setting)
^{169}Tm filament	+40 V
flow channel	0 V
entrance plate	-1.69 V
RFQ entry	-8.68 V
RFQ exit	-16 V
RFQ RF amplitude	400 V
RFQ RF	1.080 MHz
extraction plate	-170 V
transport electrode 1	-200 V
transport electrode 2	-85 V

electrodes was measured. The efficiency was calculated taking the ratio of both measured currents, leading to an efficiency through the RFQ and extraction plate of roughly 75% under the given conditions. This was an increase in efficiency compared to the old combination of RFQ and mini-RFQ, which showed an efficiency of roughly 50% using the former Mach-5-nozzle.
The efficiency of the new RFQ structure was remeasured using the low-stagnation-pressure nozzle (Mach-8.5-nozzle) under the optimal working conditions of $p_0 = 80\,\text{mbar}$ and $p_{\text{bg}} = 6.5 \cdot 10^{-3}\,\text{mbar}$, which will be used during the next on-line campaign. The measurement configuration was similar as shown in Fig. 4.33 although a battery box with 85 V was used. ^{169}Tm was used as a filament. A two-step ionization scheme was applied using the wavelengths $\lambda_1 = 322.37\,\text{nm}$ (FES) and $\lambda_2 = 313\,\text{nm}$ (SES, non-resonant). In the first measurement step the negative terminal of the battery box was connected to all RFQ electrodes. No voltage was applied on the shielding plate. An ion current of $\approx 225(5)\,\text{pA}$ was measured from the impinging ions on the RFQ electrodes. In the next step the negative terminal was connected to transport electrode 2 and the voltage set from Table 4.7 applied. An end-cap was installed at the end of transport electrode 2 in order to measure all impinging ions without any loss. An ion current of $\approx 175(5)\,\text{pA}$ was measured, resulting in an transport efficiency of 78(4) %. The transport settings were optimized on maximum measurable efficiency.
Additionally, the efficiency solely through the RFQ structure was investigated. The first measurement step (1) was performed as explained in the previous section leading to an ion current of $\approx 65(5)\,\text{pA}$. The measured ion current was lower than in the previously described measurement as the filament was colder this time. In the next step the -85 V battery box was connected to the extraction plate. An ion current of $\approx 65(5)\,\text{pA}$ was measured, resulting in a transport efficiency of 85 - 100 %. This indicates that the ions in the gas-jet are bend by the RFQ structure, enabling an efficient transport towards the detector.

4.10. Mimicking on-line cycle with ^{nat}Yb

To mimic the on-line measurement conditions a continuously heated ^{nat}Yb filament, operated under conditions that predominantly evaporated atoms (see Fig. 4.34 a), was installed at the gas cell entrance and a voltage of +350 V applied. The cage structure was operated with a DC gradient of -1.4 V/cm and the funnel structure with a DC gradient of -26.0 V/cm. A wired tantalum filament (see Fig. 4.34 b) was installed inside of the flow channel and a voltage of -120 V applied to efficiently guide the ions on the tantalum surface. Both the ^{nat}Yb filament and the wired filament were resistively heated individually. The transport settings are given in Table 4.8. By applying RIS using different configurations as shown in Fig. 4.35, information about the filament efficiency and temperature, as well as the background rate were gained. In the first step (a) both FES and SES were applied with a 10 kHz-repetition-rate behind the ^{nat}Yb filament in the gas cell with pulse energies of 25 nJ/pulse and 130 nJ/pulse, respectively. The excitation scheme shown in Fig. 4.12 was applied, whereas the autoionizing step at 53 839.28(1) cm^{-1} was used as the ionization step (see appendix Fig. A.3). The laser ions were guided towards the detector and counted. In this case, the filament was on

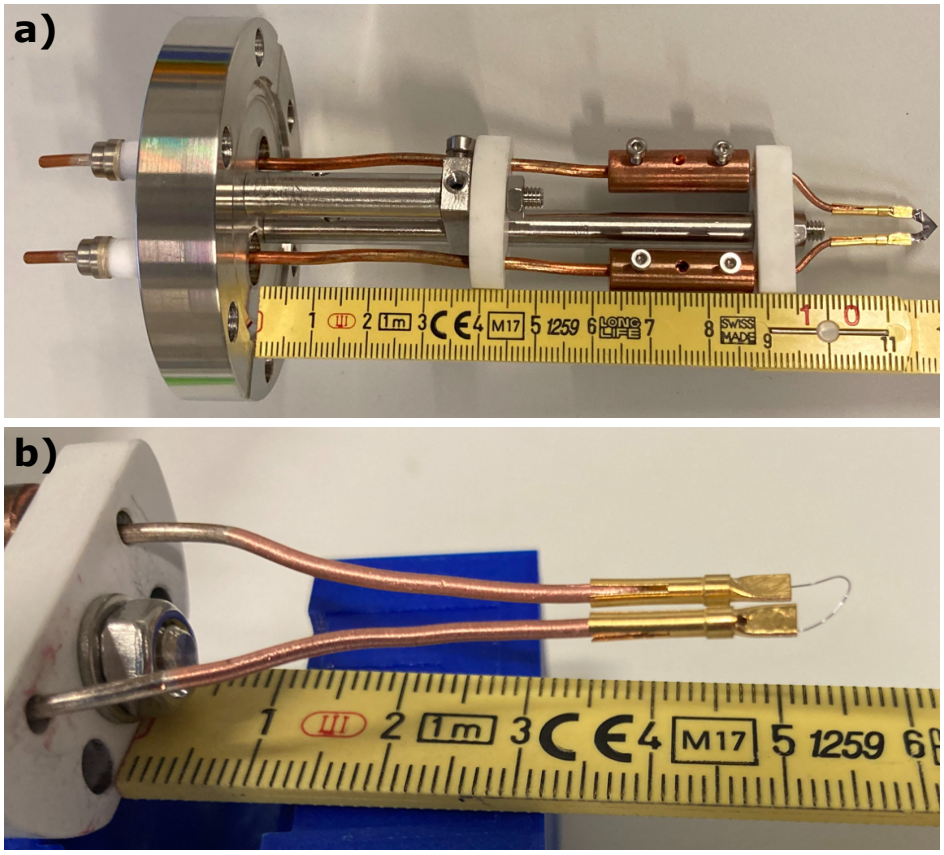

Figure 4.34.: Filaments needed to mimick an on-line cycle. a) ^{nat}Yb filament installed at the gas cell entrance. b) Wired tantalum filament installed inside of the flow channel.

Table 4.8.: Optimized transport parameters for mimicking the on-line cycle.

Electrode	Setting
^{nat}Yb filament	+350 V
cage 1	+232 V
cage 2	+226 V
cage 3	+222 V
cage 4	+218 V
cage 5	+214 V
cage 6	+210 V
funnel 1	+210 V
funnel 2	+150 V
funnel 3	+120 V
funnel 4	+80 V
funnel 5	+70 V
flow channel	0 V
tantalum filament	-120 V
entrance plate	-1.68 V
RFQ entry	-8.86 V
RFQ exit	-26 V
RFQ RF amplitude	400 V
RFQ RF	1.080 MHz
extraction plate	-25.9 V
transport electrode 1	-250 V
transport electrode 2	-1000 V
CEM	-2000 V

ground potential and not heated. A count rate of $\approx 160\,000$ counts/s was measured.
In the next step (b) the wired tantalum filament was heated and a potential of -120 V applied. The laser created ions in the gas cell were adsorbed on the tantalum surface, neutralized and desorbed as neutrals. RIS inside of the gas-jet was performed by propagating the FES in a perpendicular (elliptical beam shape of ≈ 50 mm horizontal and ≈ 5 mm vertical) and the SES (spherical beam shape of $3 \times 3\,\mathrm{mm}^2$) in an anticollinear configuration. The pulse energies used for the FES and SES were 40 - 45 nJ/pulse (400 - 450 µW, beam spot area: $A = \pi \cdot 0.005\,\mathrm{m} \cdot 0.05\,\mathrm{m} = 7.85 \cdot 10^{-4}\,\mathrm{m}^2$, $I = 0.51\,\mathrm{W/m}^2$) and 5 000 nJ/pulse (50 mW, beam spot area: $A = \pi \cdot (0.003\,\mathrm{m})^2 = 2.83 \cdot 10^{-5}\,\mathrm{m}^2$, $I = 1770\,\mathrm{W/m}^2$), respectively. The atoms were re-ionized in the jet and guided towards the detector, resulting in a count rate of $\approx 1\,100$ counts/s. This correlates to a loss factor of ≈ 150, which could have multiple reasons. First the laser powers could not saturate both transitions of ytterbium. The satura-

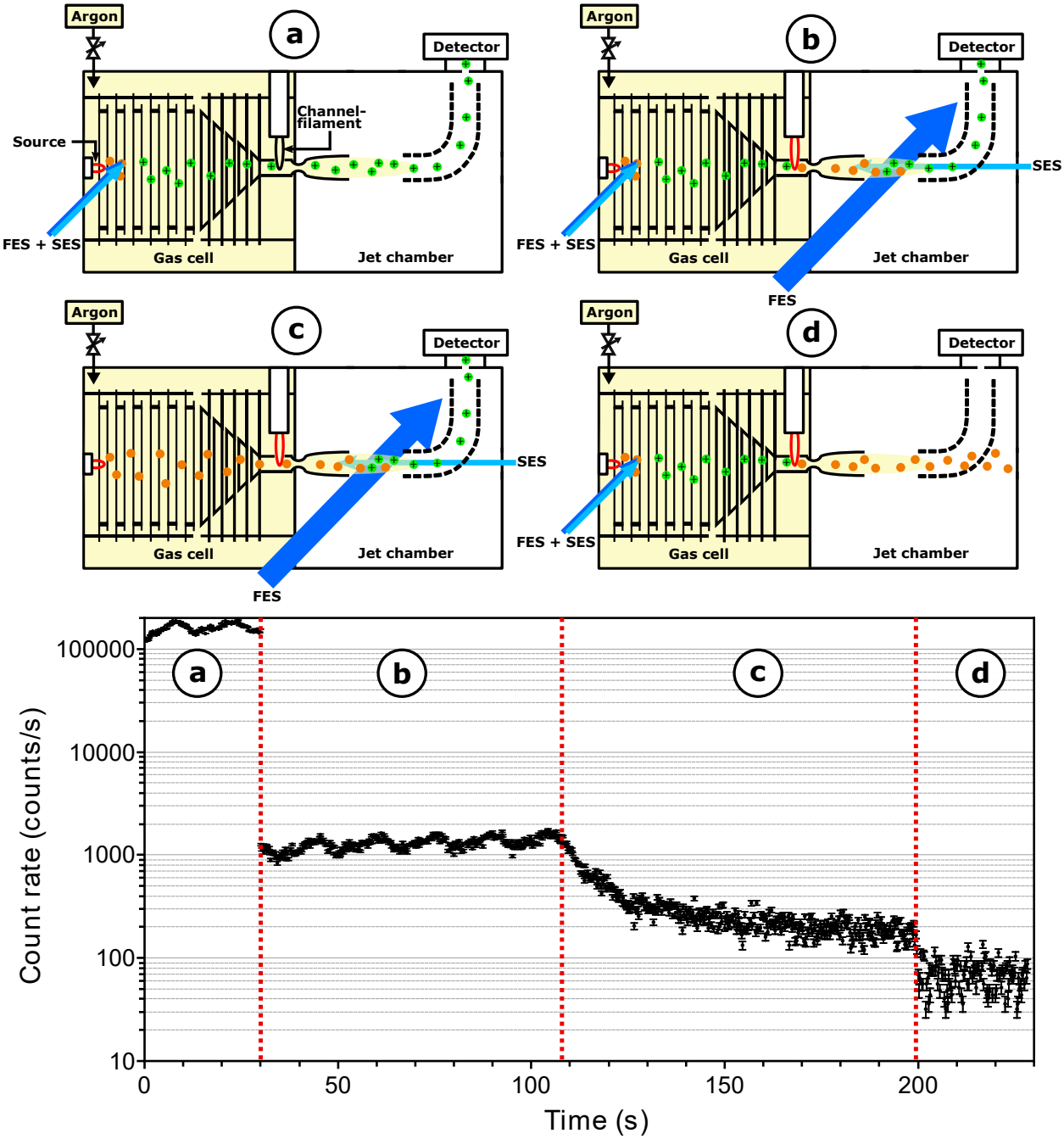

Figure 4.35.: Mimicking an on-line cycle by installing a ^{nat}Yb source at the gas cell entrance. Different measurements were performed to determine the filament efficiency (a and b), detected ^{nat}Yb count rate as a function of the filament temperature (c), and the background rate from, e.g., surface ionization or glow emission (d). The bottom graph shows the measured count rate for each of these different measurements. For more details see text.

tion intensity I_{sat} can be estimated using equation 2.54 [57]. For the FES with a wavelength of $\lambda = 398.91\,\text{nm}$ and a lifetime of the excited step of $\tau \approx 5\,\text{ns}$ a saturation intensity of $I_{\text{sat}} = 655\,\text{W/m}^2$ can be calculated. Thus, the laser intensity used in the measurement was about three orders of magnitude lower than the estimated saturation intensity. However, since eqn. 2.54 was obtained under conditions different from those in the experiment (see section 2.1.9), the calculated value should be treated with caution, but nevertheless gives a rough estimate. For the autoionizing step the lifetime can be calculated using equation 2.44 [51] with the lifetimes of the excited step τ_1 and the autoionizing step τ_2, and the FWHM being described by $\delta\nu$. Using the lifetime of $\tau_1 \approx 5\,\text{ns}$ and the FHWM of $\delta\nu = 24.0(3)\,\text{GHz}$ for the $53\,839.28(1)\,\text{cm}^{-1}$ level, the lifetime of the autoionizing step can be calculated as $\tau_2 = 6.6(1)\,\text{ps}$. Using equation 2.54 the saturation intensity of the ionizing step can be estimated using a wavelength of $\lambda = 347.57\,\text{nm}$, resulting in $I_{\text{sat}} = 751\,000\,\text{W/m}^2$, which is about two orders of magnitude higher than the laser intensity used in the measurement. Again, the calculated value should be treated with caution as the same argument as previously stated applies.

Another possible explanation could be that the filament temperature was too low to efficiently neutralize and desorb the ytterbium as no pyrometer was available to measure the filament temperature. In former measurements using the RADRIS technique a filament temperature of 1175 °C was sufficient to efficiently evaporate ^{155}Yb [201].

In the third measurement (c), the lasers ionizing in the gas cell were blocked. Thus, the atoms produced in the gas cell were only transported by the gas flow towards the nozzle. RIS inside of the jet was applied using the same laser powers as mentioned under (b). Looking at the evolution of the count rate over time, a rather long exponential decay was observed. This indicates that the tantalum filament temperature was either too cold and evaporation from the filament was slow, or too hot and the atoms were re-ionized and re-attracted to the tantalum filament. For a proper temperature choice, the count rate should directly drop to the value of $\approx 200\,\text{counts/s}$. The filament temperature was not varied during this measurement as further heating of the filament led to a large background rate from glow emission, which strongly exceeded the laser-related signal. The influence of the filament temperature has to be investigated in more detail in future measurements. The first new flow channel design (Fig. 4.21 a) was used in this measurement.

In (d) the measurement performed at (a) was repeated with the only difference being the tantalum filament heated and on a voltage of -120 V. The ions produced in the gas cell were guided towards the filament, where they were neutralized. A voltage of $\approx -13\,\text{V}$ applied to the filament was sufficient to attract all gas cell related ions to the filament as shown in Fig. 4.36. No re-ionization was performed in the jet. Nevertheless a count rate of $\approx 80\,\text{counts/s}$ was observed, which originated from glow emission (see section 4.7.1) between the flow channel (flow channel (a) in Fig. 4.21) and the hot filament. This is of no disadvantage for the on-line campaign as long as the reaction products are not neutralized by this effect. In order to reduce this glow emission, a new version of the channel was designed (flow channel (b) in Fig. 4.21), which is yet to be investigated.

The described measurements (a) - (d) were repeated using the $50\,991.77(2)\,\text{cm}^{-1}$ autoionizing step with a laser power of $\approx 600\,\text{nJ/pulse}$ (6 mW, beam spot area $A = \pi \cdot (0.003\,\text{m})^2 =$

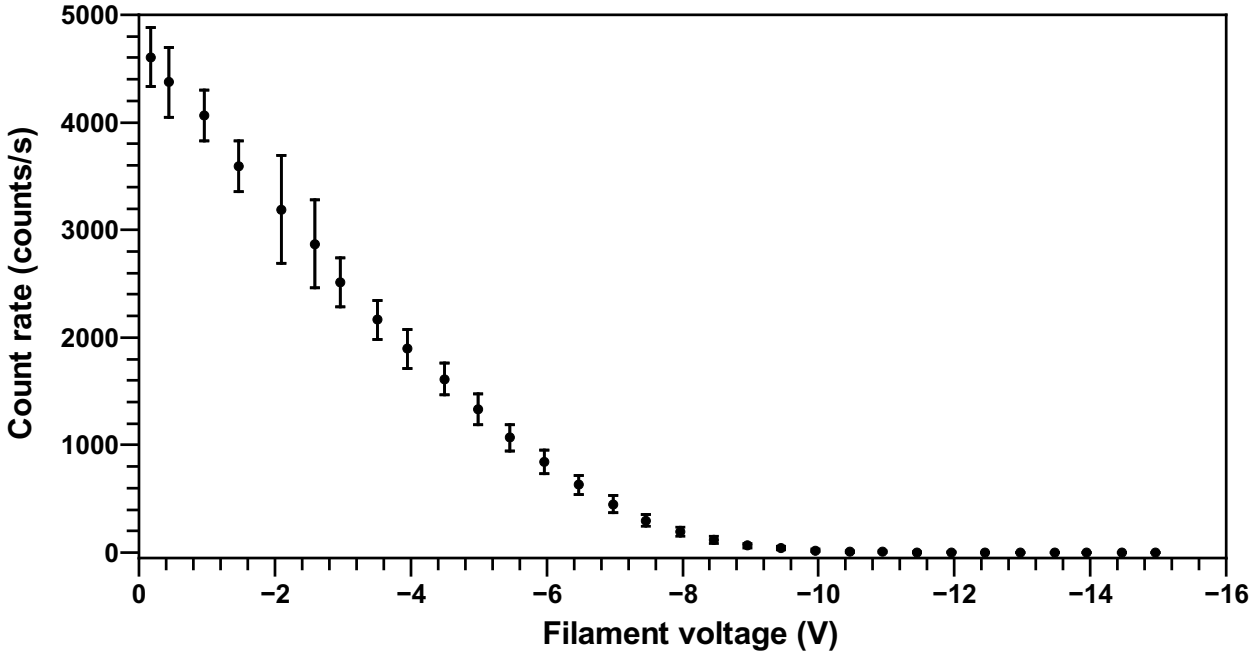

Figure 4.36.: Measured count rate dependent on the filament voltage. A voltage of $\approx -13\,\mathrm{V}$ is sufficient to fully attract and adsorb all gas cell related ions ($\leq 1\,\mathrm{count/s}$). The filament was not heated for this measurement.

$2.83 \cdot 10^{-5}\,\mathrm{m}^2$, $I = 212\,\mathrm{W/m}^2$) in the jet, whereas all other parameters remained the same. This measurement campaign resulted in a loss factor of ≈ 600, indicating that further improvements on the laser power will lead to a reduction of the loss factor of ≈ 150 received for the other AI state. The necessary saturation intensity can be calculated in the same manner as stated previously. First, the lifetime is calculated using equation 2.44. With a FWHM of $\delta\nu = 37(2)\,\mathrm{GHz}$ the lifetime is calculated as $\tau_2 = 4.3(2)\,\mathrm{ps}$. Using equation 2.54 the saturation intensity can be calculated with a wavelength of $\lambda = 385.76\,\mathrm{nm}$, resulting in $I_{\mathrm{sat}} = 843\,000\,\mathrm{W/m}^2$. The calculated saturation intensity is again three order of magnitudes larger than the laser intensity used in the experiment, but should be treated with caution as stated before. If other factors like, e.g., the filament temperature have an impact on this loss factor is still unknown and need to be further investigated.

4.11. Summary and Outlook

After a first phase of simulation and design the gas-jet apparatus was assembled, characterized and optimized in this work. The goal was to improve the setup so that a successful on-line measurement campaign on nobelium is achievable. Changes to the setup after a first unsuccessful on-line campaign in 2019 resulted in an improvement of the extraction efficiency and the spectral resolution. Further improvements and tests are planned prior to the next on-line campaign. One of these is a measurement campaign to determine the overall efficiency and ion extraction times using radioactive samples with known atom numbers in

the LARISSA laboratory, making use of Ti:Sa lasers to saturate the transitions of the investigated samples. It is also planned to use non-resonant ionization in order to characterize the setup in a configuration similar to the configuration, which will be used in the nobelium on-line campaign. These measurements will determine if the setup is ready for the planned on-line measurements or if further design improvements and simulations are necessary.

Part II.

Resonance ionization spectroscopy on ^{253,254,255}Es

5. Einsteinium

In the following sections, an overview over the known properties of ^{253,254,255}Es and their production scheme is given before introducing the Resonance Ionization Spectroscopy in Collinear geometry (RISIKO) mass separator technique and the laser system, which was used to perform the measurements in this work. Subsequently, an insight into new findings of the atomic structure and nuclear structure of ^{253,254,255}Es is presented.

5.1. Known properties of ^{253,254,255}Es

Einsteinium and fermium were discovered in 1952 within the material of a nuclear explosion test [202]. Shortly after its discovery, einsteinium was produced artificially by nuclear fusion reactions of nitrogen with uranium and by neutron irradiation of plutonium in a reactor, leading to the extraction of first information about the half life and the radioactive decay properties of ^{253,254}Es [203, 204, 205, 206, 207].
In high-flux research reactors like the High Flux Isotope Reactor (HFIR) (see Fig. 5.2) only the einsteinium isotopes ^{253,254,255}Es are available in weighable quantities from breeding processes. Therefore, atomic and nuclear information on the isotopes of einsteinium are scarce in literature.
^{253}Es ($T_{1/2} = 20.47\,\mathrm{d}$) was investigated in 1968 - 1974 with optical spectroscopy using samples with total amounts of up to 100 µg in discharge lamps [208] as well as Fourier-transform spectrographs [32, 209, 210]. These emission spectra studies yielded atomic transitions and hyperfine structure (HFS) splittings, enabling the assignment of the nuclear spin to $I(^{253}\mathrm{Es}) = 7/2^+$. Here, the unpaired proton configuration is assigned to $\pi_{7/2}[633]$ [116]. 290 emission lines were observed in the emission spectra, which were assigned to 15 atomic transitions between neutral einsteinium (Es I) levels and 23 atomic transitions to the two known lowest levels of the einsteinium ion (Es II). The first excited atomic state of the ion ($5f^{11}7s\ ^3I^0$) was observed at an energy of $938.66\,\mathrm{cm}^{-1}$ [32]. Furthermore, hyperfine structure constants A and B were derived by an analysis of the hyperfine structure of assigned Es II lines for ^{253}Es. From these constants, a nuclear magnetic dipole moment of $\mu_I(^{253}\mathrm{Es}) = 3.6(4)\mu_\mathrm{N}$ and a quadrupole moment of $Q_s(^{253}\mathrm{Es}) = 6.0(8)\,e\mathrm{b}$ were derived [32]. More recently, the emission spectra data were re-analyzed resulting in newly determined energy levels and some changes in the former level assignments [31, 33]. Due to unobserved lines in the infrared region and the unavailability of larger quantities of einsteinium, only slow progress was achieved in regard to atomic structure and nuclear structure information about einsteinium [31, 33]. Nevertheless, a following and more accurate measurement of the ground-state HFS in ^{253}Es via atomic-beam magnetic-resonance (ABMR) in 1975 on sample sizes of a few µg each enabled the determination of the ground-state total angular momentum $J = 15/2$ and the hyperfine structure constants $A = 817.153(7)\,\mathrm{MHz}$ and $B = -4316.254(76)\,\mathrm{MHz}$. The more precise magnetic diple moment of $\mu_I = 4.10(7)\mu_\mathrm{N}$ and the spectroscopic electric quadrupole moment of $Q_s = 6.7(8)\,e\mathrm{b}$ were derived from these constants [34]. The ABMR technique

is based on the observation of transitions between magnetic substates in the Zeeman structure, originating from the hyperfine levels of an atom in an external magnetic field due to the Zeeman splitting. Measurements of the resonance frequencies under different external field settings permits the calculation of the nuclear spin and the hyperfine structure constants [211].
Despite its long lifetime, ^{254}Es ($T_{1/2}$ = 275.7 d) was investigated almost three decades later in 1998 using the resonance ionization mass spectroscopy (RIMS) technique with a three-step scheme as shown in Fig. 5.1. In this experiment, a previously unknown highly-excited Es I level (32 924.9 cm^{1}) was populated by two-step RIS. The ionization step was scanned across the ionization threshold in the presence of an applied electric field, with the electric field strength being varied between 25 - 270 V/cm. A sudden onset of the ion signal indicated the ionization threshold, resulting in a determination of the ionization potential (IP) to a value of E_{IP} = 51 358(5) cm^{-1} (6.3676(5) eV) [35, 212]. Furthermore, a hyperfine structure splitting in the 5f^{11}7s^2 → 5f^{11}7s7p transition (17 803 cm^{-1}) was recorded, although with low spectral resolution and statistics. Nevertheless, the hyperfine structure parameters A and B were extracted for the ground state (A_{gs} = 334(7) MHz, B_{gs} = −2 830(900) MHz) and excited state (A_{exc} = 839(7) MHz, B_{exc} = 1 250(940) MHz), with the ratio of the A-factors of 2.51 being in agreement with the ratio extracted in the isotope ^{253}Es. The release of einsteinium as neutral atoms was achieved in this measurement by using a tantalum filament. Einsteinium was electrodeposited onto the tantalum surface and afterwards a ≈ 1 µm titanium metal layer sputtered on top. The evaporation temperature of einsteinium was found to be as low as ≈ 630 − 650 °C [35, 212]. One filament contained ≈ 10^{12} atoms of ^{254}Es (≈ 420 pg), thus only a minor fraction of material was required compared to the former measurements.
In 2009, the angular distributions of α-particles from oriented ^{253,254}Es nuclei were investi-

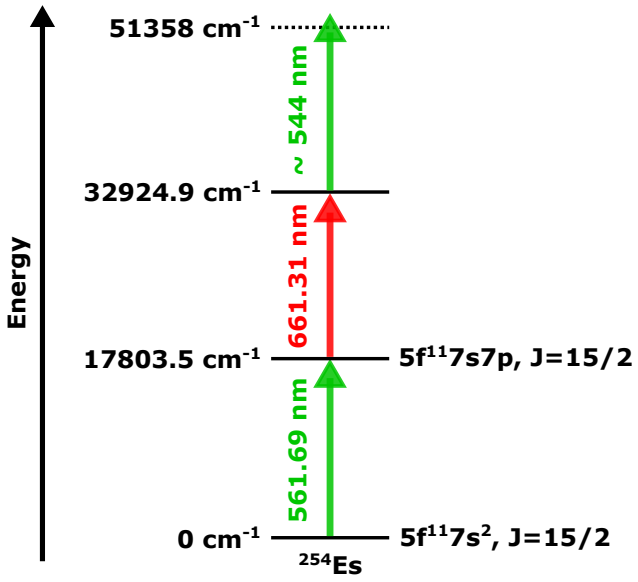

Figure 5.1.: Three-step RIS scheme used during the first laser spectroscopic studies in 1998. Figure adapted from [35, 212].

Table 5.1.: Energy levels of Es I (in cm^{-1}) and hyperfine structure constants A and B (in MHz). Uncertain assignments are given in parantheses.

E	J	Configuration	A	B	Ref.
0.00	15/2	$5f^{11}7s^2$	817.153(7)	-4 316.254(76)	[33, 34, 36]
7 894.54	9/2	$5f^{11}7s^2$			[31, 36]
8 759.24	11/2	$5f^{11}7s^2$	872.70	119.92	[33, 36]
10 224.29	(13/2, 17/2)	$5f^{11}7s^2$			[31, 36]
17 802.87	15/2	$5f^{11}7s7p$	2 047.88		[33]
19 209.02	17/2	$5f^{11}7s7p$	2 814.15	-6 145.75	[33]
19 367.92	15/2	$5f^{11}7s7p$	-125.91	180	[33]
19 788.22	13/2	$5f^{11}7s7p$	-1 284.61	-4 497	[33]
20 162.56	15/2	$5f^{10}6d7s^2$	844.22	-1 559	[33]
20 817.85	13/2	$5f^{10}6d7s^2$	(971.3)		[33]
20 871.30	17/2	$5f^{10}6d7s^2$	822.63		[33]
23 333.05	19/2	$5f^{11}7s7p$	2 654.66	0	[33]
23 934.19	17/2	$5f^{11}7s7p$	(2 284.4)		[33]
24 338.29	15/2	$5f^{11}7s7p$	(1 531.9)		[33]
24 390.58	11/2	$5f^{11}7s7p$	(-1 927.7)		[33]
24 489.42	13/2	$5f^{11}7s7p$	(98.9)		[33]
28 118.58	13/2	$5f^{11}7s7p$	1 331.1	2 638.2	[33]
28 372.78	(13/2, 15/2, 17/2)	$5f^{10}6d7s^2$			[31, 32, 36]
28 447.02	13/2	$5f^{11}7s7p$	2 784.23	-5 138.44	[31, 32, 36]
28 578.71	17/2	$5f^{11}7s7p$	-132.51	-1 949	[33]
28 689.74	(15/2, 17/2)	$5f^{10}6d7s^2$			[31, 32, 36]
29 159.28	15/2	$5f^{11}7s7p$	(557.6)		[33]
29 204.89	13/2	$5f^{11}7s7p$	1 911.54	-2 287.42	[31, 32, 36]
31 829.03	11/2		2 885.0	608.6	[31, 36]
31 886.30	13/2	$5f^{10}6d7s^2$			[31, 32, 36]
32 770.06	13/2		2 736.27	1 717.8	[31, 36]
32 924.9					[35]
33 829.35	17/2	$5f^{11}7s8s$			[31, 36]
34 068.94	15/2	$5f^{11}7s8s$			[31, 36]
34 192.60	9/2				[31, 36]
35 507.74	13/2				[31, 36]
37 485.58	15/2	$5f^{10}6d7s7p$	2 068.57		[33]
38 634.04	11/2				[31, 36]

E	J	Configuration	A	B	Ref.
40 478.25	13/2	$5f^{11}7s7d$	3 999.53		[33]
40 536.93	15/2	$5f^{11}7s7d$	3 510.87		[33]
40 704.55	19/2	$5f^{11}7s7d$	2 912.78		[33]
40 744.46	17/2	$5f^{11}7s7d$	3 188.29		[33]
40 862.81	21/2	$5f^{11}7s7d$	(2 671.2)		[33]
40 977.22	19/2	$5f^{11}7s7d$	2 895.10		[33]
41 101.95	17/2	$5f^{11}7s7d$	3 116.04		[33]
41 602.40	17/2	$5f^{11}7s7d$	-1 493.57		[33]
41 682.02	15/2	$5f^{11}7s7d$	(-1 445.0)		[33]
41 819.18	19/2	$5f^{11}7s7d$	-1 337.1		[33]
41 907.59	17/2	$5f^{11}7s7d$	-1 514.85		[33]
41 910.78	15/2	$5f^{11}7s7d$	-590.6		[33]

gated to extract information about the hyperfine interaction in an iron host lattice [37, 39]. The ^{253,254}Es activity was loaded into an oven of a positive surface ionization ion source, mass separated and implanted into a high-purity annealed 100 µm iron foil, with the total number of $\approx 10^8$ ions implemented. The sample was afterwards further prepared for the nuclear orientation experiments [37]. Here, information on the magnetic moment and the hyperfine magnetic field for einsteinium in an iron foil were determined from the emission anisotropies of α-particles from oriented ^{253,254}Es. With the assumption of a nuclear spin of $I = 7$, taken from a tentative assignment from decay spectroscopy [213], a nuclear magnetic dipole moment of $|\mu_I(^{254}\text{Es})| = 4.35(41)\mu_\text{N}$ was derived [37, 38, 39] and compared to theoretical calculations using a single-particle model [214]. Assuming a $\pi_{7/2}[633]\nu_{7/2}[613]$ ground-state configuration, a magnetic dipole moment of $\mu_I(^{254}\text{Es}) = 3.52\mu_\text{N}$ can be calculated, whereas the assumption of a $\nu_{7/2}[624]$ neutron ground state configuration (see Fig. 2.7) results in a magnetic dipole moment of $\mu_I(^{254}\text{Es}) = 4.57\mu_\text{N}$. Both calculated values are in fair agreement with the extracted experimental value for the magnetic moment, thus supporting the reliability of the extracted hyperfine field for einsteinium in iron [37, 39]. The tentative spin assignment for ^{254}Es of $I(^{254}\text{Es}) = (7)$ results from a coupling of the $\pi_{7/2}[633]$ proton configuration and the $\nu_{7/2}[613]$ neutron configuration to maximum spin. The $\pi_{7/2}[633]$ proton configuration is known to be the ground-state configuration in the neighboring isotope ^{253}Es and the assumed and calculated configuration for ^{255}Es. The $\nu_{7/2}[613]$ neutron configuration is known to be the ground-state configuration of the isotone ^{255}Fm [116, 215, 216]. Additionally, this spin assignment to $I(^{254}\text{Es}) = (7)$ is consistent with observed electron capture (EC) and low β^--decay branches to ^{254}Cf and ^{254}Fm, respectively [38]. The isomer $^{254\text{m}}$Es ($T_{1/2} = 39\,\text{h}$) was investigated additionally in the ABMR measurements, leading to a spin assignment of $I = 2$ [34].

The nuclear spin of ^{255}Es with one unpaired proton is only tentatively assigned in literature to $I(^{255}\text{Es}) = (7/2)$ [215]. The spin was assumed based on a systematic trend along the isotopes of einsteinium as well as Nilsson-model calculations giving a $\pi_{7/2}[633]$ ground-state

proton configuration [117]. Additionally, the α-decay scheme to ^{251}Bk does not conflict with that assignment [217]. However, the $\pi_{3/2}[521]$ proton configuration is predicted by theoretical calculations to be energetically higher but still close-lying to the $\pi_{7/2}[633]$ orbital as shown in Fig. 2.6 [117, 118]. A ground-state spin of 3/2 is indeed assigned to ^{251}Es in contrast to the theoretical 7/2 prediction [117, 218].
For neutral einsteinium, the atomic structure with only 45 reported atomic levels in the literature remained only rudimentary known [31, 32, 33, 34, 35, 36], with table 5.1 summarizing the reported atomic levels. Nonetheless, a prerequisite for laser spectroscopy studies of all elements is the knowledge of suitable atomic transitions. The available information in einsteinium about the atomic level energies, the ionization potential, nuclear spins, and hyperfine structure splittings, helped to find suitable atomic transitions for the measurements on ^{253,254,255}Es performed in this work. Additionally, the highly-precise known ground-state hyperfine structure parameters A and B of ^{253}Es from the ABMR measurements enabled a more precise extraction of the electromagnetic moments.

5.2. Production of transcurium elements

A sample containing the isotopes ^{253,254,255}Es, with neutron numbers beyond the deformed shell closure at $N = 152$ close to the line of β-stability, was produced at Oak Ridge National

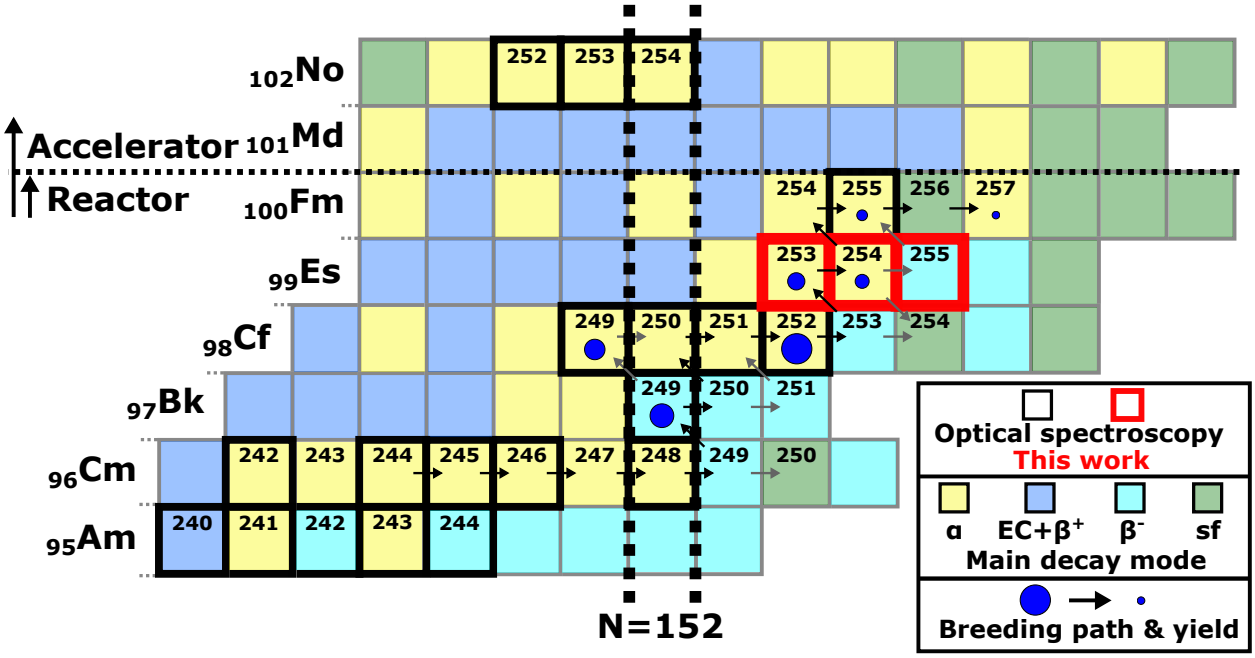

Figure 5.2.: Excerpt of the chart of nuclides. Indicated are nuclides investigated by optical spectroscopy [3, 46] and the breeding path (black and grey arrows) for Es and Fm starting from a mixed Cm target as given in [4, 5, 219]. The main decay mode is indicated by the different colors. The size of the blue circles indicate the final breeding yield if known.

Laboratory (ORNL) in the HFIR [5]. Four targets each containing about 6.3 g of mixed isotopes $^{244\text{-}248}$Cm were irradiated by thermal neutrons, initiating nuclear transmutation in a series of neutron captures ensued by β^- decays [220]. The targets were allowed to cool for 90 days after irradiation, eliminating short-lived fission and activation products, especially iodine-131. Afterwards the targets were dissolved and chemically separated into fractions containing individual elements in the hot cells at the Radiochemical Engineering Development Center [4]. A sample containing ≈ 2 ng ^{253}Es, ≈ 4 ng ^{254}Es, and ≈ 4 pg ^{255}Es was dried and afterwards shipped to the Nuclear Chemistry division at Johannes Gutenberg University (JGU) Mainz. Here, the sample was further processed, before being investigated using the RISIKO mass separator technique (see section 5.3).
Fig. 5.2 shows the breeding path in the HFIR at ORNL as black and grey arrows, whereby the black arrows mark the main breeding path. The line of β-stability is visible by the color scheme used for the different main decay modes, and the known final breeding yield are indicated by different sizes of blue circles. ^{257}Fm is the heaviest element, which can be bred in an high-flux reactor, as none of the fermium isotopes $^{254\text{-}257}$Fm, which can be produced via breeding, undergo a β^- decay. Thus, heavier elements than fermium ($Z > 100$) need to be produced at accelerator facilities in fusion-evaporation reactions (see section 3.1). Besides the breeding pathways, nuclides investigated by optical spectroscopy are indicated by black boxes [3, 46] in Fig. 5.2, adding the isotopes $^{253\text{-}255}$Es in this work (red boxes).

5.3. RISIKO

The Resonance Ionization Spectroscopy in Collinear geometry (RISIKO) mass separator is located in the Laser Resonance Ionization Spectroscopy for Selective Applications (LARISSA) laboratory at Johannes Gutenberg-University in Mainz. It makes use of the resonance ionization mass spectrometry (RIMS) technique, where resonance ionization spectroscopy applied inside of a hot-cavity (denoted as atomizer) is coupled to a magnetic mass separator enabling element and isotope selective measurements. Although it is very similar to the radioactive ion beam (RIB) facility Isotope Separation On-Line Device (ISOLDE) at European Organization for Nuclear Research (french: Conseil européen pour la recherche nucléaire, CERN), it is only used as an off-line device by externally inserting samples. Nevertheless the RISIKO setup has an operation permission for a variety of long-lived radionuclides, e.g., $^{253\text{-}255}$Es.
Originally the RISIKO mass separator was designed for trace analysis of strontium radioisotopes in environmental samples by K. Zimmer [148] as a reaction to the Chernobyl nuclear power plant incident in 1986. Some modular parts of RISIKO can be exchanged, enabling different applications. As of today, the main applications are isotope separation and ion beam implantation into collector foils, calorimetric detectors [221, 222, 223], and laser resonance ionization spectroscopy of stable and long-lived isotopes [224].
The combined vacuum chambers have a total length of around 7 m with pressures in the range of 10^{-7} to 10^{-8} mbar. Fig. 5.3 shows a schematic overview over the RISIKO mass separator configuration used for laser spectroscopy measurements, which can be divided into four main parts. These four parts contain the ion source (atomizer combined with RIS), extraction and shaping of the ion beam, mass separation using a dipole magnet combined

with a slit in the focal plane, and ion detection. Each of these parts will now shortly be explained in the following, whereas further information can be found in [148, 225].
The atomizer (Fig. 5.3 colored red) is a tubular oven (inner diameter: 2.5 mm, wall thickness: 1 mm, length: 35 mm), which is mounted between a water-cooled multi-layer spring and a water-cooled panel, both made out of tantalum. In this work, a sample containing ≈ 2 ng ^{253}Es, ≈ 4 ng ^{254}Es and ≈ 4 pg ^{255}Es was dissolved in 0.1 M nitric acid (HNO_3) and aliquots of 3 µL containing about 10^{10} atoms of ^{254}Es (≈ 4 pg ^{254}Es) each were placed on a zirconium (Zr) foil. Thus, each sample contained $\approx 10^7$ atoms ^{255}Es. The zirconium foil acts as a reducing agent to ensure the release of neutral atoms during evaporation within the atomizer, as the dried sample is usually oxidized [226, 227]. The foil was folded to fully enclose the $^{253\text{-}255}$Es sample and placed in the atomizer. Resistive heating produced an atomic einsteinium vapor, which was then probed using two-step RIS by the incident laser beams. In order to obtain low background rates in the order of at most a few counts per second from surface ionization and remaining activity on the detector, the atomizer was preconditioned at about 2000 K for several hours before inserting the einsteinium sample. Einsteinium atoms were released from the zirconium foil at temperatures of ≥ 700°C, which is slightly higher than the temperatures of $630 - 650$ °C reported in [35, 212].
The ions are extracted and accelerated to a 30 keV ion beam in the next step. The ion optics (Fig. 5.3 colored orange) consists of an extraction electrode, an einzel lens, a pair of horizontal and vertical deflectors, and three quadrupole lenses. First, the extraction electrode, which is located in 40 mm distance from the atomizer, acts with typically +20 kV as a first acceleration stage and counteracts beam expansion due to the conical shape at the tip. After 400 mm flight distance, the ion beam reaches the grounded first electrode of the einzel lens with an energy of 30 keV. The einzel lens consists of three cylindrical electrodes.

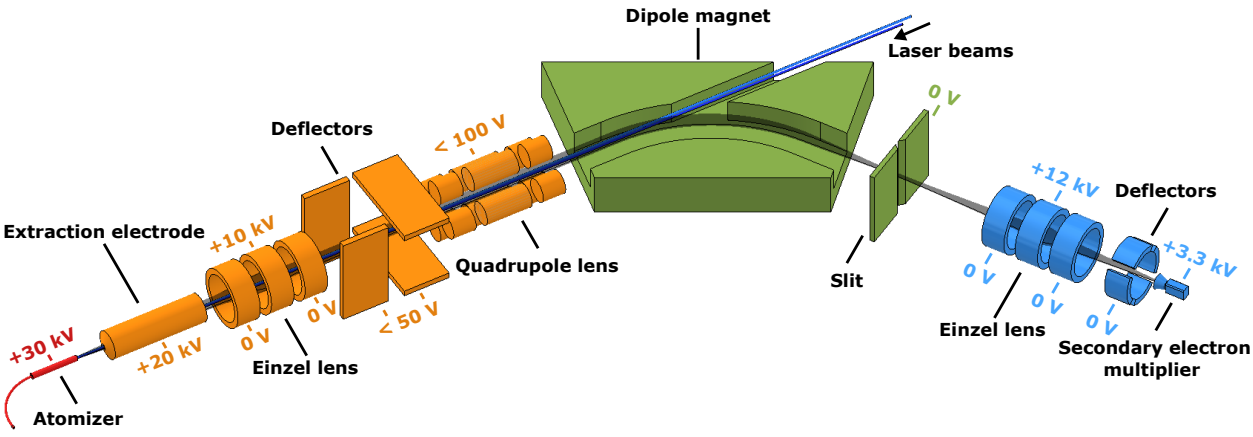

Figure 5.3.: Schematic overview of the RISIKO mass separator setup. From left to right the ion source (red), extraction and shaping of the ion beam (orange), mass separation (green), and ion detection (blue) are shown. The scale for each part was adapted for better visualization. Typical voltages are indicated by the different colored numbers. For details see text. The figure was adapted from [221].

The outer electrodes are on ground potential, while the middle electrode is on +10 kV. The ion beam can be focused in order to adjust beam size and divergence without changing the beam energy by making use of deceleration followed by acceleration. Minor corrections of the ion beam direction can be performed using the two pairs of deflector plates, each plate being 140 mm long and in 50 mm distance from the ion beam. In the last stage, three quadrupole lens are used to compensate for an astigmatism in the ion beam. After all these beam shaping, the ion beam should be well collimated in both axes.
After the ion extraction and beam shaping, the ions are guided towards a dipole magnet selecting them according to their mass-to-charge ratio. This is achieved by ions (charged particles) being circular deflected when traveling in a magnetic field B at a given velocity. By tuning the magnetic field, the mass of interest can be transmitted through the slit, which is placed at the focal plane of the magnet. The mass-resolving power of the RISIKO dipole magnet is $R = m/\Delta m \approx 1000$ [40].
Ions passing the separator slit aperture can be detected using a secondary electron multiplier (SEM, MasCom MC-217). In order to guide the respective ions towards the SEM, the diverging ion beam passes an einzel lens. This einzel lens focus the ion beam, which can be steered by the following set of deflectors in order to shape the ion beam for SEM detection.

5.4. Laser systems @ RISIKO

The laser system at the LARISSA laboratory, which was used for the measurements in einsteinium, will be described shortly. The specifications were taken out of [225, 228, 229, 230, 231, 232, 233], which I refer to for more insight on the laser system.
RIS inside a hot cavity using high-power Ti:sapphire (Ti:Sa) lasers is a method ensuring

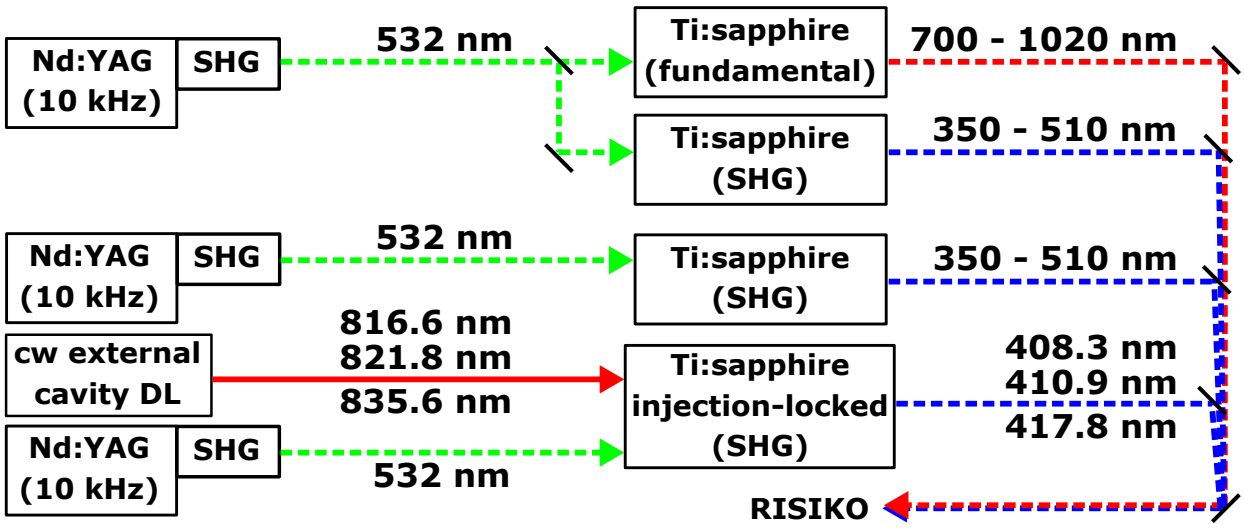

Figure 5.4.: Schematic overview over the 10 kHz-repetition-rate solid state laser system used for the einsteinium measurements. The solid and dashed lines indicate cw laser light and pulsed laser light, respectively. For more information see text.

high overall efficiency in combination with high sensitivity [1, 40]. The laser system is schematically shown in Fig. 5.4 and consisted of three Ti:Sa lasers, which were developed in 2003 by R. Horn [234] and further refined in the following years. These Ti:Sa lasers were pumped each with up to 18 W by two frequency-doubled Nd:YAG lasers (Photonics DM100-532: pulse width $\approx$ 130 ns, Photonics DM60-532: pulse width $\approx$ 190 ns) with a repetition rate of 10 kHz. The pulse width of these standard Ti:Sa lasers are between 40 ns and 60 ns with an average output power of 3 - 5 W. These lasers can be operated in a wavelength range of 700 - 1020 nm (fundamental) with spectral bandwidths of 1 - 10 GHz. Two of the three Ti:Sa lasers were equipped with a grating as the frequency-selective element and in addition featured internal SHG. Additionally, an etalon was equipped to reduce the bandwidth to 2 - 3 GHz for hyperfine spectroscopy (multi-mode spectroscopy, mms). Compared to the standard Ti:Sa operation, the grating-tuned lasers have a reduced average power of 1 - 2 W. The internal SHG process has a $\approx$ 50% conversion efficiency in comparison to the non-internal SHG process with 10 - 20 %. The third laser was an injection-locked Ti:Sa laser, which was seeded by a cw external cavity diode laser and equipped with an external single pass SHG. This laser features a bandwidth of 20 MHz, although being limited in the accessible wavelength range to those available by the cw master laser, and was therefore only used for selected transitions (single-mode spectroscopy, sms). The average output power reachable with this injection-seeded Ti:Sa laser is about 3 - 5 W.
The laser pulse length, used for the einsteinium measurements, was about 40 ns with an reduced average output power of 20 - 600 mW. The output power was optimized to a specific power for each transition in order to prevent power broadening of the spectral resolution. External triggering of the pump lasers using a pulse generator was used to synchronize the laser pulses for highest spectral resolution without diminishing the total efficiency [235]. The ions were recorded in dependence of the wavelength of the first excitation step, which was measured using commercial wavelength meters (High Finesse WS7-30 for mms, WSU-30 for sms), both with an absolute accuracy of 30 MHz ($3\,\sigma$).

5.5. Einsteinium measuremets @ RISIKO

For all measurements performed in this work, einsteinium atoms were released from the zirconium foil in a temperature range of 700 - 1300 °C. The temperature of the hot cavity was monitored during the measurements with a pyrometer. Here, a first signal of einsteinium was observed at $\approx$ 700 °C, slightly higher compared to temperatures of $630 - 650$ °C reported in [35, 212]. The experiments were conducted at higher temperatures than $\approx$ 700 °C in order to increase the atomic rate, which corresponds to a higher signal and thus a more precise measurement. The temperatures used during the HFS measurements are shown in Table 5.2.
The sample composition was initially analyzed by α spectroscopy in ORNL, which yielded a composition of 5.10 ng ^{249}Cf, 2.29 ng ^{253}Es, 4.02 ng ^{254}Es, and $1.38 \cdot 10^{-3}$ ng ^{257}Fm. Thus, the analysis indicated the absence of ^{255}Es in the sample. The sample was additionally investigated using the RISIKO mass separator. Here, the atomizer was heated, producing a vapor of the elements in the sample. A two-step-laser-ionization scheme was used to

Table 5.2.: Evaporation temperatures during the single-mode spectroscopy (sms) and multi-mode spectroscopy (mms) HFS measurements. For further details on the level schemes see Fig. 5.10.

E_{exp} (cm^{-1})	Isotope	Temperature (°C)
23 934.20(5) sms	254	≈ 1 050
23 934.20(5) mms	254	≈ 1 200
24 338.23(5) sms	254	≈ 1 050
24 489.12(5) sms	254	≈ 1 050
27 440.06(5) mms	254	≈ 1 250
28 447.03(5) mms	253	≈ 1 100
28 446.86(5) mms	254	≈ 1 100
28 446.66(5) mms	255	≈ 1 200

produce an ion beam for study. The laser wavelengths were tuned for a single element, e.g. einsteinium, as indicated in the caption of Fig. 5.5, recording the signal for each isotope using different settings of the dipole magnet. Here, the wavelength for each element was not adjusted to account for the isotope shifts due to the use of broadband lasers (no etalon) with spectral bandwidths of several GHz (see section 5.4). Afterwards, the laser frequencies were

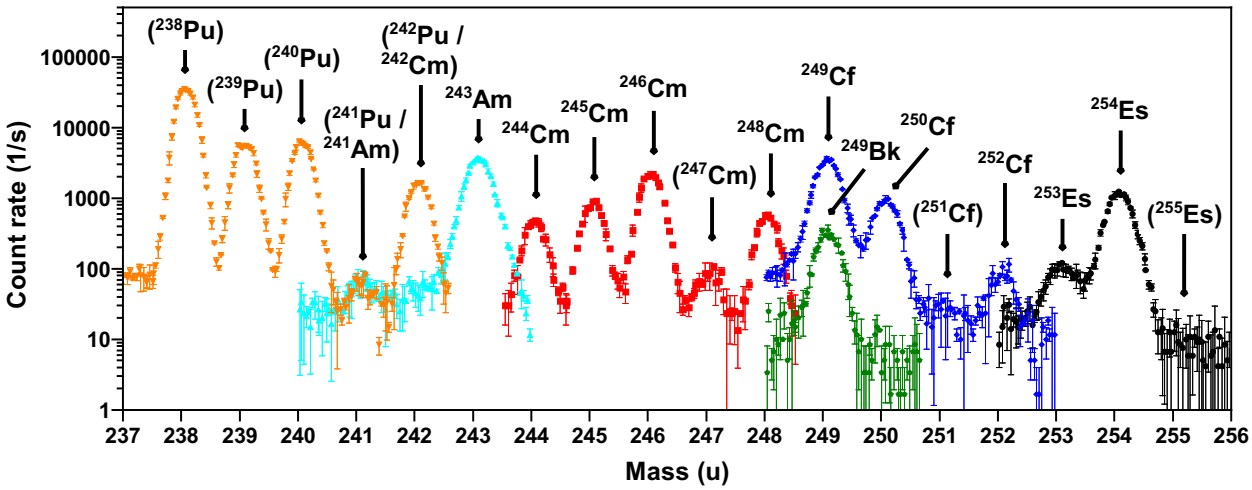

Figure 5.5.: Analysis of the sample composition by performing RIS for different elements as indicated by the colors. Isotopes of plutonium (Pu, FES: 352.58 nm), americium (Am, FES: 351.11 nm, SES: 418.03 nm), curium (Cm, FES: 352.34 nm), berkelium (Bk), californium (Cf, FES: 354.20 nm), and einsteinium (Es, FES: 364.43 nm, SES: 418.03 nm) were identified. Some wavelengths are missing as they were neither noted in the lab book nor written in the measurement file. Unclear assignments are marked with brackets. The measurement time was 1 hour.

changed to another element and the process repeated again. The recorded mass spectrum for each individual element is shown in Fig. 5.5. Fermium was not investigated during this mass scan. This method to analyze the sample composition was more sensitive compared with α spectroscopy, revealing many long-lived nuclei created during the breeding process as, e.g., ^{249}Bk and ^{253,254}Es. The assignment of the peaks to the isotopes and elements was not always unambiguous as indicated by the brackets. This is either related to a low count rate, e.g. for ^{251}Cf and ^{255}Es, or the use of laser excitation schemes exciting multiple elements, e.g. the seeming excitation of plutonium isotopes using a detuned curium excitation scheme (orange data points). This cross-talk in the ionization schemes complicated a conclusive assignment. In addition, the peak observed at $m = 238$ u could also originate from ^{238}U (uranium).

5.6. Atomic structure investigations on ^{254}Es

This section gives a brief overview over the atomic structure investigations on ^{254}Es, which are relevant for the following nuclear structure investigations (see section 5.7). The presented figures and tables were provided in courtesy by [redacted], who analyzed the atomic structure data. A more thorough and complete description of the atomic structure investigations can be found in the PhD thesis of [redacted] and in reference [236].
First, the excitation laser ($\approx 50 - 300$ mW) was scanned in the region of 22 800 - 26 800 cm^{-1} (SES: 350 nm, 300 mW) and 26 250 - 28 600 cm^{-1} (SES: 400 nm, 300 mW) to search for ground-state transitions as shown in Fig. 5.6. Here, the laser spectroscopy studies were limited to excited states with total angular momenta $J_{exc} = 13/2, 15/2$ or $17/2$ due to the ground

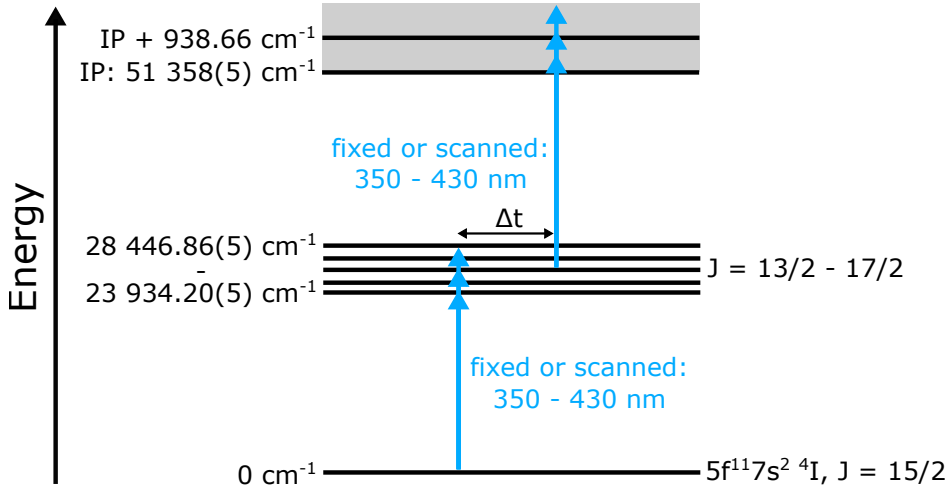

Figure 5.6.: Overview over the two-step RIS schemes used for ^{254}Es with experimental level energies, total angular momentum J assignments, and level configuration for the ground state. The values for the electron configurations, the IP and the first excited state in Es II are taken from [31, 32, 33, 212]. Figure adapted from [236] in courtesy of [redacted].

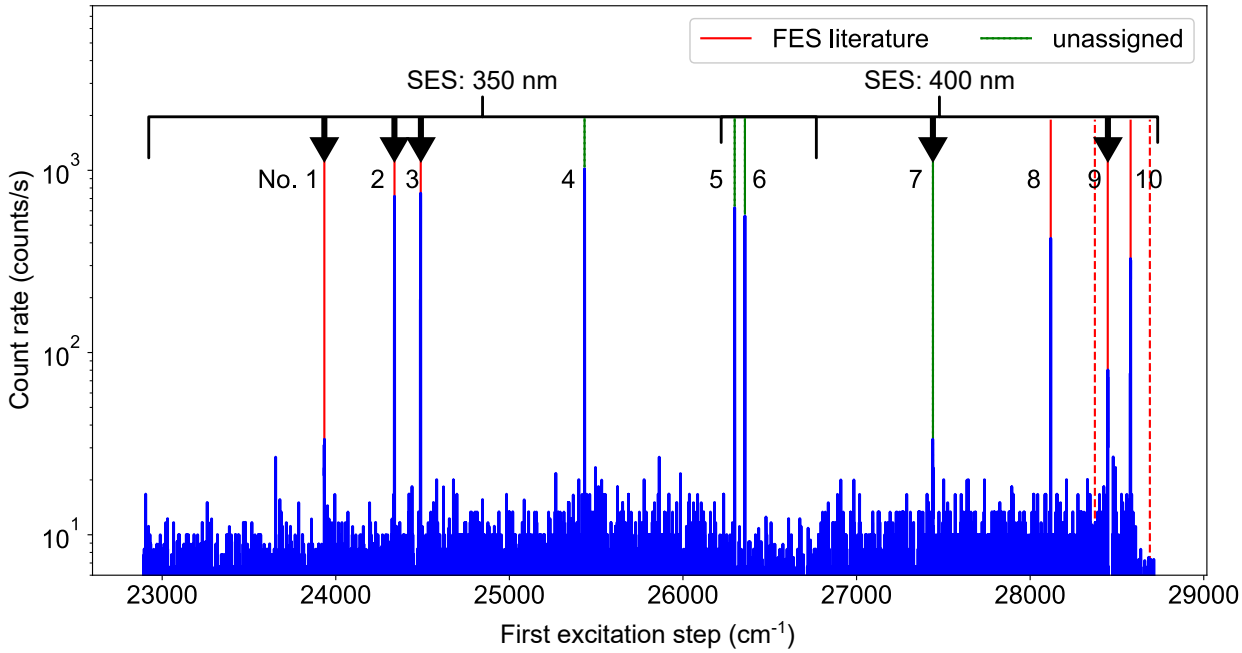

Figure 5.7.: Scan of the first excitation step in einsteinium with a fixed wavelength of the ionizing step. Assigned FES from literature [32, 33] are indicated by solid red lines, whereas reported but unobserved states are indicated by the dashed red lines. The green lines represent unassigned energy levels. The HFS was resolved in five excited states, which are marked by black arrows. Figure adapted from [236] in courtesy of [redacted].

state with $J_{gs} = 15/2$. A scanning speed of $\approx 20\,\text{cm}^{-1}$/min and 10 recorded data points per $1\,\text{cm}^{-1}$ was achieved to record the spectrum shown in Fig. 5.7. Ten resonances were identified as indicated by the solid red lines and the green lines, which can be assigned with certainty to ground-state transitions as no thermally populated low-lying state is available in einsteinium. Observed and in literature reported energy levels [32, 33] are marked by solid red lines, whereas reported but unobserved energy levels are indicated by dashed red lines. The green lines represent so far unassigned excited states. In five excited states the HFS was resolved (see section 5.7), which is indicated by the black arrows. Table 5.3 summarizes the measured excited states, for which the HFS was resolved.
After the identification of suitable first excitation steps, the ionization laser was scanned in the range from 50 640 - 54 330 cm^{-1} around the IP starting from the different observed ground-state transitions, recording spectra with broad continuum structures and numerous autoionizing states as shown exemplary in Fig. 5.8. From the observed resonances in the AI spectra the resonances with the highest ion yield are of interest for RIS to ensure an efficient ionization and are thus listed in Table 5.3. These efficient two-step schemes will enable future measurement campaigns on even more exotic and short-lived einsteinium isotopes.
Experimental lifetime determinations help in the identification and assignment of atomic levels, as the lifetime of a state is directly linked to the optical transition strengths. To mea-

Table 5.3.: Overview over the two-step RIS schemes and the observed FWHM and lifetimes of the investigated first excitation steps in ^{254}Es. The lifetimes were measured by temporal delay of the ionization pulse with respect to the excitation pulse. The AI states with the highest ion yield are reported, whereas for the HFS measurements broad AI states were favored. Table adapted from [236] in courtesy of [redacted].

$E_{\mathrm{exp,exc}}$ (cm^{-1})	FWHM (cm^{-1})	τ (ns)	AI (cm^{-1})	Signal (counts/s)
23 934.20(5)	2.8	1 133(51)	52 049.7	400
24 338.23(5)	1.3	484(11)	51 442.6	3 500
24 489.12(5)	1.3	380(6)	51 446.0	2 800
27 440.06(5)	3.0	443(19)	51 667.4	230
28 446.86(5)	2.9	$\leq$ 30	52 004.1	13 500

sure the lifetime of the five excited states reported in Table 5.3, the ion signal was recorded as a function of time delay between excitation and ionization pulse as shown exemplary in Fig. 5.9. The measured time profile can be described typically by a convolution of a

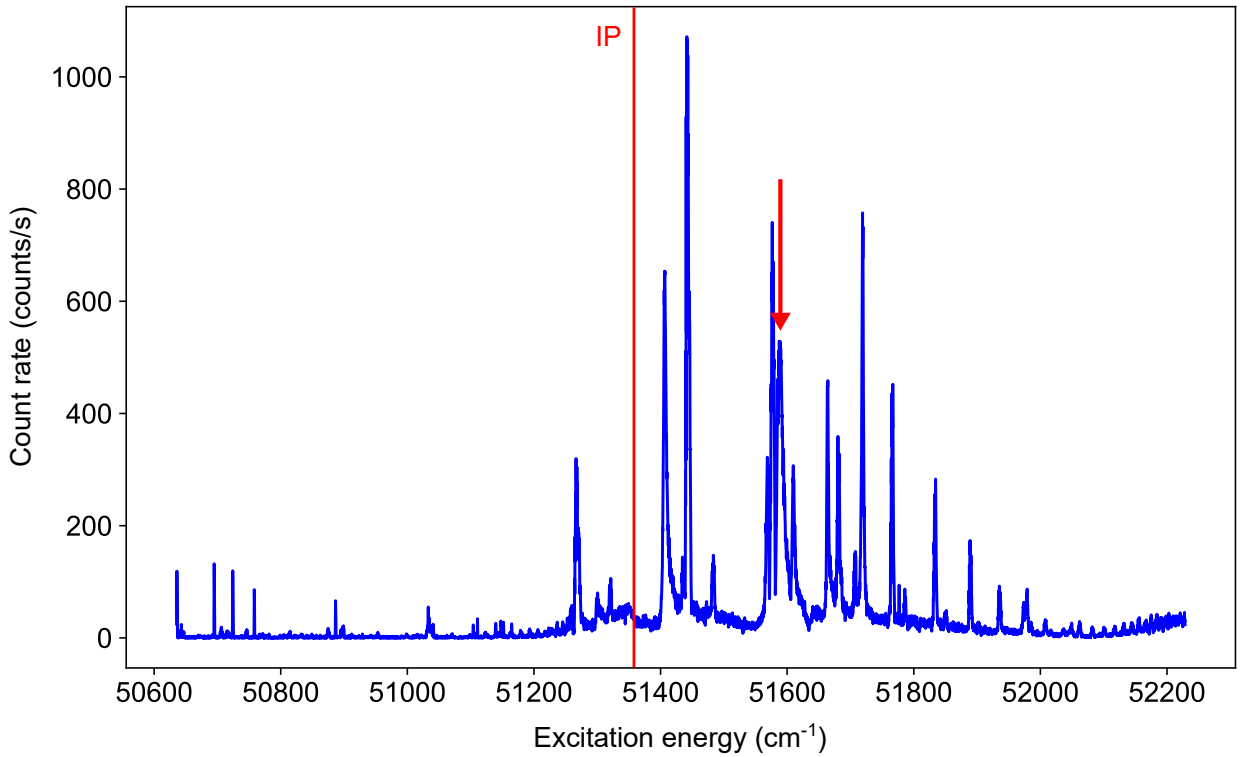

Figure 5.8.: Recorded spectrum around the IP starting from the excited state at 24338.23(5) cm^{-1}, showing a broad continuum structure and numerous autoionizing states. The solid red line indicates the IP [35, 212], whereas the red arrow indicates the AI state used for the HFS measurement.

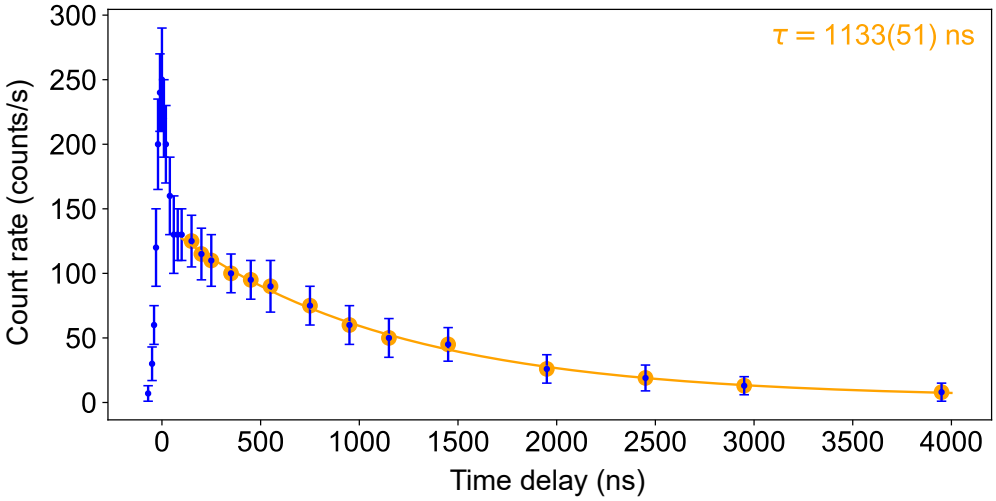

Figure 5.9.: Lifetime measurement for the excited state at 23 934.20(5) cm^{-1}. The tailing of the peak was fitted with an exponential function. Figure adapted from [236] in courtesy of [redacted].

Gaussian profile with an exponential decay. The model is not applicable if an enhancement of the recorded signal is observed, which is the case when both laser pulses coincide. This phenomenon could result from the fact that the ionization laser generates an additional ionization channel when the excitation laser is still present. In such cases the lifetime can be extracted by fitting the tailing of the decay with an exponential function (see Fig. 5.9). The measured lifetimes for the five excited states are summarized in Table 5.3. Short-lived excited states can be easily saturated, whereas longer lifetimes can be used in hyperfine structure measurements to increase the spectral resolution by delaying the ionization pulse compared to the excitation pulse [104].

5.7. Nuclear structure investigations on ^{253,254,255}Es

The following sections will cover the isotope shift and HFS measurements and is summarized in [41]. The Statistical Analysis Toolbox for Laser Spectroscopy (SATLAS) package in Python [237] was used to fit the hyperfine spectra. This package is designed especially to analyze the data of laser spectroscopy experiments, allowing for both maximum-likelihood and χ^2 fitting procedures. A model for the hyperfine structure of the isotope or species of interest is directly fitted to the experimental data, providing both resonance characteristics and hyperfine parameters. This model cannot perfectly describe all features in every transition, as especially saturation and optical pumping can lead to side effects not being described by the code. Due to the dominant contribution from Doppler broadening, together with the laser bandwidth in the case of mms, the spectra recorded in this work were fitted with a sum of Gaussian profiles using the χ^2 fitting procedure. The relative peak intensities were varied between the Racah intensities I_{Racah}, which can be calculated between the different

Table 5.4.: Overview over the extracted spectral resolution (FWHM) for each transition. For further details on the level schemes see Fig. 5.10.

E_{exp} (cm^{-1})	Isotope	FWHM (MHz)
23 934.20(5) sms	254	1 557(39)
23 934.20(5) mms	254	2 568(39)
24 338.23(5) sms	254	1 249(23)
24 489.12(5) sms	254	1 579(25)
27 440.06(5) mms	254	2 537(32)
28 447.03(5) mms	253	3 559(41)
28 446.86(5) mms	254	3 194(36)
28 446.66(5) mms	255	3 824(111)

F states from the coupling of the angular momenta according to eqn. 2.15 [237, 238], and the intensity $I(s)$ defined by

$$I(s) \sim I_{\mathrm{sat}} \cdot \Big(\exp\Big(\frac{I_{\mathrm{Racah}} \cdot s}{I_{\mathrm{sat}}}\Big) - 1\Big)\,. \tag{5.1}$$

$I(s)$ is proportional to the saturation intensity $I_{\mathrm{sat}} = 2F_{\mathrm{gs}} + 1$ with the saturation parameter s [237].
All fits were performed with open A and B HFS parameters and open ratios in both cases if not stated differently in the text. Typical linewidths of 2.5 - 3.5 GHz for mms and 1.5 GHz for sms were derived, as shown in Table 5.4.

5.7.1. Energy level scheme

Resistive heating of the atomizer produced an atomic einsteinium vapor, which was investigated by two-step RIS as shown in Fig. 5.10. Here, transitions with high transition probability were chosen for sensitivity and efficiency. With sample sizes ranging down to femtograms, the prominent 351.5 nm-ground-state transition was measured in all three isotopes $^{253\text{-}255}$Es, and four additional ground-state transitions were measured only in the isotope ^{254}Es as shown in Fig. 5.10 a. In addition, other transitions as shown in Fig. 5.10 b were probed in ^{254}Es, but the hyperfine structure was not resolved. The recorded unresolved spectra for these transitions are reported in the appendix in Fig. B.1 - B.5 and will not be covered in the following sections as no nuclear or atomic properties were extractable.

5.7.2. HFS, IS, and nuclear spin *I*

Fig. 5.11 shows the measured hyperfine spectra in ^{253,254,255}Es for the ground-state transition to the 28 447 cm^{-1} level. The recorded spectrum for ^{255}Es was investigated additionally considering a contribution from an impurity of ^{254}Es, as the measurement was performed with a ^{255}Es-sample containing 1000 times more ^{254}Es. Due to the low mass resolution of the

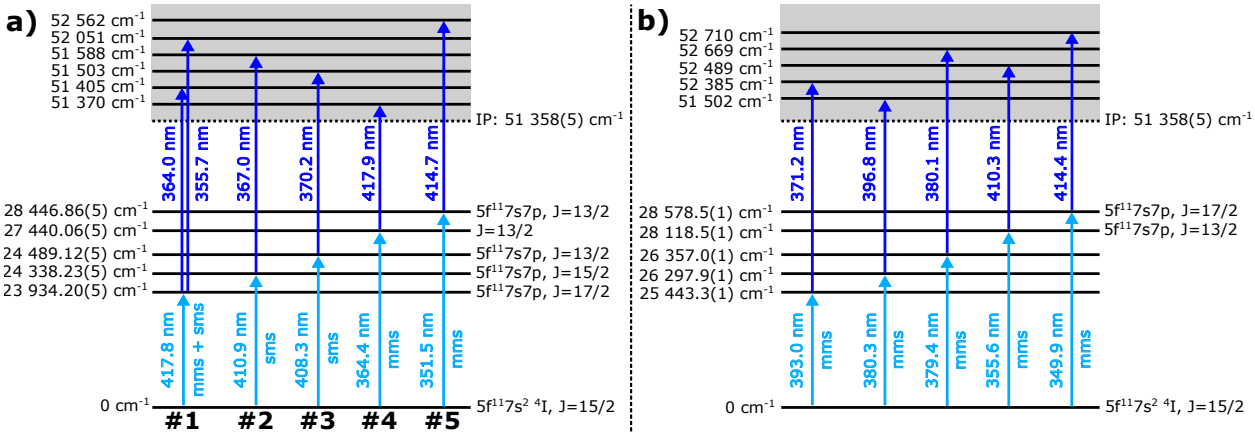

Figure 5.10.: Overview over the used laser ionization schemes with experimental level energies, total angular momentum J assignments, and level configurations. The values for the electron configurations and the IP are taken from [31, 32, 33, 239]. a) Five ground-state transitions were investigated resolving the HFS for ^{254}Es with multi-mode (mms) and single-mode spectroscopy (sms) with the corresponding level schemes shown in Fig. B.12. b) Five additional ground-state transitions were measured for ^{254}Es with mms, but without resolving the HFS.

RISIKO mass separator ^{254}Es was not sufficiently suppressed when the magnet was set to a mass-over-charge ratio of $A/q = 255$. Fig. 5.12 shows the impurity investigation. The best description of the measured data was found for an ^{254}Es impurity of 9(2)%. The extracted hyperfine parameters A and B with and without considering an impurity are consistent within the uncertainties and shown in Table 5.5.
In the literature only the nuclear spin of ^{253}Es is known to be $I(^{253}\text{Es}) = 7/2^+$ [210] (see section 5.1). Here, the unpaired proton configuration is assigned to $\pi_{7/2}[633]$. The ground-state hyperfine parameters were extracted from our fit (upper panel in Fig. 5.11), resulting in $A = 802(18)$ MHz and $B = -3916(550)$ MHz. These values agree with the values extracted from ABMR measurements [34]. The nuclear spins of ^{254,255}Es are tentatively assigned in literature to $I(^{254}\text{Es}) = (7)$ and $I(^{255}\text{Es}) = (7/2)$ [213, 215].
Generally, by using the dependence of the HFS splitting on the nuclear spin I, an assignment of the spin is possible [3]. For ^{254}Es the tentative spin assignment of $I(^{254}\text{Es}) = (7)$ results from a coupling of the $\pi_{7/2}[633]$ proton configuration and the $\nu_{7/2}[613]$ neutron configuration to maximum spin. The $\pi_{7/2}[633]$ proton configuration is known to be the ground-state configuration in the neighboring isotope ^{253}Es and the assumed and calculated configuration for ^{255}Es. The $\nu_{7/2}[613]$ neutron configuration is known to be the ground-state configuration of the isotone ^{255}Fm [215, 216]. Additionally, this spin assignment to $I(^{254}\text{Es}) = (7)$ is consistent with observed electron capture and low β^--decay branches to ^{254}Cf and ^{254}Fm, respectively [38]. From our fit to the recorded HFS of ^{254}Es, a spin of $I(^{254}\text{Es}) = 7$ supports the former tentative findings (see middle panel of Fig. 5.11). Lower spin values result in fits (also see appendix Fig. B.6 - B.11), which do not match with the observed HFS splitting. For larger spin values the individual fits to each transition result in a proper fit, but without the

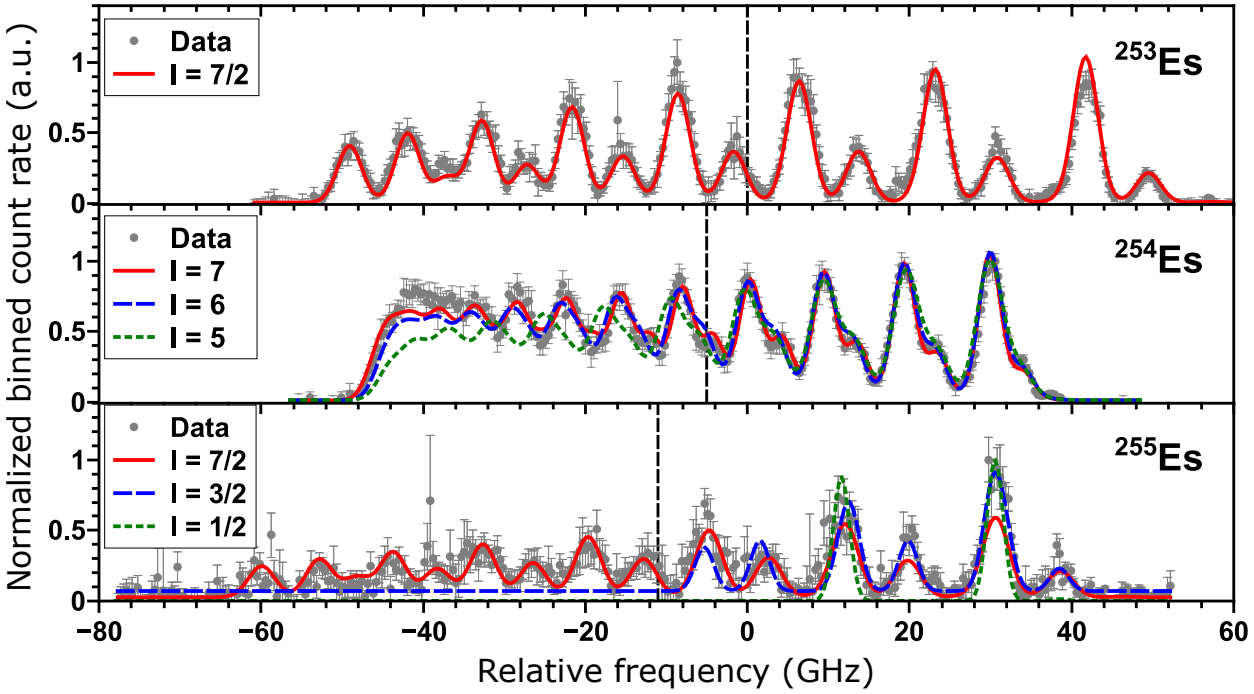

Figure 5.11.: Measured hyperfine spectra for the ground-state transition to the $E_{\mathrm{exp}}(^{253}\mathrm{Es}) = 28\,447.03(5)\,\mathrm{cm}^{-1}$ level in ^{253,254,255}Es (# 5 in Fig. 5.10). The centroid frequency ν of the ^{253}Es HFS is used as reference and the isotope shifts (centroids) are indicated by the black dashed vertical lines. The colored dashed and solid lines represent the best fits of each isotope to the measured HFS for different values of the nuclear spin I. The fit parameters are shown in Fig. 5.13. For ^{255}Es a discrepancy between measured count rate and fit is visible. This can be explained due to the low abundance of ^{255}Es in the sample, making it necessary to heat to higher temperatures. As a result, a decrease of the signal in the scanning range from right to left was observed.

five individual ground-state transitions sharing the same ground-state hyperfine parameters when $I \neq 7$. The extracted A and B parameters as well as the χ^2 of each individual fit are shown in Fig. 5.13, strongly supporting the assignment of $I(^{254}\mathrm{Es}) = 7$.
As already indicated in Fig. 5.13 by the gray data points the spectra for the two ground-state transitions to the $23\,934.20(5)\,\mathrm{cm}^{-1}$ and the $27\,440.06(5)\,\mathrm{cm}^{-1}$ levels showed an additional laser frequency dependent trend. Possible reasons causing this trend could be related to a change in evaporation rate with temperature inside of the atomizer or due to wavelength-dependent power fluctuations during the measurement. Another potential reason could be a dependency of the ionization probability from the upper (excited) F-level. The unadjusted and adjusted spectra to the $23\,934.20(5)\,\mathrm{cm}^{-1}$ and the $27\,440.06(5)\,\mathrm{cm}^{-1}$ levels are shown in Fig. 5.14 and Fig. 5.15, respectively. It was not possible to establish the exact nature of this background behavior in the data analysis and therefore a linear correction (linear function) was applied, which would correspond to a first-order correction for slow and small variations. This linear

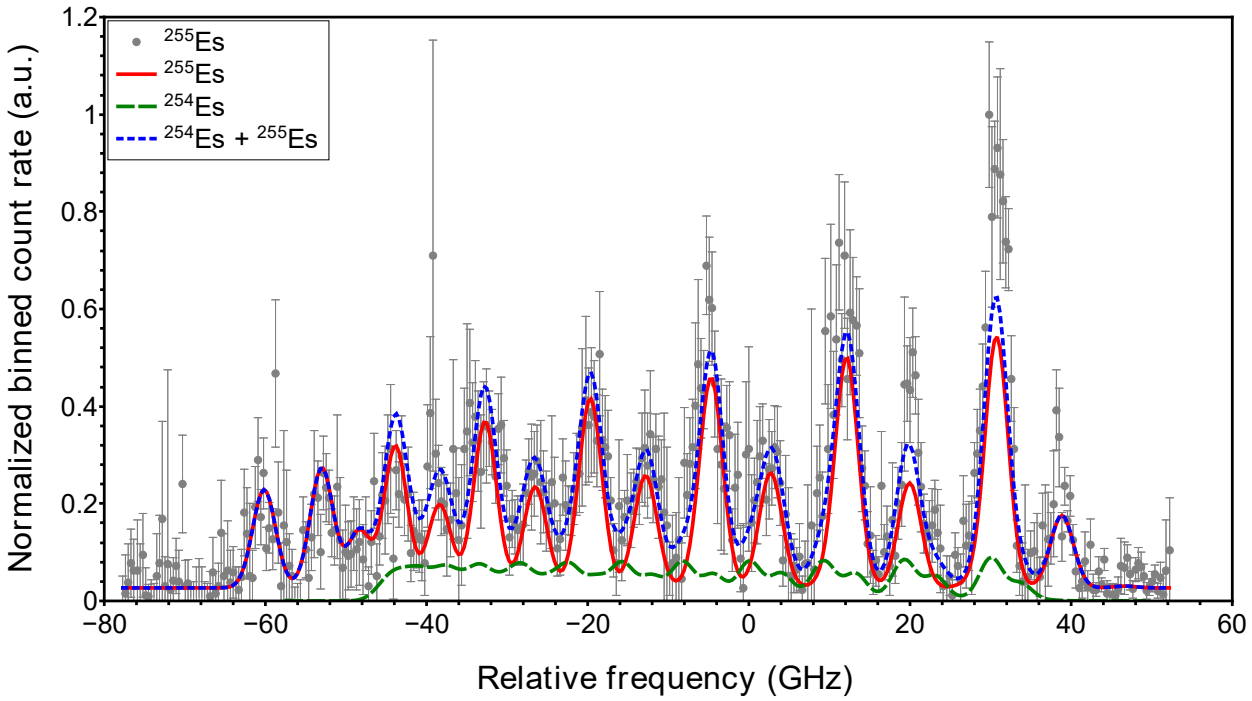

Figure 5.12.: Measured HFS of the ground-state transition to the 28 447 cm^{-1} level in ^{255}Es. Here, an impurity of ^{254}Es was investigated due to the 1000-fold reduced abundance of ^{255}Es in the sample. The best description was found for a small contribution from ^{254}Es of 9(2)%. Analog to Fig. 5.11, the relative frequency to $E_{exp}(^{253}Es) = 28\,447.03(5)\,cm^{-1}$ is shown.

function increases with rising frequency offset and is subtracted from the measured data points in order to match the fit curve using the following equation:

$$y_1 = (y_0 - b) \cdot (1 + m \cdot x) + b. \tag{5.2}$$

Here, the measured count rate is considered by y_0 and the adjusted count rate by y_1. The relative frequency to the center of gravity of the HFS spectrum in GHz is described through x, the slope of the function by m, and the background rate by b. In order to combine all five

Table 5.5.: Overview over the extracted A and B hyperfine parameters (in MHz) of the ground-state transition to the 28 447 cm^{-1} level in ^{255}Es with and without considering a contamination from ^{254}Es. The uncertainties are adjusted according to the Birge ratio. During the further analysis the hyperfine parameters considering the ^{254}Es contamination are used.

Dataset	A_{gs}	A_{exc}	B_{gs}	B_{exc}	χ^2
^{255}Es	816(41)	2 777(47)	-3 248(1290)	-3 807(1260)	1.00
^{255}Es + ^{254}Es	824(45)	2 793(51)	-3 001(1400)	-3 694(1330)	1.00

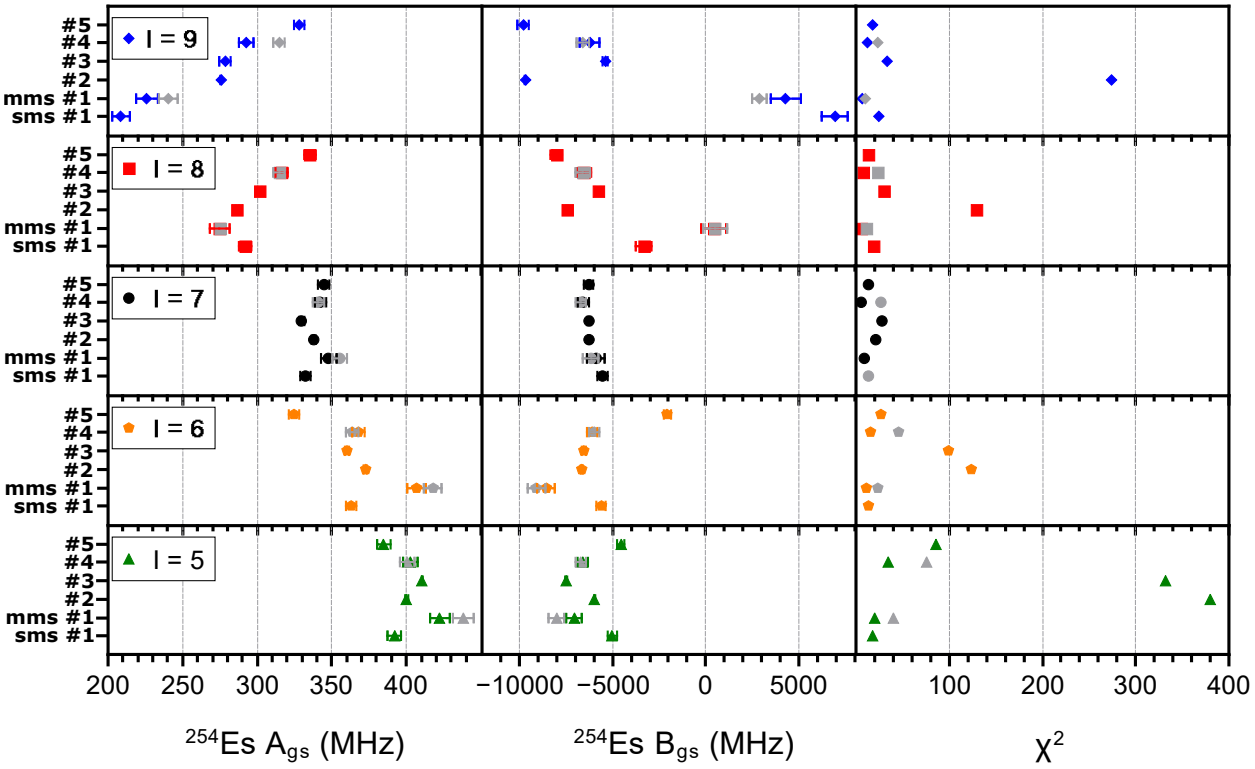

Figure 5.13.: Examination of the ^{254}Es ground-state HFS parameters in the five ground-state transitions as referenced in Fig. 5.10 for different nuclear spin assumptions. The uncertainties for the A and B parameter were increased by a factor three or two, respectively. The gray data points represent the fit parameters for the unadjusted data sets. For more details see text.

ground-state transitions, the uncertainties of the data points in Fig. 5.14 and Fig. 5.15 were increased to obtain a $\chi^2 = 1$ in the case of the adjusted data. In addition, due to the scatter of the individual ground-state parameters, the fit uncertainties were increased by a factor of three for the A parameter and a factor of two for the B parameter analyzing the respective Birge ratio (see section B.1) [240, 241]. The inflating factors were rounded to the next higher integer for a conservative estimate. The reason for the remaining mismatch at the low-energy side of the 23 934 cm^{-1} transition is still unclear. The extracted A and B parameters and reduced χ^2 of each fit are displayed in Table 5.6, indicating that the parameters coincide within the uncertainties. The main reason for the data adjustment was to additionally allow for a combined fit, where all measured data sets for ^{254}Es were fitted simultaneously with shared hyperfine structure ground-state parameters A_{gs} and B_{gs} to check the consistency of the full data set.

In order to further investigate the measured ground-state transitions in ^{254}Es, the uncertainties of the data points in all five spectra were increased to obtain a $\chi^2 = 1$ for each individual fit, using the adjusted data for the 23 934.20(5) cm^{-1} (mms) and the 27 440.06(5) cm^{-1} (mms) levels. There are multiple reasons for this procedure. First, this ensures a more reasonable

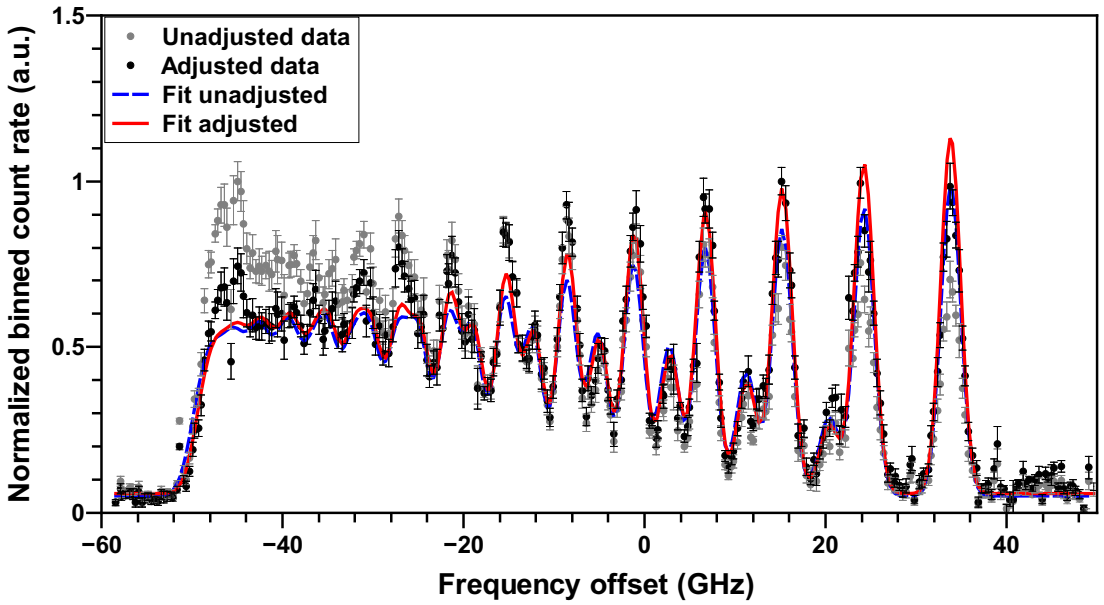

Figure 5.14.: Measured HFS of the ground-state transition to the 23 934.20(5) cm^{-1} level in ^{254}Es. The graph shows the measured data (gray points) and respective fit (blue dashed line). Additionally, the adjusted measurement data (black points) and respective fit (red solid line) are shown.

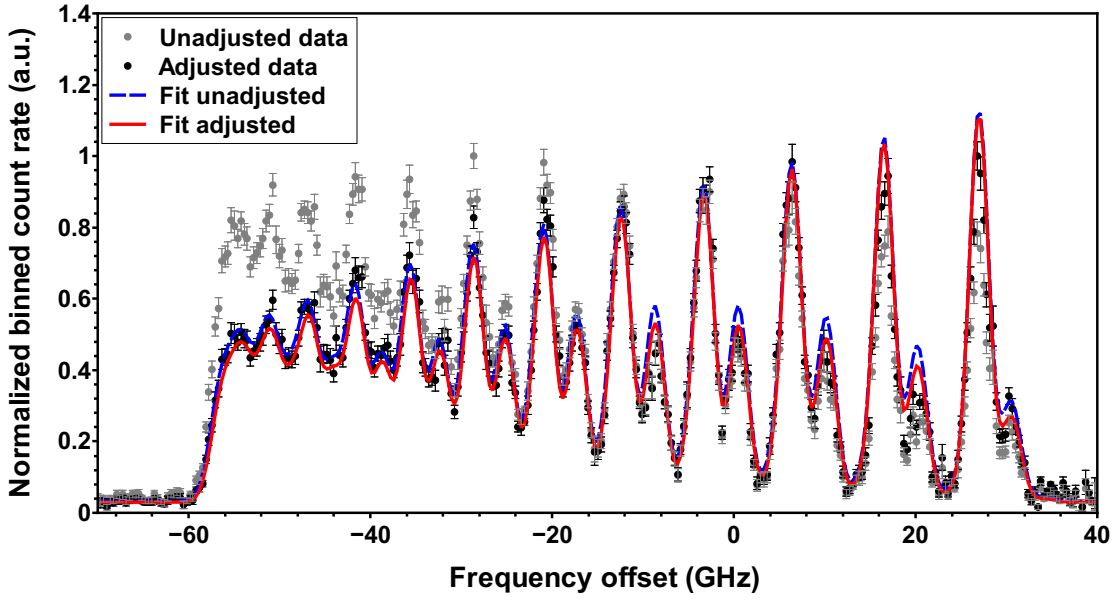

Figure 5.15.: Measured HFS of the ground-state transition to the 27 440.06(5) cm^{-1} level in ^{254}Es. The graph shows the measured data (gray points) and respective fit (blue dashed line). Additionally, the adjusted measurement data (black points) and respective fit (red solid line) are shown.

Table 5.6.: Overview over the extracted A and B hyperfine parameters (in MHz) for ^{254}Es from the adjusted and unadjusted data for a nuclear spin of $I = 7$.

	Level at 23 934.20(5) cm^{-1}			Level at 27 440.06(5) cm^{-1}		
Dataset	A	B	rel. χ^2	A	B	rel. χ^2
unadjusted	355.4(10.8)	-6 177(923)	2.76	340.9(10.4)	-6 721(713)	4.44
adjusted	348.0(11.4)	-5 887(1015)	1.00	342.4(9.5)	-6 577(772)	1.00

uncertainty from the fitting procedure. Second and more crucial is the fact that different ground-state transitions were measured in ^{254}Es. Using a normalization of χ^2 leads to an easier comparability of the changes in fit quality along the different transitions, enabling a comparison of different spin assumptions on the nuclear spin. The χ^2 normalization also ensures in the case of the combined fit that all transitions contribute equally. Therefore, each transition was individually fitted analog to Fig. 5.13 with increased uncertainties of the data points ($\chi^2 = 1$ in the case of $I = 7$) to extract the ground-state A and B parameters for ^{254}Es. The extracted A and B parameters before adjusting the uncertainties according to the Birge ratio are given in Table 5.7. The increased uncertainties adapted to the Birge ratios and the calculated weighted average of the ground state in ^{254}Es are displayed in Table 5.7 and in Fig. 5.16. In Fig. 5.16 the weighted average for the ground-state hyperfine constants A and B are marked as solid black lines with uncertainties indicated by the gray shaded areas. The extracted A factor agrees well with the reported value of $A_{\text{lit}} = 334(7)$ MHz for ^{254}Es [35, 212] (see section 5.1), whereas a discrepancy in the B value ($B_{\text{lit}} = -2\,830(900)$ MHz) can be potentially explained by insufficient resolution and statistics in the measurements on a single transition, which is why no electromagnetic moments were calculated in this work. It is important to note, that the uncertainty for the ground-

Table 5.7.: Overview over the extracted A and B hyperfine parameters from the five ground-state transitions in ^{254}Es for a nuclear spin of $I = 7$. The unadjusted (A_{gs}, B_{gs}) and adjusted uncertainties ($A_{\text{gs,Birge}}$, $B_{\text{gs,Birge}}$) according to the Birge ratios are displayed. For more details see text.

E_{exp} (cm^{-1})	A_{gs} (MHz)	$A_{\text{gs,Birge}}$ (MHz)	B_{gs} (MHz)	$B_{\text{gs,Birge}}$ (MHz)
23 934.20(5) sms	332.3(3.6)	332.3(10.8)	-5 523(417)	-5 523(834)
23 934.20(5) mms	348.0(3.8)	348.0(11.4)	-5 887(506)	-5 887(1012)
24 338.23(5) sms	337.9(1.8)	337.9(5.4)	-6 287(120)	-6 287(400)[a]
24 489.12(5) sms	329.8(2.9)	329.8(8.7)	-6 265(329)	-6 265(658)
27 440.06(5) mms	342.4(3.2)	342.4(9.6)	-6 577(386)	-6 577(772)
28 446.86(5) mms	344.6(4.7)	344.6(14.1)	-6 279(477)	-6 279(954)
Weighted average		339(4)		6 200(300)

[a]The uncertainty was increased to 200 MHz before multiplying with a factor two. For more details see text.

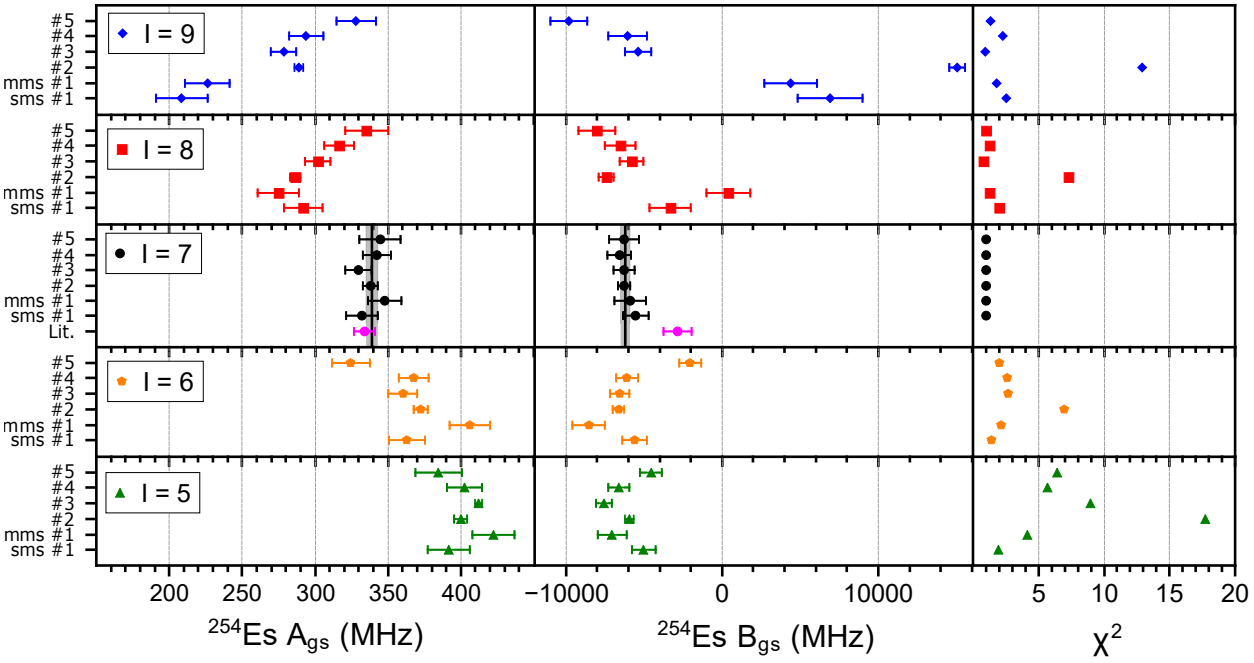

Figure 5.16.: Overview of the individual ground-state HFS parameters in ^{254}Es as referenced in Fig. 5.10 with literature values (magenta circles, see section 5.1) [35, 212] for different nuclear spin assumptions ($\chi^2 = 1$ for $I = 7$). While the A factor agrees with our extracted value, the discrepancy in the B value can be potentially explained by insufficient resolution and statistics in the measurements on a single transition in [35]. Uncertainties according to the Birge ratio are given as discussed in text. The solid black lines mark the final ground-state values (weighted average) with uncertainties as indicated by the gray shaded area.

state transition to the 24 338.23(5) cm^{-1} level was increased to 200 MHz prior to multiplying with a factor of two from the Birge ratio, as this was the only transition with such small uncertainties. It is unclear, if these small uncertainties are correlated to this transition being the only transition with a total angular momentum $J = 15/2$, or if this is just a consequence of the enhanced spectral resolution (see Table 5.4). Additionally, the uncertainties of the data points needed in order to receive a $\chi^2 = 1$ are at least a factor of 2 - 3 smaller than the uncertainties for the other recorded transitions (see appendix Fig. B.6 - B.11), giving the fit procedure less freedom and therefore leading to smaller fit uncertainties.
As a consistency check a fit sharing the same ground-state hyperfine coupling constants A and B for all five transitions (combined fit) was performed, which is shown in Fig. 5.17. Each individual recorded spectrum (level schemes are displayed in Fig. B.12) is well described by the fit result (red solid line). Ground-state parameters of $A_{gs} = 338.2(3.3)$ MHz and $B_{gs} = -6204(193)$ MHz were extracted, whereas their uncertainties were increased according to the Birge ratio. These values are in agreement with the calculated weighted averages in their uncertainties, which are summarized in Table 5.7.
As stated in section 5.1, the nuclear spin I of ^{255}Es with one unpaired proton was assumed

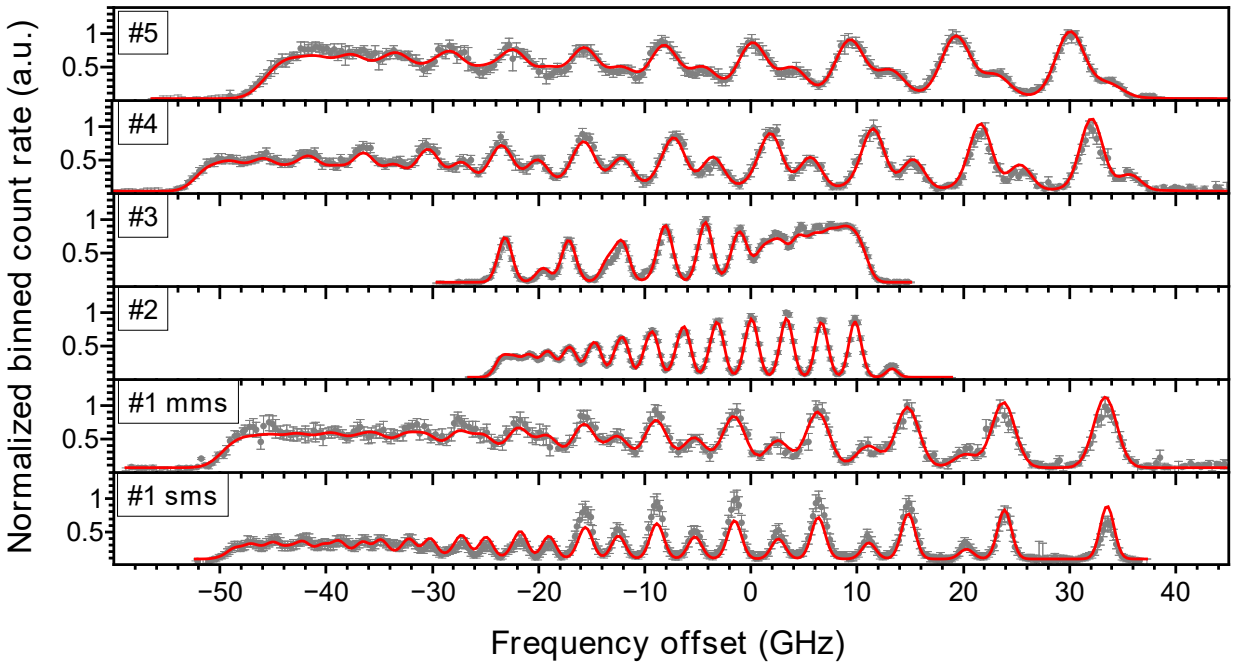

Figure 5.17.: Overview over all five ground-state transitions measured in ^{254}Es as referenced in Fig. 5.10, whereby the transition energies and level assignments were already known from literature. The frequency offset to the center of gravity of each HFS is shown in GHz. The fit (red solid lines) was performed sharing the same ground-state hyperfine coupling constants A and B for all transitions, using the adjusted data for the spectra for 23 934.20(5) cm^{-1} in mms and 27 440.06(5) cm^{-1} in mms.

based on a systematic trend along the isotopes of einsteinium as well as Nilsson-model calculations giving a $\pi_{7/2}[633]$ ground-state proton configuration [117]. Additionally, the α-decay scheme to ^{251}Bk does not conflict with that assignment [217]. However, the $\pi_{3/2}[521]$ proton configuration is predicted by theoretical calculations to be energetically higher but still close-lying to the $\pi_{7/2}[633]$ orbital [117, 118]. A ground-state spin of 3/2 is indeed assigned to ^{251}Es in contrast to the theoretical 7/2 prediction [117, 218]. From our fits to the recorded HFS of ^{255}Es only a spin of 7/2 results in a good agreement of the fit (see lower panel of Fig. 5.11). It has to be mentioned, that the fit with a spin 1/2 was not converging, so only the non optimized fit with the starting parameters is shown. Nevertheless it is clear from the measured hyperfine structure components, that this number of components can neither be reproduced with a spin of 1/2 nor 3/2.
After investigating and extracting the nuclear spin values for ^{254,255}Es, the HFS constants A and B were extracted from the individual fits and the uncertainties increased according to the Birge ratios. The hyperfine parameters are summarized in Table 5.8 and Table 5.9. As stated before, the ground-state parameters of ^{253}Es are known with high precision from the ABMR measurements, as indicated in Table 5.8. Furthermore, HFS parameters from optical spectroscopy are also reported for selected energy levels [32]. Due to the large uncertainty

Table 5.8.: Overview over the investigated energy levels of Es I (in cm^{-1}) and extracted hyperfine constants A and B (in MHz) obtained from ground-state transitions of ^{253}Es.

		^{253}Es			
J	$E_{\mathrm{exp},^{254}\mathrm{Es}}$	A_{exp}	A_{lit}	B_{exp}	B_{lit}
15/2	0	802(18)	817.153(7)‡	-3 916(550)	-4 316.254(76)‡
17/2	23 934.20(5)		(2 284(15))^{b†}		
15/2	24 338.23(5)		(1 532(15))^{b†}		
13/2	24 489.12(5)		(99(15))^{b†}		
13/2	27 440.06(5)				
13/2	28 446.86(5)	2 766(21)	2 784(5)‡‡	-4 425(530)	-5 138‡‡

^{b}Approximate values determined by optical spectroscopy. †[33], ‡[34], ‡‡ [31, 32, 33]

given for the B parameter, the ratio of the excited state (exc) and the ground state (gs) were not fixed during the evaluation.
The isotope shifts according to equation 2.16 were extracted from the fits in Fig. 5.11 to the measured HFS splittings with values of $\delta\nu^{253,254} = -5.020(54)$ GHz and $\delta\nu^{253,255} = -11.046(86)$ GHz. In literature a $5f^{11}7s^2 \rightarrow 5f^{11}7s7p$ transition is assigned in [33]. For this transition one would expect a negative isotope shift, because the electron in the s-orbital is less bound at higher mass numbers A, therefore requiring less energy for the electronic transition. The measured isotope shifts are in agreement with this expectation. The atomic factors linking isotope shifts with the change in nuclear volumes can usually only be obtained from atomic calculations in the heavy actinides [1, 3], but strong electron correlations due to open f-shell systems complicate those [98]. A typical order of magnitude for these electron correlations cannot be given due to their complex nature. Thus, einsteinium remains

Table 5.9.: Overview over the investigated energy levels of Es I (in cm^{-1}) and extracted hyperfine constants A and B (in MHz) obtained from ground-state transitions of ^{254,255}Es.

		^{254}Es		^{255}Es	
J	$E_{\mathrm{exp},^{254}\mathrm{Es}}$	A_{exp}	B_{exp}	A_{exp}	B_{exp}
15/2	0	339(4)	-6 200(300)	824(45)	-3 001(1400)
17/2	23 934.20(5)	951(8)	-6 930(690)		
15/2	24 338.23(5)	626(5)	-11 120(200)		
13/2	24 489.12(5)	28(8)	-12 945(440)		
13/2	27 440.06(5)	1 241(11)	-12 111(760)		
13/2	28 446.86(5)	1 165(16)	-5 824(930)	2 793(51)	-3 694(1330)

inaccessible for such atomic calculations until now, whereas atomic calculations for the next heavier element fermium recently became available [101]. This indicates that further progression can be expected in the future.
Throughout the chart of nuclides, an odd-even staggering (OES) in charge radii is observed. Isotopes with an odd neutron number N have a smaller charge radius than the average of its two neighbors with even N, whereas in some regions of the nuclide chart an inversion (inverse OES) is observed [242]. In our measurements, the larger isotope shift between ^{254,255}Es compared to ^{253,254}Es indicates a very small non-inverted odd-even staggering in the measured data, assuming a negligible contribution from the mass shift.

5.7.3. Magnetic-dipole moments and spectroscopic electric quadrupole moments

From the hyperfine parameters obtained for the ground state for ^{254,255}Es the magnetic-dipole moments μ and the spectroscopic electric quadrupole moments Q_s were determined using the equations 2.7 and 2.12 [3]. In both cases the HFS parameters and the known moments of ^{253}Es served as reference ("ref"). The extracted electromagnetic moments together with the obtained nuclear spins I are summarized in Table 5.10.
The nuclear magnetic-dipole moments of ^{253}Es and ^{255}Es coincide within the uncertainty bands. This indicates that in both cases the unpaired proton occupies the same single-particle orbital, therefore pointing to a $\pi_{7/2}[633]$ proton configuration for the nuclear ground-state in ^{255}Es. The extracted nuclear dipole moment of ^{254}Es deviates by about two sigma from the value of $|\mu_I(^{254}\text{Es})| = 4.35(41)\mu_\text{N}$ reported by Sereijns et al. [37] (see section 5.1), but the measurements performed in this work benefit from a large redundancy in the determination of the A and B hyperfine parameters from individual ground-state transitions. In comparison, the value reported by Sereijns et al. relies on external magnetic fields from the iron host lattice, which needs to be calibrated independently. In the same work [37], a magnetic-dipole moment of $|\mu_I(^{254}\text{Es})| = 3.52\mu_\text{N}$ was calculated assuming a $\pi_{7/2}[633]\nu_{7/2}[613]$ particle

Table 5.10.: Overview over the extracted nuclear magnetic and electric quadrupole moments of ^{254,255}Es in comparison to literature.

		This work		Literature		
Isotope	I	μ_I (μ_N)	Q_s (eb)	μ_I (μ_N)	Q_s (eb)	Ref.
^{253}Es	7/2			4.10(7)	6.7(8)[c]	[34]
^{254}Es	7	3.42(7)	9.6(1.2)	4.35(41)		[37]
^{254m}Es	2			2.90(7)	3.8(5)	[34]
^{255}Es	7/2	4.14(10)	5.1(1.7)			

[c] A value of $Q_s = 6.9(8)\,e$b is reported in the abstract of [34], which differs from the spectroscopic electric quadrupole moment reported in the main article.

configuration using a single-particle model [214]. This value is in good agreement with the extracted value in this work. Furthermore, a contribution from hyperfine anomaly [243] can be excluded, as the ratios of the hyperfine parameters of the ground state and the excited states are identical and lying well within the uncertainty bands.
The spectroscopic electric quadrupole moment Q_s for ^{254}Es is considerably larger than in ^{253}Es. From Q_s the intrinsic quadrupole moment Q, a parameter for the deformation of a nucleus, can be calculated using equation 2.13 [68]. Assuming $K = I$ for the ground-state as band head, the intrinsic quadrupole moments can be calculated. These calculations result in $Q(^{253}\text{Es}) = 14.4(1.7)\,e\text{b}$ and $Q(^{254}\text{Es}) = 14.3(1.8)\,e\text{b}$, indicating a similar deformation for both isotopes. After passing the deformed shell closure at $N = 152$ a decreasing trend in deformation towards more spherical nuclei is anticipated as maximum deformation is expected at a shell closure [119], which might be hinted in the smaller value of $Q(^{255}\text{Es}) = 10.9(3.6)\,e\text{b}$ for ^{255}Es. Due to the large uncertainties this hint in a drop of deformation should be taken with care. According to eqn. 2.57, the deformation parameter ϵ_2 can be calculated for the isotopes ^{253,254,255}Es ($Z = 99$, $N = 154/155/156$). Deformation parameters of $\epsilon_2(^{253}\text{Es}) = 0.272(0.028)$, $\epsilon_2(^{254}\text{Es}) = 0.269(0.029)$, and $\epsilon_2(^{255}\text{Es}) = 0.212(0.065)$ are needed to calculate the extracted intrinsic quadrupole moments of $Q(^{253}\text{Es}) = 14.4(1.7)\,e\text{b}$, $Q(^{254}\text{Es}) = 14.3(1.8)\,e\text{b}$, and $Q(^{255}\text{Es}) = 10.9(3.6)\,e\text{b}$, respectively. Theoretical predictions of the quadrupole deformations resulted in values of $\epsilon_2(^{253}\text{Es}) = 0.217$ [114] / 0.231 [34], $\epsilon_2(^{254}\text{Es}) = 0.208$ [114], and $\epsilon_2(^{255}\text{Es}) = 0.208$ [114]. Thus, the extracted quadrupole deformations are slightly larger than the calculated values in the case of ^{253}Es and ^{254}Es. Looking at the Nilsson diagrams for protons (Fig. 2.6) and neutrons (Fig. 2.7), one can see, that the deformed ground-state proton orbitals $\pi_{7/2}[633]$ and $\pi_{3/2}[521]$ are energetically close-lying in the deformation region $\epsilon_2 = 0.2 - 0.3$, whereas in the case of the deformed neutron orbitals $\nu_{7/2}[613]$ and $\nu_{9/2}[734]$ the ground state changes over the deformation region of interest. At a deformation of around $\epsilon_2 = 0.3$ the Nilsson model predicts the $\nu_{1/2^-}[761]$ and $\nu_{1/2^+}[620]$ orbitals to be energetically close-lying to the $\nu_{7/2^+}[613]$ and $\nu_{9/2^-}[734]$ orbitals. The spin assignment of $I(^{254}\text{Es}) = 7$ only allows the ground-state configuration $\pi_{7/2}[633]\nu_{7/2}[613]$ for the odd-odd isotope ^{254}Es. In the odd-even isotopes the spin assignments of $I(^{253}\text{Es}) = 7/2$ and $I(^{255}\text{Es}) = 7/2$ only allow the $\pi_{7/2}[633]$ orbital to be the ground state in both isotopes ^{253,255}Es, as the neutron shell is closed and thus does not contribute to the nuclear spin.

5.8. Summary

Using resonance ionization spectroscopy inside a hot cavity with a high-power Ti:sapphire laser system as a highly efficient and sensitive method, laser spectroscopy of einsteinium isotopes, with sample sizes on the femtogram scale, was performed. Ten ground-state transitions were measured in the region of 22 800 - 28 600 cm^{-1} in ^{254}Es, whereas the lifetimes and the AI states with the highest ion yield were reported for five of the ten investigated ground-state transitions in which the HFS was resolved [236]. The prominent 351.5 nm-ground-state transition was additionally measured in the isotopes ^{253,255}Es, enabling to deduce hyperfine structure constants A and B in $^{253\text{-}255}$Es located well above the deformed $N = 152$ shell closure. A detailed survey of the development of the single-

particle nucleon energies for different isotopes and thus for different deformations around this shell closure is important, as spherical (ground) states of heavier isotopes can be occupied in lighter nuclei by means of single-particle excitations at a given deformation. Considering increasing deformation, the deformed neutron orbitals $\nu_{7/2}[613]$ and $\nu_{9/2}[734]$ originating from the spherical orbitals $1\,\mathrm{i}_{11/2}$ and $1\,\mathrm{j}_{15/2}$, which are of relevance for the shell gap in spherical superheavy nuclei, are dropping strongly in energy. Thus, these orbitals can be investigated in deformed nuclei such as the measured einsteinum isotopes with the predicted quadrupole deformations $\epsilon_2 = 0.217$ (^{253}Es), $\epsilon_2 = 0.208$ (^{254}Es), and $\epsilon_2 = 0.208$ (^{255}Es) [114]. In this work the nuclear spins for ^{254,255}Es to $I(^{254}\mathrm{Es}) = 7$ and $I(^{255}\mathrm{Es}) = 7/2$ were determined from the resolved hyperfine structures, which were previously only tentatively assigned. From the deduced HFS constants the magnetic-dipole moments $\mu_I(^{254}\mathrm{Es}) = 3.42(7)\mu_\mathrm{N}$ and $\mu_I(^{255}\mathrm{Es}) = 4.14(10)\mu_\mathrm{N}$ and the electric spectroscopic quadrupole moments $Q_s(^{254}\mathrm{Es}) = 9.6(1.2)\,e\mathrm{b}$ and $Q_s(^{255}\mathrm{Es}) = 5.1(1.7)\,e\mathrm{b}$ for ^{254,255}Es were extracted, which were experimentally determined for the first time. The extracted magnetic-dipole moment of ^{254}Es is more precise than the value of $|\mu_I(^{254}\mathrm{Es})| = 4.35(41)\mu_\mathrm{N}$ reported from Severijns et al. [37], with the two deviating by about two sigma for the latter. The intrinsic quadrupole moments were calculated for all three isotopes to $Q(^{253}\mathrm{Es}) = 14.4(1.7)\,e\mathrm{b}$, $Q(^{254}\mathrm{Es}) = 14.3(1.8)\,e\mathrm{b}$, and $Q(^{255}\mathrm{Es}) = 10.9(3.6)\,e\mathrm{b}$, from which the deformation parameters with values of $\epsilon_2(^{253}\mathrm{Es}) = 0.272(0.028)$, $\epsilon_2(^{254}\mathrm{Es}) = 0.269(0.029)$, and $\epsilon_2(^{255}\mathrm{Es}) = 0.212(0.065)$ were extracted according to eqn. 2.57. These values hint towards a decrease in deformation towards a more spherical nuclear shape for ^{255}Es. The ground-state transition at 351.5 nm was measured additionally in the isotopes ^{253,255}Es. This gave access to the isotope shifts for $^{253\text{-}255}$Es with values of $\delta\nu^{253,254} = -5.020(54)\,\mathrm{GHz}$ and $\delta\nu^{253,255} = -11.046(86)\,\mathrm{GHz}$, but without the extraction of mean-square charge radii due to missing atomic theory input on the atomic factors.

Part III.

Conclusion and Outlook

Within the first part of this work a new gas-jet apparatus dedicated to high-resolution laser spectroscopy of the heaviest elements was developed, aiming to perform high-resolution laser spectroscopy with a spectral resolution of a few hundred MHz. The new gas-jet setup combines the advantages of two powerful and versatile techniques. The stopping of recoil ions in a gas-filled cell [161] as well as the ion collection and neutral desorption from a heated filament [135] are inspired from the RADRIS technique and are combined with the high-resolution gas-jet laser ionization technique developed at KU Leuven [150]. Starting from these conceptual ideas, a first technical layout was derived from simulation studies [162]. The new gas-jet setup was build accordingly and tested in multiple off-line measurements with natural ytterbium and in one on-line campaign using $^{154\text{-}156}$Yb, indicating the need of major design changes. A new version of the flow channel for instance was designed, allowing to apply a potential on the isolated part and enabling the reproducible insertion of the filament. Characterizations of this new flow channel indicated problems with glow emission, leading to the design of another flow channel. With the newest design, the glow emission was reduced but not prevented in first tests. Thus, further investigations will be performed in future experiments. Another part which was redesigned is the RFQ and mini-RFQ structure. Due to charge-up effects, the optimal transport settings changed over time, hampering the transport efficiency towards the detector. The new version of the RFQ renounced the mini-RFQ to simplify the extraction, all insulators were shielded to avoid charging up effects, and the PCB holding structure was exchanged to 316L stainless steel. New simulation studies indicated the additional need for two new transport electrodes which were designed and installed between the extraction plate and the detector, shielding the ions from the chamber on ground-potential. The most crucial and necessary change was the de Laval nozzle as no gas-jet was formed under the measurement conditions of 30 mbar stag-

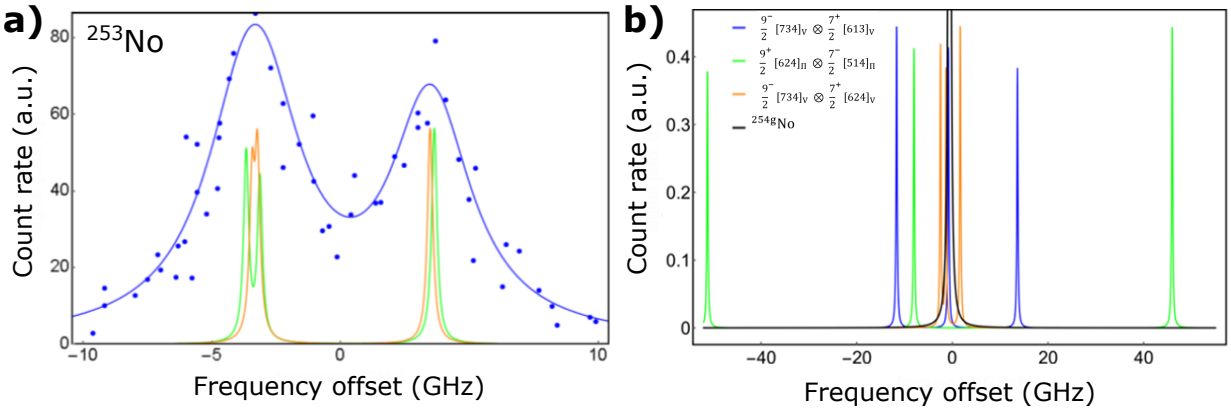

Figure 5.18.: a) Comparison between the RADRIS measurement on ^{253}No (blue) [46] and simulations of the spectrum for a spectral resolution of 400 MHz (orange) and 400 MHz increased by 1 σ (green), respectively. b) Spectrum for ^{254g}No (black) in comparison to simulated spectra for the $K = 8^-$ isomer in ^{254}No for different possible single-particle configurations as indicated by the colored spectra. The simulations were performed by [redacted].

nation pressure. Two new nozzles, namely a Mach-8 high-stagnation-pressure nozzle and a Mach-8.5 low-stagnation-pressure nozzle, were simulated, manufactured, and characterized [171, 179, 195]. The characterizations were performed via RIS on ^{nat}Yb and ^{174}Yb as well as via fluorescence measurements on dysprosium [197], the latter being not part of this work. Taking all specifications like the jet length, jet diameter, pressure conditions, and spectral resolution into consideration, the Mach-8.5 low-stagnation-pressure nozzle was chosen to be installed for future experiments. The extraction efficiency of the new RFQ was investigated with the Mach-8 high-stagnation-pressure nozzle and the Mach-8.5 low-stagnation-pressure nozzle leading to an efficiency of $\approx 75\,\%$. Lastly, the laser system was upgraded from a 100 Hz to a 10 kHz-repetition-rate system, which is required to efficiently excite and ionize the species of interest. Measurements with the new changes were performed, indicating a spectral resolution of ≤ 400 MHz, which is sufficient for the anticipated on-line campaign on nobelium. In order to mimic an on-line measurement, a ytterbium filament, operated under conditions such that atoms were predominantly evaporated, was installed in the gas cell. The atoms were ionized in the gas cell, neutralized on the hot filament, and re-ionized in the gas-jet by two-step RIS. A loss factor of ≈ 150 was observed, which needs to be investigated further in future experiments. It is not clear if the loss factor of ≈ 150 is only related to the unsaturated laser transitions, or if other factors as, e.g., the filament temperature have an influence as well. This factor has to be ruled out for a successful on-line campaign. In order to determine the sensitivity and efficiency of the setup, it is planned to move the setup to the LARISSA laboratory, where radioactive samples can be handled. Here, it is planned to investigate samples of ^{225}Ac with sample sizes of $\approx 10^9$ atoms (≈ 800 Bq) each to review the sensitivity of the setup starting from the evaporation in the flow channel until the final detection. A successful measurement of this kind would proof the suitability of the setup for low atom counts, thus being able to measure for instance ^{254}Es. Using a radioactive sample is necessary for this measurement as the number of atoms can be precisely determined from the measurable radioactivity. A short half life as in the case of ^{225}Ac ($T_{1/2} = 9.92$ d) is advantageous in order to avoid contamination of the apparatus with long-lived isotopes, which could complicate future measurements. Another crucial measurement is the investigation of the extraction efficiency starting from the entrance of the gas cell upon detection in the detector chamber. Here, a recoil source (e.g. ^{223}Ra) with an exactly known number of released ions will be mounted in the gas cell and the extraction efficiency through the setup measured by radioactive decay detection. In order to further optimize the gas-jet apparatus for the on-line measurements on nobelium (333.76 nm, $A_{ki} \geq 6.3 \cdot 10^7\,\mathrm{s}^{-1}$) [77, 173] and to gain experience with the Sirah Matisse as seed laser, experiments with thulium (Tm) (341.00 nm, $A_{ki} = 1.01 \cdot 10^7\,\mathrm{s}^{-1}$) [244] are planned due to the similar wavelength and strength of the excitation step. Analog to nobelium, the ionization step (SES) in thulium will be non-resonant. In early summer 2022, an on-line measurement campaign is planned to measure the $^1\mathrm{S}_0 \rightarrow {}^1\mathrm{P}_1$ ground-state transition in ^{253}No with the gas-jet apparatus with high spectral resolution as indicated in Fig. 5.18 a. In former measurements using the RADRIS technique, only two of the three hyperfine structure levels were resolved as indicated by the measurement points (blue dots) and the respective fit (blue line) in Fig. 5.18 a [46]. According to simulations of the spectrum, three hyperfine structure levels should be observable

with a spectral resolution of $\leq 400\,\mathrm{MHz}$, thus improving the accuracy of the hyperfine structure constants and the extracted electromagnetic moments. In addition, it is planned to study the $K = 8^-$ isomer in ^{254}No ($T_{1/2} = 0.266\,\mathrm{s}$) [18], which cannot be investigated using the RADRIS technique due to its short half life. The expected spectrum was simulated for different single-particle configurations as indicated in Fig. 5.18 b. High-resolution hyperfine spectroscopy on this isomer enables a conclusive assignment of the nucleon configuration.

The second part consisted of RIS measurements on the rare einsteinium isotopes ^{253,254,255}Es at the RISIKO mass separator in Mainz and is summarized in [41, 236]. Ten ground-state transitions were observed in ^{254}Es, whereas the lifetimes and the AI states with the highest ion yield were reported for five of the ten investigated ground-state transitions in which the HFS was resolved. With low sample sizes ranging down to femtograms, the prominent 351.5 nm-ground-state transition was measured in all three einsteinium isotopes $^{253\text{-}255}$Es. From the recorded spectra, HFS constants A and B were deduced for all isotopes, located well above the deformed $N = 152$ shell closure. A detailed investigation of the development of the single-particle nucleon energies for different isotopes and thus for different deformations around this deformed $N = 152$ shell closure is important, as the deformed orbitals originating from the spherical orbitals of heavier isotopes are strongly dropping in energy and thus can be occupied in lighter deformed nuclei. For instance, the deformed neutron orbitals $\nu_{7/2}[613]$ and $\nu_{9/2}[734]$ originating from the spherical orbitals $1\,\mathrm{i}_{11/2}$ and $1\,\mathrm{j}_{15/2}$, which are of relevance for the shell gap in spherical superheavy nuclei, can be investigated in deformed nuclei such as the measured einsteinum isotopes.
From the hyperfine structure analysis, the nuclear spins were determined to $I(^{254}\mathrm{Es}) = 7$ and $I(^{255}\mathrm{Es}) = 7/2$, as tentatively assigned before. Additionally, the magnetic-dipole moments of $\mu_I(^{254}\mathrm{Es}) = 3.42(7)\mu_\mathrm{N}$ and $\mu_I(^{255}\mathrm{Es}) = 4.14(10)\mu_\mathrm{N}$ and the spectroscopic electric quadrupole moments of $Q_s(^{254}\mathrm{Es}) = 9.6(1.2)\,e\mathrm{b}$ and $Q_s(^{255}\mathrm{Es}) = 5.1(1.7)\,e\mathrm{b}$ were experimentally determined for the first time. The extracted magnetic-dipole moment of ^{254}Es is more precise than the literature value of $|\mu_I(^{254}\mathrm{Es})| = 4.35(41)\mu_\mathrm{N}$ reported from Severijns et al. [37], deviating by about two sigma for the latter. The literature value was extracted from angular distribution measurements of α-particles from oriented ^{254}Es nuclei in an iron host lattice, revealing information on the magnetic moment and the hyperfine magnetic field. This measurement relies on external magnetic fields from the iron host lattice, which requires an independent calibration and thus could lead to the observed deviations. The intrinsic quadrupole moments Q were calculated out of the spectroscopic electric quadrupole moments Q_s, hinting towards a decrease in deformation towards a more spherical nuclear shape for ^{255}Es.
The isotope shifts for $^{253\text{-}255}$Es were measured for one ground-state transition. This work motivates further developments in atomic theory, e.g., the calculation of the field shift and mass shift parameter for the measured ground-state transition, so that in the future also mean-square charge radii can be extracted from this work. These calculations are challenged by the many-electron systems such as einsteinium with its 11 f-shell electrons.
Due to the half life of ^{254}Es ($T_{1/2} = 275.7\,\mathrm{d}$), the remaining einsteinium sample still contains a significant amount of this isotope. Parts of this sample ($\approx 10^9 - 10^{10}$ atoms) could be

used in conjunction with the gas-jet setup in the LARISSA laboratory before the on-line campaign in 2022. With the improved spectral resolution of $\leq$ 400 MHz in combination with the high-power Ti:Sa laser system the measured ground-state transitions in this work could be remeasured to improve the precision on the HFS constants A and B and deduced moments. From the analysis performed in this work it was found that the ground-state transition at 24 338 cm^{-1} has the highest sensitivity for the nuclear properties of einsteinium and is therefore recommended for further investigations. Another option would be to measure other ground-state transitions than investigated in this work or to repeat the measurements of the unresolved HFS shown in this work (see appendix B.2 and B.3) with a higher spectral resolution. Furthermore, using the remaining ^{254}Es sample or a new sample containing the isotopes ^{253,254,255}Es, the investigated ground-state transitions could be remeasured with the RISIKO setup. Here, a higher spectral resolution could be achieved using either the in-source single-mode spectroscopy (sms) method as described in this work or the perpendicularly illuminated laser ion source and trap (PI-LIST) technique. In the latter, one laser beam intersects the atomic beam effusing from the hot cavity in a perpendicular geometry instead of guiding all laser beams anticollinear to the ion beam axis into the hot cavity [225, 245]. Thus, the Doppler broadening can be greatly reduced when using narrowband lasers. This technique was not used in this work, but may allow for a significantly improved spectral resolution in future measurements. Additionally, the achieved sensitivity with the RISIKO technique paves the way for similar measurements on even rarer nuclides, e.g., the isotopes ^{255}Fm and ^{257}Fm of the next heavier element fermium ($Z = 100$). These fermium isotopes are available in macroscopic quantities from reactor breeding and could thus be investigated. Measurements on ^{255}Fm were already reported in [246] and could be used as a starting point for future measurements. Another way to produce ^{255}Fm would be to irradiate the remaining ^{254}Es sample with neutrons in a high-flux reactor. Here, ^{255}Fm would also be produced resulting from the β^- decay of ^{255}Es.

Besides the isotopes ^{253,254,255}Es, which were studied around the deformed shell closure at $N = 152$ in off-line measurements at RISIKO, further einsteinium isotopes are available at accelerator facilities from fusion-evaporation reactions. The study of extended isotopic chains below and beyond the deformed shell closure at $N = 152$ is important to understand the evolution of the nuclear mean-square charge radii. In einsteinium, isotopes with mass numbers in the range from $A = 241$ to $A = 257$ have so far been observed [36, 247]. Here, the isotopes ^{241,242,243,245}Es might be accessible for future studies using the RADRIS method or the new gas-jet based high-resolution setup on the basis of their production cross-sections, half life, and main decay mode as shown in Table 5.11. Due to the low production cross-sections and the unknown α-branches for ^{241,242}Es, it is unclear if successful measurements can be performed on these two isotopes. In the case of ^{245}Es, the mother nuclide ^{249}Md ($T_{1/2} = 23.8$ s) features a convenient α-branch of $> 60\%$ [248]. Other known isotopes of einsteinium seem not suitable for such studies, as they are either longer-lived, feature no or a low ($< 10\%$) α-branch, or are produced in unfeasible or undesirable reactions, e.g., featuring radioactive uranium targets for the production of ^{244,246,247}Es [36, 247]. For the odd mass einsteinium isotopes ^{243,245,247,249,251}Es, theoretical predictions and experimental findings of the ground-state configuration and deformation are reported in [119, 249]. Hence, accelera-

Table 5.11.: Selected einsteinium isotopes around the deformed shell closure at $N = 152$, which could be investigated in future measurements.

Isotope	$T_{1/2}$	Decay mode	Production	Cross-section	Ref.
^{241}Es	8(6) s		^{205}Tl(^{40}Ar, 4n)^{241}Es	10 nb	[250]
^{242}Es	16(6) s		^{205}Tl(^{40}Ar, 3n)^{242}Es	40 nb	[250, 251]
^{243}Es	23(3) s	α (61(6)%)	^{197}Au(^{48}Ca, 2n)^{243}Es	37(10) nb	[252]
^{245}Es	65(6) s	α (54(7)%)	^{203}Tl(^{48}Ca, 2n)^{249}Md $\xrightarrow{\alpha}$ ^{245}Es	300(80) nb	[252, 253]

tor produced isotopes give new opportunities to investigate the region around the deformed shell closure at $N = 152$.

Until now, only the isotopes $^{252\text{-}254}$No [44, 46] were investigated by optical spectroscopy using the RADRIS method in the region of $Z > 100$. Additionally, the isotope ^{255}No was recently successfully measured at RADRIS, but still has to be published. Measurements are planned to extend the isotopic chain in nobelium towards the isotope ^{251}No, which can be produced in the fusion-evaporation reaction ^{206}Pb(^{48}Ca, 3n)^{251}No with a cross-section of about 30 nb [254]. Furthermore, efforts are being made to investigate even heavier nuclides as for instance ^{255}Lr ($Z = 103$, $N = 152$) [255], for which many different ground-state transitions have been predicted by atomic theory [77, 256]. ^{255}Lr can be produced in the fusion-evaporation reaction ^{209}Bi(^{48}Ca, 2n)^{255}Lr with a cross-section of about 140 nb [257].

Part IV.

Appendix

A. Gas-jet setup

A.1. Background correction and AI levels

Fig A.1 shows the first recorded ^{nat}Yb signal with the 100 Hz repetition rate laser system. A broad, laser induced background was observed during this measurement. In order to clarify that this background was related to the laser light, both laser beams were hindered from entering into the jet cell, therefore not overlapping with the gas-jet. This resulted not only in a loss of the ^{nat}Yb signal, but also in a loss of the background signal. It is not clear what exactly caused that background. The background could be described with a Gaussian lineshape (solid red line in Fig. A.1, see inset), which was subtracted from the recorded signal in order to receive the background-corrected spectrum in Fig 4.13.
A spectrum of the ionization step used for the first measurements is shown in Fig. A.2. Two different ranges were used in order to fit the measurement data with a Lorentzian lineshape. One fit was performed using the full measured range (black solid line), while the other only used data up to 50 992.4 cm^{-1} (blue solid line). The reason to take out the data at the end is due to two reasons. First, the observation of sidemodes which seemed to be very pronounced at around 50 992.6 cm^{-1}. Second, the existence of the broad, laser induced background, which is more pronounced on the high-energy side of the spectrum. From the fit (blue solid line),

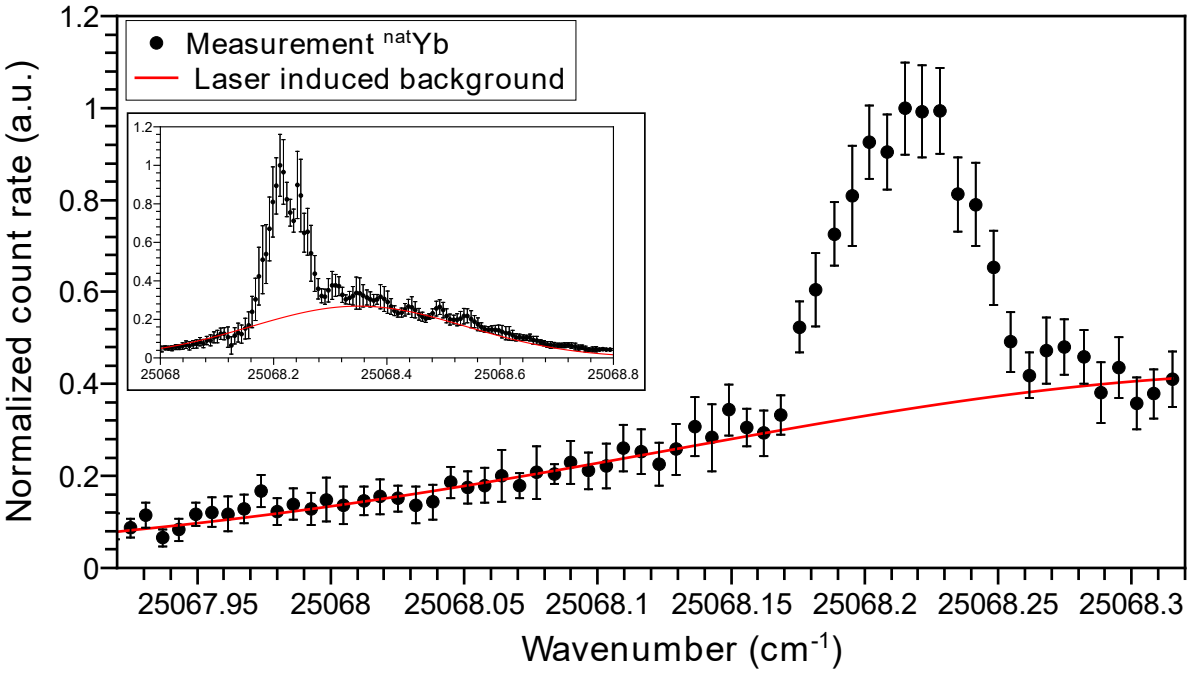

Figure A.1.: Recorded ^{nat}Yb signal. A laser induced background underneath the ytterbium signal is clearly visible. The inset shows a similar measurement, clearly indicating the Gaussian shape of the observed background.

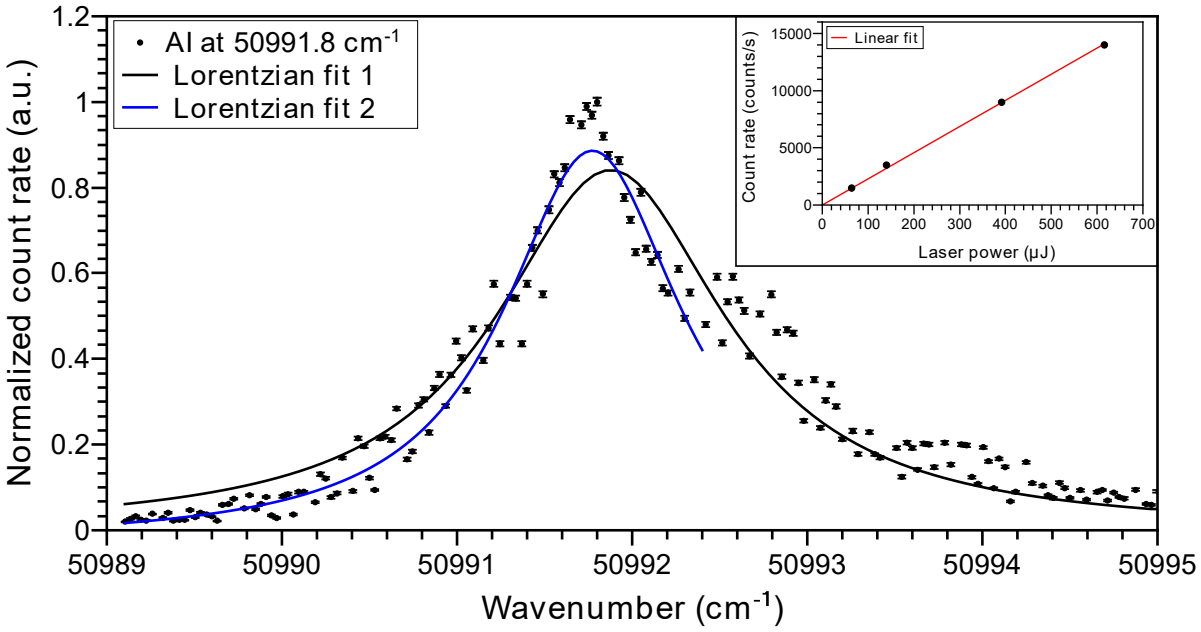

Figure A.2.: Recorded AI spectrum at 50 991.77(2) cm^{-1}. The spectrum was fitted with a Lorentzian lineshape in two different ways (blue and black solid line). The inset shows the saturation curve, indicating that no saturation was reached. For more details see text.

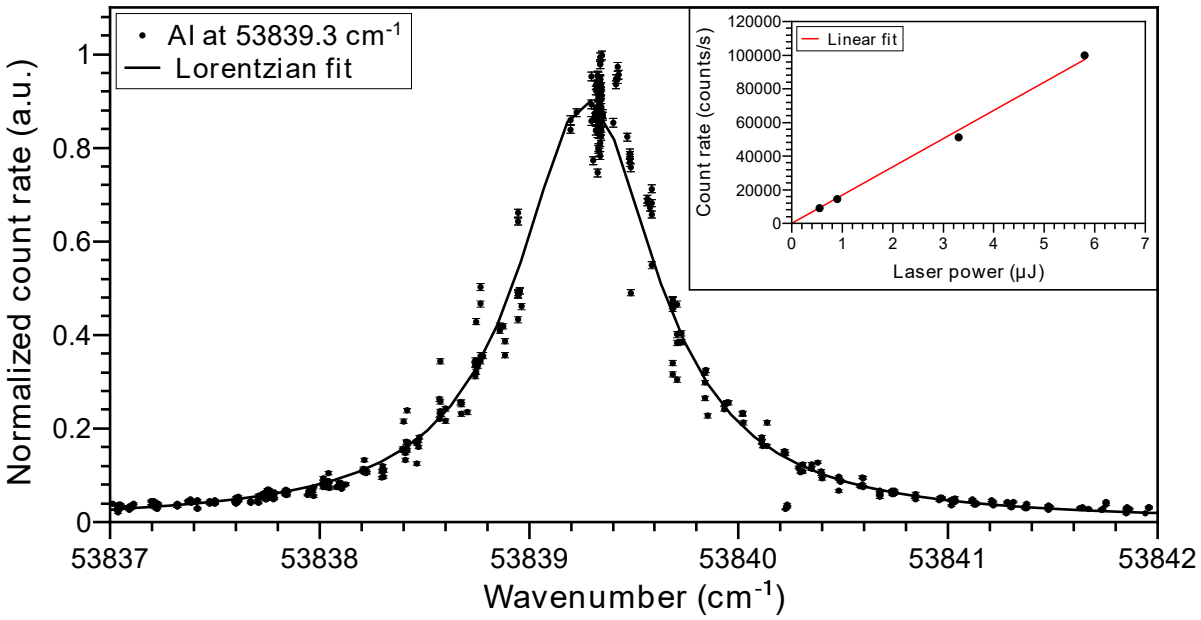

Figure A.3.: Recorded AI spectrum at 53 839.28(1) cm^{-1}. The spectrum was fitted with a Lorentzian lineshape. The inset shows the saturation curve, indicating that no saturation was reached. For more details see text.

a center frequency of 50 991.77(2) cm^{-1} and a FWHM of 1.23(6) cm^{-1} ($\approx$ 37(2) GHz) was extracted. This transition was not saturated with a laser power of up to 616 µJ/pulse (see inset in Fig. A.2).
A spectrum of the ionization step used for mimicking the on-line cycle is shown in Fig. A.3. Out of the fit (black solid line), a center frequency of 53 839.28(1) cm^{-1} and a FWHM of 0.80(1) cm^{-1} ($\approx$ 24.0(3) GHz) was extracted. This transition was not saturated with a laser power of up to 5.8 µJ/pulse (see inset in Fig. A.3).

A.2. New RFQ design

Fig A.4 a shows the mixing of the DC voltages with the applied RF field, which was realized on a PCB board outside of the jet chamber. Using a 40-way feedthrough, the RFQ is connected with this mixing box indicated by a respective label (red or yellow, numbered) on the cables (see Fig. A.4 b). Pictures of the mixing box (left), the installed RFQ (middle) and the wiring of the RFQ cables onto the 40-way feedthrough (right) are shown in the pictures on the bottom of Fig. A.4.

A.3. Transport electrodes simulations

Simulations indicated transport issues between the extraction plate and the detector. Thus, two new transport electrodes were designed to overcome this limitation. Simulations were performed with the two new transport electrodes to determine the optimal potentials as indicated in Fig. A.5 a-c. Applying a voltage of -40 V on transport electrode 1 (for the simulations connected to the extraction plate) and a voltage of -300 V on transport electrode 2 results in ion trajectories reaching the detector in a mean flight time of around 150 µs. If the voltage on transport electrode 2 is too small, e.g. -150 V as shown in Fig. A.5 a, the ions are re-attracted to the extraction plate and thus do not reach the detector.

A.4. Breakdown voltage

Paschen's law is an equation that gives the breakdown voltage V_B between two electrodes in a gas as a function of gas pressure p and gap length d [258]. It is defined as

$$V_B = \frac{B \cdot p \cdot d}{\ln(A \cdot p \cdot d) - \ln[\ln(1 + \frac{1}{\gamma})]} \tag{A.1}$$

with the secondary-electron-emission coefficient γ, the saturation ionization A in the gas, and B, which is dependent on the excitation energy and ionization energy. For argon, these parameters correspond to $A = 10.2 \frac{1}{\text{Pa·m}}$, $B = 176.27 \frac{\text{V}}{\text{Pa·m}}$ and $\gamma = 0.095$ [259]. By measuring the breakdown voltage one can calculate the shortest distance to the next electrode using eqn. A.1.

a)

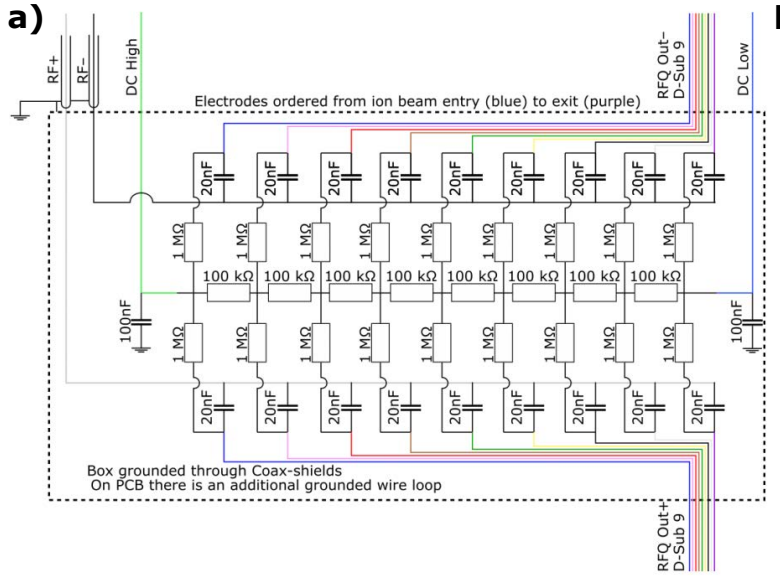

b)

Electrode	Label color	Feedthrough symbol
1	yellow	A
2	yellow	B
3	yellow	Y
4	yellow	C
5	yellow	D
6	yellow	Z
7	yellow	E
8	yellow	a
9	yellow	F
1	red	S
2	red	R
3	red	g
4	red	P
5	red	f
6	red	N
7	red	e
8	red	M
9	red	L

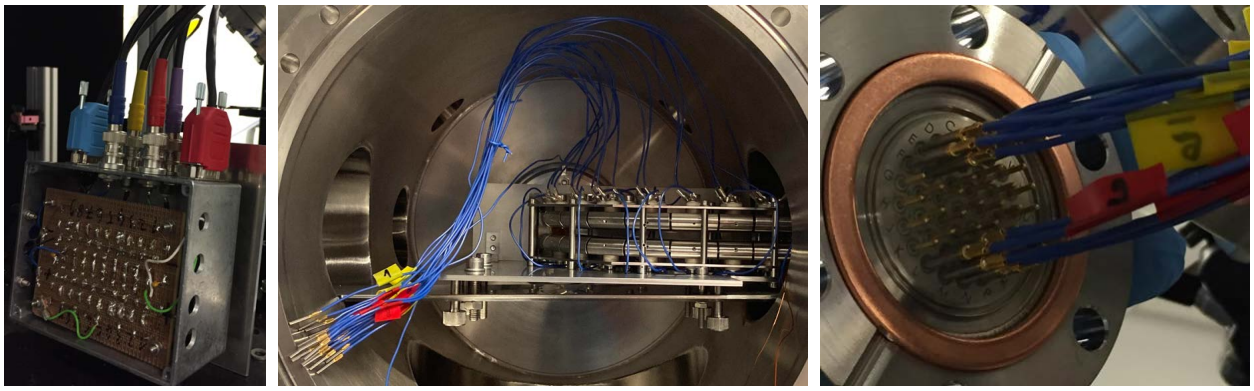

Figure A.4.: a) Mixing of DC and RF voltages on a PCB board outside of the jet chamber (photo bottom left) in order to avoid charging up inside of the chamber. Cables for each electrode are marked in different colors, starting with blue for the ion beam entry (RFQ electrode 1) towards purple for ion beam exit (RFQ electrode 9). b) Wiring of the RFQ electrodes to the 40-pin feedthrough (photo bottom right), which is connected to the RF + DC mixing board. Each electrode is labeled with a color and number for clear identification (photo middle and right). Diagonal electrodes are short-circuited.

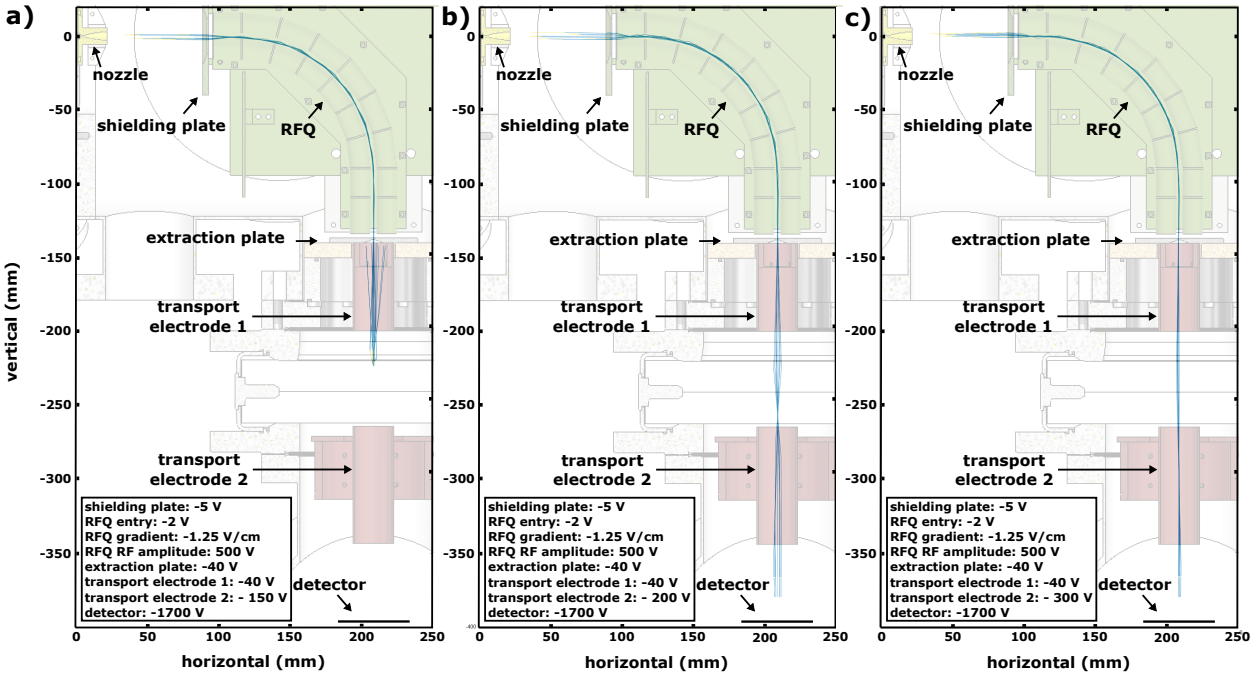

Figure A.5.: Ion extraction simulations with the new RFQ and two new transport electrodes (cylindrical electrodes) between extraction plate and detector. The simulations are shown for three different voltages applied on transport electrode 2: -150 V (a), -200 V (b) and -300 V (c). Transport electrode 1 was put on the same potential as the extraction plate, because in the first design instance they were connected to each other. In a later design stage, an insulator was placed between the extraction plate and transport electrode 1. This enabled the possibility to put a unique voltage to each electrode, improving the extraction towards the detector. The simulations were performed by [redacted].

B. Einsteinium measurements

B.1. Birge ratio

The Birge ratio [240, 241] is applied to enlarge uncertainties of the same measurand when combining inconsistent measurement results with all uncertainties being underestimated by the same common factor. The increased uncertainties according to the Birge ratio will ensure that the measurement results are consistent with each other. This method was used to combine the individual hyperfine structure constants A and B and the approach will be explained exemplary using the A parameter. First, n different values $A_1, A_2, ..., A_n$ with respective uncertainties $\Delta A_1, \Delta A_2, ..., \Delta A_n$ are combined to derive a weighted mean $\hat{A}_{\mathrm{wm}}$ with weighted uncertainty $\Delta\hat{A}_{\mathrm{wm}}$ by

$$\hat{A}_{\mathrm{wm}} = (\Delta\hat{A}_{\mathrm{wm}})^2 \cdot \sum_{i=1}^{n} \frac{A_i}{(\Delta A_i)^2} \quad \text{with} \quad \Delta\hat{A}_{\mathrm{wm}} = \left(\sum_{i=1}^{n} \frac{1}{(\Delta A_i)^2} \right)^{-1/2} . \tag{B.1}$$

In the next step a common factor, the so-called Birge ratio $\hat{\sigma}_{\mathrm{B}}$ is calculated by

$$\hat{\sigma}_{\mathrm{Birge}} = \sqrt{\frac{1}{n-1} \cdot \sum_{i=1}^{n} \frac{(A_i - \hat{A}_{\mathrm{wm}})^2}{(\Delta A_i)^2}} , \tag{B.2}$$

which is then multiplied with all standard uncertainties $A_1, A_2, ..., A_n$. The increased standard uncertainty $\Delta\hat{A}_{\mathrm{Birge}}$ associated with the weighted mean $\hat{A}_{\mathrm{Birge}}$ can be calculated by

$$\Delta\hat{A}_{\mathrm{Birge}} = \hat{\sigma}_{\mathrm{Birge}} \cdot \Delta\hat{A}_{\mathrm{wm}} \quad \text{with} \quad \hat{A}_{\mathrm{Birge}} = \hat{A}_{\mathrm{wm}} . \tag{B.3}$$

An adjustment of this method, referred to as modified Birge, was proposed in [241] because the resulting uncertainty from the Birge method associated with the adjusted value is underrated. A simple modification on the basis of an objective Bayesian inference, which is a statistical inference method, is provided in this method. This modification results in significantly increased uncertainties for small numbers n, but similar uncertainties to the ones obtained by the conventional procedure for large numbers n. As a consequence this method results in the same weighted mean but yields larger uncertainties than the conventional procedure. This modified Birge can be calculated by

$$\Delta\hat{A}_{\text{mod. Birge}} = \sqrt{\frac{n-1}{n-3}} \cdot \Delta\hat{A}_{\mathrm{Birge}} , \tag{B.4}$$

which was used to derive the increased uncertainties in this work. The increased uncertainties of B can be calculated using the same procedure.

B.2. Unresolved HFS

This section will cover four measured, but unresolved ground-state transitions in ^{254}Es. The transitions were observed at level energies of 25 433.3 cm^{-1} (see Fig. B.1), 26 297.9 cm^{-1} (see Fig. B.2), 26 357.0 cm^{-1} (see Fig. B.3), and 28 118.5 cm^{-1} (see Fig. B.4). No parameters could be extracted out of these measurements.

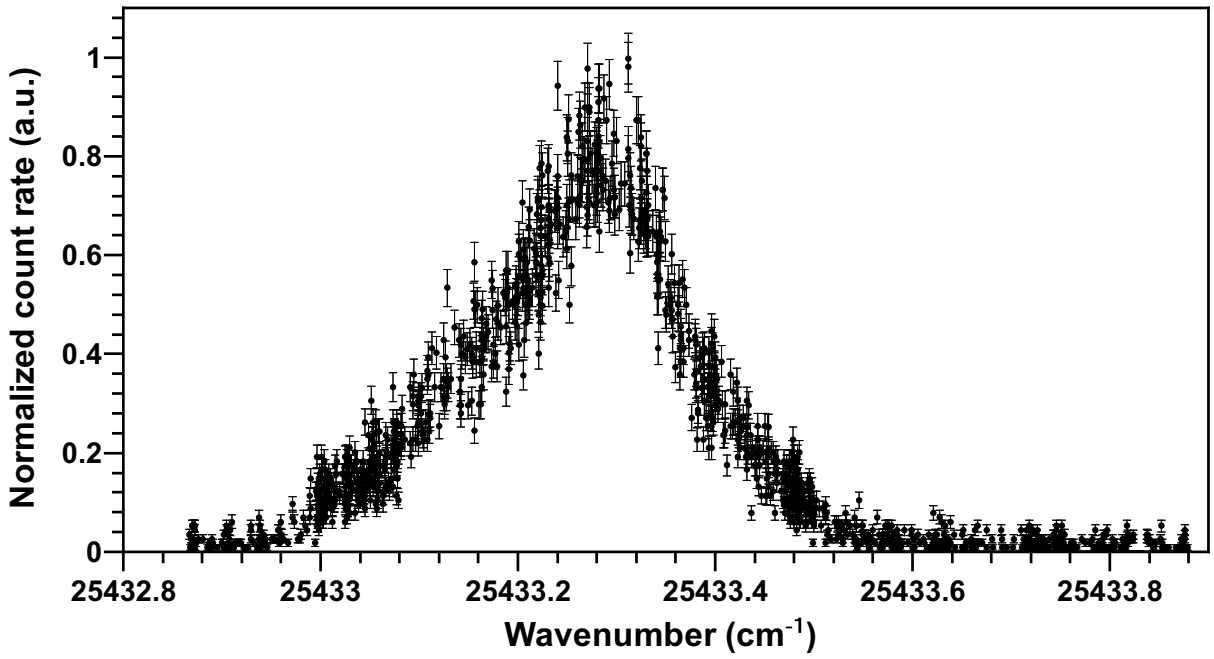

Figure B.1.: Recorded spectrum from 25 432.8 cm^{-1} to 25 433.9 cm^{-1}. The hyperfine structure was not resolved.

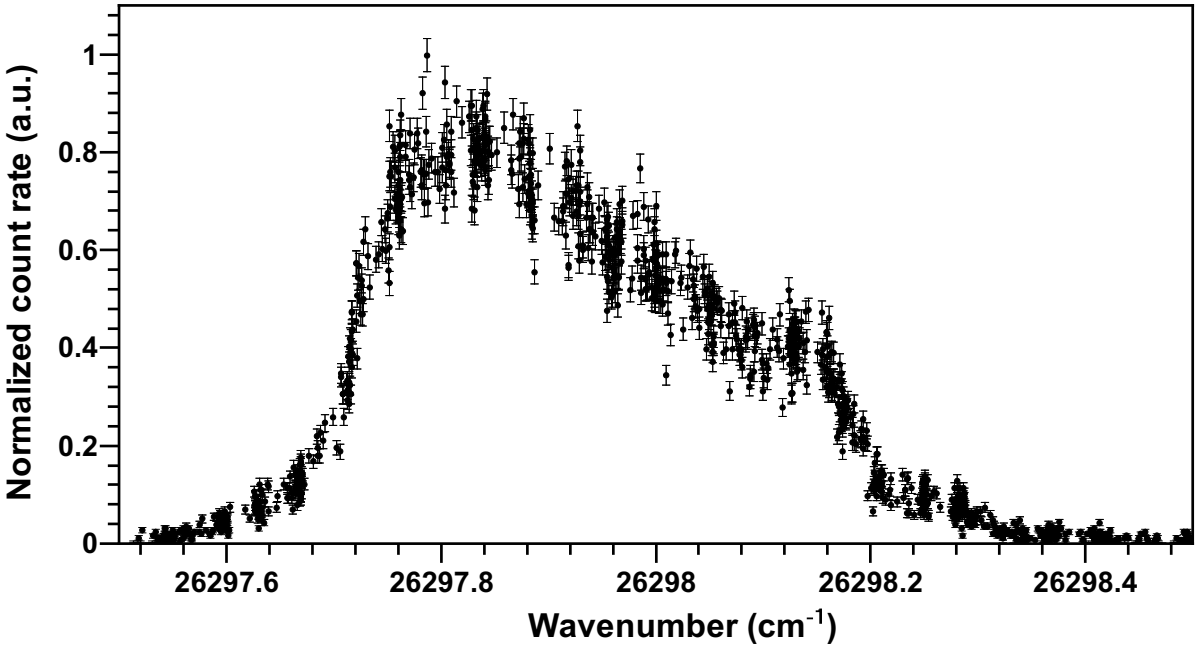

Figure B.2.: Recorded spectrum from 26 297.5 cm^{-1} to 26 298.5 cm^{-1}. The hyperfine structure was not resolved.

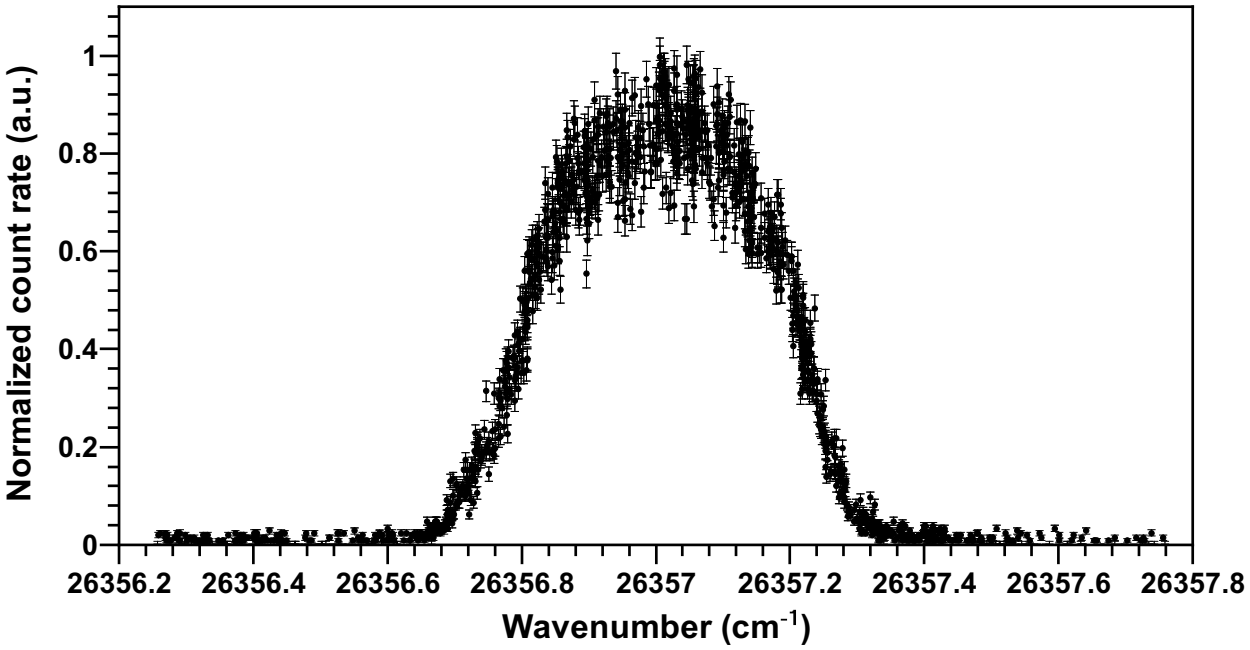

Figure B.3.: Recorded spectrum from 26 356.3 cm^{-1} to 26 357.8 cm^{-1}. The hyperfine structure was not resolved.

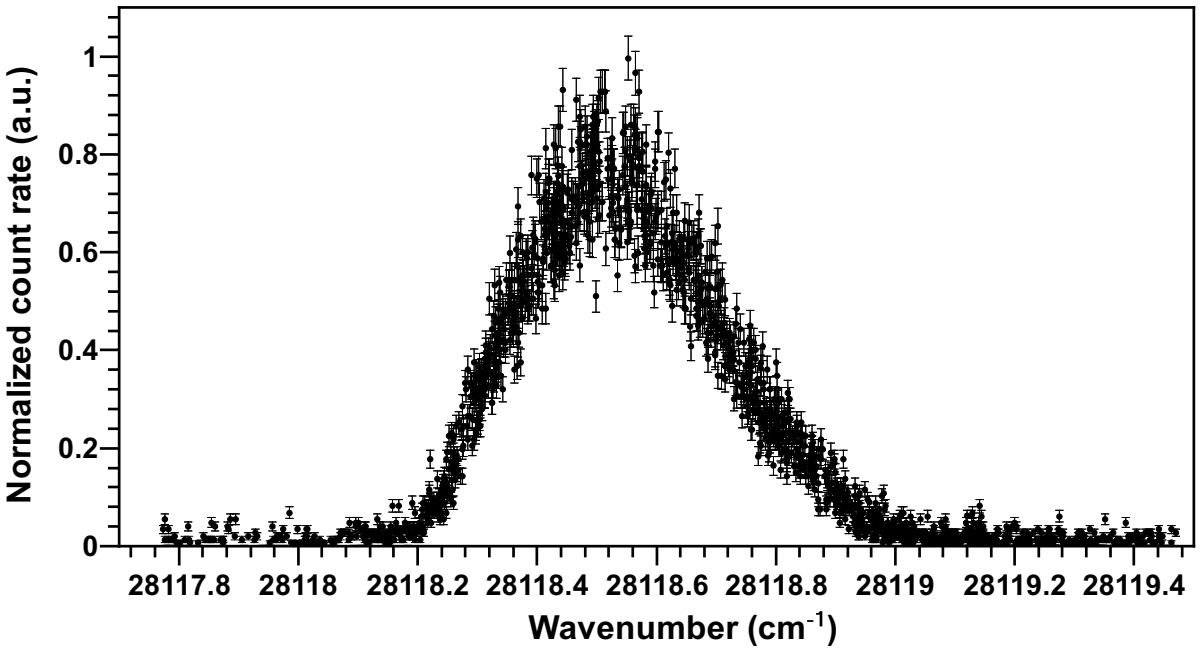

Figure B.4.: Recorded spectrum from 28 117.8 cm^{-1} to 28 119.4 cm^{-1}. The hyperfine structure was not resolved.

B.3. Partly resolved HFS

A ground-state transition to 28 578.5 cm^{-1} was partially resolved. In literature a value for the total angular momentum of $J = 15/2$ or $J = 17/2$ is assigned to the excited state [32, 33]. Fitting the hyperfine structure for both values of J resulted in partial agreement. Fig. B.5 shows both fits and it is clearly visible, that the left side of the structure is well described by both J values, whereas the right side is described by none. Both fits were not converging unless the ground-state A parameter was fixed to $A = 339$ MHz, received from the other resolved HFS. Therefore, no parameters were extracted. It is unclear what caused this discrepancy between measurement data and fit.

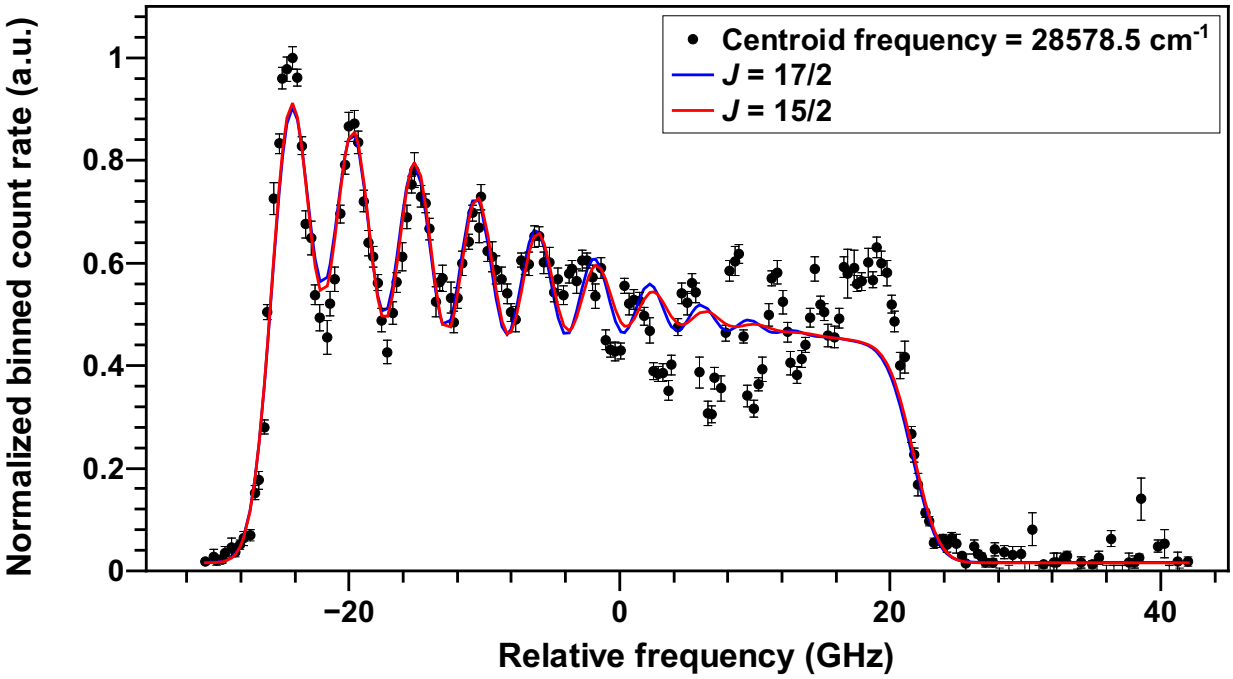

Figure B.5.: Recorded ground-state transition with a center of gravity of 28 578.5 cm^{-1}. The hyperfine structure was only partially resolved. It was tried to fit the structure for J values of 15/2 (red solid line) and 17/2 (blue solid line), but none could reproduce the measurement data.

B.4. Nuclear spin and level schemes for ^{254}Es

In order to make a conclusive spin assignment for the ground state in ^{254}Es, the recorded five individual ground-state transitions were investigated by fitting with different nuclear spins ($I = 5-9$). With the information given in section 5.7.2 and Fig. B.6 - B.11, a nuclear spin of $I = 7$ can be deduced. For nuclear spins of $I = 5$ and $I = 6$ the fit cannot describe the observed hyperfine structure, while for a spin of $I = 8$ and $I = 9$ the individual fits result in a proper fit, but without sharing the same ground-state hyperfine parameters. The only exception is the ground-state transition to the 24 338.23(5) cm^{-1} level, where only a spin of $I = 7$ can properly describe the observed spectrum.
Fig. B.12 shows the level schemes for the five ground-state transitions. Information about the level energy, laser wavelength, level configuration, hyperfine structure parameters A and B for the ground state and excited state, the total angular momentum J, and the atomic total angular momentum F are displayed if known.

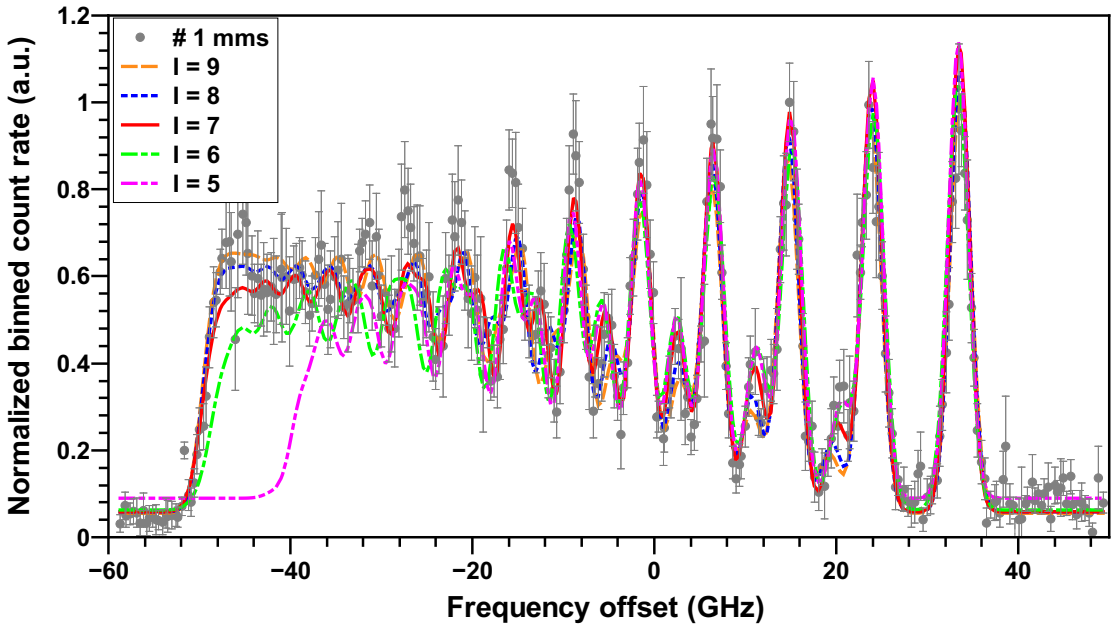

Figure B.6.: Measured HFS for the ground-state transition to the 23 934.20(5) cm^{-1} level (mms) in ^{254}Es as referenced in Fig. 5.10. The colored dashed and solid lines represent the best fits to the measured HFS for different values of the nuclear spin I.

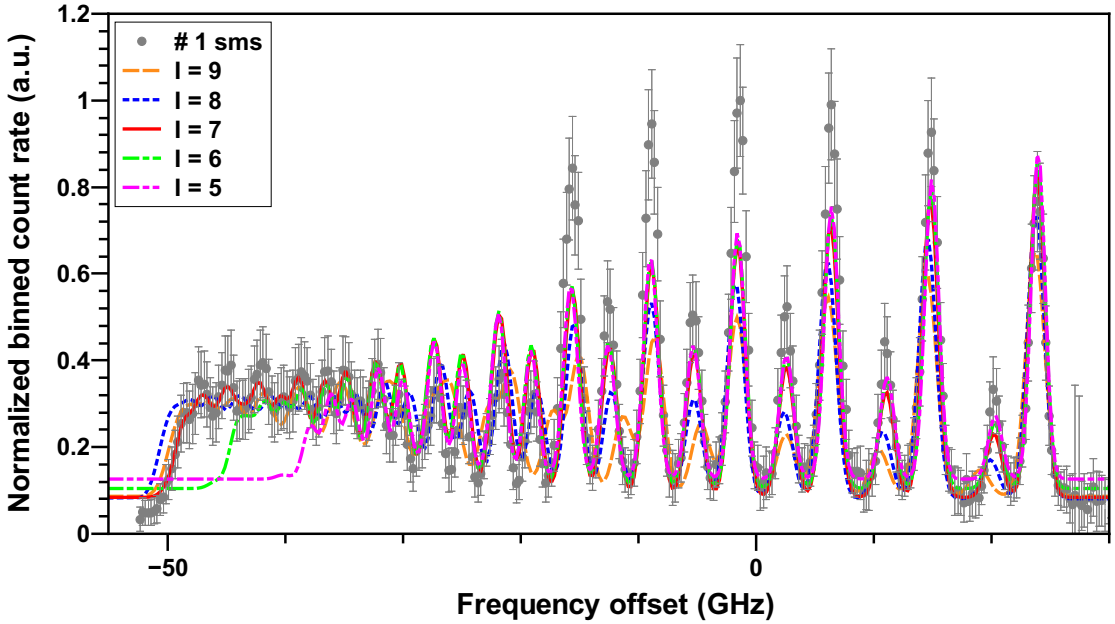

Figure B.7.: Measured HFS for the ground-state transition to the 23 934.20(5) cm^{-1} level (sms) in ^{254}Es as referenced in Fig. 5.10. The colored dashed and solid lines represent the best fits to the measured HFS for different values of the nuclear spin I.

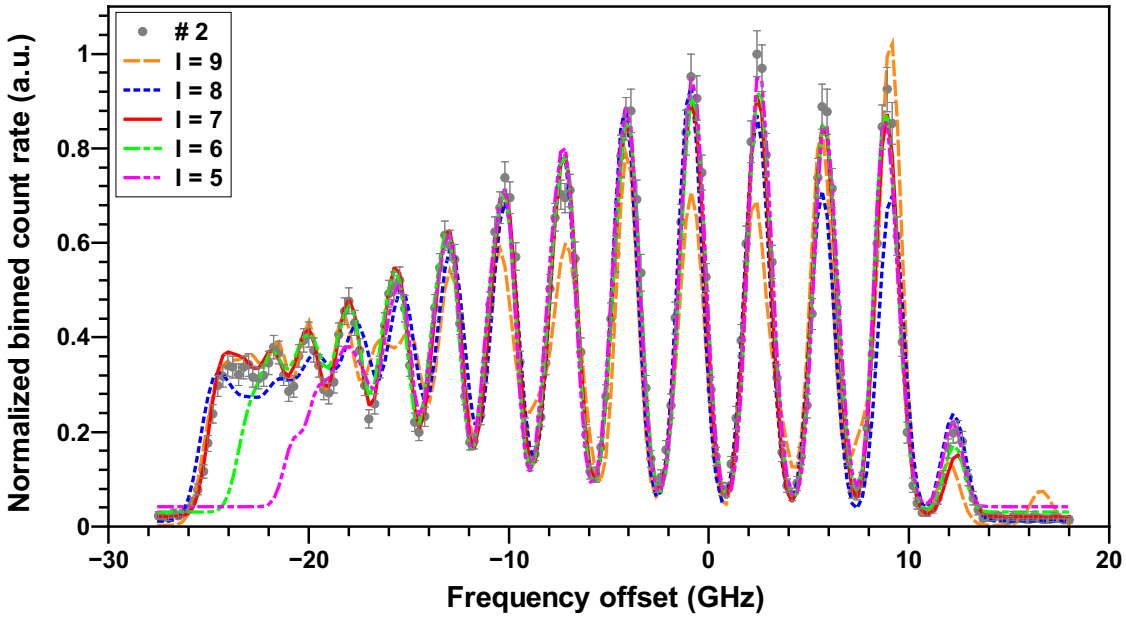

Figure B.8.: Measured HFS for the ground-state transition to the 24 338.23(5) cm^{-1} level in ^{254}Es as referenced in Fig. 5.10. The colored dashed and solid lines represent the best fits to the measured HFS for different values of the nuclear spin I.

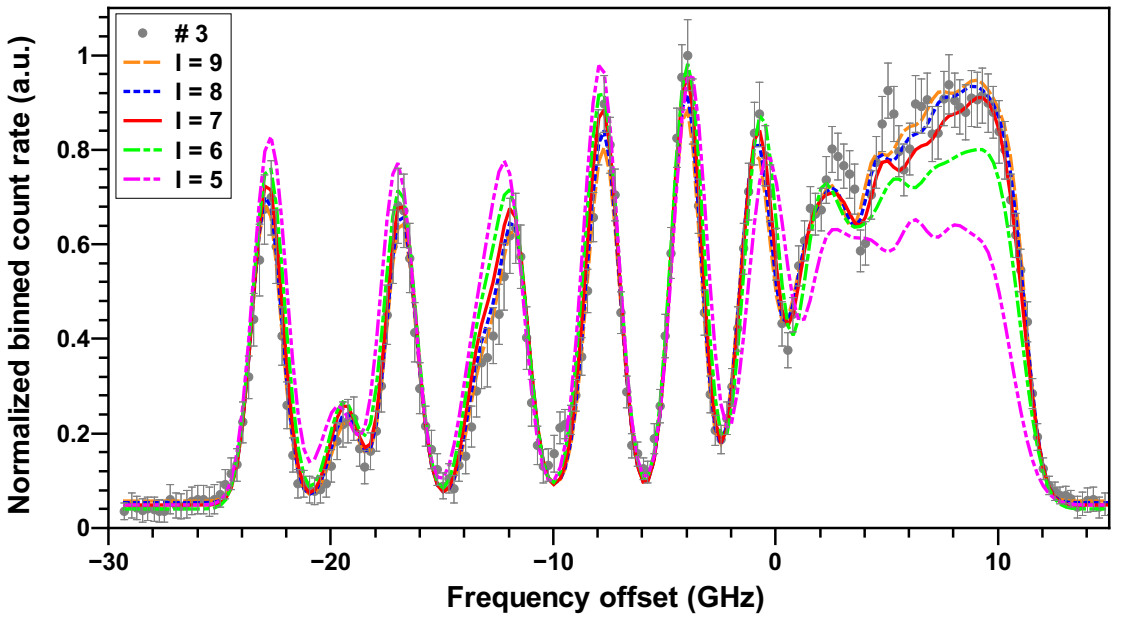

Figure B.9.: Measured HFS for the ground-state transition to the 24 489.12(5) cm^{-1} level in ^{254}Es as referenced in Fig. 5.10. The colored dashed and solid lines represent the best fits to the measured HFS for different values of the nuclear spin I.

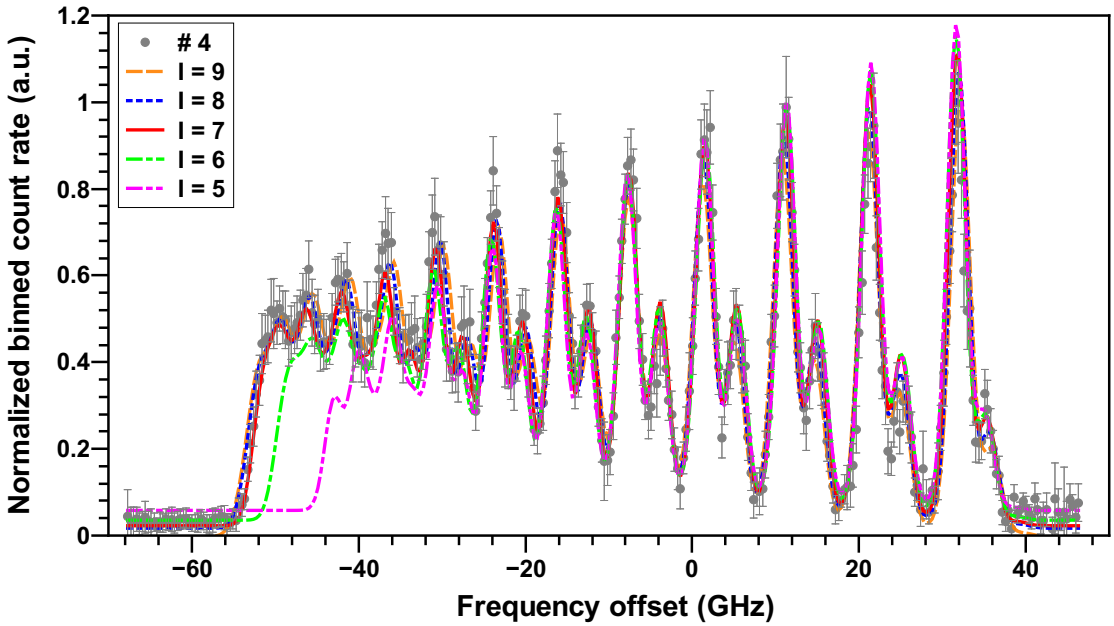

Figure B.10.: Measured HFS for the ground-state transition to the 27 440.06(5) cm^{-1} level in ^{254}Es as referenced in Fig. 5.10. The colored dashed and solid lines represent the best fits to the measured HFS for different values of the nuclear spin I.

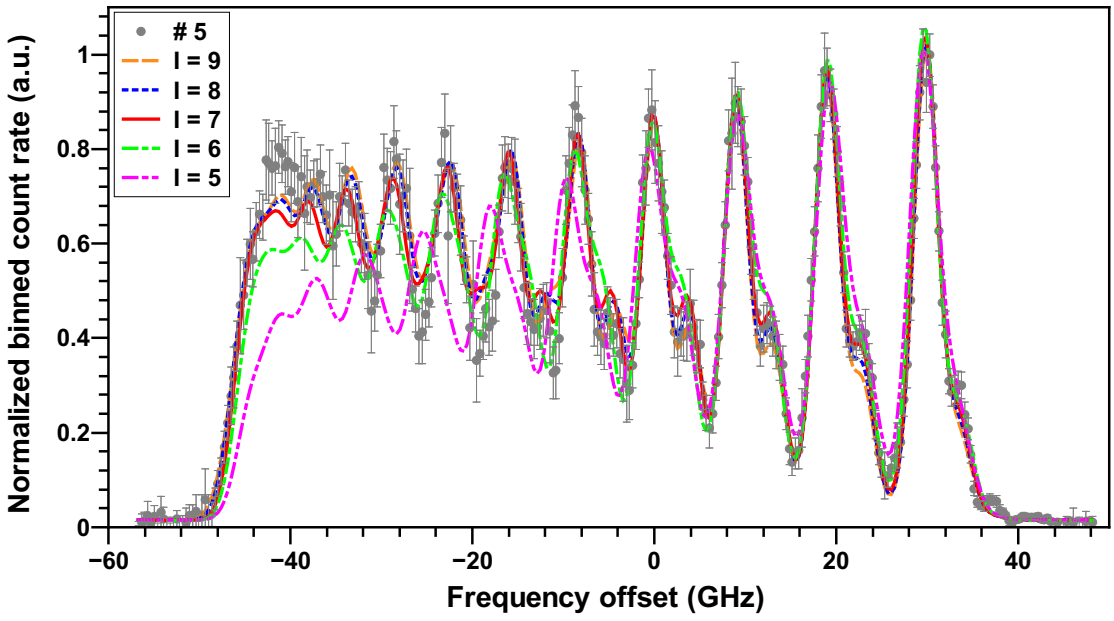

Figure B.11.: Measured HFS for the ground-state transition to the 28 446.86(5) cm^{-1} level in ^{254}Es as referenced in Fig. 5.10. The colored dashed and solid lines represent the best fits to the measured HFS for different values of the nuclear spin I.

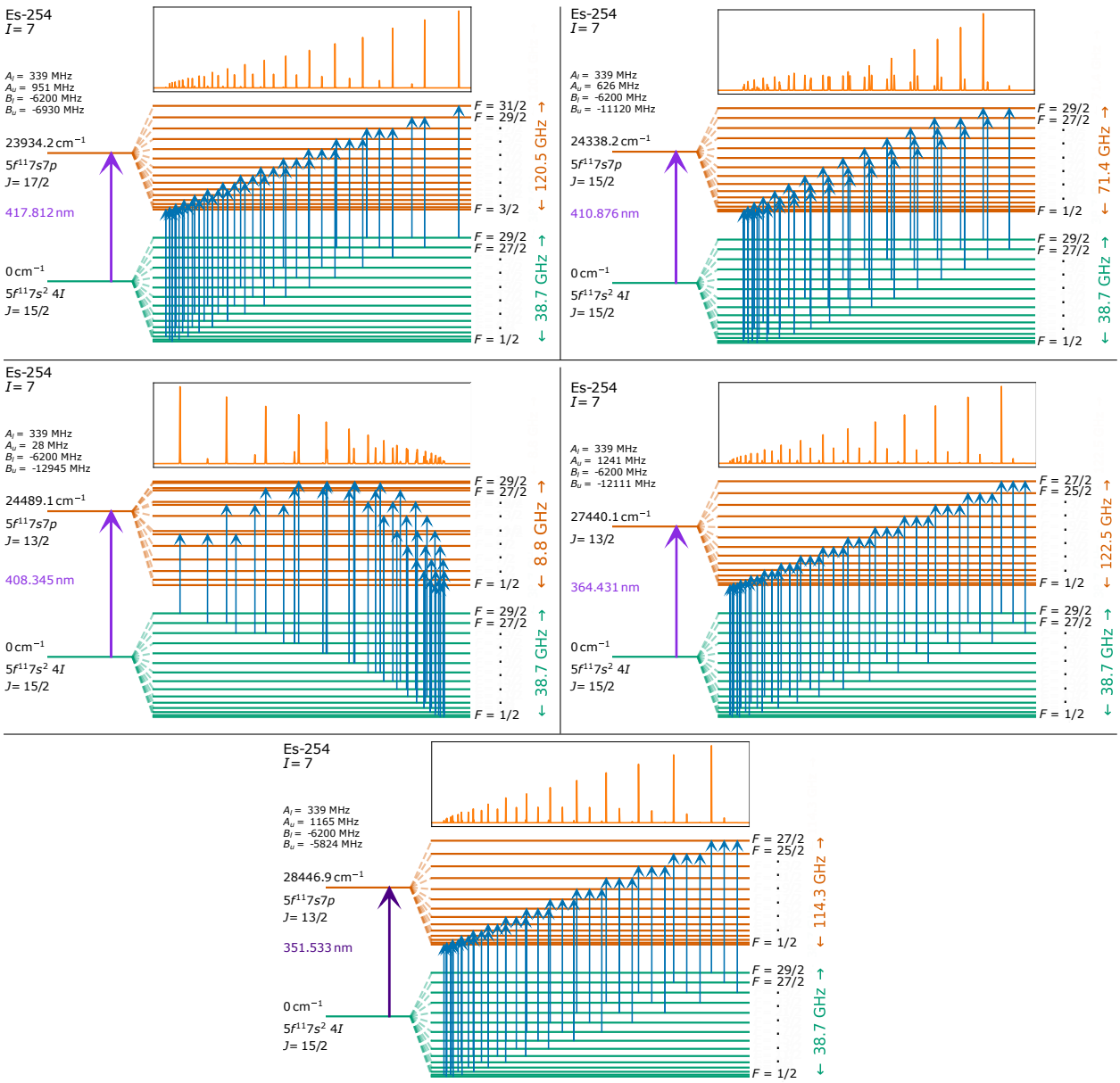

Figure B.12.: Predicted level schemes for the hyperfine structure splittings in the ground-state transitions measured for ^{254}Es. The level energy, laser wavelength, configuration, hyperfine structure parameters A and B, the total angular momentum J, and the atomic total angular momentum F are displayed in the respective scheme if known.

List of Figures

List of Tables

Bibliography

[1] M. Block, M. Laatiaoui, and S. Raeder. Recent progress in laser spectroscopy of the actinides. *Prog. Part. Nucl. Phys.*, 116:103834, 2021. doi: 10.1016/j.ppnp.2020.103834.

[2] E. Eliav, S. Fritzsche, and U. Kaldor. Electronic structure theory of the superheavy elements. *Nucl. Phys. A*, 944:518–550, 2015. doi: 10.1016/j.nuclphysa.2015.06.017.

[3] P. Campbell, I. D. Moore, and M. R. Pearson. Laser spectroscopy for nuclear structure physics. *Prog. Part. Nucl. Phys.*, 86:127–180, 2016. doi: 10.1016/j.ppnp.2015.09.003.

[4] J. B. Roberto, C. W. Alexander, R. A. Boll, J. D. Burns, J. G. Ezold, L. K. Felker, S. L. Hogle, and K. P. Rykaczewski. Actinide targets for the synthesis of super-heavy elements. *Nucl. Phys. A*, 944:99–116, 2015. doi: 10.1016/j.nuclphysa.2015.06.009.

[5] S. M. Robinson, D. E. Benker, E. D. Collins, J. G. Ezold, J. R. Garrison, and S. L. Hogle. Production of Cf-252 and other transplutonium isotopes at Oak Ridge National Laboratory. *Radiochim. Acta*, 108(9):737–746, sep 2020. doi: 10.1515/ract-2020-0008.

[6] F. Rösch. *Nuclear- and Radiochemistry / Introduction.* De Gruyter, Berlin Boston, 2014. ISBN 9783110221916.

[7] J.-V. Kratz and K. H. Lieser, editors. *Nuclear and Radiochemistry.* Wiley-VCH Verlag GmbH & Co. KGaA, 2013. ISBN 9783527653331. doi: 10.1002/9783527653331.

[8] S. A. Giuliani, Z. Matheson, W. Nazarewicz, E. Olsen, P.-G. Reinhard, J. Sadhukhan, B. Schuetrumpf, N. Schunck, and P. Schwerdtfeger. Colloquium : Superheavy elements: Oganesson and beyond. *Rev. Mod. Phys.*, 91(1):011001, 2019. doi: 10.1103/revmodphys.91.011001.

[9] M. Schädel and D. Shaughnessy, editors. *The Chemistry of Superheavy Elements.* Springer-Verlag GmbH, 2013. ISBN 9783642374661.

[10] B. Schuetrumpf, W. Nazarewicz, and P.-G. Reinhard. Central depression in nucleonic densities: Trend analysis in the nuclear density functional theory approach. *Phys. Rev. C*, 96(2):024306, 2017. doi: 10.1103/physrevc.96.024306.

[11] P. Möller. The limits of the nuclear chart set by fission and alpha decay. *EPJ Web of Conferences*, 131:03002, 2016. doi: 10.1051/epjconf/201613103002.

[12] R.-D. Herzberg. Nuclear Structure of Superheavy Elements. In *The Chemistry of Superheavy Elements*, pages 83–133. Springer Berlin Heidelberg, 2013. doi: 10.1007/978-3-642-37466-1_2.

[13] L. Öhrström and J. Reedijk. Names and symbols of the elements with atomic numbers 113, 115, 117 and 118 IUPAC Recommendations 2016. *Pure Appl. Chem.*, 88(12): 1225–1229, 2016. doi: 10.1515/pac-2016-0501.

[14] Yu. Ts. Oganessian, V. K. Utyonkov, Yu. V. Lobanov, F. Sh. Abdullin, A. N. Polyakov, R. N. Sagaidak, I. V. Shirokovsky, Yu. S. Tsyganov, A. A. Voinov, G. G. Gulbekian, S. L. Bogomolov, B. N. Gikal, A. N. Mezentsev, S. Iliev, V. G. Subbotin, A. M. Sukhov, K. Subotic, V. I. Zagrebaev, G. K. Vostokin, M. G. Itkis, K. J. Moody, J. B. Patin, D. A. Shaughnessy, M. A. Stoyer, N. J. Stoyer, P. A. Wilk, J. M. Kenneally, J. H. Landrum, J. F. Wild, and R. W. Lougheed. Synthesis of the isotopes of elements 118 and 116 in the ^{249}Cf and ^{245}Cm + ^{48}Ca fusion reactions. *Phys. Rev. C*, 74(4):044602, 2006. doi: 10.1103/physrevc.74.044602.

[15] M. G. Mayer. On Closed Shells in Nuclei. II. *Phys. Rev.*, 75(12):1969–1970, 1949. doi: 10.1103/physrev.75.1969.

[16] K. L. G. Heyde. *The Nuclear Shell Model*. Springer Berlin Heidelberg, 1994. doi: 10.1007/978-3-642-79052-2_4.

[17] M. G. Mayer. The Shell Model. *Science*, 145(3636):999–1006, 1964. doi: 10.1126/science.145.3636.999.

[18] R.-D. Herzberg, P. T. Greenlees, P. A. Butler, G. D. Jones, M. Venhart, I. G. Darby, S. Eeckhaudt, K. Eskola, T. Grahn, C. Gray-Jones, F. P. Hessberger, P. Jones, R. Julin, S. Juutinen, S. Ketelhut, W. Korten, M. Leino, A.-P. Leppänen, S. Moon, M. Nyman, R. D. Page, J. Pakarinen, A. Pritchard, P. Rahkila, J. Sarén, C. Scholey, A. Steer, Y. Sun, Ch. Theisen, and J. Uusitalo. Nuclear isomers in superheavy elements as stepping stones towards the island of stability. *Nature*, 442(7105):896–899, 2006. doi: 10.1038/nature05069.

[19] E. Minaya Ramirez, D. Ackermann, K. Blaum, M. Block, C. Droese, Ch. E. Düllmann, M. Dworschak, M. Eibach, S. Eliseev, E. Haettner, F. Herfurth, F. P. Hessberger, S. Hofmann, J. Ketelaer, G. Marx, M. Mazzocco, D. Nesterenko, Y. N. Novikov, W. R. Plass, D. Rodriguez, C. Scheidenberger, L. Schweikhard, P. G. Thirolf, and C. Weber. Direct Mapping of Nuclear Shell Effects in the Heaviest Elements. *Science*, 337(6099):1207–1210, 2012. doi: 10.1126/science.1225636.

[20] Z. Patyk and A. Sobiczewski. Main deformed shells of heavy nuclei studied in a multidimensional deformation space. *Phys. Lett. B*, 256(3-4):307–310, 1991. doi: 10.1016/0370-2693(91)91766-o.

[21] J. Dvorak, W. Brüchle, M. Chelnokov, R. Dressler, Ch. E. Düllmann, K. Eberhardt, V. Gorshkov, E. Jäger, R. Krücken, A. Kuznetsov, Y. Nagame, F. Nebel, Z. Novackova, Z. Qin, M. Schädel, B. Schausten, E. Schimpf, A. Semchenkov, P. Thörle, A. Türler, M. Wegrzecki, B. Wierczinski, A. Yakushev, and A. Yeremin. Doubly Magic Nucleus $^{270}_{108}\mathrm{Hs}_{162}$. *Phys. Rev. Lett.*, 97(24):242501, 2006. doi: 10.1103/physrevlett.97.242501.

[22] M. Bender, W. Nazarewicz, and P.-G. Reinhard. Shell stabilization of super- and hyperheavy nuclei without magic gaps. *Phys. Lett. B*, 515(1-2):42–48, 2001. doi: 10.1016/s0370-2693(01)00863-2.

[23] M. Block. Direct mass measurements and ionization potential measurements of the actinides. *Radiochim. Acta*, 107(9-11):821–831, 2019. doi: 10.1515/ract-2019-3143.

[24] R. Firestone. *Table of isotopes*. Wiley, New York, 1999. ISBN 9780471356332.

[25] R. Neugart and G. Neyens. Nuclear Moments. In *The Euroschool Lectures on Physics with Exotic Beams, Vol. II*, pages 135–189. Springer Berlin Heidelberg. doi: 10.1007/3-540-33787-3_4.

[26] W. Nörtershäuser and Ch. Geppert. Nuclear Charge Radii of Light Elements and Recent Developments in Collinear Laser Spectroscopy. In *The Euroschool on Exotic Beams, Vol. IV*, pages 233–292. Springer Berlin Heidelberg, 2014. doi: 10.1007/978-3-642-45141-6_6.

[27] R. V. Ambartzumian and V. S. Letokhov. Selective Two-Step (STS) Photoionization of Atoms and Photodissociation of Molecules by Laser Radiation. *Appl. Opt.*, 11(2):354, 1972. doi: 10.1364/ao.11.000354.

[28] G. S. Hurst, M. G. Payne, S. D. Kramer, and J. P. Young. Resonance ionization spectroscopy and one-atom detection. *Rev. Mod. Phys.*, 51(4):767–819, 1979. doi: 10.1103/revmodphys.51.767.

[29] K. Wendt, T. Gottwald, C. Mattolat, and S. Raeder. Ionization potentials of the lanthanides and actinides – towards atomic spectroscopy of super-heavy elements. *Hyperfine Interact.*, 227(1-3):55–67, 2014. doi: 10.1007/s10751-014-1041-8.

[30] K. Blaum, J. Dilling, and W. Nörtershäuser. Precision atomic physics techniques for nuclear physics with radioactive beams. *Phys. Scr.*, T152:014017, 2013. doi: 10.1088/0031-8949/2013/t152/014017.

[31] J. Blaise and J.-F. Wyart. *Constantes selectionnees niveaux d'energie et spectres atomiques des actinides*. Centre National de la Recherche Scientifique, Paris, France, 480, Paris, 1992. ISBN 2950641407.

[32] E. F. Worden, R. W. Lougheed, R. G. Gutmacher, and J. G. Conway. Hyperfine structure in the ^{253}Es emission spectrum, III: Extension of the line list, levels of Es i and Es ii, nuclear magnetic-dipole and quadrupole moments. *J. Opt. Soc. Am.*, 64(1):77, 1974. doi: 10.1364/josa.64.000077.

[33] J.-F. Wyart, J. Blaise, and E. F. Worden. Studies of electronic configurations in the emission spectra of lanthanides and actinides: application to the interpretation of Es I and Es II, predictions for Fm I. *J. Solid State Chem.*, 178(2):589–602, 2005. doi: 10.1016/j.jssc.2004.09.032.

[34] L. S. Goodman, H. Diamond, and H. E. Stanton. Nuclear and atomic moments and hyperfine-structure parameters of Es-253 and Es-254m. *Phys. Rev. A*, 11(2):499–504, 1975. doi: 10.1103/physreva.11.499.

[35] M. Nunnemann. *Bestimmung der Ionisationsenergien von Einsteinium und Uran mittels Resonanzionisationsmassenspektrometrie*. PhD thesis, 1999.

[36] L. Morss. *The chemistry of the actinide and transactinide elements*. Springer, Dordrecht, 2006. ISBN 1402035551.

[37] N. Severijns, A. A. Belyaev, A. L. Erzinkyan, P. D. Eversheim, V. T. Filimonov, V. V. Golovko, G. M. Gurevich, P. Herzog, I. S. Kraev, A. A. Lukhanin, V. I. Noga, V. P. Parfenova, T. Phalet, A. V. Rusakov, M. Tandecki, Yu. G. Toporov, C. Tramm, E. Traykov, S. Van Gorp, V. N. Vyachin, F. Wauters, D. Zákoucký, and E. Zotov. Hyperfine field of einsteinium in iron and nuclear magnetic moment of ^{254}Es. *Phys. Rev. C*, 79:064322, 2009. doi: 10.1103/PhysRevC.79.064322.

[38] B. Singh. Nuclear Data Sheets for A=254. *Nucl. Data Sheets*, 156:1–69, 2019. doi: 10.1016/j.nds.2019.02.003.

[39] G. M. Gurevich, A. L. Erzinkyan, and V. P. Parfenova. Angular distributions of α particles emitted by oriented nuclei and their relation to nuclear deformation. *Bull. Russ. Acad. Sci.: Phys.*, 75(4):520–525, 2011. doi: 10.3103/s1062873811040186.

[40] T. Kron, Y. Liu, S. Richter, F. Schneider, and K. Wendt. High efficiency resonance ionization of palladium with Ti:sapphire lasers. *J. Phys. B*, 49(18):185003, 2016. doi: 10.1088/0953-4075/49/18/185003.

[41] S. Nothhelfer, Th. E. Albrecht-Schönzart, M. Block, P. Chhetri, Ch. E. Düllmann, J. G. Ezold, V. Gadelshin, A. Gaiser, F. Giacoppo, R. Heinke, T. Kieck, N. Kneip, M. Laatiaoui, Ch. Mokry, S. Raeder, J. Runke, F. Schneider, J. M. Sperling, D. Studer, P. Thörle-Pospiech, N. Trautmann, F. Weber, and K. Wendt. Nuclear structure investigations of $^{253\text{-}255}$Es by laser spectroscopy. *Phys. Rev. C*, 105(2):l021302, 2022. doi: 10.1103/physrevc.105.l021302.

[42] F. Lautenschläger, P. Chhetri, D. Ackermann, H. Backe, M. Block, B. Cheal, A. Clark, C. Droese, R. Ferrer, F. Giacoppo, S. Götz, F. P. Heßberger, O. Kaleja, J. Khuyagbaatar, P. Kunz, A. K. Mistry, M. Laatiaoui, W. Lauth, S. Raeder, Th. Walther, and C. Wraith. Developments for resonance ionization laser spectroscopy of the heaviest elements at SHIP. *Nucl. Instrum. Methods Phys. Res. B*, 383:115–122, 2016. doi: 10.1016/j.nimb.2016.06.001.

[43] H. Backe, W. Lauth, M. Block, and M. Laatiaoui. Prospects for laser spectroscopy, ion chemistry and mobility measurements of superheavy elements in buffer-gas traps. *Nucl. Phys. A*, 944:492–517, 2015. doi: 10.1016/j.nuclphysa.2015.07.002.

[44] M. Laatiaoui, W. Lauth, H. Backe, M. Block, D. Ackermann, B. Cheal, P. Chhetri, Ch. E. Düllmann, J. Even, R. Ferrer, F. Giacoppo, S. Götz, F. P. Heßberger, M. Huyse, O. Kaleja, J. Khuyagbaatar, P. Kunz, F. Lautenschläger, A. K. Mistry, S. Raeder,

E. Minaya Ramirez, P. Van Duppen, Th. Walther, C. Wraith, and A. Yakushev. Atom-at-a-time laser resonance ionization spectroscopy of nobelium. *Nature*, 538(7626):495–498, 2016. doi: 10.1038/nature19345.

[45] P. Chhetri, D. Ackermann, H. Backe, M. Block, B. Cheal, C. Droese, Ch. E. Düllmann, J. Even, R. Ferrer, F. Giacoppo, S. Götz, F. P. Heßberger, M. Huyse, O. Kaleja, J. Khuyagbaatar, P. Kunz, M. Laatiaoui, F. Lautenschläger, W. Lauth, N. Lecesne, L. Lens, E. Minaya Ramirez, A. K. Mistry, S. Raeder, P. Van Duppen, Th. Walther, A. Yakushev, and Z. Zhang. Precision Measurement of the First Ionization Potential of Nobelium. *Phys. Rev. Lett.*, 120(26):263003, 2018. doi: 10.1103/physrevlett.120.263003.

[46] S. Raeder, D. Ackermann, H. Backe, R. Beerwerth, J. C. Berengut, M. Block, A. Borschevsky, B. Cheal, P. Chhetri, Ch. E. Düllmann, V. A. Dzuba, E. Eliav, J. Even, R. Ferrer, V. V. Flambaum, S. Fritzsche, F. Giacoppo, S. Götz, F. P. Heßberger, M. Huyse, U. Kaldor, O. Kaleja, J. Khuyagbaatar, P. Kunz, M. Laatiaoui, F. Lautenschläger, W. Lauth, A. K. Mistry, E. Minaya Ramirez, W. Nazarewicz, S. G. Porsev, M. S. Safronova, U. I. Safronova, B. Schuetrumpf, P. Van Duppen, T. Walther, C. Wraith, and A. Yakushev. Probing Sizes and Shapes of Nobelium Isotopes by Laser Spectroscopy. *Phys. Rev. Lett.*, 120(23):232503, 2018. doi: 10.1103/physrevlett.120.232503.

[47] Yu. Kudryavtsev, R. Ferrer, M. Huyse, P. Van den Bergh, and P. Van Duppen. The in-gas-jet laser ion source: Resonance ionization spectroscopy of radioactive atoms in supersonic gas jets. *Nucl. Instrum. Methods Phys. Res. B*, 297:7–22, 2013. doi: 10.1016/j.nimb.2012.12.008.

[48] S. Raeder, B. Bastin, M. Block, P. Creemers, P. Delahaye, R. Ferrer, X. Fléchard, S. Franchoo, L. Ghys, L. P. Gaffney, C. Granados, R. Heinke, L. Hijazi, M. Huyse, T. Kron, Yu. Kudryavtsev, M. Laatiaoui, N. Lecesne, F. Luton, I. D. Moore, Y. Martinez, E. Mogilevskiy, P. Naubereit, J. Piot, S. Rothe, H. Savajols, S. Sels, V. Sonnenschein, E. Traykov, C. Van Beveren, P. Van den Bergh, P. Van Duppen, K. Wendt, and A. Zadvornaya. Developments towards in-gas-jet laser spectroscopy studies of actinium isotopes at LISOL. *Nucl. Instrum. Methods Phys. Res. B*, 376:382–387, 2016. doi: 10.1016/j.nimb.2015.12.014.

[49] R. Ferrer, A. Barzakh, B. Bastin, R. Beerwerth, M. Block, P. Creemers, H. Grawe, R. de Groote, P. Delahaye, X. Fléchard, S. Franchoo, S. Fritzsche, L. P. Gaffney, L. Ghys, W. Gins, C. Granados, R. Heinke, L. Hijazi, M. Huyse, T. Kron, Yu. Kudryavtsev, M. Laatiaoui, N. Lecesne, M. Loiselet, F. Lutton, I. D. Moore, Y. Martínez, E. Mogilevskiy, P. Naubereit, J. Piot, S. Raeder, S. Rothe, H. Savajols, S. Sels, V. Sonnenschein, J.-C. Thomas, E. Traykov, C. Van Beveren, P. Van den Bergh, P. Van Duppen, K. Wendt, and A. Zadvornaya. Towards high-resolution laser ionization spectroscopy of the heaviest elements in supersonic gas jet expansion. *Nat. Commun.*, 8(1), 2017. doi: 10.1038/ncomms14520.

[50] A. Zadvornaya, P. Creemers, K. Dockx, R. Ferrer, L. P. Gaffney, W. Gins, C. Granados, M. Huyse, Yu. Kudryavtsev, M. Laatiaoui, E. Mogilevskiy, S. Raeder, S. Sels, P. Van den Bergh, P. Van Duppen, M. Verlinde, E. Verstraelen, M. Nabuurs, D. Reynaerts, and P. Papadakis. Characterization of Supersonic Gas Jets for High-Resolution Laser Ionization Spectroscopy of Heavy Elements. *Phys. Rev. X*, 8(4):041008, 2018. doi: 10.1103/physrevx.8.041008.

[51] W. Demtröder. *Laserspektroskopie - Grundlagen und Techniken*. Springer Berlin Heidelberg, 2007. ISBN 9783662082669. doi: 10.1007/978-3-540-33793-5.

[52] W. Demtröder. *Laserspektroskopie 2*. Springer Berlin Heidelberg, 2013. ISBN 9783642214479. doi: 10.1007/978-3-642-21447-9.

[53] W. Demtröder. *Experimentalphysik 3*. Springer-Verlag GmbH, 2016. ISBN 9783662490945.

[54] W. Demtröder. *Experimentalphysik 4*. Springer-Verlag GmbH, 2017. ISBN 9783662528846.

[55] G. Drake, editor. *Springer Handbook of Atomic, Molecular, and Optical Physics*. Springer New York, 2006. doi: 10.1007/978-0-387-26308-3.

[56] P. W. Atkins. *Physical chemistry*. W.H. Freeman and Co, New York, 2010. ISBN 1429218126.

[57] Ch. J. Foot. *Atomic Physics*. Oxford Univ. Pr., 2005. ISBN 0198506961.

[58] Ch. Mortimer. *Chemie - Das Basiswissen der Chemie*. Thieme, Stuttgart, 2003. ISBN 3134843080.

[59] E. Tiesinga, P. J. Mohr, D. B. Newell, and B. N. Taylor. The 2018 CODATA Recommended Values of the Fundamental Physical Constants (Web Version 8.1). Database developed by J. Baker, M. Douma, and S. Kotochigova. National Institute of Standards and Technology, Gaithersburg. 2019, MD 20899. URL `http://physics.nist.gov/constants`. Visited: 14.03.2022.

[60] B. Scott. *Elements of Quantum Optics*. ED-TECH Press, 2019.

[61] W. E. Lamb and R. C. Retherford. Fine Structure of the Hydrogen Atom by a Microwave Method. *Phys. Rev.*, 72(3):241–243, 1947. doi: 10.1103/physrev.72.241.

[62] F. F. Karpeshin and M. B. Trzhaskovskaya. The theory of the Bohr–Weisskopf effect in the hyperfine structure. *Nucl. Phys. A*, 941:66–77, 2015. doi: 10.1016/j.nuclphysa.2015.06.001.

[63] A. Bohr and V. F. Weisskopf. The Influence of Nuclear Structure on the Hyperfine Structure of Heavy Elements. *Phys. Rev.*, 77(1):94–98, 1950. doi: 10.1103/physrev.77.94.

[64] J. E. Rosenthal and G. Breit. The Isotope Shift in Hyperfine Structure. *Phys. Rev.*, 41(4):459–470, 1932. doi: 10.1103/physrev.41.459.

[65] H. Kopferman and E. E. Schneider. *Nuclear Moments*. Elsevier Science and Techn., 2013. ISBN 9781483275789.

[66] J. R. Persson. Table of hyperfine anomaly in atomic systems. *At. Data Nucl. Data Tables*, 99(1):62–68, 2013. doi: 10.1016/j.adt.2012.04.002.

[67] G. Werth. Hyperfine structure and g-factor measurements in ion traps. *Phys. Scr.*, 1995(Number T59):206, 1995.

[68] K. E. G. Löbner, M. Vetter, and V. Hönig. Nuclear intrinsic quadrupole moments and deformation parameters. *At. Data Nucl. Data Tables*, 7(5):495–564, 1970. doi: 10.1016/s0092-640x(18)30059-7.

[69] H. Kopferman, E. E. Schneider, and H. S. W. Massey. *Nuclear Moments, 2nd Edition*. Elsevier Science, 1958.

[70] E. W. Otten. Nuclear Radii and Moments of Unstable Isotopes. In *Treatise on Heavy Ion Science*, pages 517–638. Springer US, 1989. doi: 10.1007/978-1-4613-0713-6_7.

[71] E. C. Seltzer. KX-Ray Isotope Shifts. *Phys. Rev.*, 188(4):1916–1919, 1969. doi: 10.1103/physrev.188.1916.

[72] W. H. King. *Isotope Shifts in Atomic Spectra*. Springer Science + Business Media New York, 1984. ISBN 0306415623.

[73] G. Fricke, C. Bernhardt, K. Heilig, L. A. Schaller, L. Schellenberg, E. B. Shera, and C. W. Dejager. Nuclear Ground State Charge Radii from Electromagnetic Interactions. *At. Data Nucl. Data Tables*, 60(2):177–285, 1995. doi: 10.1006/adnd.1995.1007.

[74] K. M. Lynch, S. G. Wilkins, J. Billowes, C. L. Binnersley, M. L. Bissell, K. Chrysalidis, T. E. Cocolios, T. Day Goodacre, R. P. de Groote, G. J. Farooq-Smith, D. V. Fedorov, V. N. Fedosseev, K. T. Flanagan, S. Franchoo, R. F. Garcia Ruiz, W. Gins, R. Heinke, Á. Koszorús, B. A. Marsh, P. L. Molkanov, P. Naubereit, G. Neyens, C. M. Ricketts, S. Rothe, C. Seiffert, M. D. Seliverstov, H. H. Stroke, D. Studer, A. R. Vernon, K. D. A. Wendt, and X. F. Yang. Laser-spectroscopy studies of the nuclear structure of neutron-rich radium. *Phys. Rev. C*, 97(2):024309, 2018. doi: 10.1103/physrevc.97.024309.

[75] B. Cheal, T. E. Cocolios, and S. Fritzsche. Laser spectroscopy of radioactive isotopes: Role and limitations of accurate isotope-shift calculations. *Phys. Rev. A*, 86(4):042501, 2012. doi: 10.1103/physreva.86.042501.

[76] P. Jerabek, B. Schuetrumpf, P. Schwerdtfeger, and W. Nazarewicz. Electron and Nucleon Localization Functions of Oganesson: Approaching the Thomas-Fermi Limit. *Phys. Rev. Lett.*, 120(5):053001, ja 2018. doi: 10.1103/physrevlett.120.053001.

[77] A. Borschevsky, E. Eliav, M. J. Vilkas, Y. Ishikawa, and U. Kaldor. Predicted spectrum of atomic nobelium. *Phys. Rev. A*, 75(4):042514, 2007. doi: 10.1103/physreva.75.042514.

[78] E. V. Kahl, S. Raeder, E. Eliav, A. Borschevsky, and J. C. Berengut. Ab initio calculations of the spectrum of lawrencium. *Phys. Rev. A*, 104(5):052810, 2021. doi: 10.1103/physreva.104.052810.

[79] P. Schwerdtfeger, L. F. Pašteka, A. Punnett, and P. O. Bowman. Relativistic and quantum electrodynamic effects in superheavy elements. *Nucl. Phys. A*, 944:551–577, 2015. doi: 10.1016/j.nuclphysa.2015.02.005.

[80] S. Fritzsche. On the accuracy of valence-shell computations for heavy and super-heavy elements. *Eur. Phys. J. D*, 33(1):15–21, 2005. doi: 10.1140/epjd/e2005-00013-1.

[81] B. H. Bransden and C. J. Joachain. *Quantum mechanics*. Pearson, 2000. ISBN 9788131708392.

[82] B. H. Bransden and C. J. Joachain. *Physics of Atoms and Molecules*. Pearson Education (US), 2003. ISBN 058235692X.

[83] J.-P. Connerade. *Highly Excited Atoms*. Cambridge University Press, 1998. doi: 10.1017/cbo9780511524516.

[84] H. Bethe. *Intermediate quantum mechanics*. W.A. Benjamin, Reading, Mass, 1968. ISBN 9780805307559.

[85] S. Fritzsche. *Relativistische Theorie offenschaliger Atome*. PhD thesis, 1996. URL `http://www.uni-kassel.de/upress/online/frei/978-3-933146-02-1.volltext.frei.pdf`.

[86] P. Indelicato. Projection operators in multiconfiguration Dirac-Fock calculations: Application to the ground state of helium like ions. *Phys. Rev. A*, 51(2):1132–1145, 1995. doi: 10.1103/physreva.51.1132.

[87] P. Indelicato, J. P. Santos, S. Boucard, and J.-P. Desclaux. QED and relativistic corrections in superheavy elements. *Eur. Phys. J. D*, 45(1):155–170, 2007. doi: 10.1140/epjd/e2007-00229-y.

[88] A. Borschevsky. *Extension of the intermediate Hamiltonian Fock space coupled cluster method and applications to problems of heavy and superheavy elements*. PhD thesis, 2009.

[89] E. Eliav, U. Kaldor, P. Schwerdtfeger, B. A. Hess, and Y. Ishikawa. Ground State Electron Configuration of Element 111. *Phys. Rev. Lett.*, 73(24):3203–3206, 1994. doi: 10.1103/physrevlett.73.3203.

[90] J. Čížek. On the Correlation Problem in Atomic and Molecular Systems. Calculation of Wavefunction Components in Ursell-Type Expansion Using Quantum-Field Theoretical Methods. *J. Chem. Phys.*, 45(11):4256–4266, 1966. doi: 10.1063/1.1727484.

[91] J. P. Malrieu, P. Durand, and J. P. Daudey. Intermediate Hamiltonians as a new class of effective Hamiltonians. *J. Phys. A Math. Theor.*, 18(5):809–826, 1985. doi: 10.1088/0305-4470/18/5/014. URL `https://doi.org/10.1088/0305-4470/18/5/014`.

[92] V. A. Dzuba. V^{N-M} approximation for atomic calculations. *Phys. Rev. A*, 71(3):032512, 2005. doi: 10.1103/physreva.71.032512.

[93] M. S. Safronova, M. G. Kozlov, W. R. Johnson, and D. Jiang. Development of a configuration-interaction plus all-order method for atomic calculations. *Phys. Rev. A*, 80(1):012516, 2009. doi: 10.1103/physreva.80.012516.

[94] V. A. Dzuba, M. S. Safronova, and U. I. Safronova. Atomic properties of superheavy elements No, Lr, and Rf. *Phys. Rev. A*, 90(1):012504, 2014. doi: 10.1103/physreva.90.012504.

[95] V. A. Dzuba. Combination of the single-double–coupled-cluster and the configuration-interaction methods: Application to barium, lutetium, and their ions. *Phys. Rev. A*, 90(1):012517, 2014. doi: 10.1103/physreva.90.012517.

[96] W. R. Johnson and J. Sapirstein. Computation of Second-Order Many-Body Corrections in Relativistic Atomic Systems. *Phys. Rev. Lett.*, 57(9):1126–1129, 1986. doi: 10.1103/physrevlett.57.1126.

[97] V. A. Dzuba, V. V. Flambaum, and M. G. Kozlov. Combination of the many-body perturbation theory with the configuration-interaction method. *Phys. Rev. A*, 54(5):3948–3959, 1996. doi: 10.1103/physreva.54.3948.

[98] S. Fritzsche. Level Structure and Properties of Open f-Shell Elements. *Atoms*, 10(1):7, 2022. doi: 10.3390/atoms10010007.

[99] S. Fritzsche, C. Z. Dong, F. Koike, and A. Uvarov. The low-lying level structure of atomic lawrencium (Z = 103): energies and absorption rates. *Eur. Phys. J. D*, 45(1):107–113, 2007. doi: 10.1140/epjd/e2007-00136-3.

[100] B. G. C. Lackenby, V. A. Dzuba, and V. V. Flambaum. Calculation of atomic properties of superheavy elements Z=110–112 and their ions. *Phys. Rev. A*, 101(1):012514, jan 2020. doi: 10.1103/physreva.101.012514.

[101] S. O. Allehabi, J. Li, V. A. Dzuba, and V. V. Flambaum. Theoretical study of electronic structure of erbium and fermium. *J. Quant. Spectrosc. Radiat. Transf.*, 253:107137, 2020. doi: 10.1016/j.jqsrt.2020.107137.

[102] P. W. Milonni and J. H. Eberly. *Laser Physics*. John Wiley & Sons, Inc., 2010. doi: 10.1002/9780470409718.

[103] N. V. Vitanov, B. W. Shore, L. Yatsenko, K. Böhmer, T. Halfmann, T. Rickes, and K. Bergmann. Power broadening revisited: theory and experiment. *Opt. Commun.*, 199(1-4):117–126, 2001. doi: 10.1016/s0030-4018(01)01495-x.

[104] R. P. de Groote, M. Verlinde, V. Sonnenschein, K. T. Flanagan, I. Moore, and G. Neyens. Efficient, high-resolution resonance laser ionization spectroscopy using weak transitions to long-lived excited states. *Phys. Rev. A*, 95(3):032502, 2017. doi: 10.1103/physreva.95.032502.

[105] A. Kamal. Nuclear Models. In *Graduate Texts in Physics*, pages 353–423. Springer Berlin Heidelberg, 2014. doi: 10.1007/978-3-642-38655-8_6.

[106] G. Gamow. Mass defect curve and nuclear constitution. *Proc. Math. Phys. Eng. Sci.*, 126(803):632–644, 1930. doi: 10.1098/rspa.1930.0032.

[107] C. F. v. Weizsäcker. Zur Theorie der Kernmassen. *Z. Phys.*, 96(7-8):431–458, 1935. doi: 10.1007/bf01337700.

[108] M. G. Mayer. Nuclear Configurations in the Spin-Orbit Coupling Model. I. Empirical Evidence. *Phys. Rev.*, 78(1):16–21, 1950. doi: 10.1103/physrev.78.16.

[109] Th. Mayer-Kuckuk. *Kernphysik*. Teubner Verlag, 2002. doi: 10.1007/978-3-322-84876-5.

[110] P. F. A. Klinkenberg. Tables of Nuclear Shell Structure. *Rev. Mod. Phys.*, 24(2):63–73, 1952. doi: 10.1103/revmodphys.24.63.

[111] S. G. Nilsson. Binding states of individual nucleons in strongly deformed nuclei. *Dan. Mat. Fys. Medd. 29*, 16:1–69, 1955.

[112] P. Ring and P. Schuck. *The Nuclear Many-Body Problem*. Springer-Verlag GmbH, 2004. ISBN 9783540212065.

[113] B. R. Mottelson and S. G. Nilsson. Classification of the Nucleonic States in Deformed Nuclei. *Phys. Rev.*, 99(5):1615–1617, 1955. doi: 10.1103/physrev.99.1615.

[114] P. Moller, J. R. Nix, W. D. Myers, and W. J. Swiatecki. Nuclear Ground-State Masses and Deformations. *At. Data Nucl. Data Tables*, 59(2):185–381, 1995. doi: 10.1006/adnd.1995.1002.

[115] A. Bohr and B. R. Mottelson. *Nuclear Structure*. World Scientific Publishing Company, 1998. doi: 10.1142/3530.

[116] M. Sainath, K. Venkataramaniah, and P. C. Sood. Low-lying intrinsic structures in ^{254}Es. *Eur. Phys. J.*, 31(2):135–140, 2007. doi: 10.1140/epja/i2006-10201-y.

[117] S. Ćwiok, S. Hofmann, and W. Nazarewicz. Shell structure of the heaviest elements. *Nucl. Phys. A*, 573(3):356–394, 1994. doi: 10.1016/0375-9474(94)90349-2.

[118] A. Parkhomenko and A. Sobiczewski. Proton One-Quasiparticle States of Heaviest Nuclei. *Acta Phys. Pol. B*, B35(10):2447–2471, 2004. ISSN 0587-4254.

[119] F. P. Heßberger, S. Antalic, B. Streicher, S. Hofmann, D. Ackermann, B. Kindler, I. Kojouharov, P. Kuusiniemi, M. Leino, B. Lommel, R. Mann, K. Nishio, S. Saro, and B. Sulignano. Energy systematics of low-lying Nilsson levels in odd-mass einsteinium isotopes. *Eur. Phys. J.*, 26(2):233–239, 2005. doi: 10.1140/epja/i2005-10171-6.

[120] R. F. Casten. *Nuclear Structure from a Simple Perspective*. Oxford Science Publications, 2001. ISBN 0198507240.

[121] M. Block. Laser spectroscopy studies on nobelium. *EPJ Web of Conferences*, 163: 00006, 2017. doi: 10.1051/epjconf/201716300006.

[122] G. Choppin, J.-Ol. Liljenzin, J. Rydberg, and Ch. Ekberg. *Radiochemistry and Nuclear Chemistry*. Elsevier Science & Techn., 2013.

[123] S. Hofmann. Synthesis of superheavy elements by cold fusion. *Russ. Chem. Rev.*, 78 (12):1123–1138, 2009. doi: 10.1070/rc2009v078n12abeh004076.

[124] M. G. Itkis, E. Vardaci, I. M. Itkis, G. N. Knyazheva, and E. M. Kozulin. Fusion and fission of heavy and superheavy nuclei (experiment). *Nucl. Phys. A*, 944:204–237, 2015. doi: 10.1016/j.nuclphysa.2015.09.007.

[125] F. Lautenschläger. *Laserspektroskopie an Nobelium (Z=102) in einer Puffergaszelle*. PhD thesis, 2016. URL `https://tuprints.ulb.tu-darmstadt.de/5709/`.

[126] O. T. Kaleja. *High-precision mass spectrometry of nobelium, lawrencium and rutherfordium isotopes and studies of long-lived isomers with SHIPTRAP*. PhD thesis, 2020.

[127] W. Reisdorf. Analysis of fissionability data at high excitation energies. *Z. Phys. A*, 300(2-3):227–238, 1981. doi: 10.1007/bf01412298.

[128] W. Reisdorf and M. Schädel. How well do we understand the synthesis of heavy elements by heavy-ion induced fusion? *Z. Phys. A*, 343(1):47–57, 1992. doi: 10.1007/bf01291597.

[129] H. W. Gäggeler, D. T. Jost, A. Türler, P. Armbruster, W. Brüchle, H. Folger, F. P. Heßberger, S. Hofmann, G. Münzenberg, V. Ninov, W. Reisdorf, M. Schädel, K. Sümmerer, J. V. Kratz, U. Scherer, and M. E. Leino. Cold fusion reactions with ^{48}Ca. *Nucl. Phys. A*, 502:561–570, 1989. doi: 10.1016/0375-9474(89)90689-1.

[130] R.-D. Herzberg, P. T. Greenlees, P. A. Butler, G. D. Jones, I. G. Darby, S. Eeckhaudt, T. Grahn, C. Gray-Jones, F. P. Hessberger, P. Jones, R. Julin, S. Juutinen, S. Ketelhut, M. Leino, A.-P. Leppänen, S. Moon, M. Nyman, R. D. Page, J. Pakarinen, A. Pritchard, P. Rahkila, M. Sandzelius, J. Sarén, C. Scholey, A. Steer, J. Uusitalo, and M. Venhart. Isomer spectroscopy in ^{254}No. *Phys. Scr.*, T125:73–77, 2006. doi: 10.1088/0031-8949/2006/t125/016.

[131] S. Hofmann and G. Münzenberg. The discovery of the heaviest elements. *Rev. Mod. Phys.*, 72(3):733–767, 2000. doi: 10.1103/revmodphys.72.733.

[132] G. Münzenberg, W. Faust, S. Hofmann, P. Armbruster, K. Güttner, and H. Ewald. The velocity filter ship, a separator of unslowed heavy ion fusion products. *Nucl. Instrum. Methods*, 161(1):65–82, 1979. doi: 10.1016/0029-554x(79)90362-8.

[133] M. Laatiaoui, H. Backe, M. Block, F.-P. Heßberger, P. Kunz, F. Lautenschläger, W. Lauth, M. Sewtz, and Th. Walther. On laser spectroscopy of the element nobelium (Z = 102). *Eur. Phys. J. D*, 68(3), 2014. doi: 10.1140/epjd/e2014-40617-6.

[134] J. Ärje, J. Äystö, H. Hyvönen, P. Taskinen, V. Koponen, J. Honkanen, A. Hautojärvi, and K. Vierinen. Submillisecond On-Line Mass Separation of Nonvolatile Radioactive Elements: An Application of Charge Exchange and Thermalization Processes of Primary Recoil Ions in Helium. *Phys. Rev. Lett*, 54(2):99–101, 1985. doi: 10.1103/physrevlett.54.99.

[135] H. Backe, P. Kunz, W. Lauth, A. Dretzke, R. Horn, T. Kolb, M. Laatiaoui, M. Sewtz, D. Ackermann, M. Block, F. Herfurth, F. P. Heßberger, S. Hofmann, and R. Mann. Towards optical spectroscopy of the element nobelium ($Z = 102$) in a buffer gas cell. *Eur. Phys. J. D*, 45(1):99–106, 2007. doi: 10.1140/epjd/e2007-00198-1.

[136] J. B. Neumayr, L. Beck, D. Habs, S. Heinz, J. Szerypo, P. G. Thirolf, V. Varentsov, F. Voit, D. Ackermann, D. Beck, M. Block, Z. Di, S. A. Eliseev, H. Geissel, F. Herfurth, F. P. Heßberger, S. Hofmann, H.-J. Kluge, M. Mukherjee, G. Münzenberg, M. Petrick, W. Quint, S. Rahaman, C. Rauth, D. Rodríguez, C. Scheidenberger, G. Sikler, Z. Wang, C. Weber, W. R. Plaß, M. Breitenfeldt, A. Chaudhuri, G. Marx, L. Schweikhard, A. F. Dodonov, Y. Novikov, and M. Suhonen. The ion-catcher device for SHIPTRAP. *Nucl. Instrum. Methods Phys. Res. B*, 244(2):489–500, 2006. doi: 10.1016/j.nimb.2005.10.017.

[137] S. A. Eliseev, M. Block, A. Chaudhuri, Z. Di, D. Habs, F. Herfurth, H.-J. Kluge, J. B. Neumayr, W. R. Plaß, C. Rauth, P. G. Thirolf, G. Vorobjev, and Z. Wang. Extraction efficiency and extraction time of the SHIPTRAP gas-filled stopping cell. *Nucl. Instrum. Methods Phys. Res. B*, 258(2):479–484, 2007. doi: 10.1016/j.nimb.2007.01.291.

[138] M. Wada, Y. Ishida, T. Nakamura, Y. Yamazaki, T. Kambara, H. Ohyama, Y. Kanai, T. M. Kojima, Y. Nakai, N. Ohshima, A. Yoshida, T. Kubo, Y. Matsuo, Y. Fukuyama, K. Okada, T. Sonoda, S. Ohtani, K. Noda, H. Kawakami, and I. Katayama. Slow RI-beams from projectile fragment separators. *Nucl. Instrum. Methods Phys. Res. B*, 204: 570–581, 2003. doi: 10.1016/s0168-583x(02)02151-1.

[139] K. D. A. Wendt, K. Blaum, Ch. Geppert, P. Müller, W. Nörtershäuser, A. Schmitt, P. Schumann, N. Trautmann, and B. A. Bushaw. Laser Based Techniques for Ultra Trace Isotope Production, Spectroscopy and Detection. *Hyperfine Interact.*, 162(1-4): 147–157, 2006. doi: 10.1007/s10751-005-9219-8.

[140] H.-J. Kluge, B. A. Bushaw, G. Passler, K. Wendt, and N. Trautmann. Resonance ionization spectroscopy for trace analysis and fundamental research. *Fresenius J. Anal. Chem.*, 350(4-5):323–329, 1994. doi: 10.1007/bf00322490.

[141] V. S. Letokhov. *Laser photoionization spectroscopy.* Academic Press, Orlando, 1987. ISBN 0124443206.

[142] M. Savina and R. Trappitsch. Resonance ionization mass spectrometry (RIMS): Fundamentals and applications including secondary neutral mass spectrometry, October 2020.

[143] E. Kugler. The ISOLDE facility. *Hyperfine Interact.*, 129(1/4):23–42, 2000. doi: 10.1023/a:1012603025802.

[144] R. Neugart, J. Billowes, M. L. Bissell, K. Blaum, B. Cheal, K. T. Flanagan, G. Neyens, W. Nörtershäuser, and D. T. Yordanov. Collinear laser spectroscopy at ISOLDE: new methods and highlights. *J. Phys. G: Nucl. Part. Phys.*, 44(6):064002, 2017. doi: 10.1088/1361-6471/aa6642.

[145] V. Fedosseev, K. Chrysalidis, T. D. Goodacre, B. Marsh, S. Rothe, C. Seiffert, and K. Wendt. Ion beam production and study of radioactive isotopes with the laser ion source at ISOLDE. *J. Phys. G: Nucl. Part. Phys.*, 44(8):084006, 2017. doi: 10.1088/1361-6471/aa78e0.

[146] P. Bricault, F. Ames, T. Achtzehn, M. Dombsky, F. Labrecque, J. Lassen, J.-P. Lavoie, and N. Lecesne. An overview on TRIUMF's developments on ion source for radioactive beams (invited). *Rev. Sci. Instrum.*, 79(2):02A908, 2008. doi: 10.1063/1.2801344.

[147] A. Voss, M. R. Pearson, J. Billowes, F. Buchinger, B. Cheal, J. E. Crawford, A. A. Kwiatkowski, C. D. P. Levy, and O. Shelbaya. First Use of High-Frequency Intensity Modulation of Narrow-Linewidth Laser Light and Its Application in Determination of ^{206,205,204}Fr Ground-State Properties. *Phys. Rev. Lett*, 111(12):122501, 2013. doi: 10.1103/physrevlett.111.122501.

[148] K. Zimmer. Konzeption, Aufbau und Test der Ionenoptik des RISIKO-Massenseparators. *Diploma thesis, Johannes Gutenberg-Universität, Mainz*, 1990.

[149] R. E. Smalley, L. Wharton, and D. H. Levy. Molecular optical spectroscopy with supersonic beams and jets. *Acc. Chem. Res.*, 10(4):139–145, 1977. doi: 10.1021/ar50112a006.

[150] Yu. Kudryavtsev, P. Creemers, R. Ferrer, C. Granados, L. P. Gaffney, M. Huyse, E. Mogilevskiy, S. Raeder, S. Sels, P. Van den Bergh, P. Van Duppen, and A. Zadvornaya. A new in-gas-laser ionization and spectroscopy laboratory for off-line studies at KU Leuven. *Nucl. Instrum. Methods Phys. Res. B*, 376:345–352, 2016. doi: 10.1016/j.nimb.2016.02.040.

[151] W. Paul and H. Steinwedel. Notizen: Ein neues Massenspektrometer ohne Magnetfeld. *Z. Naturforsch. A*, 8(7):448–450, 1953. doi: 10.1515/zna-1953-0710.

[152] W. Paul and M. Raether. Das elektrische Massenfilter. *Z. Phys.*, 140(3):262–273, 1955. doi: 10.1007/bf01328923.

[153] W. Paul, H. P. Reinhard, and U. von Zahn. Das elektrische Massenfilter als Massenspektrometer und Isotopentrenner. *Z. Phys.*, 152(2):143–182, 1958. doi: 10.1007/bf01327353.

[154] W. Paul, O. Osberghaus, and E. Fischer. *Ein Ionenkäfig*. Forschungsberichte des Wirtschafts- und Verkehrsministeriums Nordrhein-Westfalen, Nr. 415, 1958. ISBN 3663046893.

[155] E. Fischer. Die dreidimensionale Stabilisierung von Ladungsträgern in einem Vierpolfeld. *Z. Phys.*, 156(1):1–26, 1959. doi: 10.1007/bf01332512.

[156] J. H. Gross. *Massenspektrometrie*. Springer Berlin Heidelberg, 2012. ISBN 3827429803. URL `https://link.springer.com/book/10.1007/978-3-8274-2981-0`.

[157] G. Bollen. Traps for Rare Isotopes. *Lect. Notes Phys.*, 651:169–210, 2004.

[158] R. Ferrer, B. Bastin, D. Boilley, P. Creemers, P. Delahaye, E. Liénard, X. Fléchard, S. Franchoo, L. Ghys, M. Huyse, Yu. Kudryavtsev, N. Lecesne, H. Lu, F. Lutton, E. Mogilevskiy, D. Pauwels, J. Piot, D. Radulov, L. Rens, H. Savajols, J. C. Thomas, E. Traykov, C. Van Beveren, P. Van den Bergh, and P. Van Duppen. In gas laser ionization and spectroscopy experiments at the Superconducting Separator Spectrometer (S3): Conceptual studies and preliminary design. *Nucl. Instrum. Methods Phys. Res. B*, 317:570–581, 2013. doi: 10.1016/j.nimb.2013.07.028.

[159] D. Rodriguez Rubiales. *An RFQ buncher for accumulation and cooling ofheavy radionuclides at SHIPTRAP and highprecision mass measurements on unstable Krisotopes at ISOLTRAP*. PhD thesis, 2003.

[160] A. Kellerbauer, T. Kim, R. B. Moore, and P. Varfalvy. Buffer gas cooling of ion beams. *Nucl. Instrum. Methods Phys. Res. A*, 469(2):276–285, 2001. doi: 10.1016/s0168-9002(01)00286-8.

[161] W. Lauth, H. Backe, M. Dahlinger, I. Klaft, P. Schwamb, G. Schwickert, N. Trautmann, and U. Othmer. Resonance ionization spectroscopy in a buffer gas cell with radioactive decay detection, demonstrated using Tl 208. *Phys. Rev. Lett.*, 68(11): 1675–1678, 1992. doi: 10.1103/physrevlett.68.1675.

[162] S. Raeder, M. Block, P. Chhetri, R. Ferrer, S. Kraemer, T. Kron, M. Laatiaoui, S. Nothhelfer, F. Schneider, P. Van Duppen, M. Verlinde, E. Verstraelen, Th. Walther, and A. Zadvornaya. A gas-jet apparatus for high-resolution laser spectroscopy on the heaviest elements at SHIP. *Nucl. Instrum. Methods Phys. Res. B*, 463:272–276, 2020. doi: 10.1016/j.nimb.2019.05.016.

[163] S. Nothhelfer. Entwicklungen für hochauflösende Laserspektroskope an Actiniden. Master's thesis, 2019.

[164] A. W. Johnson and J. B. Gerardo. Electronic-Recombination Coefficient of $^3He_2^+$ Compared to $^4He_2^+$. *Phys. Rev. A*, 7(4):1339–1341, 1973. doi: 10.1103/physreva.7.1339.

[165] R. Cooper, R. J. van Sonsbeek, and R. N. Bhave. Pulse radiolysis studies of ion-electron recombination in gaseous argon. *J. Chem. Phys.*, 98(1):383–389, 1993. doi: 10.1063/1.464631.

[166] J. F. Ziegler, M. D. Ziegler, and J. P. Biersack. SRIM: The stopping and range of ions in matter (2010). *Nucl. Instrum. Methods Phys. Res. B*, 268(11-12):1818–1823, 2010. doi: 10.1016/j.nimb.2010.02.091.

[167] J. F. Ziegler. Srim. *Online (URL: www.srim.org)*, 2016.

[168] D. Wittwer, F. Sh. Abdullin, N. V. Aksenov, Yu. V. Albin, G. A. Bozhikov, S. N. Dmitriev, R. Dressler, R. Eichler, H. W. Gäggeler, R. A. Henderson, S. Hübener, J. M. Kenneally, V. Ya. Lebedev, Yu. V. Lobanov, K. J. Moody, Yu. Ts. Oganessian, O. V. Petrushkin, A. N. Polyakov, D. Piguet, P. Rasmussen, R. N. Sagaidak, A. Serov, I. V. Shirokovsky, D. A. Shaughnessy, S. V. Shishkin, A. M. Sukhov, M. A. Stoyer, N. J. Stoyer, E. E. Tereshatov, Yu. S. Tsyganov, V. K. Utyonkov, G. K. Vostokin, M. Wegrzecki, and P. A. Wilk. Gas phase chemical studies of superheavy elements using the Dubna gas-filled recoil separator - Stopping range determination. *Nucl. Instrum. Methods Phys. Res. B*, 268(1):28–35, 2010. doi: 10.1016/j.nimb.2009.09.062.

[169] C. Droese, S. Eliseev, K. Blaum, M. Block, F. Herfurth, M. Laatiaoui, F. Lautenschläger, E. Minaya Ramirez, L. Schweikhard, V. V. Simon, and P. G. Thirolf. The cryogenic gas stopping cell of SHIPTRAP. *Nucl. Instrum. Methods Phys. Res. B*, 338: 126–138, 2014. doi: 10.1016/j.nimb.2014.08.004.

[170] D. A. Dahl. SIMION for the Personal Computer in Reflection. *Int. J. Mass Spectrom.*, 200(1-3):3–25, 2000. doi: 10.1016/s1387-3806(00)00305-5.

[171] E. Verstraelen. *Laser Spectroscopy of Actinides: Octupole Deformation and Gas-Jet Characterization*. PhD thesis, 2021.

[172] Comsol multiphysics. *URL: https://www.comsol.de/*, 2018.

[173] P. Chhetri. *Laser spectroscopy of nobelium isotopes*. PhD thesis, 2018.

[174] K. B. Blagoev and V. A. Komarovskii. Lifetimes of Levels of Neutral and Singly Ionized Lanthanide Atoms. *At. Data Nucl. Data Tables*, 56(1):1–40, 1994. doi: 10.1006/adnd.1994.1001.

[175] M. Aymar, A. Debarre, and O. Robaux. Highly excited levels of neutral ytterbium. *J. Phys. B*, 13(6):1089–1109, 1980. ISSN 0022-3700.

[176] K. Deilamian, J. D. Gillaspy, and D. E. Kelleher. Isotope shifts and hyperfine splittings of the 398.8-nm Yb i line. *J. Opt. Soc. Am. B.*, 10(5):789, 1993. doi: 10.1364/josab.10.000789.

[177] T. Loftus, J. R. Bochinski, and T. W. Mossberg. Simultaneous multi-isotope trapping of ytterbium. *Phys. Rev. A*, 63(5):053401, 2001. doi: 10.1103/physreva.63.053401.

[178] R. Ohmukai, S. Urabe, and M. Watanabe. Atom lithography with ytterbium beam. *Appl. Phys. B*, 77(4):415–419, 2003. doi: 10.1007/s00340-003-1281-9.

[179] R. Ferrer, M. Verlinde, E. Verstraelen, A. Claessens, M. Huyse, S. Kraemer, Yu. Kudryavtsev, J. Romans, P. Van den Bergh, P. Van Duppen, A. Zadvornaya, O. Chazot, G. Grossir, V. I. Kalikmanov, M. Nabuurs, and D. Reynaerts. Hypersonic nozzle for laser-spectroscopy studies at 17K characterized by resonance-ionization-spectroscopy-based flow mapping. *Phys. Rev. Res.*, 3(4):043041, 2021. doi: 10.1103/physrevresearch.3.043041.

[180] Yu. Khazov, A. Rodionov, and G. Shulyak. Nuclear Data Sheets for A = 146. *Nucl. Data Sheets*, 136:163–452, 2016. doi: 10.1016/j.nds.2016.08.002.

[181] N. Nica. Nuclear Data Sheets for A = 147. *Nucl. Data Sheets*, 110(4):749–997, 2009. doi: 10.1016/j.nds.2009.02.003.

[182] N. Nica. Nuclear Data Sheets for A = 148. *Nucl. Data Sheets*, 117:1–229, mar 2014. doi: 10.1016/j.nds.2014.02.001.

[183] S. K. Basu and A. A. Sonzogni. Nuclear Data Sheets for A = 150. *Nucl. Data Sheets*, 114(4-5):435–660, 2013. doi: 10.1016/j.nds.2013.04.001.

[184] B. Singh. Nuclear Data Sheets for A = 151. *Nucl. Data Sheets*, 110(1):1–264, 2009. doi: 10.1016/j.nds.2008.11.035.

[185] M. J. Martin. Nuclear Data Sheets for A = 152. *Nucl. Data Sheets*, 114(11):1497–1847, 2013. doi: 10.1016/j.nds.2013.11.001.

[186] L. Groening, A. Adonin, M. Baschke, X. Du, Ch. E. Düllmann, R. Hollinger, H. Hähnel, E. Jäger, M. Maier, S. Mickat, H. Podlech, U. Ratzinger, A. Rubin, P. Scharrer, B. Schlitt, G. Schreiber, A. Seibel, R. Tiede, H. Vormann, C. Xiao, A. Yakushev, and C. Zhang. Upgrade of the Universal Linear Accelerator UNILAC for FAIR. *Proceedings of the 7th International Particle Accelerator Conference - IPAC2016*, IPAC2016:880–882 (2016). doi:10.18429/JACoW, 2016. doi: 10.15120/GSI-2018-00067.

[187] O. Kaleja, B. Anđelić, K. Blaum, M. Block, P. Chhetri, C. Droese, Ch. E. Düllmann, M. Eibach, S. Eliseev, J. Even, S. Götz, F. Giacoppo, N. Kalantar-Nayestanaki, M. Laatiaoui, E. Minaya Ramirez, A. Mistry, T. Murböck, S. Raeder, L. Schweikhard, and P. G. Thirolf. The performance of the cryogenic buffer-gas stopping cell of SHIPTRAP. *Nucl. Instrum. Methods Phys. Res. B*, 463:280–285, 2020. doi: 10.1016/j.nimb.2019.05.009.

[188] O. Kaleja. Massenmessung von ^{197}Au mit SHIPTRAP und der erste on-line Test der neuen kryogenen Gaszelle an SHIP. Master's thesis, 2016.

[189] E. Browne and J. K. Tuli. Nuclear Data Sheets for A = 235. *Nucl. Data Sheets*, 122: 205–292, 2014. doi: 10.1016/j.nds.2014.11.002.

[190] M. S. Basunia. Nuclear Data Sheets for A = 237. *Nucl. Data Sheets*, 107(8):2323–2422, 2006. doi: 10.1016/j.nds.2006.07.001.

[191] B. Singh and E. Browne. Nuclear Data Sheets for A = 240. *Nucl. Data Sheets*, 109 (10):2439–2499, 2008. doi: 10.1016/j.nds.2008.09.002.

[192] H. Geiger and J. M. Nuttall. LVII. The ranges of the α particles from various radioactive substances and a relation between range and period of transformation. *The London, Edinburgh, and Dublin Philosophical Magazine and Journal of Science*, 22 (130):613–621, 1911. doi: 10.1080/14786441008637156.

[193] G. Gamow. Zur Quantentheorie des Atomkernes. *Z. Phys.*, 51(3-4):204–212, 1928. doi: 10.1007/bf01343196.

[194] A. Zadvornaya. *Characterization of the spectral resolution of the in-gas-jet laser ionization spectroscopy method*. PhD thesis, 2018.

[195] S. Roelens. Characterization of a hypersonic nozzle for laser spectroscopy of singly-charged thorium ions. Master's thesis, 2021.

[196] V. Gorshkov, V. Komarovskii, A. Oserovich, N. Penkin, and R. Khefferlin. Lifetimes of Dy I and Dy II excited levels. Oscillator strengths of Dy I spectral lines. *Opt. Spectrosc.*, 48:362–364, 1980.

[197] D. Münzberg, M. Block, A. Claessens, R. Ferrer, M. Laatiaoui, J. Lantis, S. Nothhelfer, S. Raeder, and P. Van Duppen. Resolution characterizations of the gas-jet apparatus Mainz using ^{164}Dy. *Atoms, to be published*.

[198] P. H. Dawson, editor. *Quadrupole Mass Spectrometry and Its Applications*. American Inst. of Physics, 1997. ISBN 1563964554.

[199] M. Verlinde, R. Ferrer, A. Claessens, C. A. Granados, S. Kraemer, Yu. Kudryavtsev, D. Li, P. Van den Bergh, P. Van Duppen, and E. Verstraelen. Single-longitudinal-mode pumped pulsed-dye amplifier for high-resolution laser spectroscopy. *Rev. Sci. Instrum.*, 91(10):103002, 2020. doi: 10.1063/5.0017985.

[200] M. Verlinde. *Towards the in-Gas Jet Laser Ionization Spectroscopy of the Th-229 Isomer*. PhD thesis, 2021. URL `https://limo.libis.be/primo-explore/fulldisplay?docid=LIRIAS3368224&context=L&vid=Lirias&search_scope=Lirias&tab=default_tab&fromSitemap=1`.

[201] P. Chhetri, D. Ackermann, H. Backe, M. Block, B. Cheal, J. Even, R. Ferrer, F. Hessberger, P. Kunz, M. Laatiaoui, F. Lautenschlaeger, W. Lauth, S. Raeder, T. Walther, and C. Wraith. Search for the optical transition in nobelium. *GSI Report 2015-1*, 2015. doi: 10.15120/GR-2015-1-MU-NUSTAR-SHE-P-10.

[202] A. Ghiorso, S. G. Thompson, G. H. Higgins, G. T. Seaborg, M. H. Studier, P. R. Fields, S. M. Fried, H. Diamond, J. F. Mech, G. L. Pyle, J. R. Huizenga, A. Hirsch, W. M. Manning, C. I. Browne, H. L. Smith, and R. W. Spence. New Elements Einsteinium and Fermium, Atomic Numbers 99 and 100. *Phys. Rev.*, 99(3):1048–1049, 1955. doi: 10.1103/physrev.99.1048.

[203] S. G. Thompson, A. Ghiorso, B. G. Harvey, and G. R. Choppin. Transcurium Isotopes Produced in the Neutron Irradiation of Plutonium. *Phys. Rev.*, 93(4):908–908, 1954. doi: 10.1103/physrev.93.908.

[204] M. H. Studier, P. R. Fields, H. Diamond, J. F. Mech, A. M. Friedman, P. A. Sellers, G. Pyle, C. M. Stevens, L. B. Magnusson, and J. R. Huizenga. Elements 99 and 100 from Pile-Irradiated Plutonium. *Phys. Rev.*, 93(6):1428–1428, 1954. doi: 10.1103/physrev.93.1428.

[205] P. R. Fields, M. H. Studier, J. F. Mech, H. Diamond, A. M. Friedman, L. B. Magnusson, and J. R. Huizenga. Additional Properties of Isotopes of Elements 99 and 100. *Phys. Rev.*, 94(1):209–210, 1954. doi: 10.1103/physrev.94.209.

[206] G. R. Choppin, S. G. Thompson, A. Ghiorso, and B. G. Harvey. Nuclear Properties of Some Isotopes of Californium, Elements 99 and 100. *Phys. Rev.*, 94(4):1080–1081, may 1954. doi: 10.1103/physrev.94.1080.

[207] A. Ghiorso, G. B. Rossi, B. G. Harvey, and S. G. Thompson. Reactions of U^{238} with Cyclotron-Produced Nitrogen Ions. *Phys. Rev.*, 93(1):257–257, 1954. doi: 10.1103/physrev.93.257.

[208] E. F. Worden, R. G. Gutmacher, and J. G. Conway. Use of Electrodeless Discharge Lamps in the Analysis of Atomic Spectra. *Appl. Opt.*, 2(7):707, 1963. doi: 10.1364/ao.2.000707.

[209] E. F. Worden, R. G. Gutmacher, R. W. Lougheed, J. E. Evans, and J. G. Conway. Hyperfine Structure in the ^{253}Es Emission Spectrum. *J. Opt. Soc. Am.*, 58(7):998, 1968. doi: 10.1364/josa.58.000998.

[210] E. F. Worden, R. G. Gutmacher, R. W. Lougheed, J. G. Conway, and R. J. Mehlhorn. Hyperfine Structure in the ^{253}Es Emission Spectrum II Nuclear Spin, Nuclear Magnetic Dipole Moment, and Energy Levels of Es ii. *J. Opt. Soc. Am.*, 60(10):1297, 1970. doi: 10.1364/josa.60.001297.

[211] L. S. Goodman and S. Wexler. Nuclear Spin and Magnetic Moment of 3.1-hr Cs^{134m}. *Phys. Rev.*, 99(1):192–198, 1955. doi: 10.1103/physrev.99.192.

[212] J. R. Peterson, N. Erdmann, M. Nunnemann, K. Eberhardt, G. Huber, J. V. Kratz, G. Passler, O. Stetzer, P. Thörle, N. Trautmann, and A. Waldek. Determination of the first ionization potential of einsteinium by resonance ionization mass spectroscopy (RIMS). *J. Alloys Compd.*, 271-273:876–878, 1998. doi: 10.1016/s0925-8388(98)00238-2.

[213] K. J. Moody, R. W. Lougheed, J. F. Wild, R. J. Dougan, E. K. Hulet, R. W. Hoff, C. M. Henderson, R. J. Dupzyk, R. L. Hahn, K. Sümmerer, G. D. O'Kelley, and G. R. Bethune. Decay properties of heavy mendelevium isotopes. *Nucl. Phys. A*, 563(1):21–73, 1993. doi: 10.1016/0375-9474(93)90010-u.

[214] C.-D. Herrmann, B. Prillwitz, V. Dämmrich, K. Freitag, P. Herzog, D. Mayer, K. Schlösser, and I. Ragnarsson. Magnetic dipole moments of the ground state of ^{228,230}Pa. *Nucl. Phys. A*, 493(1):83–90, 1989. doi: 10.1016/0375-9474(89)90533-2.

[215] E. Browne and J. K. Tuli. Nuclear Data Sheets for A = 251–259 (odd). *Nucl. Data Sheets*, 114(8-9):1041–1185, 2013. doi: 10.1016/j.nds.2013.08.002.

[216] M. Asai, K. Tsukada, M. Sakama, H. Haba, T. Ichikawa, Y. Ishii, A. Toyoshima, T. Ishii, I. Nishinaka, Y. Nagame, Y. Kasamatsu, M. Shibata, Y. Kojima, and H. Hayashi. Ground-state configuration of the N=157 nucleus ^{259}No. *Phys. Rev. C*, 87:014332, 2013. doi: 10.1103/PhysRevC.87.014332.

[217] B. Buck, A. C. Merchant, and S. M. Perez. Favoured alpha decays of odd-mass nuclei. *J. Phys. G Nucl. Part. Phys.*, 18(1):143–164, 1992. ISSN 0954-3899.

[218] I. Ahmad, R. K. Sjoblom, R. F. Barnes, E. P. Horwitz, and P. R. Fields. Nuclear decay properties of light einsteinium isotopes. *Nucl. Phys. A*, 140(1):141–153, 1970. doi: 10.1016/0375-9474(70)90890-0.

[219] W. S. Aaron, C. W. Alexander, R. L. Cline, E. D. Collins, J. A. Klein, J. B. Knauer, Jr, and S. Mirzadeh. Oak Ridge Isotope Products and Services - Current and Expected Supply and Demand. In *Office of Scientific & Technical Information Technical Reports*. Oak Ridge National Laboratory (ORNL), Oak Ridge, TN, 1999. URL `https://www.osti.gov/servlets/purl/7457`.

[220] S. Hogle, C. W. Alexander, J. D. Burns, J. G. Ezold, and G. I. Maldonado. Sensitivity Studies and Experimental Evaluation for Optimizing Transcurium Isotope Production. *Nucl. Sci. Eng.*, 185(3):473–483, 2017. doi: 10.1080/00295639.2016.1272973.

[221] T. Kieck, S. Biebricher, Ch. E. Düllmann, and K. Wendt. Optimization of a laser ion source for ^{163}Ho isotope separation. *Rev. Sci. Instrum.*, 90(5):053304, 2019. doi: 10.1063/1.5081094.

[222] F. Schneider, K. Chrysalidis, H. Dorrer, Ch. E. Düllmann, K. Eberhardt, R. Haas, T. Kieck, C. Mokry, P. Naubereit, S. Schmidt, and K. Wendt. Resonance ionization

of holmium for ion implantation in microcalorimeters. *Nucl. Instrum. Methods Phys. Res. B*, 376:388–392, 2016. doi: 10.1016/j.nimb.2015.12.012.

[223] T. Kieck, H. Dorrer, Ch. E. Düllmann, V. Gadelshin, F. Schneider, and K. Wendt. Highly efficient isotope separation and ion implantation of ^{163}Ho for the ECHo project. *Nucl. Instrum. Methods. Phys. Res. A*, 945:162602, 2019. doi: 10.1016/j.nima.2019.162602.

[224] T. Kron. *Pushing the Limits of Resonance Ionization Mass Spectrometry - Ionization Efficiency in Palladium and Spectral Resolution in Technetium.* PhD thesis, 2016.

[225] D. Studer. *Probing atomic and nuclear structure properties of promethium by laser spectroscopy.* PhD thesis, 2020.

[226] B. Eichler, S. Hübener, N. Erdmann, K. Eberhardt, H. Funk, G. Herrmann, S. Köhler, N. Trautmann, G. Passler, and F.-J. Urban. An Atomic Beam Source for Actinide Elements: Concept and Realization. *Radiochim. Acta*, 79(4), 1997. doi: 10.1524/ract.1997.79.4.221.

[227] K. Zhang, D. Studer, F. Weber, V. M. Gadelshin, N. Kneip, S. Raeder, D. Budker, K. Wendt, T. Kieck, S. G. Porsev, Ch. Cheung, M. S. Safronova, and M. G. Kozlov. Detection of the Lowest-Lying Odd-Parity Atomic Levels in Actinium. *Phys. Rev. Lett.*, 125(7):073001, 2020. doi: 10.1103/physrevlett.125.073001.

[228] S. Rothe, B. A. Marsh, C. Mattolat, V. N. Fedosseev, and K. Wendt. A complementary laser system for ISOLDE RILIS. *J. Phys. Conf. Ser.*, 312(5):052020, 2011. doi: 10.1088/1742-6596/312/5/052020.

[229] C. Mattolat. *Spektroskopische Untersuchungen an Technetium und Silizium: Ein Festkörperlasersystem für die Resonanzionisationsspektroskopie.* PhD thesis, 2010.

[230] A. Teigelhöfer, P. Bricault, O. Chachkova, M. Gillner, J. Lassen, J. P. Lavoie, R. Li, J. Meißner, W. Neu, and K. D. A. Wendt. Grating tuned Ti:Sa laser for in-source spectroscopy of Rydberg and autoionizing states. *Hyperfine Interact.*, 196(1-3):161–168, 2010. doi: 10.1007/s10751-010-0171-x.

[231] V. Sonnenschein, I. D. Moore, S. Raeder, M. Reponen, H. Tomita, and K. Wendt. Characterization of a pulsed injection-locked Ti:sapphire laser and its application to high resolution resonance ionization spectroscopy of copper. *Laser Phys.*, 27(8):085701, 2017. doi: 10.1088/1555-6611/aa7834.

[232] V. Sonnenschein. *Laser developements and high resolution resonance ionization spectroscopy of actinide elements.* PhD thesis, 2014.

[233] P. Naubereit. Weiterentwicklung eines weitabstimmbaren Titan:Saphir-Lasers und sein Einsatz zur Spektroskope hochliegender Resonanzen in Holmium. Master's thesis, 2014.

[234] R. Horn. *Aufbau eines Systems gepulster, abstimmbarer Festkörperlaser zum Einsatz in der Resonanzionisations-Massenspektrometrie*. PhD thesis, 2003.

[235] R. P. de Groote, I. Budinčević, J. Billowes, M. L. Bissell, T. E. Cocolios, G. J. Farooq-Smith, V. N. Fedosseev, K. T. Flanagan, S. Franchoo, R. F. Garcia Ruiz, H. Heylen, R. Li, K. M. Lynch, B. A. Marsh, G. Neyens, R. E. Rossel, S. Rothe, H. H. Stroke, K. D. A. Wendt, S. G. Wilkins, and X. Yang. Use of a Continuous Wave Laser and Pockels Cell for Sensitive High-Resolution Collinear Resonance Ionization Spectroscopy. *Phys. Rev. Lett.*, 115(13):132501, 2015. doi: 10.1103/physrevlett.115.132501.

[236] F. Weber, Th. E. Albrecht-Schoenzart, M. Block, P. Chhetri, Ch. E. Düllmann, J. G. Ezold, V. Gadelshin, A. Gaiser, F. Giacoppo, R. Heinke, T. Kieck, N. Kneip, M. Laatiaoui, Ch. Mokry, S. Nothhelfer, S. Raeder, J. Runke, F. Schneider, J. M. Sperling, D. Studer, P. Thörle-Pospiech, N. Trautmann, and K. Wendt. Resonance laser ionization spectroscopy on einsteinium. *To be submitted*.

[237] W. Gins, R. P. de Groote, M. L. Bissell, C. Granados Buitrago, R. Ferrer, K. M. Lynch, G. Neyens, and S. Sels. Analysis of counting data: Development of the SATLAS Python package. *Comput. Phys. Commun.*, 222:286–294, 2018. doi: 10.1016/j.cpc.2017.09.012.

[238] P. C. Magnante and H. H. Stroke. Isotope Shift between ^{209}Bi and 6.3-day ^{206}Bi. *J. Opt. Soc. Am.*, 59(7):836, 1969. doi: 10.1364/josa.59.000836.

[239] N. Erdmann, M. Nunnemann, K. Eberhardt, G. Herrmann, G. Huber, S. Köhler, J. V. Kratz, G. Passler, J. R. Peterson, N. Trautmann, and A. Waldek. Determination of the first ionization potential of nine actinide elements by resonance ionization mass spectroscopy RIMS. *J. Alloys Compd.*, 271-273:837–840, 1998. doi: 10.1016/s0925-8388(98)00229-1.

[240] R. T. Birge. Probable Values of the General Physical Constants. *Rev. Mod. Phys.*, 1 (1):1–73, 1929. doi: 10.1103/revmodphys.1.1.

[241] O. Bodnar and C. Elster. On the adjustment of inconsistent data using the Birge ratio. *Metrologia*, 51(5):516–521, 2014. doi: 10.1088/0026-1394/51/5/516.

[242] A. E. Barzakh, J. G. Cubiss, A. N. Andreyev, M. D. Seliverstov, B. Andel, S. Antalic, P. Ascher, D. Atanasov, D. Beck, J. Bieroń, K. Blaum, Ch. Borgmann, M. Breitenfeldt, L. Capponi, T. E. Cocolios, T. Day Goodacre, X. Derkx, H. De Witte, J. Elseviers, D. V. Fedorov, V. N. Fedosseev, S. Fritzsche, L. P. Gaffney, S. George, L. Ghys, F. P. Heßberger, M. Huyse, N. Imai, Z. Kalaninová, D. Kisler, U. Köster, M. Kowalska, S. Kreim, J. F. W. Lane, V. Liberati, D. Lunney, K. M. Lynch, V. Manea, B. A. Marsh, S. Mitsuoka, P. L. Molkanov, Y. Nagame, D. Neidherr, K. Nishio, S. Ota, D. Pauwels, L. Popescu, D. Radulov, E. Rapisarda, J. P. Revill, M. Rosenbusch, R. E. Rossel, S. Rothe, K. Sandhu, L. Schweikhard, S. Sels, V. L. Truesdale, C. Van Beveren, P. Van den Bergh, P. Van Duppen, Y. Wakabayashi, K. D. A. Wendt, F. Wienholtz, B. W. Whitmore, G. L. Wilson, R. N. Wolf, and K. Zuber. Inverse odd-even staggering

in nuclear charge radii and possible octupole collectivity in ^{217,218,219}At revealed by in-source laser spectroscopy. *Phys. Rev. C*, 99(5):054317, 2019. doi: 10.1103/physrevc.99.054317.

[243] S. Büttgenbach. Magnetic hyperfine anomalies. *Hyperfine Interact.*, 20(1):1–64, 1984. doi: 10.1007/bf02043319.

[244] N. P. Penkin and V. A. Komarovsky. Oscillator strengths of spectral lines and lifetimes of atoms of rare earth elements with unfilled 4f-shell. *J. Quant. Spectrosc. Radiat. Transf.*, 16(3):217–252, 1976.

[245] R. Heinke, T. Kron, S. Raeder, T. Reich, P. Schönberg, M. Trümper, C. Weichhold, and K. Wendt. High-resolution in-source laser spectroscopy in perpendicular geometry. *Hyperfine Interact.*, 238(1), 2016. doi: 10.1007/s10751-016-1386-2.

[246] H. Backe, A. Dretzke, S. Fritzsche, R. G. Haire, P. Kunz, W. Lauth, M. Sewtz, and N. Trautmann. Laser Spectroscopic Investigation of the Element Fermium (Z = 100). In *Laser 2004*, pages 3–14. Springer-Verlag. doi: 10.1007/3-540-30926-8_1.

[247] D. Meierfrankenfeld, A. Bury, and M. Thoennessen. Discovery of scandium, titanium, mercury, and einsteinium isotopes. *At. Data Nucl. Data Tables*, 97(2):134–151, 2011. doi: 10.1016/j.adt.2010.11.001.

[248] E. Browne and J. K. Tuli. Nuclear Data Sheets for A = 245. *Nucl. Data Sheets*, 112 (2):447–494, 2011. doi: 10.1016/j.nds.2011.01.002.

[249] F. P. Heßberger, S. Antalic, D. Ackermann, Z. Kalaninová, S. Heinz, S. Hofmann, B. Streicher, B. Kindler, I. Kojouharov, P. Kuusiniemi, M. Leino, B. Lommel, R. Mann, K. Nishio, Š. Šáro, B. Sulignano, and M. Venhart. Alpha-gamma decay studies of ^{253}No and its daughter products ^{253}Md, ^{249}Fm. *Eur. Phys. J.*, 48(5), 2012. doi: 10.1140/epja/i2012-12075-8.

[250] R. Hingmann, W. Kuehn, V. Metag, R. Novotny, A. Ruckelshausen, H. Stroeher, F. Hessberger, S. Hofmann, G. Muenzenberg, and W. Reisdorf. Radioactive decays of neutron deficient actinide nuclei. *GSI Scientific report GSI-85-1 (1984) (Darmstadt, 1985)*, page 88. URL `http://repository.gsi.de/record/53546`.

[251] V. Ninov, F. P. Heßberger, S. Hofmann, H. Folger, G. Münzenberg, P. Armbruster, A. V. Yeremin, A. G. Popeko, M. Leino, and S. Saro. Identification of new mendelevium and einsteinium isotopes in bombardments of ^{209}Bi with ^{40}Ar. *Z. Phys. A.*, 356(1): 11–12, 1996. doi: 10.1007/s002180050141.

[252] R. Briselet, Ch. Theisen, M. Vandebrouck, A. Marchix, M. Airiau, K. Auranen, H. Badran, D. Boilley, T. Calverley, D. Cox, F. Déchery, F. Defranchi Bisso, A. Drouart, B. Gall, T. Goigoux, T. Grahn, P. T. Greenlees, K. Hauschild, A. Herzan, R. D. Herzberg, U. Jakobsson, R. Julin, S. Juutinen, J. Konki, M. Leino, A. Lightfoot, A. Lopez-Martens, A. Mistry, P. Nieminen, J. Pakarinen, P. Papadakis, J. Partanen,

P. Peura, P. Rahkila, J. Rubert, P. Ruotsalainen, M. Sandzelius, J. Saren, C. Scholey, J. Sorri, S. Stolze, B. Sulignano, J. Uusitalo, A. Ward, and M. Zielińska. Production cross section and decay study of ^{243} and ^{249}Md. *Phys. Rev. C*, 99(2):024614, 2019. doi: 10.1103/physrevc.99.024614.

[253] S. Antalic, F. P. Heßberger, S. Hofmann, D. Ackermann, S. Heinz, B. Kindler, I. Kojouharov, P. Kuusiniemi, M. Leino, B. Lommel, R. Mann, and Š. Šáro. Studies of neutron-deficient mendelevium isotopes at SHIP. *Eur. Phys. J.*, 43(1), 2009. doi: 10.1140/epja/i2009-10896-0.

[254] F. P. Heßberger, S. Hofmann, D. Ackermann, S. Antalic, B. Kindler, I. Kojouharov, P. Kuusiniemi, M. Leino, B. Lommel, R. Mann, K. Nishio, A. G. Popeko, B. Sulignano, S. Saro, B. Streicher, M. Venhart, and A. V. Yeremin. Alpha-gamma decay studies of ^{255}Rf, ^{251}No and ^{247}Fm. *Eur. Phys. J.*, 30(3):561–569, 2006. doi: 10.1140/epja/i2006-10137-2.

[255] F. P. Heßberger. GSI experiments on synthesis and nuclear structure investigations of the heaviest nuclei. *Eur. Phys. J. D*, 45(1):33–37, 2007. doi: 10.1140/epjd/e2007-00146-1.

[256] A. Borschevsky, E. Eliav, M. J. Vilkas, Y. Ishikawa, and U. Kaldor. Transition energies of atomic lawrencium. *Eur. Phys. J. D*, 45(1):115–119, 2007. doi: 10.1140/epjd/e2007-00130-9.

[257] S. Antalic, F. P. Heßberger, S. Hofmann, D. Ackermann, S. Heinz, B. Kindler, I. Kojouharov, P. Kuusiniemi, M. Leino, B. Lommel, R. Mann, K. Nishio, Š. Šáro, B. Streicher, B. Sulignano, and M. Venhart. Decay studies of neutron-deficient lawrencium isotopes. *Eur. Phys. J.*, 38(2):219–226, 2008. doi: 10.1140/epja/i2008-10665-7.

[258] M. A. Lieberman and A. J. Lichtenberg. *Principles of Plasma Discharges and Materials Processing*. John Wiley & Sons, Inc., 2005. doi: 10.1002/0471724254.

[259] K. T. A. L. Burm. Calculation of the Townsend Discharge Coefficients and the Paschen Curve Coefficients. *Contrib. to Plasma Phys.*, 47(3):177–182, 2007. doi: 10.1002/ctpp.200710025.

Abbreviations and Symbols

Abbreviations

List of abbreviations in alphabetical order.

ABMR	Atomic-Beam Magnetic-Resonance
AC	Alternating Current
AI	Autoionization
a.u.	Arbitrary Units
CEM	Channel Electron Multiplier
CERN	European Organization for Nuclear Research (french: Conseil Européen pour la Recherche Nucléaire)
CC	Coupled Cluster
CI	Configuration Interaction
CI + MBPT	Configuration Interaction Many-Body Perturbation Theory
CN	Compound Nucleus
CSF	Configuration State Functions
cw	Continuous Wave
DC	Direct Current
DCM	4-(Dicyanmethylen)-6-(4-dimethylaminostyryl)-2-methyl-4H-pyran
DF	Dirac-Fock
DL	Diode Laser
EC	Electron Capture
EVR	EVaporation Residue
FES	First Excitation Step
FS	Field Shift
FSCC	Fock Space Coupled Cluster
FWHM	Full Width at Half Maximum
HIM	Helmholtz Institute Mainz
HF	Hartree-Fock
HFIR	High Flux Isotope Reactor
HFS	HyperFine Structure
IGISOL	Ion-Guide Isotope-Separator On-Line
IHFSCC	Intermediate Hamiltonian Fock Space Coupled Cluster
IP	Ionization Potential
IS	Isotope Shift
ISAC	Isotope Separator and ACcelerator
ISOL	Isotope Separator On-Line

ISOLDE	Isotope Separation On-Line DEvice
JGU	Johannes Gutenberg University
KU Leuven	Katholieke Universiteit Leuven
LARISSA	Laser Resonance Ionization Spectroscopy for Selective Applications
LASER	Light Amplification by Stimulated Emission of Radiation
LDM	Liquid Drop Model
LIF	Laser Induced Fluorescence
MCDHF	MultiConfiguration Dirac-Hartree-Fock
MLM	Multi Longitudinal Mode
mms	Multi-Mode Spectroscopy
MNT	MultiNucleon Transfer
MS	Mass Shift
NMS	Normal Mass Shift
OES	Odd-Even Staggering
ORNL	Oak Ridge National Laboratory
PCB	Printed Circuit Board
PEEK	PolyEther Ether Ketone
PI-LIST	Perpendicularly Illuminated Laser Ion Source and Trap
PIPS	Passivated, Implanted, Planar Silicon
QED	Quantum ElectroDynamics
RADRIS	RAdiation Detected Resonance Ionization Spectroscopy
RCC	Relativistic Coupled Cluster
RF	RadioFrequency
RFQ	RadioFrequency Quadrupole
RIB	Radioactive Ion Beam
RIMS	Resonance Ionization Mass Spectrometry
RIPS	RIken Projectile fragment Separator
RIS	Resonance Ionization Spectroscopy
RISIKO	Resonance Ionization Spectroscopy In COllinear geometry (german: ResonanzIonisations-Spektroskopie In KOllinearer Geometrie)
SATLAS	Statistical Analysis Toolbox for LAser Spectroscopy (python package)
SEM	Secondary Electron Multiplier
SES	Second Excitation Step
SHE	SuperHeavy Elements
SHG	Second Harmonic Generation
SHIP	Separator for Heavy Ion reaction Products
SLM	Single Longitudinal Mode
SM	Shell Model
sms	Single-Mode Spectroscopy
SMS	Specific Mass Shift
SRIM	Stopping and Range of Ions in Matter
THG	Third Harmonic Generation
TOF	Time-Of-Flight

UNILAC UNIversal Linear ACcelerator
VKI Von Karman Institute for Fluid Dynamics

Symbols and Elements

Symbols for important parameters, constants, and elements.

a	Dimensionless parameter
a	Constant measuring the surface diffuseness of nuclei
α	Fine-structure constant (Sommerfeld's constant)
α_i	Dirac-matrices
$a(\nu)$	Absorption coefficient
A	Magnetic hyperfine coupling constant
A	Effective area of excitation
A	Saturation ionization in a gas
A/A'	Atomic mass
A_{ki}	Transition strength (Einstein-coefficients)
A_{21}	Einstein coefficient of the spontaneous emission
$\hat{A}_{\mathrm{wm}}$	Weighted mean
$\Delta\hat{A}_{\mathrm{Birge}}$	Increased standard uncertainty
$\Delta\hat{A}_{\mathrm{wm}}$	Weighted uncertainty
Ac	Actinium
Am	Americium
b	Dimensionless parameter
b	Background rate of the linear function
B	Electric hyperfine coupling constant
B	Magnetic field
B_{ij}	Breit correction term
B_J	Magnetic field of the electronic shell at the nucleus
B_{12}	Einstein coefficient of the absorption
B_{21}	Einstein coefficient of the stimulated emission
β_2	Deformation parameter
Bi	Bismuth
Bk	Berkelium
c	Speed of light
c	Speed of sound
c_i	Coefficients
C_i	Expansion parameters
c_v	Mixing coefficient of the respective base
Ca	Calcium
Cf	Californium
Cm	Curium
d	Gap length
Δ	Laplace operator
${}^1\Delta^2$	Differential hyperfine anomaly

Dy	Dysprosium
$^{\mathrm{nat}}$Dy	Natural dysprosium composed of seven stable isotopes ^{156,158,160,161,162,163,164}Dy
e	Electron charge
E	Energy
E^*	Inner excitation energy of the compound nucleus
E_{thr}	Threshold energy of a nuclear reaction
E_{C}	Coulomb energy
E_{CB}	Coulomb barrier
E_{kin}	Kinetic energy
E_{nucl}	Attractive nuclear potential
E_{pot}	Potential energy
ϵ_0	Vacuum permittivity
ϵ_2	Quadrupole deformation parameter
ϵ_{BR}	Breit-Crawford-Rosenthal-Schawlow correction
ϵ_{BW}	Bohr-Weisskopf effect
ϵ_m	Dirac-Fock energies of corresponding single-electron basis states
$\tilde{\epsilon}_v$	Dirac-Fock energy of the lowest orbital
e^S	Exponential formalism
Er	Erbium
Es	Einsteinium
Es I	Neutral einsteinium
Es II	Einsteinium ion
F	Atomic total angular momentum
F_{FS}	Field shift constant
$\vec{F}$	Force
Fm	Fermium
γ	FWHM
γ	Secondary-electron-emission coefficient
G	Gain
g_I	Landé g-factor
G_{thr}	Threshold gain
Gd	Gadolinium
h	Planck constant
$\hat{h}_1(r_i)$	Individual single-electron Hamiltonian
$\hat{h}_2(r_i, r_j)$	Operator representing the interaction between the valence electrons
h_D	One-electron Dirac operator
H	Hamiltonian
H^{eff}	Effective Hamiltonian
H_{DC}	Dirac-Coulomb-Hamiltonian
H_{DCB}	Dirac-Coulomb-Breit-Hamiltonian
He	Helium
HNO_3	Nitric acid
Ho	Holmium

I	Nuclear spin
$I_{F \to F'}$	Theoretical line intensity
I_0	Resonance intensity
$I(\nu)$	Intensity of a frequency distribution
$I(\nu_0)$	Resonance intensity
$I(\omega_0)$	Resonance intensity
$I(\omega)$	Intensity of a frequency distribution
I_{Racah}	Racah intensity
I_{sat}	Saturation intensity
j	Total angular momentum of an electron
J	Total angular momentum of the atomic shell
$J(t)$	Photon flux
K	Projection of the nuclear spin upon the symmetry axis
k_{B}	Boltzmann constant
K_{MS}	Mass shift constant
l	Angular momentum quantum number
L	Total orbital angular momentum
L	Resonator length
λ	Wavelength
λ_1	Wavelength of the excitation step
λ_2	Wavelength of the ionization step
Λ	Projection of total orbital angular momentum L on the symmetry axis
La	Lanthanum
Li	Lithium
Lr	Lawrencium
Lu	Lutetium
M	Mach number
M	Total number of valence electrons in the neutral atom
m	Mass
m	Slope of the linear function
m_l	Magnetic quantum number
m_s	Magnetic spin quantum number
Δm	Mass uncertainty
μ	Modifying factor
μ	Reduced mass
μ_I	Magnetic-dipole moment
μ_{N}	Nuclear magneton
n	Principal quantum number
n	Neutron
N	Neutron number
N	Total number of electrons in the neutral atom
N_1 / N_2	Populations of ground state / excited state
$\bar{N}_1$ / $\bar{N}_2$	Steady-state solutions

N_B	Density of atom B
Nd	Neodymium
Ne	Neon
No	Nobelium
n_z	Oscillator quantum number parallel to symmetry axis
$n_\perp$	Oscillator quantum number perpendicular to symmetry axis
ν	Frequency
ν_0	Center frequency
$\delta\nu$	Line broadening
$\Delta\nu$	Line shift
$\delta\nu_\mathrm{jet}$	Doppler broadening of the jet
$\delta\nu_\mathrm{laser}$ / $\delta\nu_\mathrm{L}$	Laser bandwidth
$\delta\nu_\mathrm{nat}$	Natural linewidth
$\delta\nu^{A,A'}$	Isotope shift
Og	Oganesson
ω	Angular frequency
Ω	Projection of total angular momentum J on the symmetry axis
$\Omega[Nn_z\Sigma]$	Nilsson quantum number
p	Momentum
p	Projectile
P	Pumping rate
P	Laser power
p	Pressure
p_0	Stagnation pressure in the gas cell
p_bg	Background pressure in the jet cell
p_Det	Pressure in the detector cell
Pb	Lead
PbS	Lead sulfide
ϕ_i	Functions constructed from the single-electron valence basis states
$\phi_i(r)$	Radial part of the wavefunction
Φ_0	Total potential
π	Parity
Ψ	Wavefunction
$\lvert\Psi_e(0)\rvert^2$	Probability density of the electron
$\Psi(PJM)$	Bound atomic wavefunction
Pu	Plutonium
q	Electric charge
Q	Intrinsic quadrupole moment
Q_s	Spectroscopic electric quadrupole moment
Q-value	Amount of energy of a nuclear reaction
r	Relative coordinate in respect to the system's center of mass
r	Distance of the nucleons to the center of the nucleus
r_C	Coulomb radius

r_{nucl}	Nuclear radius
R	Mass-resolving power
R	Nuclear radius
R	Distance of the nucleon from the center at which $V = V_0/2$
r_0	Free radius of the RFQ
$\langle r^2 \rangle$	Nuclear mean-square charge radius
$\delta\langle r^2 \rangle^{A,A'}$	Change in nuclear mean-square charge radius
$R_{n,l}(r)$	Radial function
R_{21}	Collision induced transition probability
R_y	Rydberg constant
R_{rod}	Rod radius of the RFQ
ρ_{mv}	Excitation coefficient of the atomic wave function
$\rho(\vec{r})$	Charge density function
Rf	Rutherfordium
S	Sulfur
S	Total spin
S	Saturation parameter
S	Excitation operator
s	Spin quantum number
σ	Cross-section
$\hat{\sigma}_{\mathrm{B}}$	Birge ratio
Σ	Projection of total spin S on the symmetry axis
$\hat{\Sigma}_1$	Correlation potential operator
$\hat{\Sigma}_2$	Correlation correction operator
Σ_{mv}	Matrix element of the correlation interaction of a valence electron with the core
Sn	Tin
t	Time
T	Temperature
T	Target
Ta	Tantalum
Tb	Terbium
Th	Thorium
Ti	Titanium
Ti:Sa	Titanium-sapphire laser
Tm	Thulium
τ	Dimensionless parameter
τ	Lifetime
τ_{eff}	Effective lifetime
τ_{pulse}	Pulse width
$T_{1/2}$	Half life
U	Uranium
u_{nl}	Eigenfunction
v	Velocity

v_w	Most likely speed
V_0	Depth of the Woods-Saxon potential
V_B	Breakdown voltage
V_c	Coulomb potential
V^{N-M}	Frozen core Dirac-Fock potential
$\mathrm{V_{PP}}$	Peak-to-peak voltage
$V_{zz}(0)$	Electric field gradient at the nucleus
W	Tungsten
$dW(t)$	Excitation probability
x	Relative frequency to the center of gravity of the HFS
x	Distance between the projectile and target nuclei
$X_{nl}(r)$	Exchange function
y_0	Measured count rate
y_1	Adjusted count rate
YAG	Yttrium aluminum garnet
Yb	Ytterbium
$^{\mathrm{nat}}$Yb	Natural ytterbium composed of seven stable isotopes ^{168,170,171,172,173,174,176}Yb
$Y_l^m(\vartheta, \varphi)$	Angular spherical harmonics
$Y_{nl}(r)$	Coulomb potential
Z	Proton number
$\zeta_i(\eta)$	Spin dependent part of the wavefunction
Zr	Zirconium

Acknowledgements

Personenbezogene Daten

Funding

This research was supported by the U.S. Department of Energy, Office of Science, Office of Basic Energy Sciences, Heavy Elements Chemistry Program, under Award DE-FG02-13ER16414. The isotopes used in this research were supplied by the U.S. DOE Isotope Program, managed by the Office of Science. This work has been supported by the Bundesministerium für Bildung und Forschung (BMBF, Germany) under project number 05P18UMCIA. This project has received funding from the European Union's Horizon 2020 research and innovation programme under grant agreement No 861198 – LISA – H2020-MSCA-ITN-2019.

Publications

- S. Nothhelfer, Th. E. Albrecht-Schoenzart, M. Block, P. Chhetri, Ch. E. Düllmann, J. G. Ezold, V. Gadelshin, A. Gaiser, F. Giacoppo, R. Heinke, T. Kieck, N. Kneip, M. Laatiaoui, Ch. Mokry, S. Raeder, J. Runke, F. Schneider, J. M. Sperling, D. Studer, P. Thörle-Pospiech, N. Trautmann, F. Weber and K. Wendt. Nuclear structure investigations of $^{253\text{-}255}$Es by laser spectroscopy. *Phys. Rev. C*, 105(2):1021302, 2022.
- F. Weber, Th. E. Albrecht-Schoenzart, M. Block, P. Chhetri, Ch. E. Düllmann, J. G. Ezold, V. Gadelshin, A. Gaiser, F. Giacoppo, R. Heinke, T. Kieck, N. Kneip, M. Laatiaoui, Ch. Mokry, S. Nothhelfer, S. Raeder, J. Runke, F. Schneider, J. M. Sperling, D. Studer, P. Thörle-Pospiech, N. Trautmann, and K. Wendt. Resonance laser ionization spectroscopy on einsteinium. To be pusblished.
- S. Raeder, M. Block, P. Chhetri, R. Ferrer, S. Kraemer, T. Kron, M. Laatiaoui, S. Nothhelfer, F. Schneider, P. Van Duppen, M. Verlinde, E. Verstraelen, Th. Walther and A. Zadvornaya. A gas-jet apparatus for high-resolution laser spectroscopy on the heaviest elements at SHIP. *Nucl. Instrum. Meth. B*, 463:272-276, 2020.

Conferences, Schools and Trainings

Personenbezogene Daten

Curriculum Vitae

Personenbezogene Daten